Lights, Camera, Reaction!

The Influence of Interfacial Chemistry on Nanoparticle Photoreactivity

by

Jeffrey Michael Farner Budarz

Department of Civil and Environmental Engineering
Duke University

Date:_____

Approved:

_____
Mark R. Wiesner, Supervisor

_____
Claudia K. Gunsch

_____
Jerome Rose

_____
Richard T. Di Giulio

Dissertation submitted in partial fulfillment of
the requirements for the degree of Doctor
of Philosophy in the Department of
Civil and Environmental Engineering in the Graduate School
of Duke University

2016

ABSTRACT

Lights, Camera, Reaction!

The Influence of Interfacial Chemistry on Nanoparticle Photoreactivity

by

Jeffrey Michael Farner Budarz

Department of Civil and Environmental Engineering
Duke University

Date:_____

Approved:

_____
Mark R. Wiesner, Supervisor

_____
Claudia K. Gunsch

_____
Jerome Rose

_____
Richard T. Di Giulio

An abstract of a dissertation submitted in partial
fulfillment of the requirements for the degree
of Doctor of Philosophy in the Department of
Civil and Environmental Engineering in the Graduate School of
Duke University

2016

Abstract

The ability of photocatalytic nanoparticles (NPs) to produce reactive oxygen species (ROS) has inspired research into several new applications and technologies, including water purification, contaminant remediation, and self-cleaning surface coatings. As a result, NPs continue to be incorporated into a wide variety of increasingly complex products. With the increased use of NPs and nano-enabled products and their subsequent disposal, NPs will make their way into the environment. Currently, many unanswered questions remain concerning how changes to the NP surface chemistry that occur in natural waters will impact reactivity. This work seeks to investigate potential influences on photoreactivity – specifically the impact of functionalization, the influence of anions, and interactions with biological objects - so that ROS generation in natural aquatic environments may be better understood.

To this aim, titanium dioxide nanoparticles (TiO_2) and fullerene nanoparticles (FNPs) were studied in terms of their reactive endpoints: ROS generation measured through the use of fluorescent or spectroscopic probe compounds, virus and bacterial inactivation, and contaminant degradation. Physical characterization of NPs included light scattering, electron microscopy and electrophoretic mobility. These systematic investigations into the effect of functionalization, sorption, and aggregation on NP

aggregate structure, size, and reactivity improve our understanding of trends that impact nanoparticle reactivity.

Engineered functionalization of FNPs was shown to impact NP aggregation, ROS generation, and viral affinity. Fullerene cage derivatization can lead to a greater affinity for the aqueous phase, smaller mean aggregate size, and a more open aggregate structure, favoring greater rates of ROS production. At the same time however, fullerene derivatization also decreases the $^1O_2$ quantum yield and may either increase or decrease the affinity for a biological surface. These results suggest that the biological impact of fullerenes will be influenced by changes in the type of surface functionalization and extent of cage derivatization, potentially increasing the ROS generation rate and facilitating closer association with biological targets.

Investigations into anion sorption onto the surface of TiO_2 indicate that reactivity will be strongly influenced by the waters they are introduced into. The type and concentration of anion impacted both aggregate state and reactivity to varying degrees. Specific interactions due to inner sphere ligand exchange with phosphate and carbonate have been shown to stabilize NPs. As a result, waters containing chloride or nitrate may have little impact on inherent reactivity but will reduce NP transport via aggregation, while waters containing even low levels of phosphate and carbonate may decrease "acute" reactivity but stabilize NPs such that their lifetime in the water column is increased.

Finally, ROS delivery in a multicomponent system was studied under the paradigm of pesticide degradation. The presence of bacteria or chlorpyrifos in solution significantly decreased bulk ROS measurements, with almost no •OH detected when both were present. However, the presence of bacteria had no observable impact on the rate of chlorpyrifos degradation, nor chlorpyrifos on bacterial inactivation. These results imply that investigating reactivity in simplified systems may significantly over or underestimate photocatalytic efficiency in realistic environments, depending on the surface affinity of a given target.

This dissertation demonstrates that the reactivity of a system is largely determined by NP surface chemistry. Altering the NP surface, either intentionally or incidentally, produces significant changes in reactivity and aggregate characteristics. Additionally, the photocatalytic impact of the ROS generated by a NP depends on the characteristics of potential targets as well as on the characteristics of the NP itself. These are complicating factors, and the myriad potential exposure conditions, endpoints, and environmental systems to be considered for even a single NP highlight the need for functional assays that employ environmentally relevant conditions if risk assessments for engineered NPs are to be made in a timely fashion so as not to be outpaced by, or impede, technological advances.

Dedication

No work is produced in a vacuum (don't believe the particle physicists), and so this dissertation is dedicated to everyone who has contributed to this endeavor. Truly without your collaboration, ideas, and support, in ways both large and small, I would not find myself here.

Contents

List of Tables

List of Figures

Acknowledgements

While there are numerous individuals to thank who contributed directly to the science contained herein, in all likelihood there are an equal, if not greater, number who set the stage and who are similarly culpable. This is by no means an exhaustive list, but it is an attempt to show my appreciation to those who played so integral a role. Bear with me.

First and foremost, to my advisor, Mark Wiesner. Thank you for your support these *ahem* several years and for allowing me the space to explore and figure it all out. The manner in which you embrace your job is inspiring, and the confidence you have in your students is enabling. You've created an environment that fosters professional (and at least once, personal) relationships that is remarkably collaborative and supportive. Thank you for the belief that any semi-reasonable excuse to travel (conferences, collaborations, general knowledge) is sufficient, and that, once there it's worth an extra week to see and experience the location. Thank you, in the same vein, for continually inviting others to come and spend time at Duke. My research and my life have both been greatly enriched because of this. I can't imagine having joined another research group, and I'm honored to be a part of this amalgam of musicians and artists, of non-joiners

and mushroom hunters, of Blockus champions, bon-vivants, and science geeks. Wieslandia is a magical realm, and we are fortunate to have stumbled into it.

Secondly, to my committee, who have improved this work immeasurably. To Claudia Gunsch, who has been unfailingly willing to meet and discuss research and roadblocks and to provide advice. Thank you for your support when things were moving slowly. To Jerome Rose, your input has been invaluable, and the interest you have shown in this work and its success is deeply appreciated. Thank you for going out of your way to enrich the times I've visited the CEREGE and for accommodating my doomed experiments in your valuable beam time. To Rich Di Giulio, thank you for your support and research suggestions. The opportunities you've provided through the Superfund program have helped to add context to my work, and it's inspiring to see someone who clearly enjoys their job as much as you do.

I would especially like to thank those who have most supported this work through their collaborations. To Soryong Chae, who provided my first glimpse into the abyss that would be NP photoreactivity. This is arguably all your fault, so thank you. To Raju Badireddy, a secret lover of heavy metal and a great collaborator and friend. I have enjoyed working with you immensely and hope to do so again soon. To David Jassby, the force of nature who can sleep anywhere. Your ability to view a project from a distance and to see the missing piece is inspiring. To Andrea Turolla, who seamlessly balances science and adventure. I'll be lucky to end up half the researcher you are.

Thank you for showing me Milan; I hope I can repay the favor soon. To Ellen Cooper, for always falling for my ruse of offering to buy you coffee when I really wanted to ask for your help. To Courtney Gardner, the microbial expert, lover of books, and part time weightlifter. Thank you for helping meow with all the bacteria work and for not killing me every time I tried to change or redo an experiment.

Next, I need to thank Team Wiesner, aka, the Wiesnerds. You have provided support, camaraderie, and frustrations befitting a family and have been, quite possibly, the greatest part of this adventure. To Mathieu Therezien, who is both a modeler and a model, the modern day Viking with whom graduate school will always be most closely associated: from coursework and qualifying exams to aggregation theory. For someone who pretends to dislike people so frequently, you, sir, have a heart of gold. I should know, I've taken advantage of this countless times. Our ping-pong battles have become legendary in my mind. Thank you for the fights over who pays for coffee and for the conversations that followed. Your friendship is more appreciated than I can convey. You're still a giant nerd, though.

To Amalia Turner, who lives deliberately and collectively. Thank you for demonstrating the courage to try something nobody around you knows anything about and then being willing to talk about experiments gone horribly wrong (I know many of them go right, but everyone loves to talk about those). More importantly, thank you for the countless lunches, dinners, beers, ABP cookie breaks, and the resulting conversations

that have enriched even small moments. Thank you for being someone who will debate the relative quality levels of pizza in Durham. I'm so glad you joined our office, but also glad you got the stubby desk.

To Judy Winglee, employee of the month forever, a rogue joiner in the midst of the misfit toys, she of the church of flying disc, spikeball, and afternoon naps. I truly enjoyed the discussions, and friendship, that arose from our writing our prelims concurrently – I never realized Brooklyn backed up into Connecticut so seamlessly.

To Charles de Lannoy, he of the ascot and an unapologetic believer in beauty. I'm inspired by your ability to balance the demands of coursework, research, and life with earnest, and at times inebriated, grace and wit, and by your willingness to question all things. While our experimental rabbit holes may not have led anywhere, the act of jumping down them was both entertaining and enlightening.

To Zak Hendren, I'm thankful our friendship has transcended the basement of Hudson. I admire you greatly. Let's get together soon and drink some scotch.

To Christine Hendren, whose cheerful optimism in the face of adversity is only one of several indicators of her amazing strength. You're better at this science thing than I think you realize, and it's awesome to have had a front row ticket to watch. Thank you for your unyielding support and overwhelming faith in people.

To Niall O'Brien, who is proof that perpetual motion may actually be possible. If our research paths should intertwine again, I will be quite pleased indeed. To Shihong

Lin, the most thoughtful inhabitant of Wieslandia. You're brilliant and we all know it. Conversations with you could go anywhere and often carried off in the perfect direction. To Benjamin Espinasse, the pink-trucked boxer who can always find a deal. I'm still not sure how the lab runs without you. Thank you for group lunches and farmhouse dinners. To Stella Marinakos, thank you for putting up with us all. That you haven't strangled someone yet only underscores your patience. While we're all feeling our way through a pitch-black maze, you're frequently the one with a flashlight. To Nick Geitner, the only one who ever took Tie Tuesday seriously. Great things are in your future, and you deserve them all. To Jacelyn Rice, who, when faced with a number of great opportunities, had the guts to chose moving halfway across the world. I'm so excited for you. To Nathan Bossa, whose easy laugh and eagerness has been a great addition to the circle. To Alexis Carpenter, who showed us all up with her immaculate lab notebook, to say nothing of her science. To Fabienne Schwab, the swiss cornhole terrorist. To Marielle DuToit, the most hipster membrane scientist of them all.

To our French family – Jean-Yves Bottero, Melanie Auffan, Jerome Rose, Jerome Labille, Armand Masion, and everyone at the CEREGE. It's rare to find a lab that goes so far out of their way to make you feel at home and to help you in your endeavors. I'm grateful for your hospitality and for the time spent in Aix. It's always a joy when you come to Durham – that you are all world-class researchers is an added bonus.

To everyone in the department who keeps the clockwork running. Without you, we'd all be helpless. To Eileen Kramer, the gatekeeper who doesn't know slow. Thank you for your support (and ever-appreciated tip offs to free food). One of the best parts of the CSSC has been getting to know you better. To Dwina Martin, who can fix anything, or knows someone who can. I still hold you directly responsible for the most recent time I've dislocated my shoulder, but I'm sure I owe you a diet coke for something, so let's call it even. To Ruby Nell Carpenter, who from first email to defense scheduling has been a guide post in a confusing wilderness. Your dedication to the students of this department is greatly undervalued.

To Duke cycling, you've kept me sane, provided an outlet when I desperately needed one, and have been the most overwhelmingly positive addition to my life here. I'll cherish the countless hours, either on a bike, in a van, or standing in the blazing sun or freezing rain. To Zhan Khaw and Kevin McDonnell, from those first rides, to trips to the mountains, to nationals in Richmond, to Pitbull. To Matt Rinehart, possibly the single most supportive and encouraging teammate Duke cycling will ever know. To Kaleb Naegeli, K-swiss, the cartographer. You're everything I like about Indiana, and I'm thankful to have ridden with you and to know you. To Hoël Wiesner, potentially the single greatest person to have on a ride, and an equally great person off the bike. Your worldview is generally impeccable, although raccoons over opossums any day. Wizard cats for life. To Jacob Miller, the only person I know with a greater love for puns and

quite possibly the heart of Duke cycling. I'm glad to be leaving when you are. To Chelsea Richwine, for do-rags and dried mango. For hotel tea and cookies, music playlists back from West Virginia, and almost constant exasperation. I'm pretty sure there's a spider on your leg. To Laurel Beth Wheeler, Spike, my doppelganger/spirit animal - she of cocktail hour and obsolete phones - I'm still only 72% sure you're not a secret agent. To Gina Turrini, G-rex, Mustang, the only one who needs coffee more than me. Don't worry; I'm not going to call you Peanut. To Ben Turits, the supposed ringleader, for bluegrass, fire-and-brimstone preachers, and classic rock over the radio in a cargo van with missing side view mirrors. I'm pretty sure this is just a way to never grow up, and I like it. To Steven, Ginny, Robin, and Josh. To Becky and Owen and Matt, Brenna and Dave. To Brandon, Mulvi and the Bananas. To Emma, Peter, and Tiki the race dog. To all our frenemies in the ACCC. I've never felt more a part of a team, and that wouldn't be the case without you all. Really, the racing is secondary.

To Carley Gwin, who has navigated life, graduate school, and motherhood with a grace not often seen. You're doing a good job. Thank you for calling me out when I've needed it and for many long hours writing at Cocoa Dos. To Gretchen Gehrke, who takes on everything and somehow pulls it off, for long conversations about the idea of grad school, the state of universities, of things to come, and what it all means. And for equally long bike rides. To Milton and Ginger: you are, each in your own way, who I hope to become. Thank you for letting us borrow your lawnmower that first weekend

we moved to Durham, for dinner shortly thereafter, and for everything that followed. To ThuNDer, for the friendships that form when people eat together and the chaos that arises when more than 5 people try to use the same stove.

To my family for, among so many things, your faith and the independence you fostered in me, even though it's come back to haunt you. To my Dad, for modeling the importance of a college degree and for being willing to drive 6 hours late on Christmas Eve to a small Kentucky town when my car breaks down so I can make it home in time for Christmas. To my Mom, for supporting my decisions, even when it means moving farther away, and for always telling me I was the best thing you ever did. I hope I've lived up to that. To Nancy, for modeling the belief that if you want to do something different in life, you can and, what's more, you should. To Nathan, for modeling what pursuing your passion looks like. To Amy, for the eagerness and completeness with which you dive into life. I'm pretty sure you're doing it right. To my Grandparents, for never outright questioning when I'll get a real job, and for always being proud of me. To Grandpa Britt, for always believing that more education is a worthy endeavor and for never meeting a cup of coffee you didn't like. I've used that line countless times these past years.

To Miiam, I've never known a more ardent supporter of her family, even when it was in direct opposition to her personal happiness. I'm glad to fall within that circle. To Timo, for making grad school look appealing and, in a total lie, easy. And to the entire

Budarz Clan, for being outrageously generous with your time. Through your unending willingness to help, you have often modeled the best of what a family can be.

To Casa FaBu, I couldn't imagine a finer house. A source of infinite frustration and work, but also of accomplishment, joy and comfort. There was nothing more satisfying than to physically tear down a wall when I was up against one in the lab, and while I'll straight up punch the previous owner in the nose if I ever see him, all the unanticipated projects transformed you into my first home. You've hosted family, parties, holiday dinners, ThuNDer, and countless Airbnb guests – some who became good friends in a short period of time, and some who became good stories. I'd say you're finally finished, but we all know that would be a lie, and it doesn't really matter anyways.

To Luna, the would-be super villain who only ever cared for two people. It's a good thing you didn't have claws, Lune-dog, else you'd have been much less lovable. You're sorely missed. To Sir Banjo Fiddlesticks. I can't imagine a kinder, more handsome muttly, and I'm sure even those you've humped along the way feel the same. Thank you for following me around constantly no matter how long it's been.

And most of all to Sara Farner Budarz, whose unfounded belief that I could do this is perhaps the single greatest reason I find myself here. Thank you for being the impetus for our relocation to North Carolina and the only one who would be foolhardy and courageous enough to buy a house with me in a city we've never really seen just as

we're about to lose most of our income. Through beautiful, messy years of a half destructed house, the rigors of us both in grad school, and the complexities of life, you have remained my most ardent supporter. If this became my home, it is because of you. If the world has been a more exciting place to explore, it is because of you. I've long suspected you'd be the better academic, and I'm proud to see you proving me right. That you live fully and unapologetically, only adds to your myth. Continue to demand the most out of life, you deserve it.

And lastly, to Durm in the fine state of North Carolina, the first place I've not wanted to leave. Small enough to pedal home and big enough to find anything you need. Thank you for great shows, amazing restaurants, beautiful sunsets blocked out by trees, bike races, soccer, and amazing people to experience it all with. These acknowledgements were written during a farewell tour of sorts: at Motorco and Fullsteam, Cocoa, Surf Club and Ponysaurus. Thank you for being the backdrop to some amazing years.

1. Introduction

1.1 Motivation

Nanoparticles are not new. Nature has long coexisted with and employed environmentally generated nanoparticles for many significant geological processes (e.g., cloud nucleation, heavy metal and radionucleotide transport, phytoplankton growth leading to atmospheric CO_2 regulation) [1]. Environmentally generated NPs arise from many natural phenomena, including volcanoes and fire (CNTs and fullerenes) and mineral weathering, redox chemistry, or biological interactions (metallic NPs) [1-6].

Our ability to manipulate NPs and produce them on a large scale, however, is new. Since NPs were first discovered, their study and potential uses have driven demand and production. Primarily, the appeal of NPs, and the incentive for their adoption in technology and manufacturing, lies with their useful properties, such as increased strength or reactivity [7]. Given the largely proprietary nature of NP manufacturing, precise volumes are difficult to identify though estimates of total yearly NP production are on the order of tens to hundreds of thousands of tons, corresponding to hundreds of billions of dollars [7-9]. These NPs are incorporated into a wide variety of increasingly complex products, though there is oftentimes considerable difficulty in identifying which products use NPs and significant uncertainty in the composition of the NPs included within consumer products [10-12].

1.2 Scope

Nanoparticle reactivity can refer to a variety of phenomena, such as electron transfer from nanoparticulate zero valent iron (NZVI), catalysis by gold nanoparticles, or photocatalysis by semiconducting NPs. An intriguing constraint specific to photocatalysis is that it requires an external source of light to produce ROS - highly reactive and unstable oxygen containing compounds that eagerly participate in oxidation-reduction reactions. As a result of their instability, ROS have extremely short lifetimes, often on the order of micro to milliseconds. The ability of some NPs to produce ROS has inspired research aimed at using nanotechnology to inactivate viruses and bacteria and to degrade contaminants in aquatic environments [13-16].

Whether by intentional design or through incidental interactions, nanoparticles will not remain pristine for any appreciable length of time. NP functionalization, coatings, and incorporation into matrices such as polymers or thin films will depend on the use and desired functionality of user end products. All of these alterations will affect the reactivity of the NP. The use and ageing of NP containing products will result in the release of particles into the environment where further transformations are likely to occur [9].

Risk is commonly viewed as a function of two contributing factors: hazard and exposure [17-21]. For photocatalytic nanoparticles, transformations are expected to affect both factors. For example, aqueous dispersions of fullerenes exposed to UV light have

been shown to undergo hydroxylation [22-24], which can lead to greater ROS production (hazard). Alternatively, sorption of natural organic matter (NOM) has been shown to affect the transport and reactivity of nanoparticles [25-28], affecting potential levels of exposure. As a result, it is important to understand how the reactivity of a nanoparticle is affected by its environment. Despite the investigations that have been undertaken regarding NP reactivity, this area presents many challenges, and many unanswered questions remain [29].

The primary motivation for this work is to investigate the influences on photoreactivity (e.g. impact of functionalization, influence of anions, interactions with biological objects) so that ROS generation in natural aquatic environments may be better understood. Much of the research to date has proceeded on a case-by-case basis, focused on modifying elemental makeup (doping) or functional groups to optimize ROS, or looking at specific conditions to determine reactivity and ecotoxicity [30-35]. In this work, the attempt has been to understand trends that impact nanoparticle reactivity. A comprehensive risk assessment of NP photoreactivity falls outside the scope of this work. Instead, photoreactivity is viewed as one aspect of any risk assessment involving NPs that may undergo photo-excitation. As such, the primary focus of this work is on the potential for photoreactivity to be used as a marker of eco-toxicity.

This research probes how surface functionalization, physicochemical sorption, and aggregation of nanoparticles in the environment impact reactivity through

differences in characteristics such as aggregate size, aggregate morphology, and photo-excitation. To achieve this, photocatalytic NPs - titanium dioxide (TiO_2) and fullerene nanoparticles (FNPs) - were studied in terms of their reactive endpoints: ROS generation, virus and bacterial inactivation, and contaminant degradation. Investigating these interactions has allowed for greater precision in determining the reactivity of nanoparticles when considering their fate and transport in the environment. Results from these experiments have improved our understanding of reactivity and represent a step towards enabling ROS generation to be employed as a simple, measurable endpoint for use in a functional assay approach to NP risk assessment. End users of this research range from those who design and manufacture nanoënabled technologies to aquatic ecologists and government entities studying water quality to regulatory commissions who are currently grappling with establishing use and disposal protocols.

1.3 Hypotheses and Objectives

The primary hypotheses of this work build from the understanding that surface interactions will determine the reactivity of NPs in a system. Specifically, 1) that functionalization of FNPs will reduce aggregation and impact ROS generation, 2) that water chemistry and interactions with organic or ionic compounds at the NP surface will determine the reactivity of the system, and 3) that multiple, coexisting constituents will compete for ROS delivery.

ROS generation will be impacted by the size and structure of the aggregates that are formed resulting from these interactions, in addition to any specific interactions that alter the quantum yield and surface chemistry of the nanoparticles. These studies have systematically investigated the impacts of functionalization, sorption, and aggregation on NP aggregate structure, size, and reactivity - monitored as ROS generation as well as compound degradation or microbiological inactivation. In doing so, specific interactions have been identified and separated from aggregation affects. Ultimately, investigating how these surface interactions affect reactivity furthers our understanding of the impact from NP release into the environment.

To determine how engineered functionalization impacts NP aggregation and ROS generation (hypothesis 1), stable suspensions of derivatized FNPs (in which various function groups are attached to the C_{60} cage, i.e. aminated or hydroxylated fullerenes) have been created. These suspensions were then characterized in terms of aggregate size, electrophoretic mobility, ROS generation, and virus inactivation.

Investigations on how the sorption of compounds to the surface of a NP impacts aggregation and reactivity (hypothesis 2) have been undertaken by monitoring TiO_2 aggregation in various inorganic ions common to surface waters. Photoreactivity of TiO_2 aggregates in the presence of the same ions was then measured both at the NP surface and in the bulk solution and results were analyzed to determine the importance of specific interactions between the NP surface and ion.

Finally, ROS delivery in a multicomponent system (hypothesis 3) was studied under the paradigm of pesticide degradation. The impact of bacteria and chlorpyrifos on bulk NP photoreactivity was determined individually before investigating the implications of their combination with TiO_2.

2. Background

Photocatalysis is essentially the process of turning the energy in light into chemical reactions. The ability of some materials to absorb and transfer the energy of a photon has been known since the early 1900s, but the realization of the commercial utility of photocatalysis is generally agreed to have origins in the studies using TiO_2 to split water by Fujishima and Honda in the early 1970s [36-38]. Many reviews exist that cover the photocatalysis literature of FNPs and semiconductors [15, 16, 39-43]. Creating and manipulating material at the nanoscale has resulted in both improved electrochemical efficiency and increased interactions with contaminants in either air or water, leading to applications that range from energy capture and storage, to water treatment and contaminant degradation, to self-cleaning surfaces [38, 44-48]. When considering NP photocatalysis, efficiency will depend on particle surface chemistry and on the dynamics of particle interactions – particularly their tendency to form aggregates. As a result, investigations should be designed so that potential influences are considered and their impact on NP aggregation is accounted for.

This chapter provides an overview of nanoparticle photoreactivity and describes the fundamental interactions that are expected to impact the reactivity of NPs in aqueous environments. First, photocatalysis and the production of reactive oxygen species (ROS) are described, including ROS detection and quantification. Secondly, the two primary types of photoreactive nanoparticles used in this work, fullerene

nanoparticles and titanium dioxide, are introduced, each with an overview of their photoreactivity and additionally pertinent physicochemical properties. Thirdly, the fundamental processes leading to NP aggregation are described, followed by a discussion of how aggregation and interfacial chemistry are expected to impact NP photoreactivity. Lastly, efforts to understand the impact of NP photoreactivity in complex, natural environments are discussed in light of the challenges associated with NP risk assessment.

2.1 Photocatalysis

The Plank-Einstein equation describes the energy, E, of light with a given wavelength, λ:

$$E = \frac{hc}{\lambda} \qquad \text{(Eq 1.)}$$

where h is plank's constant and c, the speed of light. This energy is transferred to a molecule through the absorbance of photons, exciting the electrons, which can follow a variety of pathways to return to the ground state (Figure 1). This may take the form of heat dissipation through vibration, light emission (fluorescence or phosphorescence), or further energy transfer (sensitization) – all of which result in no net change to the molecule. Alternatively, a molecule absorbing photons of sufficient wavelength may undergo a chemical reaction resulting in fragmentation, rearrangement, or electron transfer [49].

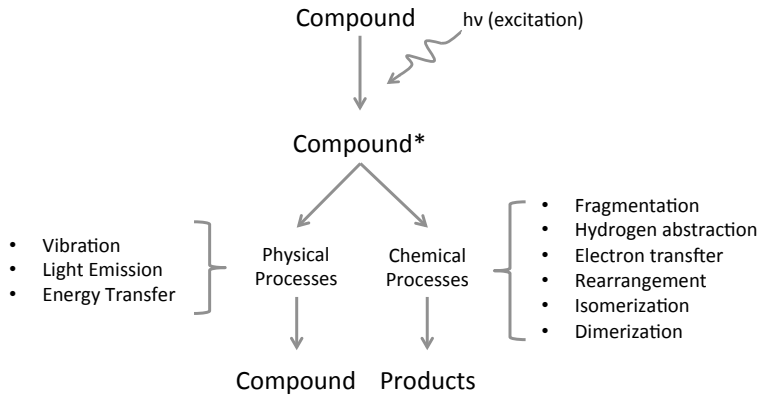

Figure 1: Physical and chemical relaxation pathways of excited species. Adapted from [49].

The absorption of light of sufficient energies has the capacity to degrade plastics or pollutants and inactivate bacteria via direct photolysis, though the kinetics of such reactions are often slow from an engineering standpoint [50-55]. However, reaction rates may be increased, or unfavorable reactions facilitated, by the presence of catalysts in suspension [49]. If the catalyst is of the same phase as the reactant, such as dissolved iron participating in hydroxyl radical generation in the photo-Fenton reaction [56, 57], the reaction is classified as homogeneous photocatalysis. Conversely, the reaction is termed heterogeneous photocatalysis if the catalyst is of a different phase such as photosensitized nanoparticles [40, 58]. This work focuses on the latter of these options and how interactions at the surface of suspended NPs affect the photosensitized reaction.

2.1.1 Reactive Oxygen Species

Heterogeneous photocatalysis in oxygenated waters primarily leads to the production of reactive oxygen species. This can occur either by the sensitizer facilitating electron transfer, denoted type I, or through the transfer of energy from the photocatalyst, denoted type II [16, 59]. These two pathways will produce differing types of ROS, but the net result in both cases is to convert absorbed light into chemical energy. As a result, an effective photocatalyst will have both high light absorbance and high quantum yields [49].

ROS is a family of oxygen containing compounds with unpaired or excited electrons. ROS and reactive nitrogen species (RNS) play important roles in cellular signaling and other biological processes, though they are also associated with cellular toxicity [60-64]. On a larger scale, ROS is common in surface waters, created primarily by the chromaphoric components of dissolved organic matter (CDOM), which have been associated with maintaining biological balance and contaminant degradation. [65-69].

The presence of excited or unpaired electrons in ROS destabilizes the compound and leads to large redox potentials. As a result, radicals are short-lived, highly unstable, and fairly unspecific. They readily react with other compounds as well as with water itself, and the potential pathways of radical reactions are often complex [16, 70, 71]. The

three primary reactive oxygen species considered herein are singlet oxygen ($^1O_2$), superoxide (O_2•-), and hydroxyl radical (•OH).

Singlet oxygen is the result of type II sensitization in which an electron in the oxygen molecule is excited from the π to the π^* antibonding orbital [49]. This excitation results in $^1O_2$ being nearly 1V more oxidizing than ground state triplet oxygen [16, 72]. $^1O_2$ reacts most readily with carbon-carbon double and triple bonds, phenols, sulfides, amines, and other anions [72]. $^1O_2$ sensitizers are often organic dyes, aromatic hydrocarbons and organic matter, though porphyrins and some inorganics such as transition metal complexes and semiconducting metal oxides are also effective generators [72].

$$O_2 + P^* \rightarrow {}^1O_2 + P \qquad \text{(Eq 2.)}$$

Superoxide is the result of the single electron addition to molecular oxygen. Sensitized dyes are readily capable of forming O_2•- in the presence of an electron donor [16]. A moderate reductant and nucleophile, O_2•- may react through proton removal, halide replacement, or as a single electron donor [59].

$$O_2 + e^- \rightarrow O_2^{\bullet -} \qquad \text{(Eq 3.)}$$

The hydroxyl radical, the single electron oxidation product of hydroxide, is the most oxidizing of the three primary forms of ROS (E_H = 1.8V at pH 7) [16]. •OH reacts primarily through the abstraction of a hydrogen atom, OH addition, or the one electron oxidation to return to the hydroxide anion.

$$^{-}OH + h^{+} \rightarrow {}^{\bullet}OH \quad \text{(Eq 4.)}$$

2.1.1.1 ROS Detection

ROS measurements, given the short half-lives involved, are often achieved via probe compounds that are either oxidized or reduced upon reaction with the produced radicals. These measurements are feasible because of the high reaction rate constants of the probe compounds and the changes that result in spectroscopic properties (monitored as fluorescence or absorption). Probe response generally indicates cumulative ROS production over a measured exposure time, and care should be taken to limit the factors (e.g. NP concentration, duration of exposure) that would result in an overabundance of ROS production and hinder the probe's reaction efficiency. Many probes are available and their usage depends on experimental constraints such as bacterial toxicity, matrix effects, pH, and solution chemistry [72-77]. Often these have been designed to monitor endogenous ROS production for biological endpoints but can be used for exogenous measurements. Other techniques, such as laser flash photolysis and electron paramagnetic resonance spectroscopy (EPR) are effective but require extensive instrumentation that makes them difficult to use with complex systems or in real time environmental studies [78-80]. Monitoring specific compound degradation has been effectively used to monitor multiple ROS species simultaneously, however liquid chromatography is necessary for analysis, which can be time consuming [77, 81, 82].

Table 1: Selected ROS standard generators, probes, and quenchers.

Use	Species	Compound	Reference
Probes	$^1O_2$	Singlet Oxygen Sensor Green	[83, 84]
	O_2•-	Tetrazolium salt, XTT	[73, 85]
		Hydrethidium	[75, 86]
	•OH	Terephthalic Acid	[76, 87-89]
Quenchers	$^1O_2$	β-Carotene	[90]
		L-Histidine	[91, 92]
	O_2•-	SOD	[16, 81]
	•OH	N-Acetyl-l-cysteine	[93]
		Sodium Azide	[94]
Generators	$^1O_2$	Rose Bengal	[95-97]
		Methylene Blue	[72, 97]
	O_2•-	Xanthine / Xanthine Oxidase	[98]
	•OH	Hydrogen Peroxide	[99, 100]

For measurements of hydroxyl radical production, the oxidation of terephthalic acid (TA), shown in Figure 2, to 2-hydroxy terephthalic acid (2HTA), can be followed by the fluorescence (315ex/425em) of the product. Using a standard curve, this fluorescence can be quantified and tracked over time as a measure of cumulative hydroxyl radical production [76, 87-89].

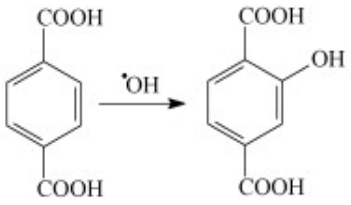

Figure 2: Terephthalic acid hydroxylation produces the fluorescent 2-hydroxy-terepthalic acid. Adapted from [89].

Superoxide production can be measured in a similar fashion using 2,3-bis(2-Methoxy-4-nitro-5-sulphophenyl)-5-[(phenylamino)carbonyl]-2H-tetrazolium hydroxide (XTT). Reduction of the compound by two superoxide molecules produces XTT-formazon, which can be tracked via the formation of an absorption peak at 470nm (Figure 3) [73, 85]. Alternatively, the reaction of superoxide with hydroethidine (HE) has been shown to result in strong fluoresce (480ex/567em) [75, 86].

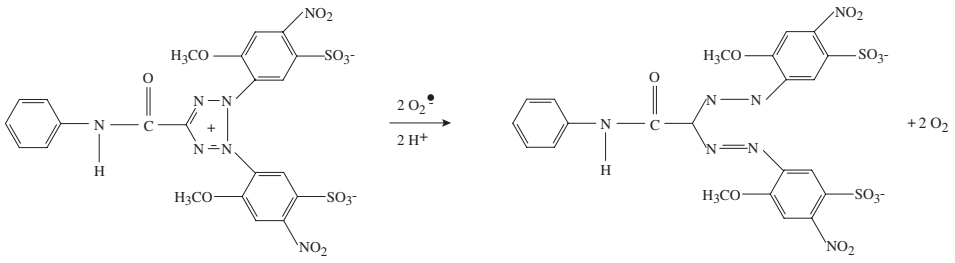

Figure 3: Reduction of XTT by superoxide. Adapted from [73].

Singlet oxygen generation can be measured using the florescent probe Singlet Oxygen Sensor Green (SOSG) (Life Sciences, NY, USA). Oxidation of the weakly fluorescent starting compound produces an endoperoxide (SOSG-EP), which fluoresces

much more strongly (Figure 4) [83, 95, 101, 102]. Though there are some concerns about autoflourescence and indications that the molecule itself may act as a photosensitizer, for lower concentrations of $^1O_2$ and shorter timeframes, the response is linear and efficient [83, 84].

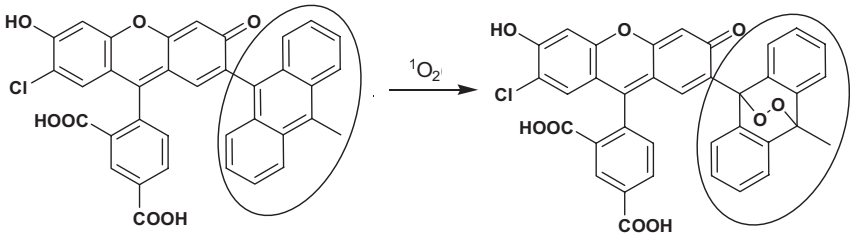

Figure 4: Oxidation of SOSG by $^1O_2$. Adapted from [83].

2.1.1.2 ROS Standard Generators

Quantification of ROS production detected via probe compounds is possible using known ROS generators. Often, these are dyes or other chromaphores. For example, rose bengal exposed to UV light at 365nm will generate singlet oxygen with a quantum yield of 0.75 [95-97, 103]. By measuring UV fluence and the absorbance of the sensitizer at a given concentration, the $^1O_2$ generation rate can be calculated. This can then be combined with the response of the probe compound to create a standard response curve. Similarly, xanthine combined with xanthine oxidase is a known superoxide generator [98], while hydrogen peroxide can be used to generate hydroxyl radicals [99, 100].

2.1.1.3 ROS Quenchers

The use of quenching agents can help to isolate the effect of a single species when investigating the ROS mediated inactivation of bacteria or viruses. Because the pathways though which ROS can react are often complex and interrelated, the use of compounds that specifically react with a given radical at a rate large enough to outcompete other reactions can greatly clarify observations [70, 71, 104]. Frequently employed quenching agents are typically biologically synthesized molecules that are produced to protect cells from the oxidizing and inflammatory effect of free radicals such as superoxide dismutase for superoxide, or β-carotene and histidine for singlet oxygen [90-92, 105]. Care should be taken in selecting an appropriate quencher when studying biological systems as some options (e.g. N-acetyl-cysteine) are biologically safe while others (e.g. sodium azide) have known toxicity, though both are effective •OH quenchers [93, 94, 106].

2.2 Photoreactive Nanoparticles

Photoreactive nanoparticles may be semiconductors, often metal oxides (e.g. WO_3, $SrTiO_3$, Fe_2O_3, ZnO) or metal sulfides (CdS, ZnS), or carbon based NPs (e.g. fullerene nanoparticles (FNPs), carbon nanotubes (CNTs), and graphene) [16, 107, 108]. In semiconductors, the difference in energy levels between the highest occupied molecular orbital (HOMO) and the lowest unoccupied molecular orbital (LUMO) is sufficient that electrons are unable to freely occupy higher orbitals due to relatively

insignificant changes in energy (as is the case for conductive metals), but not so great that the band gap between the HOMO and LUMO is insurmountable (as is the case for insulators).

As the difference in the HOMO and LUMO determines the energy necessary to promote an electron into the conduction band, a small band gap is desirable for photocatalysis, which enables excitation by photons of greater wavelength. The absorption of a photon with energy greater than or equal to the band gap will promote an electron from the HOMO, across the band gap into the LUMO, leaving behind a photogenerated hole, h+. From here, the presence of vacant orbitals permits the migration of the photoëxcited electron through the conduction band, while the photogenerated hole is free to migrate through the valence band [40]. Once the electron-hole pair has been generated, they may recombine, releasing energy via fluorescence. Alternatively, migration to the surface of the sensitizer and interaction of h+ with water or the electron with oxygen can produce hydroxyl radicals and superoxide, respectively (Figure 7).

To be practically useful, the semiconductor should be insoluble and inert in water. Additionally, the band gap should span the redox potential of water in order to permit •OH production [108]. While TiO_2 is often selected for its inert nature and relative abundance, the band gap of 3.2 and 3.0 V for anatase and rutile, respectively means that light with wavelengths of less than 415 nm for rutile, and 385 nm for anatase,

is necessary for photoëxcitation [16]. This is a significant limiting factor, with implications for cost and practicality. When considering TiO_2 for photocatalytic processes, it necessitates the use of UV lamps, and considerable research has investigated semiconductor doping in an attempt to decrease the band gap so that less expensive visible light (i.e. solar) sources can be effectively employed [41, 109, 110]. While this is an extensive and active field of research, it falls outside the scope of work presented in this dissertation.

Similarly, for carbonaceous NPs the absorption of light excites an electron into the LUMO [111, 112]. Relaxation can take the form of radiative decay (phosphorescence), increased vibration (heat exchange), or chemical transformation. Chemical transformations will either take place through degradation, typically oxidation in the presence of dissolved oxygen, or catalysis in which energy is transferred through either type I or type II sensitization (Figure 6) [40].

In determining the efficacy of a sensitizer, the quantum yield, the ratio of absorbed photons resulting in this latter pathway to all non-catalytic pathways, is employed. This propensity for chemical reactions ranges from zero (no reaction) to unity (all absorbed photons result in a reaction) [49]. Knowing this, the incident light intensity, and the absorptivity of the compound, one can calculate the ROS production from a given concentration of a photocatalyst.

2.2.1 Fullerene Nanoparticles

Fullerene, first described in the literature in 1985 [113], is a carbon allotrope most commonly composed of 60 carbon atoms (C_{60}) forming interlocked hexagonal and pentagonal rings in sp^2 hybridization, Figure 5 (a). The extensive π-electron bonding throughout the carbon cage gives rise to a number of interesting and potentially useful parameters, including strength, resistance to degradation, photocatalytic ability, and, in a complicating factor when considering their employment in aqueous systems, significant hydrophobicity [26, 114, 115].

Due to this hydrophobic nature of C_{60}, larger aggregates composed of "n" number of individual monomers, referred to as nC_{60}, are generally formed in aqueous suspensions. In an attempt to minimize the size and number of monomers within aggregates, multiple methods of dispersion have been attempted including long term stirring, solvent exchange, and high power ultrasonication, to varying degrees of success and particle alteration [116, 117]. Though solvent exchange, often with tetrahydrofuran, was initially utilized for FNP dispersions, toxicity measurements were complicated by residual solvent [118-120]. Additionally, long term stirring and sonication have been observed to hydroxylate FNP aggregates in suspension [121, 122].

Additionally, derivatization of the carbon cage, wherein some of the π-electron bonding is disrupted to allow for the addition of functional groups to the outside of the cage, has been employed to increase solubility. Frequently this is instigated through the

addition of hydroxyl, amine, or other small functional groups, though large side chains have been used both for aqueous stabilization, cross-linking with polymer substrates, or vehicles for drug delivery [123-126]. The most commonly studied functionalized fullerene, nominally with 24 hydroxyl groups, is fullerol ($C_{60}(OH)_{24}$) Figure 5 (b) [22, 78, 127-129]. Functionalization not only alters solubility but impacts many other physical and photochemical properties of the FNP.

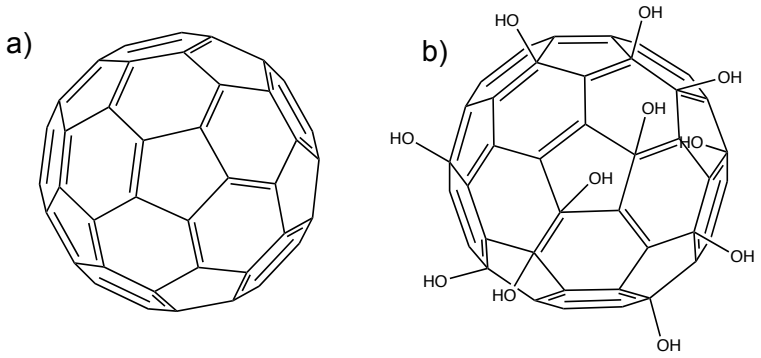

Figure 5: (a) C_{60}, fullerene and (b) $C_{60}(OH)_{24}$, fullerol.

2.2.1.1 FNP Reactivity

Fullerenes are efficient photosensitizers capable in solution of transferring energy from absorbed light to dissolved oxygen [112, 130, 131]. This occurs as the absorption of UV light propagates an electron from the ground state to the excited singlet state. This short lived energy state rapidly (order of nanoseconds) decays to the relatively stable excited triplet state (tens of microseconds) where energy can further be transferred to dissolved oxygen in solution, creating $^1O_2$ as shown in Figure 6 [111].

Alternatively, if an electron donor is present, the excited triplet state may abstract that electron, producing a radical anion, after which the reaction with dissolved oxygen will produce superoxide (O2•-) [130-132].

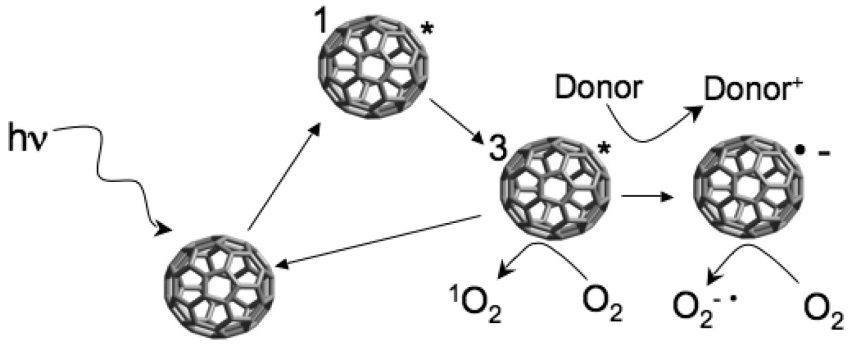

Figure 6: Photosensitization of and ROS production by C_{60}. Adapted from [81].

Nucleophilic addition reactions are capable of producing a vast number of products by adding functional groups to the fullerene cage [123]. The functionalization of C_{60} has been shown to change singlet state absorption and decay and decrease photochemical ability [80, 133]. However, most investigations have involved the addition of large functional groups compared to the relatively small carbon cage [125, 134-136]. This trend has been continued more recently through investigations of singlet production and virus inactivation after large chain additions [32, 137, 138]. The presence of simple, low molecular weight additions has not yet been thoroughly investigated.

Given the photoreactivity of FNPs, there has been interest in their antimicrobial and anti-viral capabilities, both as a targeted application of FNPs or an unintended

consequence of environmental release [52]. Badireddy et al. investigated the inactivation of MS2 virus by fullerol and observed that viral inactivation was due predominantly to singlet oxygen production [128]. Generally, no inactivation is seen under dark conditions for sonicated aqueous suspensions [139].

2.2.1.2 FNP Physical Transformations

Owing to the hydrophobicity of C_{60}, the size distributions of aqueous dispersions are often highly heterogeneous. Chae et al. demonstrated the relationship between aggregate diameter and characteristics such as pH, ORP, and the coefficient of attachment efficiency (α) by filtering a suspension nC_{60} to different pore sizes [121]. The conclusion was that the stability of a fullerene or aggregate changes as a result of surface hydroxylation during suspension preparation.

This work built upon previous studies looking at the possibility of surface transformations either during or after suspension preparation. Brant et al., in looking at the effect of varying solvent exchange dispersion methods, found through light scattering that the internal structure, as well as aggregate size, differed based on dispersion methods [116]. These findings were attributed to varying degrees of aggregate stabilization due to electrostatic and hydration interactions, a conclusion that was supported by later studies looking at the irreversible hydration and hydroxylation of nC_{60} aggregates during sonication as evidenced by FTIR and NMR [122]. The reaction of nC_{60} with hydroxyl radicals produced via cavitation was proposed to be the primary

mechanism for this hydroxylation, which was further supported by the work of Lee et al. using gamma radiation to expose C_{60} suspensions to hydroxyl radicals [140]. Surface hydroxylation was also observed through the evolution of UV-vis absorption spectra by Chang et al. during long-term stirring of C_{60} in aqueous suspensions without any solvent exchange [117]. Together, these studies point to the changes that necessarily occur to pristine, powdered C_{60} in creating quasi-stable aqueous dispersions.

Furthermore, UV irradiation of prepared C_{60} suspensions was shown by Lee et al. to alter the fullerenes into mono- and di-oxygenated products [24]. Others have shown similar UV-mediated transformations of fullerene [23, 129, 141]. Hwang et al. detailed changes in suspension characteristics over 21 days, with transformations likely continuing afterwards [142].

2.2.2 Titanium Dioxide

TiO_2 is a semiconducting metal oxide with three different crystalline phases: anatase, brookite, and rutile. Of these, rutile is the most stable, while brookite is the least and readily transforms to rutile [143]. Due to it's photoelectronic characteristics, TiO_2 has widely been studied for many applications, including pigmentation, advanced oxidation processes, photovoltaics, and biomedical therapies [15, 144-147].

2.2.2.1 TiO_2 Reactivity

Of the three crystalline phases of TiO_2, anatase shows the greatest photoactivity [146, 148]. Rutile appears to be a generally less efficient photocatalyst than anatase for

the majority of compounds, but has shown high photocatalytic ability for some [15, 149]. Brookite is the least often employed, owing partly to its difficulty to prepare and purify [150, 151]. Additionally, Bakardjieva et al. found the inclusion of brookite did not markedly improve reactivity when testing various combinations of crystalline phases [152, 153].

As a semiconductor, the absorption of light greater than or equal to the band gap will promote an electron from the HOMO to the LUMO, leaving behind a positive hole. For undoped TiO_2 in the anatase crystalline phase, this occurs at approximately 385nm (corresponding to a band gap of 3.2 V) [16]. As shown in Figure 7, once separated, both the electron and the hole may migrate to the surface of the particle where they are capable of undergoing a number of reactions, either reducing or oxidizing compounds present on the crystalline surface [40, 154, 155]. Additionally, they may recombine, releasing the absorbed energy through photoluminescence or non-radiative decay in processes that produce no chemical transformation. For ROS forming pathways, the electron, after migrating to the surface, is capable of reducing dissolved oxygen to produce superoxide, while the hole is able to abstract an electron from hydroxide, producing the highly oxidizing hydroxyl radical [15, 156].

While much of the environmental TiO_2 research focuses on compound degradation [40, 107, 146, 157-160], photoactivated TiO_2 has proven effective at bacteria and virus inactivation, with •OH playing a predominant role in toxicity [71, 161-163].

With TiO_2 increasingly used in consumer products manufacturing (e.g. sunscreens, polymers and paints, cements) [164-168], the release of TiO_2 into the environment will continue to increase [169-171]. As such, applications should also take into account the potential for unintended biological impacts resulting from these products [172-174].

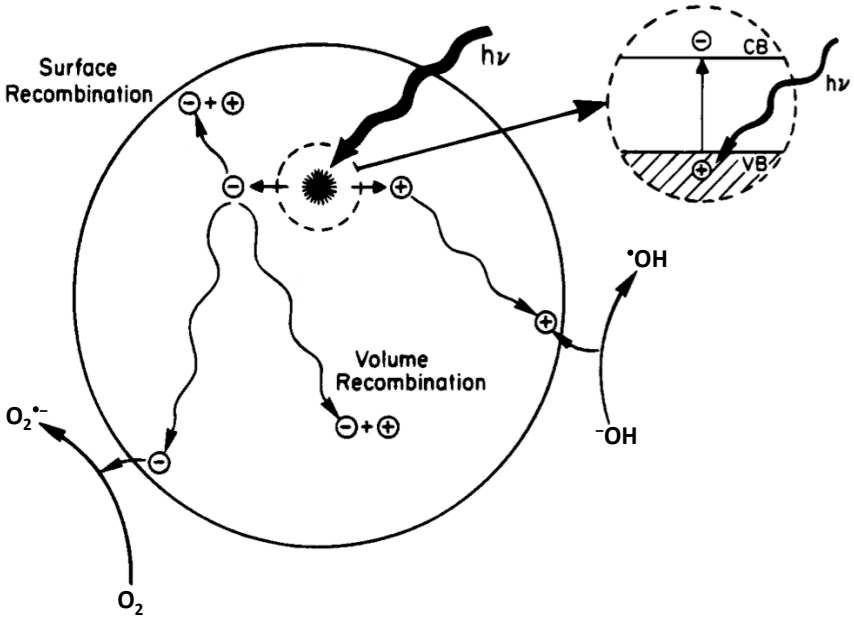

Figure 7: Photosensitization of and ROS production by TiO_2. Adapted from [40].

2.2.2.2 P25 TiO_2

P25, manufactured by Evonik (Germany), is the most commonly cited commercial TiO_2 product in the literature and consists of a combination of the rutile and anatase phases fused together in roughly a 20:80 ratio [175]. The individual particle size is nominally 25nm with a BET surface area of about 55 $m^2\ g^{-1}$ [15, 175, 176], however the

fused nature of the particles results in ultrasonicated dispersions of hundreds of nanometers [177, 178]. P25 has been observed to produce greater •OH than similar dispersions of anatase alone (Figure 8), attributed in part to the formation of trapping sites at the rutile-anatase junctions [155]. Bakardjieva et al. also demonstrated that the ratio of anatase to rutile impacts particle size, pore size and, ultimately photoreactivity [153]. None of their samples bettered P25 at the degradation of 4-chlorophenol, though similar ratios behaved with much the same effectiveness.

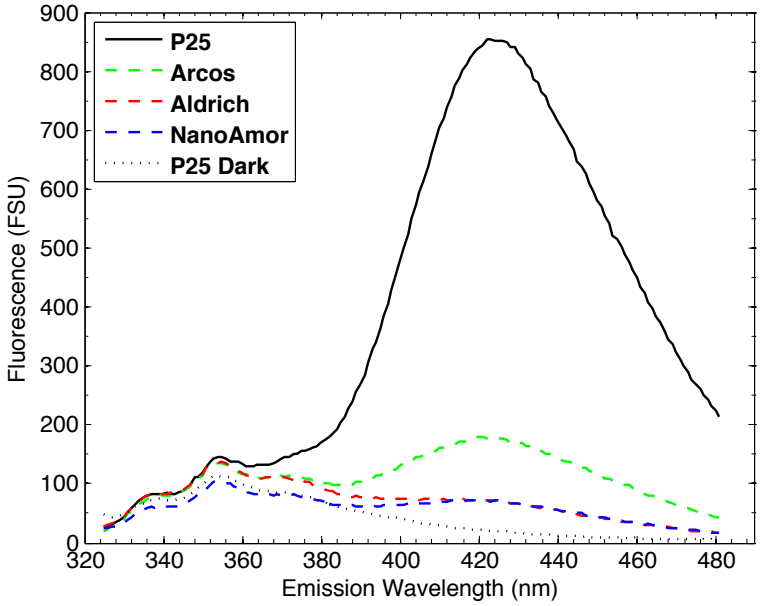

Figure 8: •OH production of various TiO_2 suspensions at 20ppm, measured by TA and graphed as fluorescence intensity vs. emission wavelength after 5 minutes of UV-A exposure. Unpublished data.

2.3 Particle Stability and Aggregation

2.3.1 Particle Attachment

When two particles collide in a fluid, the likelihood that they will attach and produce an aggregate is indicated by the parameter α, the coefficient of attachment efficiency. This "stickiness coefficient" is the ratio of particle attachment occurrences to particle collisions, ranging from zero (no attachment) to unity (every collision results in attachment), and is governed primarily by the surface chemistry of the particle [179]. Van der Waal's forces, the weakly attractive forces between two particles, are easily overcome by electrostatic repulsion in the bulk. As two similarly charged particles come towards each other, the net repulsive force increases. However, because the charge on the surface of a particle is finite, and van der Waal's attraction forces continually increase as the separation distance drops to zero, the net force, considering these two phenomena, will typically be attractive at a sufficiently small separation distance. Thus particles brought closely enough together will continue to approach each other until the electron clouds of individual atoms begin to overlap, as dictated by Born repulsion. DLVO theory quantitatively describes this net attractive or repulsive force for particles of varying separation distances (Figure 9) [180, 181].

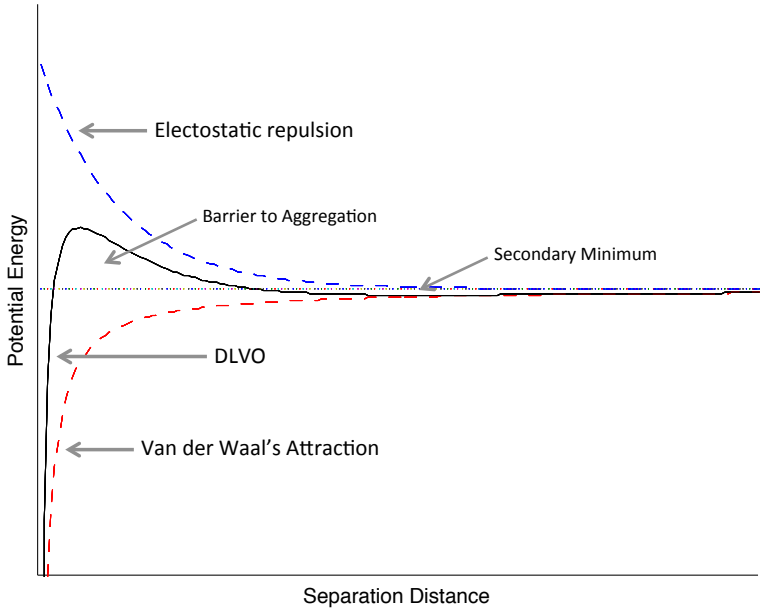

Figure 9: DLVO schematic illustrating the sum (solid black line) of electrostatic repulsion (blue dashed line) and van der Waal's attraction (red dashed line) as a function of separation distance.

The magnitude of electrostatic repulsive forces depends on the surface charge, conferred by lattice structure, surface defects in the crystalline phase, and adsorbed species or functional groups. Effectively, this charge on the surface of a particle draws near a fixed layer of ions of opposite charge existing in solution as a counterbalance, the Stern layer. The concentration of counter-ions decreases with distance from the surface until it reaches an effective balance between positive and negative at which point particles no longer feel the impact of each other. The distance over which this occurs, the Debeye length (κ^{-1}), depends on the magnitude of the charge on the surface, however, as

is seen in Equation 5, for a given surface charge, this length can be decreased though charge screening, accomplished by increasing the ionic strength of the solution:

$$\kappa^{-1} = \sqrt{\frac{\varepsilon k_B T}{2 N_A e^{-2} I}} \qquad \text{(Eq 5.)}$$

Here ε is the permittivity of the system, k_B is the Boltzman constant, T is temperature, N_A is Avagadro's number, e is the charge of an electron, and I is the ionic strength of the solution. When measuring particle stability via electrophoretic mobility, the value calculated as the zeta (ζ) potential is the net charge at the slipping plane rather than the charge on the surface itself or at the Stern layer. Together, these regimes make up the electrical double layer of a particle [182].

Additionally, adsorbed species or functional groups on the surface of a particle can increase stability through steric hindrance, preventing other particles from approaching close enough to overcome the repulsive force [29, 183]. This often occurs to particles naturally from environmental organic matter or biological molecules [184-187] and can be engineered through the use of various surfactants and stabilizers [25, 188, 189]. Under these cases, classical DLVO theory breaks down, and a number of equations have been derived to describe extended DLVO behavior based on the particle characteristics [29, 189-191].

2.3.2 Rectilinear Transport and Particle Collisions

For two particles to aggregate, they must first be brought together. The process by which particles come into contact is governed by both the characteristics of the particles and the solution. In a rectilinear transport model, interactions between the stream lines of approaching particles are ignored and transport is assumed to follow straight flow lines. Three collision mechanisms are typically considered: fluid shear (k_{SH}), Brownian motion (k_B), and differential settling (k_{DS}) such that

$$\beta = k_{SH} + k_B + k_{DS} \qquad \text{(Eq 6.)}$$

where β is the combined rate of collisions between particles in units of per number concentration per time.

Fluid shear is governed by the velocity gradients within the fluid and produces a ballistic transport mechanism. Particles carried along a path of higher velocity will overtake those travelling at a lower velocity denoted in Equation 7 where d_i and d_j are the diameters of particles i and j, respectively, and G is the mean velocity gradient produced by mixing in units of second^{-1}.

$$k_{SH}(i,j) = \frac{(d_i - d_j)^3 G}{6} \qquad \text{(Eq 7.)}$$

Brownian motion is determined by the viscosity of the fluid, μ, and the internal energy (i.e. temperature) of the particle. The contribution from Brownian motion dominates for small particles under quiescent conditions.

$$k_B(i,j) = \frac{2k_BT}{3\mu}\left(\frac{1}{d_i} + \frac{1}{d_j}\right)\left(d_i + d_j\right) \quad \text{(Eq 8.)}$$

Differential settling (Equation 9) applies to particles or aggregates of varying size, in which the settling rate of larger or denser particles causes them to travel more quickly, overcoming smaller or less dense particles in their path. Here, g is the force of gravity.

$$k_{DS}(i,j) = \frac{\pi g(\rho_i - \rho_j)}{72\mu}(d_i + d_j)^2(d_i^2 - d_j^2) \quad \text{(Eq 9.)}$$

The overall rate of aggregation is a combination of both particle attachment (α) and transport (β), described by the Smoluchowski equation:

$$\frac{dN_k}{dt} = \frac{1}{2}\alpha\sum_{i+j=k}\beta_{ij}N_iN_j - \alpha N_k\sum_{i=1}^{\infty}\beta_{ik}N_i \quad \text{(Eq 10.)}$$

Here $\frac{dN_k}{dt}$ describes the accumulation of particles of a given size, k, with generation due to the combination of smaller size classes, i and j, and loss due to aggregation of size class k to larger sizes [192, 193].

The rate of aggregation impacts not only the size of aggregates, but also their structure. The size of an aggregate and number of primary particles can be related to the density by the fractal dimension, D_f, which constitutes a description of aggregate self-similarity across length scales [194].

2.3.3 Fractal Dimension

If particles are fully destabilized (α=1), aggregation is considered diffusion limited (DLA) (Figure 10 (a)). Under DLA, the barrier to attachment is effectively nonexistent, and a particle will attach to the first surface with which it collides, rapidly producing relatively large, open aggregates with fractal dimensions around 1.8 [195]. Conversely, smaller, denser aggregates are produced if aggregation is slow and multiple collisions are necessary before attachment occurs. This latter condition is termed reaction limited aggregation (RLA) and is characterized by D_f values of 2.1 or greater (Figure 10 (b)) [195, 196]. Particles brought together by fluid flow or deposition (in contrast to Brownian motion) undergo ballistic aggregation, resulting in aggregates for which the D_f generally lies in between values for DLA and RLA aggregation [196, 197].

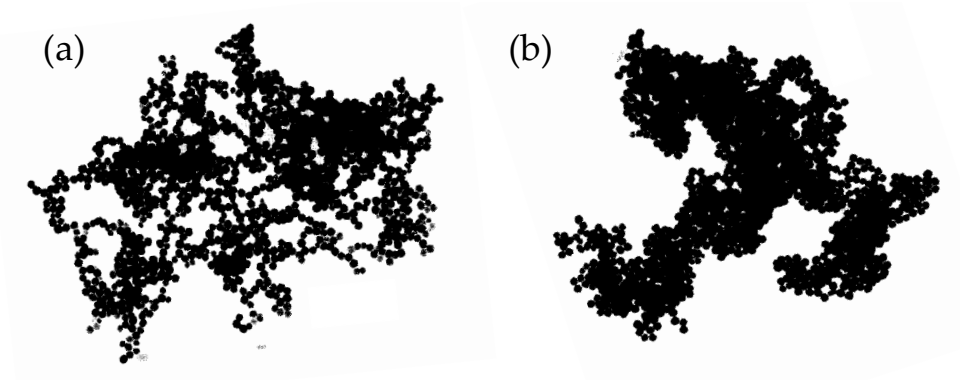

Figure 10: TEM images of 25nm hematite NPs aggregated under (a) DLA (D_f = 1.68) and (b) RLA (D_f = 2.20) schemes. Adapted from [198].

Measurements of D_f consistent with predictions for both RLA and DLA aggregation schemes have been observed for TiO_2 [177, 199], fullerenes [200], and several other NPs in unmixed systems [198, 201-203]. In mixed systems, loose aggregates are more susceptible to shear forces, resulting in breakup and reordering. The process of re-aggregation produces denser aggregates and increases D_f [204, 205].

2.3.4 Changes to the Smoluchowski Equation Due to the Fractal Nature of Aggregates

Among the simplifications made by Smoluchowski is that flocculation occurs between coalescing spheres (particle volume is constant) without taking into account fluid flow around the particles (rectilinear model) [179]. In fact, as aggregation between non-coalescing particles occurs, the aggregate volume fraction increases as fluid is included in the aggregate. In addition to curvilinear effects observed between two approaching solid particles, Adler demonstrated the compression of flow lines near the surface of porous particles as fluid flows around and through the particle [206]. The ability of streamlines to flow through aggregates was further supported by the recognition from Li and Ganczarczyk that naturally forming aggregates exhibit a fractal nature [207]. Chellam and Wiesner demonstrated mathematically that this fractal nature has a direct impact on floc permeability, indicating that very loose aggregates approach the behavior of the rectilinear model, while for dense aggregates, the curvilinear model better describes transport [208]. Ultimately however, the rectilinear and curvilinear

models bound the possibilities for aggregate interactions, with true aggregate behavior falling somewhere in between.

The primary implication when considering fractal aggregates is when two aggregates combine, the resulting occupied volume is greater than the sum of the two initial volumes, with the exception of when $D_f = 3$ [179]. Thus, the porosity of aggregates is no longer fixed, but rather increases with radial distance from the center of the aggregate. Veerapeneni and Wiesner, continuing the work by Chellam and Wiesner, demonstrated this by dividing aggregates into multiple shells of decreasing porosity. The fluid collection efficiency, the amount of fluid that passes through an aggregate divided by the amount that approaches the aggregate, of an aggregate decreases with increasing fractal dimension, effectively pushing streamlines to the outside of the aggregate, as illustrated in Figure 11 [209].

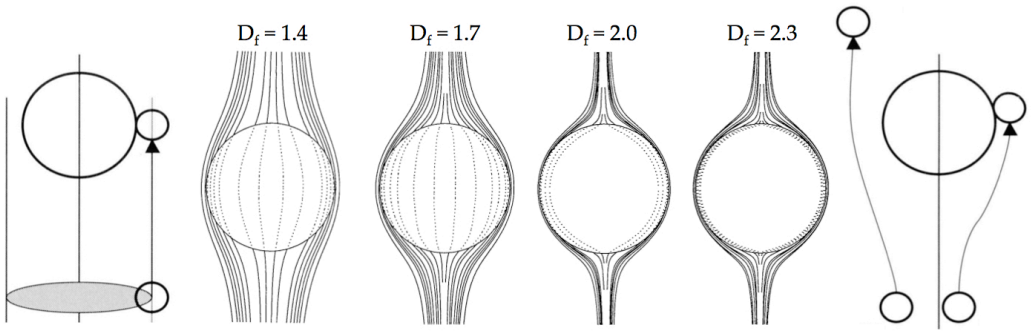

Figure 11: Schematic of rectilinear (far left) and curvilinear (far right) transport models alongside calculations of flow lines in fractal aggregates with radially varying permeability. Adapted from [210] and [209].

Practically, the curvilinear model drastically reduces the relative contribution of mixing in flocculation [210]. The inability of theoretical settling rates for impenetrable spheres to mirror experimental data has been demonstrated [211, 212]. Porosity decreases the drag force slowing the particle's fall, and experimental velocities of settling aggregates are often orders of magnitude greater than would be expected from Stokes' law for solid spheres. Furthermore, the attachment a of small particles by a large aggregate is overestimated if only aggregate diameter is considered, as flow lines that pass through large pores between clusters in an aggregate often carry small monomers with them unaffected [212]. By including fluid collection efficiency and the effective permeability of fractal aggregates, equations for shear and differential settling which better reflect experimental observations, as well as breakup due to shear stresses have been determined [179].

The fractal nature also determines the susceptibility of aggregates to shear stresses and helps determine the stable particle size distribution in a mixed system [213]. Breakup for denser aggregates occurs through the loss of monomers from the surface whereas lose aggregates are more susceptible to more dynamic aggregate fracturing [179, 214].

2.3.5 Measuring Fractal Dimension via Light Scattering

The fractal dimension of aggregates can be determined by studies employing light, x-ray, or neutron scattering [215]. In each case, the approach is the similar; the

intensity of scattered light depends on the scattering of the primary particles, P(q), and the structure of the aggregate, S(q) according to Equation 11,

$$I(q) \propto P(q)S(q) \qquad \text{(Eq 11.)}$$

Where q is the scattering vector in units of length^{-1}, given by

$$q = \frac{4\pi n}{\lambda}\sin\left(\frac{\theta}{2}\right) \qquad \text{(Eq 12.)}$$

Different length scales can be probed by changing the angle of detection, θ. Depending on the size of primary particles and of the aggregates, these length scales will fall under one of several regimes (Figure 12, Table 2).

Table 2: Light scattering regimes of fractal aggregates.

Regime	Region
Rayleigh	$\frac{1}{q} > R_g$
Guinier	$\frac{1}{q} \approx R_g$
Power Law	$R_g >> \frac{1}{q} >> a$
Porod	$a > \frac{1}{q}$

Scattering in the Rayleigh regime occurs for small q values, where the length scales probed are larger than the radius of gyration of the aggregate, R_g, and the intensity of scattering is determined by the suspension as a whole. Conversely, if the wavelength is small enough (x-rays or neutrons), or if particles are large, information about the surface

of the particles can be obtained in the Porod regime [215]. The power law regime corresponds to small length scales that fall between the radius of the primary particle, a, and the radius of gyration of the aggregate. In the power law regime, the intensity of scattering scales to the power of the fractal dimension such that plotting the intensity

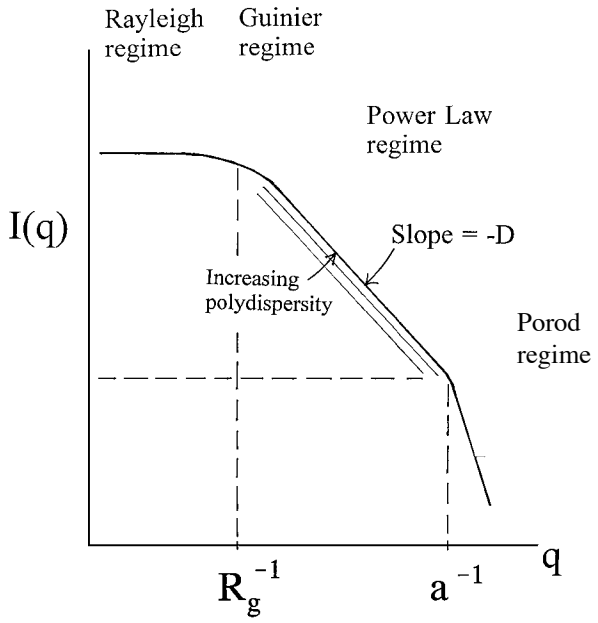

Figure 12: Illustration of light scattering regimes when plotting SLS data as intensity vs. scattering vector. Adapted from [196]

versus the scattering vector on a log scale returns a line whose slope is equal to the fractal dimension:

$$I(q) \sim q^{D_f} \qquad \text{(Eq 13.)}$$

2.4 Effect of Aggregation on Reactivity

In the case of reactive nanoparticles where reactions occur on the particle surface, reaction rates will vary, in part, as a function of the concentration of surface in the suspension. Particle aggregation produces differences in the local particle surface concentration within an aggregate, and changes in mass transport that depend on the aggregate morphology (as quantified for example by fractal dimension). It is therefore not surprising that changes in reactivity have been observed as particles are destabilized and form aggregates. Gilbert et al. demonstrated that the capacity for metal ion adsorption by iron oxyhydroxide nanoparticles decreased as fractal dimension increased [216]. ROS production has been linked to both aggregate size and structure [82, 121, 177, 217]. Lee et al. looked at how the preparation method affects ROS generation by FNPs, and found that ROS production was likely dependent upon the extent of aggregation [218]. This difference in ROS generation was hypothesized to result from increased quenching of the excited triplet state in larger, denser aggregates. Laser flash photolysis showed that the lifetime of the excited triplet state of individual C_{60} cages of small aggregates suspended via surfactants was orders of magnitude greater (tens of microseconds) than aggregated nC_{60} clusters (picoseconds) [132].

These observations were supported mathematically in a model proposed by Hotze et al., who demonstrated the influence of both aggregate size and structure on the presence of the excited tripled state [219]. Additionally, the Hotze model helps to

explain the conflicting ROS production findings for C_{60} and fullerol in early experiments. Often suspensions of nC_{60} were observed to produce little to no ROS while fullerol, possessing a decreased quantum yield and therefore a theoretically lower production capacity per cage, produced greater bulk ROS concentrations [127, 132, 220-222]. By taking into account the morphology of aggregates, the decrease in quantum yield for fullerol versus fullerene can be compensated for with the smaller, more open aggregates that are oftentimes formed.

Chae et al., in filtering FNPs showed not only a greater degree of hydroxylation for smaller aggregates, but also a substantial increase in ROS production as the average aggregate size decreased [121]. Hu et al. showed that as hydroxylation due to UV irradiation increased over the course of 15 hours, the degradation rate of furfuryl alcohol due to singlet oxygen production also increased, attributed to the production of a larger number of smaller, more stable aggregates [141]. The potential for these transformations, either of C_{60} as a result of suspension preparation or of nC_{60} suspensions resulting from UV exposure, underscores the need to further investigate the dependency of ROS production and aggregate stability on surface functionalization.

In studies using TiO_2 and ZnO, Jassby et al. observed and modeled the decrease in •OH generation as particles aggregated in various ionic strengths [177]. In addition to aggregate size, fractal dimension strongly impacted the reactivity of the material on a per monomer basis. A previous study by Jassby and Wiesner using coated and uncoated

ZnS nanoparticles demonstrated that aggregation to a critical size resulted in the sharp increase in photoluminescence [217]. It was hypothesized that after sufficient particle-particle interactions were induced by aggregation, a decrease in surface tension in the aggregate resulted in greater electron-hole recombination, observed as photon emission at 284nm. The magnitude of the photoluminescence is likely due to aggregate structure, with denser aggregates absorbing less incident light and producing less photoluminescence, though the exact interplay is not yet well determined [29].

2.5 NPs in Environmental Waters

Nanoparticles released into environmental waters will be exposed to various chemistries that will affect their aggregation state and ROS production capacity. These factors influencing NP aggregation include inorganic ions, natural organic matter, metals and organic pollutants. Some ions (e.g. phosphate, nitrate) and organic pollutants (e.g. pesticides, PCBs) are often found at elevated concentrations in urban waters [223].

While there is significant variation, typical surface waters range from pH values of 5.7 to 9, with carbonate, chloride, sulfate, and nitrate the most common anions at approximately μM concentrations [182, 224]. Carbonate is a particularly efficient radical quencher, and although the resultant carbonate radical is a weaker oxidant than •OH, it can itself participate in a number of reactions [225].

In addition to promoting aggregation due to compression of the electrical double layer, specific interactions with the TiO_2 surface will likely further impact stability and

ROS generation [29, 177, 226]. Phosphorus concentrations are typically low in natural freshwaters, though the extensive use of fertilizers in both urban and agricultural landscapes creates nearly ubiquitously elevated concentrations in these locations. Additionally, phosphate is known to specifically interact with the TiO_2 surface, which has been seen to increase NP stability [227, 228]. As NPs are often negatively charged, the presence of metal cations, such as sodium, magnesium, calcium and aluminum, will play a significant role in inducing aggregation.

Natural organic matter (NOM) is a ubiquitous chromaphore, primarily comprised of degradation products of biomolecules existing in surface waters at concentrations widely varying around 1 mg L^{-1} (ranging from 0.1 to 100, depending on water type) [182, 229, 230]. NOM coatings such as humic and fulvic acids have been shown to increase nanoparticle stability and transport by increasing steric hindrance [184, 185, 231]. Furthermore, the redox chemistry and photosensitizing ability of NOM will likely complicate attempts to determine net photoreactivity in mixed NP/NOM systems [65-68].

Under environmental release scenarios a nanoparticle or aggregate will interact with suspended background particles, producing mixed aggregates [232-235]. The vast difference in particle number concentrations makes it likely that aggregates will consist mostly of colloidal matter with nanoparticles incorporated into the structure. What remains unclear, however, is how this combination will impact NP reactivity. In some

instances, the creation of heteroäggregates has been shown to increase ROS production. This has been demonstrated for mixtures of TiO_2 and SiO_2 processed at high temperatures [236-238], though nanoparticles released into surface waters and exposed to UV light are unlikely to be exposed to such extreme conditions. Conversely, the same effects of aggregate size and structure seen in homoäggregates to impact NP reactivity will take place during heteroäggregation. While some studies have looked at heteroäggregation under environmentally relevant conditions, very little research into the impacts of these interactions on NP reactivity has been undertaken [170].

2.6 Possible Risks Posed by Nanomaterials

While the working definition of NPs hinges on one dimension being less than 100nm, the useful properties (e.g. increased reactivity, dissolution, toxicity) resulting from this small scale are the primary drivers of NP production and innovation rather than their bulk counterparts [107, 226, 239, 240]. However, along with the promise of emerging technologies come concerns surrounding the impact of inevitable NP release into the environment. The opportunity exists with NPs to enable advancements of technology in an environmentally responsible manner, and from the onset, a concerted effort has been made to concurrently develop the technology and understand the risk associated with the implementation of said technology [7]. This drive has come from government regulation as well as public concern, and at the heart of these concerns are still-unanswered questions about how the intriguing properties of a NP that we look to

harness, such as reactivity, are affected by the fundamental interactions (e.g., transport, aggregation, sorption) that will occur when exposed to various environments [10, 18, 241, 242].

Assessing the risk of engineered NPs in a timely fashion so as not to be outpaced by, or to impede, technological advancement has proven difficult. While the challenges presented by NPs are not dissimilar to other emerging contaminants, conventional chemical toxicology does a poor job at predicting risk for NPs, as actual exposure often is not the same as predicted exposure [242]. Environmental impacts of NP release have not yet been observed or established, however monitoring and research are unable to keep pace with the increasing development of nanotechnology [7]. The myriad potential exposure conditions, endpoints and environmental systems to be considered for even a single NP render a comprehensive understanding of the associated risk an intractable problem [243]. Neither the time, the funding, nor the research hours are available to realize every potential permutation in which a NP could impact the environment. Furthermore, the analytical instrumentation to do so is often inadequate. There is general agreement that research should be undertaken at realistic exposures, though in the absence of observed impacts, a consensus of what constitutes "environmental relevance" has not yet been reached [242].

Progress has been made in toxicity and fate/transport modeling based on the combined data of individual experiments but to date this has been slow, and the vast

number of possible combinations makes studying each condition individually untenable [244]. To effectively utilize the models we have and are developing, the most likely scenarios should be given priority. Data generated from these targeted tests will then become model inputs to more effectively improve predictability [242]. The emerging nanoinformatics field looks to facilitate both the identification of what constitutes relevant data as well as the integration of these data into workable databases [241].

2.6.1 Need for Standardized Systems and Tests – Functional Assays

Predicting the impact of NP photoreactivity relies on the idea that physicochemical properties of NPs determine exposure and hazard (risk), yet approaching NPs this way has not lead to effective guidelines or regulations. This is largely due to the path-dependent changes to these physicochemical properties that govern transport, reactivity, etc. As discussed above, released NPs will significantly transform and age, resulting in different behaviors and reactivity depending on the environments encountered [29, 245]. NP form, shape, aggregation state, surface area, and coatings will all be impacted by environmental conditions, and these will in turn dictate effective dose, toxicity, bioavailability and reactivity. Tracking, measuring, and predicting these changes are not trivial tasks as these interactions are not yet well understood. Perhaps because of this, with no established ageing protocols or agreed upon realistic endpoints, most research has focused on pristine or minimally aged NPs [242]. Identifying the major pathways through which NPs might reasonably travel and

impact their environment would lead to risk assessments for a focused list of standard chemistries and release scenarios - a much more attainable goal [10, 11].

To facilitate this, it has been proposed to establish an agreed upon set of representative environmental conditions that can be paired with specifically monitored endpoints for which a NP should reasonably be investigated [241, 242]. The use of functional assays (FAs) can yield data at specific endpoints for NPs in complex reference systems that take into account this path-dependent nature. Thus, under representative environmental conditions, FAs will employ behavioral tests (akin to BOD_5 or K_{OW} measurements) to measure an expected outcome or impact of the NP, endpoints that will incorporate but not require a fully mechanistic understanding of NP behavior. Ultimately, FAs will provide a framework for individualized experimental measurements to more effectively test and describe scientific theory, determining rates of processes or interactions that will enable parameterization of models [241]. In the absence of agreed upon representative environmental conditions, investigating trends in nanoparticle reactivity and the primary variables that impact ROS production represents an important step forward in our understanding.

3. Methods

Nanoparticle reactivity will depend greatly on aggregation state and solution chemistry. Therefore, to effectively study the impact of surface chemistry, not only do reactive endpoints (e.g. ROS generation, bacteria inactivation) need to be measured, but NP suspensions should also be well characterized (e.g. aggregate size and structure, surface charge). This chapter provides common methods for the NP photoreactivity studies in this dissertation. Specifics to the three cases considered in this research are included in Chapter 4 (Sections 4.1.2, 4.2.2 and 4.3.2).

3.1 NP Suspension Preparation

The method of preparing consistent, stable suspensions of NPs depends largely on the type of NP being used and the solution into which it is to be dispersed. For NPs that do not readily disperse in solution, probe sonication was performed using a high-energy probe (S-4000, Misonix, Qsonica, LLC, Newtown, CT) with a 1/2" diameter tip.

3.1.1 FNP Suspensions

C_{60}, $C_{60}(OH)_6$, $C_{60}(OH)_{24}$ and $C_{60}(NH_2)_6$ were purchased in powder form from MER Corp. (Tucson, AZ). A colloidal suspension of fullerene (aqu-nC_{60}) in NanoPure water (NPW) was prepared by probe sonication of 100 mg C_{60} powder in 200 mL NPW (resistivity > 18 MΩ cm and TOC< 30 $\mu g\ L^{-1}$) for 10 hours operated in pulse mode (10 min ON, 20 min OFF) in the dark. Following sonication, the suspension was filtered through a 100 nm nylon membrane filter (Magna, GE Osmonics, Minnetonka, MN). The

filtrate was then concentrated via rotavaporator (Büchi, Flawil, Switzerland). DLS measurements of the suspension before and after concentration indicated no change in average aggregate size.

Well dispersed stock suspensions of $C_{60}(OH)_6$, $C_{60}(OH)_{24}$, and $C_{60}(NH_2)_6$ were prepared by adding powder directly to ultrapure water and stirring overnight and filtering to < 100 nm. The total carbon concentration of all stock suspensions post filtration was measured (TOC-L, Shimadzu, Japan), and stocks were diluted to a concentration of 5 mg C L^{-1} for experiments.

3.1.2 TiO_2 Suspensions

Suspensions of TiO_2 were prepared through probe sonication of NP power in the desired media. 2 mg of powdered TiO_2 NPs (P25 Aeroxide TiO_2, Evonik Industries, Essen, Germany) were weighed with an analytical microbalance (Mettler Toledo, USA) in the hood and transferred to 30 mL of NPW. To this 20 mL was added to reach a final volume of 50 mL, resulting in 40 mg L^{-1} TiO_2 in a solution of desired chemistry. Following the protocol of Taurozzi et al. NP suspensions were placed in an ice bath and probe sonicated at 60% amplitude in pulse mode (12 s on 3 s off) for a total of 5 min sonication time, resulting in a suspension having a median aggregate radius of approximately 100 nm as measured by DLS.

TiO_2 suspensions close to the PZC (6.2-6.3) will not remain in suspension for appreciable lengths of time, and aggregates will double in size in tens of minutes. For

this reason, pH values were adjusted sufficiently far from the PZC, and the use of a pH buffer (e.g. phosphate) was frequently employed. Even within a buffered solution, overnight storage of suspensions is not recommended, and new TiO_2 stocks were created immediately prior to each use.

3.2 UV Illumination

UV irradiation was performed in a Pelco UVC2 Cryo Chamber (Ted Pella, USA) equipped at the top with a manifold containing two Phillips TL-D 15W BLB bulbs (Phillips, Netherlands) The output of these bulbs centered at 365 nm and was modeled as a normal distribution with mean at 365 nm and standard deviation of 10 nm. The lamps were separated from the chamber by a shutter, enabling the flux of light to be interrupted and samples collected without turning off the lamps. Prior to experiments, the lamps were turned on and allowed to stabilize, as an initial spike in UV flux occurred which then decayed to a stable output after approximately 30 minutes. Temperature was held constant at 22 ± 2 °C though the use of a chiller. Irradiance was measured throughout the duration of experiments with a radiometer equipped with a UV-A filter (UVX , UVP, Inc., USA and ILT1400 and SEL033 UV-A filter, International Light Technologies, USA).

The flux of UV light was observed to depend on location in the UV chamber, both along the z-axis (distance from the bulbs) as well as x-y positioning. Four locations of equal flux were identified such that measurements could be run in triplicate and the

radiometer employed at the same time. Magnetic stir plates were positioned at these locations, and experiments were run as stirred batch reactors. The geometry of the reaction beaker (H=3.5 cm, Ø=5 cm) produced a 0.5 cm thickness liquid layer, including the stir bar (3 x 10 mm). For experiments in which volatilization was a concern, reactors were covered with glass petri dishes, though this reduced the flux slightly.

3.3 ROS Measurements

ROS production was measured with fluorescent probes and quenching agents as described below. For $^1O_2$ and •OH, standard curves were produced to quantify ROS generation.

3.3.1 $^1O_2$ Measurements with SOSG

$^1O_2$ concentrations were measured as the increase in fluorescence units (FSU) as Singlet Oxygen Sensor Green (SOSG, Molecular Probes-Invitrogen) was oxidized to SOSG-EP. Excitation of SOSG-EP between 460-490 nm results in fluorescence between 510-550 nm. A Modulus fluorometer (Modulus Single Tube 9200, Promega, USA) equipped with a blue optical kit filter was used to measure fluorescence. The blue optical filter consisted of an excitation wavelength at 460 nm and a band pass emission filter ranging from 515 – 570 nm, which corresponds well with SOSG-EP.

SOSG (Invitrogen, Thermo Fisher Scientific, USA) was ordered in packaged aliquots of 100 μg that were stored at -20 °C. The probe was prepared by suspending one aliquot of SOSG in 33 μL of methanol. This was combined with 0.97 mL of NPW by

carefully drawing the solution in and out of a pipette tip, resulting in a SOSG stock concentration of 165 μM. 0.1 mL of this solution was spiked into 10 mL samples to measure singlet oxygen at a final SOSG concentration of 1.65 μM. β-carotene was used as a quenching agent at a final concentration of 50 μm. Stocks in methanol stored in the freezer were diluted to a 1 mM solution and bath sonicated to ensure dissolution prior to use.

3.3.1.1 Standard Curve Preparation

Singlet oxygen production was determined by comparing the measured fluorescence of SOSG in fullerene suspensions versus a Rose Bengal (RB) standard curve. Oxidation of SOSG at various RB concentrations was measured over 5 minutes, and a linear fluorescence response was determined for a RB concentration range of 0.005 – 0.1 μM.

The rate of photons hitting the sample per second was calculated from the output of the lamps, the liquid surface area, and the Plank-Einstein equation as follows:

$$r_{photon} = \frac{irr \cdot a \cdot \lambda}{h \cdot c} \qquad \text{(Eq 14.)}$$

where irr is the irradiance in W/cm^2, a is the illuminated area of the reaction vial, c is the speed of light, λ is the wavelength, and h is plank's constant. Combining this with absorption measurements of the RB standard solution at 365 nm, ABS_{365}, the quantum yield, Φ, and Avogadro's number, N_A, gives the rate of singlet oxygen production in molar concentration per time:

$$r_{^1O_2} = \frac{r_{photon}(1-10^{-ABS_{365}})\phi}{V \cdot N_A} \quad \text{(Eq 15.)}$$

Knowing this, the fluorescence response of SOSG can then be equated to the singlet oxygen production rate as follows. Accumulation of singlet oxygen in suspension can be modeled as

$$\frac{d[^1O_2]}{dt} = r_{^1O_2} - k_d[^1O_2] \quad \text{(Eq 16.)}$$

where k_d is the rate of quenching in water ($k_d = 2.4 \times 10^5$ sec^{-1}) [373]. Making the steady state approximation, an equation for $[^1O_2]_{ss}$, in moles, can be calculated as

$$[^1O_2]_{ss} = \frac{r_{^1O_2}}{k_d} \quad \text{(Eq 17.)}$$

Thus, from the Rose Bengal standard suspensions, the fluorescence response due to a given steady state singlet oxygen concentrations can be calculated as

$$\frac{dFSU}{dt} = k_{^1O_2}[^1O_2]_{ss}[SOSG] \quad \text{(Eq 18.)}$$

where FSU is the detected fluorescence resulting from the cumulative reaction of SOSG with the produced $^1O_2$ over the irradiance time t, k_{1O2} is the second order rate constant, and $[^1O_2]_{ss}$ is the steady state $^1O_2$ concentration. By using a sufficiently large [SOSG] compared to produced $^1O_2$ and short irradiance times, the concentration of unreacted SOSG in solution can be assumed constant, giving the pseudo first order kinetics:

$$\frac{dFSU}{dt} = k'_{^1O_2}[^1O_2]_{ss} \quad \text{(Eq 19.)}$$

Here, k'_{102} is the pseudo-first order rate constant whose units are FSU uM^{-1} min^{-1}. Typically, pseudo-first order and first order rate constants have units of concentration per concentration per time, which reduces to simply units of per time. Because fluorescence, which does not have units of concentration, was modeled, the reactivity rate constant is slightly modified. The observed increase in fluorescence was plotted versus calculated singlet oxygen concentration, and the slope (with units of FSU uM^{-1} min^{-1}) was used to convert the observed rate of fluorescence into the singlet oxygen concentration in solution. Concentrations of irradiated fullerene suspensions were adjusted to maintain fluorescent responses within the linear standard range.

3.3.2 •OH Measurements with TA

Hydroxyl radical production tests were performed on samples of 20 mg L^{-1} P25 TiO_2 through the hydroxylation of TA to 2-HTA (ex 315, em 425). 0.5 mM TA stock solutions were prepared by adding 8.36 g TA to 100 mL NPW. The solubility of the probe increases with pH so a buffer solution or pH adjustment was necessary for preparation. Stock solutions were stirred on a magnetic stir plate for 24 hours to ensure dissolution, filtered with a disposable sterile 0.22μm cellulose acetate filter system (Corning, USA) and stored in the dark. TA was dosed at a final concentration of 125 μM in solution.

Hydroxyl radical measurements were made by adding a 0.5 mL sample aliquot to 0.75 mL deionized water in a 2 mL centrifuge tube. For conditions of low expected •OH production, this dilution step was skipped, and 1.5 mL was sampled directly. The presence of NPs was observed to influence fluorescence measurements due to light scattering, so samples were centrifuged for 5 minutes at 12,000 RPM to separate the TiO_2 from the solution. 1 mL of the resulting supernatant was transferred to a plastic cuvette (10 mm optical path) and fluorescence was measured (Varian Eclipse fluorometer, Agilent, USA) at an excitation wavelength set to 315 nm. 2-HTA fluorescence was recorded from 325-540 nm to collect the full emission peak. The gain on the photomultiplier was adjusted depending on experiment to ensure that fluorescence from small amounts of ROS generation was detectable but did not saturate the detector at longer timepoints. All samples were measured using the same gain setting to enable comparison between experiments. No auto-fluorescence was observed in blanks or dark samples, nor did overhead fluorescent lighting influence results. N-acetyl-L-cysteine (N-AC) (Sigma-Aldrich) was used as a •OH quencher. 16.3 mg N-AC was dissolved in 10 mL NPW and filtered in a 0.22 μm syringe filter to sterilze, resulting in a 10 mM stock concentration. For quenching experiments, 0.2 mL was spiked into 10 mL samples for a final concentration of 200 μM.

3.3.2.1 Standard Curve Preparation

Fluorescence was converted to 2-HTA concentration using a standard curve created by diluting a 0.125 mM 2-HTA stock solution to 6 points ranging from 0.0025 to 0.1 M, as determined by fluorescence limits and detector saturation. Hydroxyl radical concentrations were estimated with the following reaction, assuming 80% trapping efficiency for $OH^{\bullet}$ by TA [87] and considering sample dilution prior to centrifugation:

$$TA + {}^{\bullet}OH \rightarrow 2 - HTA \qquad \text{(Eq 20.)}$$

3.3.3 $O_2\bullet^-$ Measurements with HE

Superoxide ($O_2\bullet$-) was detected as the increase in fluorescence from 540 to 800 nm (max 586 nm, excitation at 510 nm) resulting from the transformation of dihydroethidium (DHE) (Invitrogen, Thermo Fisher Scientific, USA) in solution to 2-hydroxyethidium (2-HE). Stock solutions of HE were prepared by dissolving 1 mg HE in 100 μL DMSO to which was added 900 μL NPW, resulting in a 3.17 mM stock solution. For quenching experiments, 160 μL were spiked into 10 mL samples for a final concentration on 50.7 μM (0.16% v/v DMSO).

Superoxide dismutase (SOD) (Sigma-Aldrich) was used as the $O_2\bullet$- quenching agent. Stock solutions were made at 3,000 U mL^{-1} by adding 10 mL NPW to the 5.8 mg container and stored at -20 °C. For quenching experiments 100 μL SOD stock was spiked into 10 mL samples for a final concentration of 30 U mL^{-1}.

3.4 Additional Reactivity Endpoints

When employing biological endpoints, all glassware, stir bars and pipette tips were autoclaved prior to use. With the exception of UV exposure experiments, reactions were covered in aluminum foil to limit contamination. Stocks and samples were kept on ice during experiments and during the transfer of samples.

3.4.1 Viral Inactivation

For viral inactivation experiments, a 0.1x phosphate buffered saline (PBS) solution was used to maintain virus viability. Bacteriophage MS2 (American Type Culture Collection (ATCC) 15597-B1) was propagated on *E. coli* (ATCC 15597) and enumerated using the double-top agar assay. A highly purified, high-titer virus stock in PBS was prepared as follows. First, MS2 was cultured on double-layer agar plate with *E. coli* as the host incubated at 37 °C. Next, the phages on the top agar were extracted into 1x PBS and precipitated using 10% polyethylene glycol at 4 °C for 1 h. The precipitated phages were centrifuged at 10000*g* for 15 min at 4 °C, and the supernatant was decanted and the pellet resuspended in PBS and incubated overnight at 4 °C. The residual bacterial debris and polyethylene glycol in the phage suspension were removed by centrifugation at 5000 *g* for 10 minutes at 4 °C and the addition of chloroform (1:1 sample-to-chloroform), respectively. The phage-containing aqueous phase was separated from the organic phase by centrifugation as before. The suspension was furthermore concentrated by ultracentrifugation at 103,000 *g* for 2.5 h at 12 °C, and the

phage pellet was then resuspended in PBS. The viruses were counted in terms of plaque forming units (PFU). This procedure yielded an initial stock concentration of $1.1x10^{12}$ PFU mL^{-1}. MS2 toxicity was calculated as log inactivation relative to time 0 min.

3.4.2 Bacterial Inactivation

All bacterial inactivation experiments employed a Minimal Davis media (MD) designed to stabilize the particles, buffer the pH at 7.5, and maintain bacterial viability, as described by Lyon et al. [366]. Briefly, the recipe for 1x MD is a follows: 45 mg K_2HPO_4, 50 mg $(NH_4)_2SO_4$, 25 mg sodium citrate, and 5 mg $MgSO_4 \bullet 7H_2O$ were dissolved in 100 mL NPW. MD stock solutions were created at a 10x concentration and bath sonicated, after which they were sterilized via filtration with at 0.22 μm cellulose acetate disposable filtration unit, and stored in the fridge until use. The cavitation induced by probe sonication was observed to sufficiently sterilize TiO_2 stock suspensions.

Pure cultures Gram Positive *Bacillus subtilis* strain 168 ATCC 23857 and Gram Negative *Acinetobacter baumannii* ATCC 49466 (ATCC, Manassas, VA, USA) were grown overnight at 37 ^oC in tryptic soy broth. Cells were pelleted at 8,000 rpm for 10 minutes and washed thrice with MD. Cells were then resuspended in MD to a final concentration of 10^9 cells mL^{-1}. 2 mL aliquots of the bacteria suspension were added to each batch reactor.

Samples taken from the reactors for inactivation measurements were serially diluted to obtain a final concentration of 10^3 CFU mL^{-1}. 100 μL of the final dilution was

then spread onto tryptic soy agar plates in triplicate and allowed to grow overnight at 37 ^{o}C. The resulting colonies were then counted, and ROS and CPF toxicity was calculated as log inactivation relative to time zero.

3.4.3 Inactivation Kinetics and ROS Dose

Inactivation kinetics were calculated using the Chick-Watson model employing the idea of CT, the dose measurement for conventional disinfectants, where

$$CT = \frac{FSU(t)}{k'_{ROS}} = [ROS]_0 t \qquad \text{(Eq 21.)}$$

Here, CT is the disinfectant concentration, C, multiplied by the contact time, t. The disinfectant concentration, C, is the steady state ROS concentration probed on or very near the surface of the NP, calculated using the experimental standard curve, above. Log inactivation was then plotted vs. CT to determine dose response.

3.4.4 CPF Degradation

Chlorpyrifos (99.5%, Chem Service, West Chester, PA, USA) stocks were made in methanol at 1.5 g L^{-1} and stored in the fridge for up to 1 month. Working stocks were created at 1.5 mg L^{-1} by spiking 10 µL of the stock in 90 mL NanoPure water on a stir plate. To this, 10 mL of 10x MD media was added dropwise. For all experiments, CPF was spiked into samples at 375 µg L^{-1}. Stocks of CPF degradation products CPF Oxon (analytical standard, AccuStandard, New Haven, CT, USA) and 3,5,6-trichloro-2-pyridinol (TCP) (analytical standard, Sigma-Aldrich) suspensions were similarly

prepared. Chlorpyrifos, CPF Oxon, and TCP concentrations were determined via LC/MS as outlined in Chapter 4.3.2.

3.5 Aggregate Characterization

3.5.1 Transmission Electron Microscopy

High-magnification images of suspensions were obtained by transmission electron microscopy (TEM) (FEI Tecnai G2 Twin, Hillsboro, OR). For NP imaging, 10 μL was deposited on a lacey carbon/Cu grid (300 mesh, Electron Microscopy Sciences, USA) and dried in air before TEM measurement. MS2 bacteriophages were negatively stained with 2.5% phosphotungstic acid (Fluka, Milwaukee, WI) prior to imaging. Bacteria were deposited on the grid, fixed with 2.5% glutaraldehyde, and sequentially dehydrated with graded ethanol and washed with 1x PBS in order to maintain structural integrity.

3.5.2 Aggregate Size by Laser Diffraction

Laser diffraction (Mastersizer 3000, Malvern Instruments, England) was used to determine TiO_2 aggregate size and fractal dimension (Section 3.5.4). In-line light scattering measurements were performed using a peristaltic pump located downstream of the instrument by which samples were fed from a beaker continuously mixed on a magnetic stirrer at 400 RPM. The pump rate was set at approximately 15 mL min^{-1} to minimize shear within the tubing, and 600 mL samples were used so that the suspension was not recirculated, avoiding changes in aggregation state due to the pump. Prior to data collection, background measurements were collected using the same solution

chemistry and sample flow rate as in NP aggregation samples. Time resolved size measurements, reported in terms of median hydrodynamic diameter (D_{50}) both as number weighted and volume weighted intensity, were set to 10 s duration with a 100 s delay, resulting in measurements being collected every two minutes.

3.5.3 Particle Size by Dynamic Light Scattering

Dynamic light scattering (DLS) measurements were performed with the Zetasizer Nano ZS (Malvern Instruments, England), which is equipped with a He-Ne laser (633nm) and a detector fixed at 173°. A minimum of 3 measurements were collected, with aggregate size reported both as unweighted and number weighted. The polydispersity index (PDI) is a value ranging from 0 – 1 and indicates the degree to which aggregates in suspension are uniformly distributed with larger PDI values indicating more heterogeneous aggregate sizes.

3.5.4 Fractal Dimension by Static Light Scattering

Static light scattering (SLS) measurements were collected with the Mastersizer and were performed concurrent with aggregate size measurements. Data recorded for each sample by an array of detectors consisted of the scattering intensity, I(q), over a range of scattering vectors, q, corresponding to 0.8 - 42°. The aggregate fractal dimension, D_f, was determined as the negative slope of the linear power law region when plotting log(I(q)) vs. log(q) [215]:

$$I(q) = q^{-D_f} \quad \text{(Eq 22.)}$$

The multiple detectors of the Mastersizer correspond to scattering vectors from 0.18 – 9.47 μm^{-1}, with q related to the detector angle, theta, as follows

$$q = \frac{4\pi n}{\lambda} \sin\frac{\theta}{2} \quad \text{(Eq 23.)}$$

where n is the refractive index of the medium (1.33 for water) and λ is the wavelength of scattered light (633 nm) [194, 215]. Equation 22 holds when

$$qR_h > 1 \quad \text{(Eq 24.)}$$

i.e. for length scales, (q^{-1}) less than the radius of the aggregate, R_h.

At each timepoint, D_f was calculated via linear regression over the power law region of the scattering curve. Linearity was determined to hold when the difference between the local slope for a given q value and the slope of a line drawn between the same q value and the final q value was no greater than 12%. The process of calculating fractal dimension from scattering data was automated by code written in Matlab.

3.5.5 Electrophoretic Mobility and pH Titrations

Particle electrophoretic mobility (EPM) was measured a minimum of 3 times (Zetasizer Nano ZS) and reported as zeta potential (calculated via the Henry equation). As EPM is highly dependent on solution chemistry, measurements were performed under the same conditions as those being tested.

TiO_2 nanoparticle pH titrations were performed on 50 mL suspensions of 20 mg L^{-1} P25 TiO_2 at various anion concentrations. Suspensions were continually stirred in a beaker placed on a magnetic stir plate while pH was monitored and adjusted with either 0.01 M or 0.1 M KOH or HCl. At each pH step, the rate of stirring was increased and sufficient acid or base was added to move the solution pH approximately 0.2 units. This was allowed to mix briefly before stirring was reduced again and pH was allowed to equilibrate. 0.7 mL sacrificial aliquots were taken for electrophoretic mobility measurements and the isoelectric point (IEP) was identified as the pH for which the EPM of a suspension was zero.

4. Results and Discussion

4.1 Bacteriophage Inactivation by UV-A Illuminated Fullerenes: Role of Nanoparticle-Virus Association and Biological Targets

Abstract

Inactivation rates of the MS2 bacteriophage and $^1O_2$ generation rates by four different photosensitized aqueous FNP suspensions were observed to follow the same order: aqu-nC_{60} < $C_{60}(OH)_6$ ≈ $C_{60}(OH)_{24}$ < $C_{60}(NH_2)_6$. Alterations to capsid protein secondary structures and protein oxidation were inferred by detecting changes in infrared vibrational frequencies and carbonyl groups respectively. MS2 inactivation appears to be the result of loss of capsid structural integrity (localized deformation) and the reduced ability to eject genomic RNA into its bacterial host. Evidence is also presented for possible capsid rupture in MS2 exposed to UV-A illuminated $C_{60}(NH_2)_6$ through TEM imagery and detection of RNA infrared fingerprints in ATR-FTIR spectra. FNP-virus mixtures were also directly visualized in the aqueous phase using a novel enhanced dark-field transmission optical microscope fitted with a hyperspectral imaging (HSI) spectrometer. Perturbations in intermolecular extended chains, HSI, and electrostatic interactions suggest that inactivation is a function of the relative proximity between nanoparticles and viruses and $^1O_2$ generation rate. MS2 log survival ratios were linearly related to CT (product of $^1O_2$ concentration, C, and exposure time, T) demonstrating the applicability of Chick-Watson kinetics for all fullerenes employed in

this study. Results suggest that antiviral properties of FNPs can be increased by adjusting the type of surface functionalization and extent of cage derivatization thereby increasing the $^1O_2$ generation rate and facilitating closer association with biological targets.

4.1.1 Introduction

Generation of singlet oxygen ($^1O_2$) by photosensitized FNPs is known to inactivate bacteria and viruses, which is of interest to water disinfection [246-248], photodynamic therapy [249], and other medical and environmental applications [250]. Ecological risks arising from unplanned releases of nanoparticles can also be partially attributed to reactive oxygen species (ROS) production or oxidative stress [81, 251, 252]. Therefore, toxicological effects of fullerenes can be expected to be strongly dependent on the effective delivery of exogenous ROS generated by nanoparticles to the biological target. It is known that ROS production is determined by the morphology of nanoparticle aggregates, types of surface functional groups, and extent of surface derivatization [253-255], all of which also influence the effective separation distance between the nanoparticles and their biological targets. In this context, we hypothesize that both the $^1O_2$ generation rate and the relative proximity between fullerenes and viruses are important determinants of inactivation particularly since the lifetime of $^1O_2$ in aqueous solutions is only 3 – 4 ms [256, 257]. Limited data available in the literature supports our assertion even though direct evidence has not yet been provided. For

example, the differential inactivation of MS2 and *Escherichia coli*, by illuminated TiO_2 nanoparticles was likely correlated to varying amounts of association with TiO_2 [258]. Additionally, malonic acid adduct fullerenes were more phototoxic to Jurkat cells compared with a dendritic fullerene because they were postulated to associate more closely with the biological target even though their $^1O_2$ quantum yield was lower [259]. Also, electrostatic attraction between negatively charged viruses and cationic aminated FNPs very efficiently inactivated MS2 [33]. Even close association with natural organic matter (NOM) enhances MS2 inactivation since $^1O_2$ concentrations are elevated within the macromolecule [251]. While these studies indirectly postulate the significance of nanoparticle-microorganism association, the simultaneous interplay of proximity and $^1O_2$ generation during virus inactivation has not been explicitly examined to date.

While ROS-mediated antiviral activity of fullerenes and their derivatives has been amply demonstrated e.g. [33, 121, 246, 260], much less is known about the underlying virucidal mechanisms. Recent evidence points to oxidation of capsid proteins by exogenous ROS [247, 261, 262], but more detailed information on changes in structure is necessary to better understand underlying causes of inactivation. We hypothesize that $^1O_2$ modifies conformation of virus capsid proteins leading to loss of infectivity. The F-specific ssRNA coliphage MS2 was employed as a surrogate for nonenveloped enteric human viruses and to facilitate comparisons with other studies e.g. [33, 121, 246, 262].

Herein, we test the hypotheses that (i) virus inactivation is caused by changes in capsid integrity arising from oxidative protein conformational alterations or deformation and (ii) the rate of virus inactivation by photosensitized FNPs is controlled by their relative proximity as well as the $^1O_2$ generation rates. MS2 inactivation kinetics and $^1O_2$ generation rates were measured in the presence of UV-A illuminated suspensions of aqu-nC_{60}, $C_{60}(OH)_6$, $C_{60}(OH)_{24}$, and $C_{60}(NH_2)_6$. Oxidative damages to MS2 capsid proteins were characterized using attenuated total reflectance Fourier transform infrared spectroscopy (ATR–FTIR), OxyBlot protein oxidation assay, and sodium dodecyl sulfate polyacrylamide gel electrophoresis (SDS-PAGE). A novel hyperspectral microscopy technique was utilized to directly visualize association between nanoparticles and viruses in the aqueous phase. Hyperspectral imaging (HSI) allowed the superposition of a large number of images (~ 400) at high resolution (~ 1.5 nm) and identifying their components by matching their spectral signature instead of material color eliminating the need for sample dehydration. While HSI has been employed for military applications, mineral exploration, quality assurance, food safety, forensics, and health care e.g. [263], this is one of the first reports of its use in virus/nanoparticle identification. Further, the applicability of Chick-Watson disinfection kinetics "CT" (product of $^1O_2$ concentration C and exposure time T) for ROS-based inactivation is discussed with particular emphasis on the relative proximity of nanoparticles to the viral target and physicochemical parameters associated with $^1O_2$ generation.

4.1.2 Materials and Methods

4.1.2.1 Cultures, Phage Purification and Enumeration

Bacteriophage MS2 (American Type Culture Collection (ATCC) 15597-B1) was propagated on *E. coli* (ATCC 15597) and enumerated using the double-top agar assay. A highly purified, high-titer virus stock in PBS (10^{13} PFU (plaque forming unit) mL^{-1}), free of bacterial debris and media residues was prepared by centrifugation, precipitation, extraction, and ultracentrifugation [121].

4.1.2.2 Fullerene Suspensions

C_{60} (99.9%), $C_{60}(OH)_6$, $C_{60}(OH)_{24}$ and $C_{60}(NH_2)_6$ were purchased in powder form (MER Corp., Tucson, AZ). The aqueous fullerene suspension (aqu-nC_{60}) was prepared by ultrasonication and filtration (see Appendix A for details). Well dispersed stock suspensions of $C_{60}(OH)_6$, $C_{60}(OH)_{24}$, and $C_{60}(NH_2)_6$ were prepared by adding powder directly to ultrapure water and stirring overnight and filtering to < 100 nm. Particle size distributions were obtained via dynamic light scattering at 90° (ALV/LSE-5004, Langen, Germany) (see Appendix A, Figure 35). Electrophoretic mobilities were measured via Zetasizer Nano (Malvern Instruments, Bedford, MA). A concentration of 5 mg C L^{-1} (measured as total carbon, TOC-5050A, Shimadzu) was employed for all nanoparticles.

4.1.2.3 Irradiation and $^1O_2$ Detection

$^1O_2$ concentrations were measured as the increase in fluorescence units (FSU) (Modulus Single Tube 9200, Turner Biosystems) of Singlet Oxygen Sensor Green (SOSG,

Molecular Probes-Invitrogen) and quantified through Rose Bengal standard curves (Appendix A, Figure 36 and Figure 37). Two 15 W fluorescent bulbs (Philips TLD 15W/08) provided low-pressure UV irradiation, which had an output spectrum peak at 365 nm in the UV-A region and an intensity of 2.3 mW cm^{-2} as measured by a UVX Radiometer (UVP, Inc. Upland, CA) (see Appendix A for output spectrum, Figure 38). Test suspensions consisted of (1) MS2 + UV-A, (2) MS2 + FNP + UV-A, (3) MS2 + FNP in the dark, and (4) MS2 + FNP + β-carotene + UV-A. All vials were continually stirred, experiments were performed in triplicate, and β-carotene, an efficient $^1O_2$ scavenger served as a negative control.

4.1.2.4 ATR-FTIR Spectroscopy

The mid-infrared spectra (1800-1000 cm^{-1}) of MS2 (in solid form) treated with UV-A alone and UV-A sensitized fullerenes were collected using a Nicolet Magna 750 spectrometer equipped with infrared source, DTGS detector, and a KBr beamsplitter. Samples were prepared by first freezing a 45 mL sample in polypropylene vials overnight at -81 °C. Next, the vials were transferred to a sample holder attached to a freeze drier operating under vacuum for 48 h. The sample pellet from each vial was harvested and stored in 1.5 mL centrifuge tubes at 4 °C. Sufficient sample powder was deposited to cover the entire Ge internal reflection element (IRE) surface and the IR spectrum for each sample was obtained by averaging 512 scans collected at 4 cm^{-1} resolution. Background spectra were collected on a clean Ge IRE. All spectra were

processed using OMNIC v.5.29 software (Nicolet-Thermo Electron). Absorption peaks were assigned based on the second derivative of the original spectra and the sample constituents contributions to the peaks were described based on amino acids, proteins, and viruses [264, 265]. The peaks in the region 1700-1500 cm^{-1} were decomposed to separate overlapping peaks and then fitted to a Lorentzian-Gaussian model.

4.1.2.5 OxyBlot Protein Oxidation Assay

Prior to quantifying the carbonyl groups formed by the reactions of $^1O_2$ with amino-acid side chains, MS2 samples after 5 minutes of irradiation were concentrated to get 3-4 $\mu g\ \mu L^{-1}$ of total proteins (measured by Modified Lowry Assay). 10 μL aliquot of denatured-proteins was reacted with 2,4-dinitrophenylhydrazine (DNPH) for 15 min to form 2,4-dinitrophenylhydrozone (DNP-hydrazone), which confirms the presence of carbonyls in the sample. The amount DNP-hydrozone product formed was quantified by following a series of steps involving SDS-polyacrylamide gel electrophoresis (SDS-PAGE), Western blot analysis and treatment with antibodies, and chemiluminescent reagents (see Appendix A for detailed explanation). The oxidative status of each protein was then analyzed quantitatively by comparing the signal intensity (at 428 nm) of the same protein in different lanes on the same gel. A negative control was also prepared as described but without protein.

4.1.2.6 SDS-PAGE

SDS-PAGE was used to examine MS2 phage protein samples for the presence of cross-linkages induced by $^1O_2$ during illumination of fullerene suspensions [247].

4.1.2.7 Dark-Field based Hyperspectral Imaging Microscopy

An enhanced dark-field transmission optical microscope (Olympus BX41) equipped with a hyperspectral imaging (HSI) spectrometer (CytoViva® Hyperspectral Imaging System, Auburn, AL) was employed to simultaneously visualize fullerenes and viruses. This was equipped with novel optics that achieve Koehler and Critical illumination concurrently, which brightens particles 150 times more than conventional dark field microscopy. Koehler illumination is pre-aligned and fixed whereas Critical illumination is adjustable (up or down), which aids in finding the focal point including the position and size of the illuminated spot on the sample. This facilitated observation of non-diffraction limited optical effects and an improved point spread function extending the resolution well beyond diffraction limits of a conventional microscope to obtain spatial details of the sample [266]. The complete composite spectrum of each pixel (25x25 nm at 100x magnification) in the visible and near infrared wavelengths (400-1000 nm) was collected at 1.5 nm resolution in a hyperspectral image. The spatial distribution and spectral information of nanoparticles and viruses was derived from each hyperspectral image using the Environment for Visualization ENVI v.4.4 software. Samples were stained with 2.5% phosphotungstic acid (10 μL to 1 mL sample) for 30

seconds and 10 μL aliquots were imaged using glass slides. All images were acquired at a constant high gain and a 250 ms exposure time and background subtracted using ten dark-current images obtained prior to the sample scan. Using n-dimensional visualizer, the most spectrally active materials (i.e. endmembers) were identified, then compared with the spectral library of the materials, and finally using mixture tuned matched filtering technique, individual endmembers were mapped in the sample's hyperspectral image. The endmembers (spectral library plots) for pure and mixtures of MS2 and fullerenes were derived from hyperspectral images using ENVI's Spectral Hourglass algorithm (see Appendix A for HSI details, Figure 40). Three to five images with a field of view of 350-400 mm for each sample was examined and analyzed.

4.1.3 Results and Discussion

4.1.3.1 $^1O_2$ Generation by UV-A Sensitized Fullerenes

$^1O_2$ production was determined by comparing the measured fluorescence of SOSG in suspensions versus a Rose Bengal standard curve. Standard suspensions of Rose Bengal, a known $^1O_2$ sensitizer ($\Phi = 0.75$ [267]), were exposed to UV-A light centered at 365 nm. From the irradiance and reaction vial geometry, the cumulative $^1O_2$ generated was determined from the FSU measurements (see Appendix A for more details).

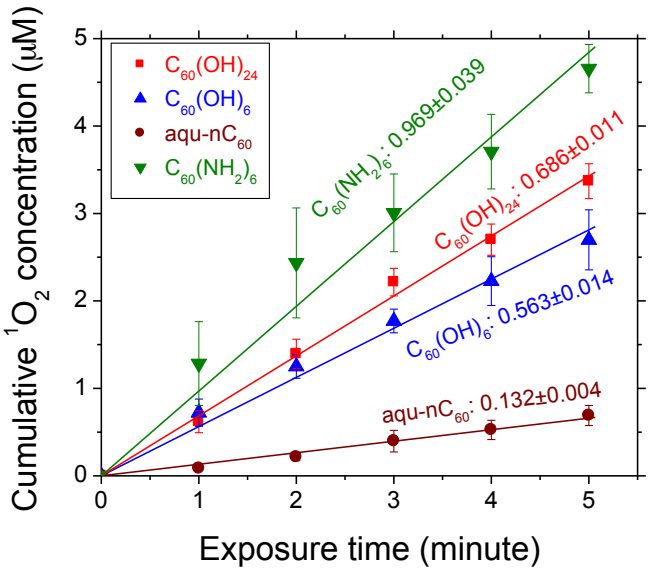

Figure 13: $^1O_2$ generation rates in UV-A sensitized FNP suspensions (15 mM PBS)

As summarized in Figure 13, UV-A-sensitized $C_{60}(NH_2)_6$ generated $^1O_2$ at the highest rate (0.969±0.039 μM min^{-1}) followed by $C_{60}(OH)_{24}$ (0.686±0.011 μM min^{-1}), $C_{60}(OH)_6$ (0.563±0.014 μM min^{-1}), and aqu-nC_{60} (0.132±0.004 μM min^{-1}). $^1O_2$ production depends on the quantum yield of primary nanoparticles and aggregate morphology [219, 268]. Shielding by particles on the outer surface of aggregates reduces absorption of the excitation radiation by those in the interior (an effect which becomes more pronounced for denser aggregates). On a per monomer basis, this shielding leads to a decreased rate of optically induced transitions and ultimately, lower ROS production. Additionally, for light absorbed by particles in the interior of the aggregate, a more dense morphology will increase the probability of physical and chemical quenching, which also lowers ROS production [254].

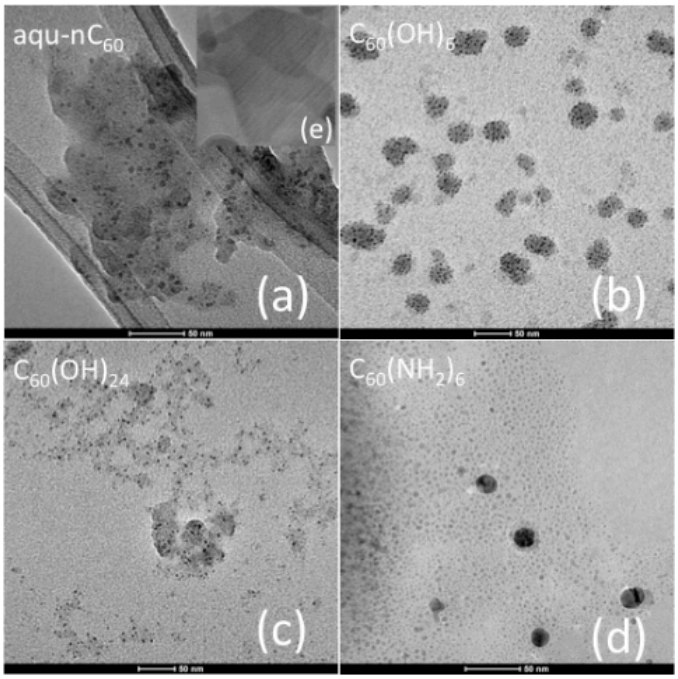

Figure 14: TEM images depicting the morphology of nanoparticle aggregates. Aqu-nC$_{60}$ crystal lattice planes are visible in (e).

For $C_{60}(OH)_6$ (number weighted average size of 8.46±0.22 nm), we see an increase in $^1O_2$ generation compared with aqu-nC_{60} (average size of 80.50±0.46 nm) despite a more disturbed π-electron shell arising from functionalization. This is likely because hydroxylation results in a smaller, more open aggregate compared with the crystalline structure that is seen for nC_{60} in TEM images (Figure 14 (a) and (e)). The fact that the $^1O_2$ generation has not overtaken that of the highly dendritic fullerol aggregates further illustrates the importance of extent of functionalization and aggregate morphology. The addition of six amine functional groups to the fullerene cage appears to create a more loosely associated configuration similar to $C_{60}(OH)_{24}$, as can be seen in Figure 14 (c) and (d), while doing so with a lesser degree of π-bond interruption, which further illustrates

the importance of the type of functional group. This combination, in addition to a smaller aggregate size (average size of 1.92±0.46 nm) compared to $C_{60}(OH)_{24}$ (average size of 4.46±0.38 nm), results in the highest $^1O_2$ production rate of all nanoparticles investigated.

4.1.3.2 $^1O_2$ Mediated MS2 Inactivation

In suspensions of MS2 + fullerenes + 90 μM β-carotene (an efficient $^1O_2$ quencher), the inactivation rates were similar to the rate measured with UV-A alone (see Appendix A, Table 7). Also, the production of superoxide, as measured by XTT (2,3-bis(2-methoxy-4- nitro-5-sulfophenyl)-2H-tetrazolium-5- carboxanilide) was negligible in all suspensions. Hence, exogenous $^1O_2$ was predominantly responsible for enhanced MS2 inactivation rates in UV-A sensitized fullerene suspensions. This result was expected given the lack of electron donor needed for type I sensitization and confirms previous results [246].

Virus inactivation in illuminated nanoparticle suspensions closely followed first order kinetics (Figure 15). aqu-nC_{60}, $C_{60}(OH)_6$, $C_{60}(OH)_{24}$, and $C_{60}(NH_2)_6$ increased MS2 inactivation rates by a factor of 1.7, 5.1, 5.5, and 11.4 respectively compared with UV-A alone following the same trend as $^1O_2$ production. No dark inactivation demonstrated that the FNPs investigated herein were not directly virucidal (Appendix A, Table 8). Inactivation by UV-A alone could be due to the formation of cross-linkages via disulfide bonds in Cys and Trp photooxidation, (Cys and Trp each constitute ~ 1.6% of the capsid)

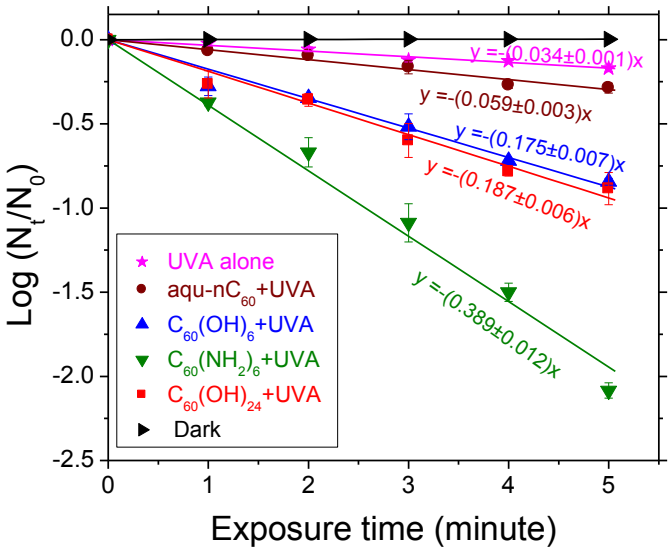

Figure 15: MS2 inactivation by UV-A alone and UV-A sensitized aqu-nC_{60}, $C_{60}(OH)_6$, $C_{60}(OH)_{24}$, $C_{60}(NH_2)_6$.

[269, 270]. The photoinactivation rate with 6.9 μM $C_{60}(OH)_{24}$ in this study (0.187 min^{-1}) was significantly higher than that obtained in our earlier using 40 mM $C_{60}(OH)_{24}$ (0.102 min^{-1}) indicating that looser and smaller fullerol aggregates generated higher $^1O_2$ concentrations and/or more closely associated with MS2. (Note that in this study, a 100 nm filtration step was introduced to remove very large aggregates.) Biochemical transformations in viruses were probed next.

4.1.3.3 Alterations to Protein Secondary Structures

Peak assignments in the mid-infrared region (1800-1000 cm^{-1}) are summarized in Appendix A, Table 9. $^1O_2$-induced changes to protein secondary structures in MS2 after 5

minutes of exposure were quantified from relative peak areas in curve fitted amide I spectra in the region 1700-1600 cm^{-1} (Figure 16).

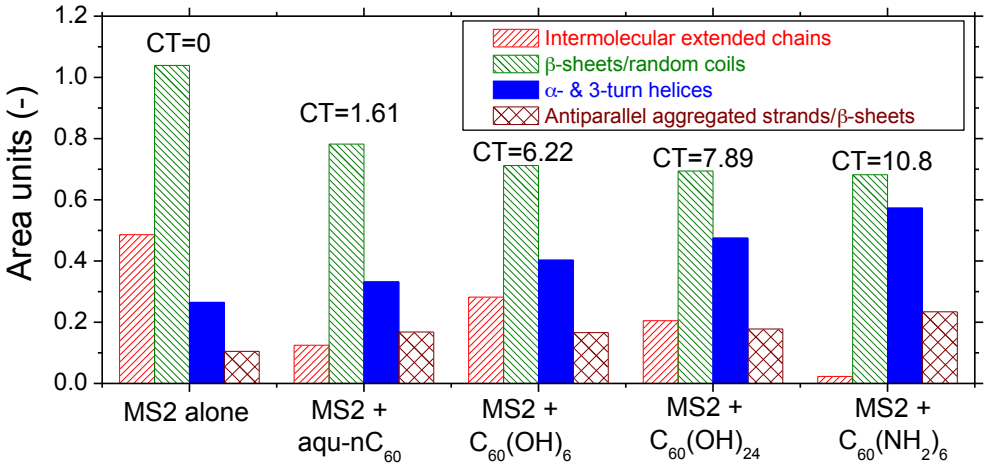

Figure 16: Changes in protein secondary structures (intermolecular extended chains, β-sheets and random coils, α- and 3-turn helices, and antiparallel β-sheets and aggregated strands following 5 minute exposure to UV-A illuminated FNP suspensions from ATR-FTIR. CT values correspond to 10^{-9} mg min L^{-1}.

Photoilluminated nanoparticles increased peak areas of α- and 3-turn helices and antiparallel aggregated strands/β-sheets but decreased infrared vibrational freedom of intermolecular extended chains and β-sheets/random coils in viruses. Changes in the interactions between α-helical structures and β-structures suggests unfolding of subunits of coat proteins and capsid destabilization via deformation or rupture [271]. Bonds in intermolecular extended chains, β-sheets, and random coils were potentially strained resulting in the loss of molecular tensional energy needed for maintaining structural integrity of the capsid [272]. Peak shifts associated with intermolecular chains also indicate morphological disorder in the capsid (Appendix A, Figure 41). Since the A-

protein assists in storing tension or strain energy in the coat protein [272], MS2 inactivation might also be associated with reduced ability to inject *E. coli* with its genomic RNA.

4.1.3.4 Formation of Carbonyl Groups and Protein Conformational Changes

Carbonyl groups, which appear between 1740 and 1730 cm^{-1} of the mid-infrared spectrum were detected in all viruses exposed to photoactivated fullerenes (but not UV-alone) demonstrating oxidation of capsid proteins as seen in Figure 17 [273, 274].

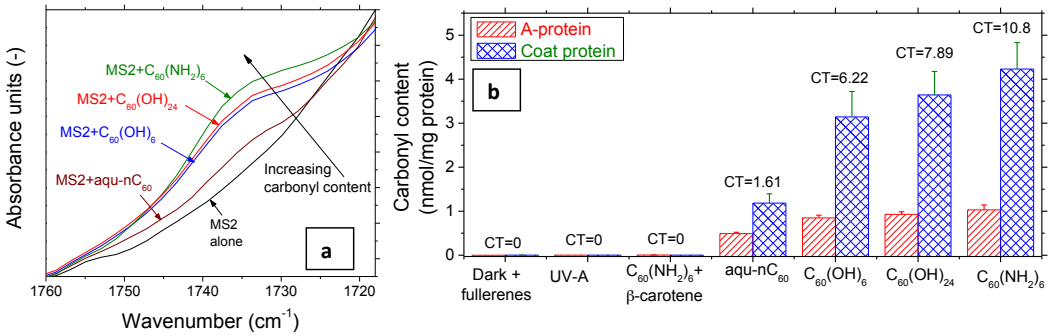

Figure 17: (a) Evolution of carbonyl groups in MS2 upon $^1O_2$ oxidation from ATR-FTIR. (b) The extent of MS2 protein oxidation by $^1O_2$ at the end of 5 min of UV-A sensitization is shown here in terms of carbonyl concentrations from the OxyBlot assay. CT values correspond to 10^{-9} mg min L^{-1}.

Total carbonyl groups relative peak areas (aqu-nC_{60} 0.0088, $C_{60}(OH)_6$ 0.0316, $C_{60}(OH)_{24}$ 0.0337 and $C_{60}(NH_2)_6$ 0.0523 area units) evolved monotonically with CT (Figure 17 (a), details of CT calculations are in the final section of this Chapter and Appendix A). Importantly, since no carbonyl groups were detected in viruses exposed to fullerenes in the dark, UV-A alone, or photoactivated fullerenes + β-carotene, protein oxidation is directly related to exogenous $^1O_2$ delivered to the capsid and the degree of inactivation

(Figure 17 (b)). SDS-PAGE and Western blot analysis as described by the OxyBlot assay allowed the quantification of carbonyl content of A- and coat-protein. As summarized in Figure 17 (b), it appears that carbonyl formation in A-protein stopped increasing significantly beyond a CT of only 1.61×10^{-9} mg min L^{-1} ($C_{60}(OH)_6$) whereas it continued to increase in coat proteins consistent with its much higher protein content and consequent greater availability of amino acid residues for reactions with $^1O_2$. Note that each MS2 virion has 180 copies of the coat protein but only one copy of the A-protein. The highest degree of oxidation occurred in $C_{60}(NH_2)_6$ suspensions (A-protein: 1.03±0.11 nanomoles carbonyls mg^{-1} protein and coat protein: 4.23±0.60 nanomoles carbonyls mg^{-1} protein). Carbonyl group content in both A-protein and coat protein increased with $^1O_2$ doses confirming FTIR results (Figure 17 (b)). 7% of the amino acids in the MS2 capsid are highly reactive with $^1O_2$ (His, Trp, Tyr, Met, and Cys; Appendix A, Table 10), which are also present in the A-protein that is crucial for infection. SDS PAGE confirmed conformational changes such as unfolding of subunits or cross-linkages (slower migration of bands in lanes D, E, F, G and I in Appendix A, Figure 42) in A-protein and coat proteins of MS2 across all treatments including UV-A alone. Oxidative damages to the A-protein suggest alterations in MS2-host interactions attributing inactivation to the loss of infectivity similar to DNA viruses such as PRD1 and T7 [247].

4.1.3.5 Evidence for Capsid Rupture or Deformation

As seen in Figure 18, certain amino acids (Pro, His, Trp, and Ser) peaks and RNA appeared in spectra of MS2 exposed to illuminated FNPs but not UV-A alone. This suggests capsid rupture/deformation and the broadened peaks in the region 1190-1130 cm^{-1} likely indicate oxidation of exposed RNA. The appearance of new peaks show localized capsid damages potentially at the locations of Pro, His, Trp, and Ser on the capsid, or even rupture as seen in Figure 19 (e).

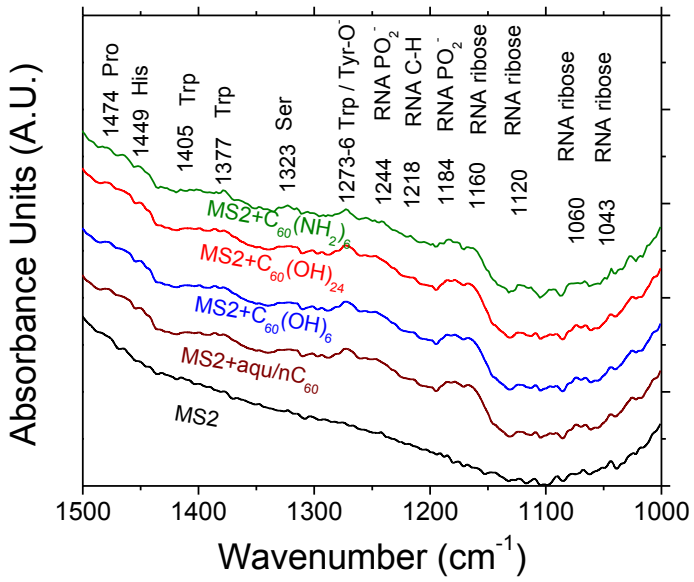

Figure 18: ATR-FTIR spectra of MS2 exposed to UV-A illuminated FNPs showing the development of amino acid residues and RNA compared to UV-A alone.

4.1.3.6 Direct Qualitative Evidence for Differential Association of FNPs with MS2

Figure 19 (a)-(d) show representative 5-fold zooms of mixture-tuned matched filtering (MTMF) results from HSI analysis of MS2 with $C_{60}(NH_2)_6$, aqu-nC_{60} $C_{60}(OH)_6$, and $C_{60}(OH)_{24}$ respectively in aqueous media. The following trends were consistently

observed; $C_{60}(NH_2)_6$ and MS2 were closest to each other, the polyhydroxylated fullerols and MS2 were most separated, whereas aqu-C_{60} was at intermediate distances from MS2. These images were obtained in the wet phase with limited sample preparation thereby closely capturing conditions during nanoparticles photoactivation and subsequent virus inactivation. Although not conclusive because of the necessary sample dehydration, TEM imagery (Figure 19 (e)-(h)) confirms HSI results where $C_{60}(NH_2)_6$ nanoparticles were present closer to MS2 compared with aqu-nC_{60}, $C_{60}(OH)_6$, and $C_{60}(OH)_{24}$.

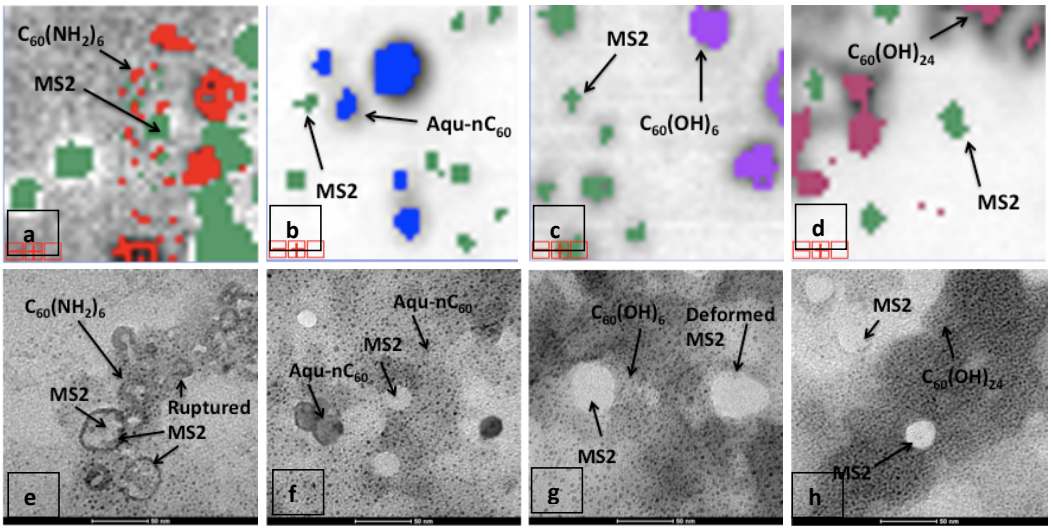

Figure 19: Relative proximity of various fullerenes with MS2 following MTMF analysis of hyperspectral images. 5-fold zoom-ins (1 cm = 20 μm) of noise-free image data with superimposed classification results are shown. MS2 viruses appear as green pixels after staining with 2.5% phosphotungstic acid. (a) $C_{60}(NH_2)_6$ is shown in red, (b) aqu-nC_{60} in blue, (c) $C_{60}(OH)_6$ in purple, and (d) $C_{60}(OH)_{24}$ in pink. (e) –(h) Corresponding TEM images after sample dehydration.

Under our experimental conditions, the electrophoretic mobilities of MS2, $C_{60}(NH_2)_6$, aqu-nC_{60}, $C_{60}(OH)_6$, and $C_{60}(OH)_{24}$ were -1.09±0.09, -1.09±0.10, -1.76±0.29, -3.65±0.31, and -3.57±0.30 ($x10^{-8}$ m^2 V^{-1} s^{-1}), respectively. ζ potentials were then calculated

from EPM using the Henry equation (Appendix A, Table 6). The observed trends in separation distances are therefore consistent with electrostatic interactions with proximity of nanoparticles to phages increasing with decreasing magnitude of the ζ potential. Greater affinity allows the more efficient transfer of $^1O_2$ from nanoparticles to viruses, especially given its short lifetime thereby facilitating inactivation. Capsid rupture and deformations seen in Figure 19 (e)-(h) are attributed to oxidative damage by $^1O_2$.

4.1.3.7 $^1O_2$ Delivery and Proximity Implications for Chick-Watson Kinetics

Log virus survival ratios were quantified using the Chick-Watson model reported for conventional disinfectants [275] and cationic fullerenes [33]. Measurements of fluorescence over time represent a cumulative production of $^1O_2$. The change in fluorescence over time therefore represents the instantaneous $^1O_2$ consumption following the second order reaction between SOSG and $^1O_2$, presumed to take place near the FNP surface where the $^1O_2$ concentration is $[^1O_2]_0$ such that:

$$\frac{dFSU}{dt} = k_{^1O_2}[^1O_2]_0[SOSG] \qquad \text{(Eq 25.)}$$

where FSU is the detected fluorescence resulting from the cumulative reaction of SOSG with the produced $^1O_2$ over the irradiance time, T, and $k_{^1O_2}$ is a second order rate constant. Using a sufficiently large SOSG concentration compared with $^1O_2$ and short irradiance times gives the pseudo first order equation:

$$\frac{dFSU}{dt} = k'_{^1O_2}[^1O_2]_0 \qquad \text{(Eq 26.)}$$

where $k'_{^1O_2}$ = 5.8x10^9 FSU mM^{-1} min^{-1}, determined experimentally for our conditions (see Appendix A). Integrating, an expression for a pseudo-CT is obtained in terms of the time required to achieve a given level of inactivation and the steady state $^1O_2$ concentration probed by SOSG on or very near the surface of fullerene:

$$CT = \frac{FSU(t)}{k'_{^1O_2}} = [^1O_2]_0 t \qquad \text{(Eq 27.)}$$

MS2 log survival ratios corresponding to the four nanoparticles evaluated in this study all conformed to Chick-Watson kinetics with all data falling on a single straight line in Figure 20. This suggests that similar inactivation mechanisms were associated with each nanoparticle. However, the $^1O_2$ concentration near the virus capsid, and thus the time required to achieve a given level of inactivation may vary with proximity between fullerenes and viruses. $^1O_2$ decays rapidly with distance from a photosensitizer source, decreasing in concentration for example, by over an order of magnitude after only approximately 10 nm for the case of humic acid [67]. This implies that for a given measured surface concentration of $^1O_2$ there are many combinations of separation distance between virus and fullerene and the associated time required to produce a given level of inactivation that will satisfy the constraint that CT is constant for all fullerene types. In other words, the effective concentration that the virus is exposed to should depend not only on the generation rate of $^1O_2$ but also the separation distance

between the nanoparticles and the viruses. Inactivation rates followed the order: aqu-nC$_{60}$ < C$_{60}$(OH)$_6$ ≈ C$_{60}$(OH)$_{24}$ < C$_{60}$(NH$_2$)$_6$ (Figure 15), which could be due to either differences in $^1O_2$ production rates arising from changes in the quantum yield and aggregate structure or differences in proximity between the fullerenes and MS2, both of which followed similar trends. EPM measurements and visual evidence by HSI and TEM indicate that the derivatization of the fullerene cage affected the affinity of the particle for the viral surface. For example, C$_{60}$(NH$_2$)$_6$ was not only the most copious $^1O_2$ producer but it also associated most closely with MS2, leading to its highest efficacy for virus inactivation in Figure 15. Thus, when examining inactivation rates in this study, the importance of particle morphology could not be differentiated from virus proximity as all FNPs conformed to the same CT curve seen in Figure 20. Had virus log survival ratio differed for the same CT dose, it would be possible to distinguish between the two factors contributing to inactivation, i.e. $^1O_2$ concentration and proximity.

The only other examination of the applicability of Chick-Watson kinetics to MS2 inactivation by nanoparticles [33], used a derivatized cationic fullerene and reported CT values that are orders of magnitude greater than our measurements. Differences in CT between the two studies are likely to arise given the effects of proximity and

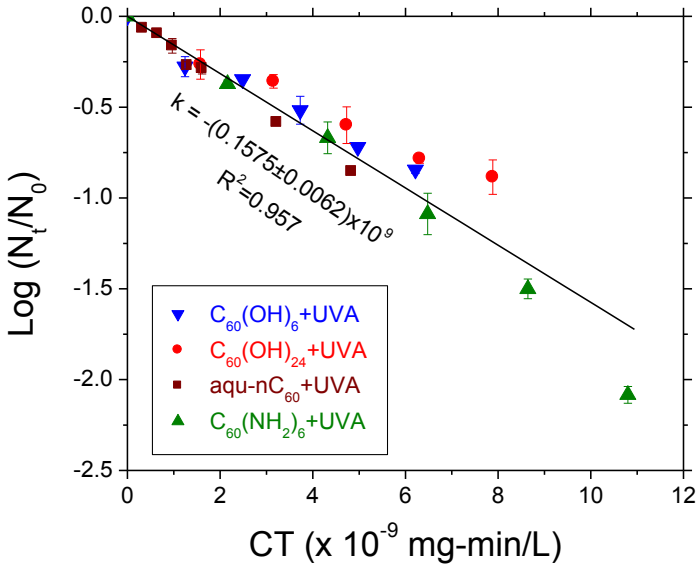

Figure 20: Evaluation of the Chick-Watson model to describe MS2 inactivation kinetics by all four nanoparticles.

morphology on dose described herein. The change in electrostatic interactions arising from a positively charged fullerene versus negatively charged fullerenes should favor increased inactivation, though the derivatization used by Cho et al. [33] caused substantial aggregation that would be expected to hinder delivery of generated $^1O_2$, resulting in decreased inactivation. Aggregates in their work were over 1 μm in size as indicated by dynamic light scattering [276] which could both limit transport of generated $^1O_2$ away from the interior of the aggregate and decrease the total surface area available to interact with viruses. The uncertainty of these factors in producing the greater apparent dose necessary to achieve similar inactivation levels between the two studies highlights the need for further investigation.

Additionally, differences in CT could arise from differences in $^1O_2$ detection and measurement. Indeed, CT values reported by Cho et al. [33] differ significantly not only from our current study, but also from other estimates [277] reiterating the difficulties in accurately determining $^1O_2$ concentrations in the proximity of viruses, which is what effectively determines the extent and kinetics of inactivation. In fact, quantifying differences in inactivation induced by cationic and anionic fullerenes using a consistent and uniform $^1O_2$ detection method is the subject of our ongoing research.

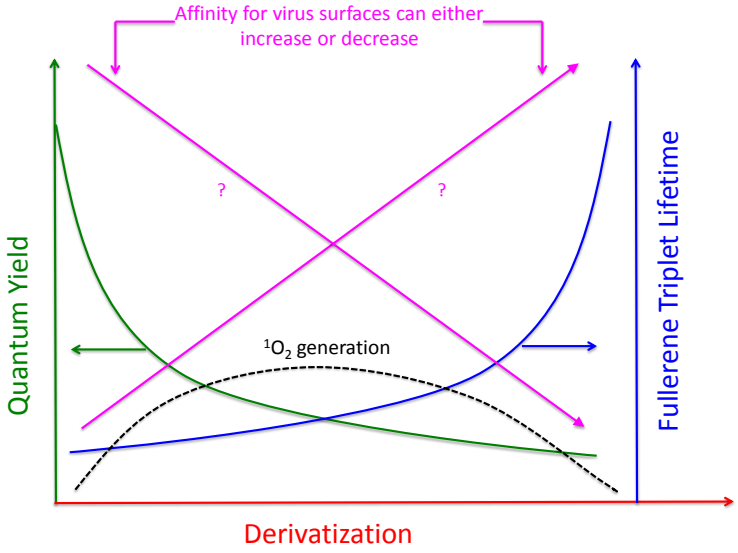

Figure 21: Conceptual interplay between fullerene derivatization, quantum yield, and $^1O_2$ generation.

4.1.4 Conclusions

Differences in MS2 damage, separation distance, and $^1O_2$ generation highlight the importance of both affinity and particle morphology (size, structure, extent and type of derivatization) to facilitate the effective delivery of $^1O_2$ to the capsid. Fullerene cage derivatization can lead to a greater affinity for the aqueous phase (less hydrophobic),

smaller mean aggregate size, and a more open aggregate structure [22, 219, 247]. These factors tend to favor a longer lifetime for the triplet state of the excited fullerene and higher rates of $^1O_2$ generation. However, fullerene derivatization also decreases the $^1O_2$ quantum yield [254, 278] and may either increase or decrease its affinity to the viral surface.

These considerations suggest that both the extent and the type of derivatization should be optimized to balance $^1O_2$ generation and fullerene-virus association to achieve maximum disinfection as illustrated schematically in Figure 21. Though the quantitative shape of the curves are not yet known, increasing derivatization disrupts the pi-electron shell, decreasing the quantum yield and $^1O_2$ generation. However, derivatization also leads to smaller, more open aggregates, reducing the likelihood of triplet-triplet annihilation and self quenching and thereby increasing the lifetime of the excited triplet state, resulting in greater $^1O_2$ production. The observed $^1O_2$ production will thus be limited by the quantum yield for highly derivatized FNPs and by the triplet lifetime for lesser derivatized FNPs such that a maximum will occur at some optimal extent and type of derivatization. Furthermore, depending on the derivatization, the affinity for a virus surface may either increase or decrease. An optimal derivatization maximizing $^1O_2$ generation as well as increasing affinity for the biological target will facilitate inactivation.

4.2 Influence of Inorganic Anions on the Reactivity of TiO_2 Nanoparticles

ABSTRACT

The influence of inorganic anions on the photoreactivity and aggregation of titanium dioxide nanoparticles was assessed by dosing carbonate, chloride, nitrate, phosphate and sulfate as potassium salts at multiple concentrations. Nanoparticle stability was monitored in terms of aggregate morphology and electrophoretic mobility (EPM). Aggregates size and fractal dimension were measured over time by laser diffraction, and the isoelectric point (IEP) as a function of anion and concentration was obtained by measuring EPM vs pH. Phosphate, carbonate, and to a lesser extent, sulfate, all decreased the IEP of TiO_2 and stabilized NP suspensions due to specific surface interactions, whereas this was not observed for nitrate and chloride. TiO_2 NPs were exposed to UV-A radiation and photoreactivity was assessed by monitoring the production of reactive species over time both at the NP surface (photogenerated holes) and in the bulk solution (hydroxyl radicals) by observing their reactions with the selective probe compounds iodide and terephthalic acid, respectively. The generation of photogenerated holes and hydroxyl radicals was impacted by each inorganic anion to varying degrees. Carbonate and phosphate inhibited the oxidation of iodide, and this interaction was successfully described by a Langmuir-Hinshelwood mechanism and related to the characteristics of TiO_2 aggregates. Chloride and nitrate do not specifically interact with TiO_2, and sulfate creates relatively weak interactions with the TiO_2 surface

such that no decrease in photogenerated hole reactivity was observed. A decrease in hydroxyl radical generation was observed for all inorganic anions. Quenching rate constants for the reaction of hydroxyl radicals with each inorganic anion do not provide a comprehensive explanation for the magnitude of this decrease, which arises from the interplay of several physicochemical phenomena. This work shows that the reactivity of NPs will be strongly influenced by the waters they are released to. The impact of anion species on hydroxyl radical inhibition was as follows: carbonate > chloride > phosphate > nitrate > sulfate.

4.2.1 Introduction

Titanium dioxide (TiO_2) nanoparticles (NPs) are widely used in a multitude of commercial products, including food, personal care products, paints, coatings, paper, and fibers due to their brightness, high refractive index, and UV resistance [8, 12, 171, 279]. Applications related to their photoëlectrochemical properties are of particular research interest involving solar energy conversion, photocatalytic pollution remediation and photo-induced superhydrophilicity [13, 280]. In particular, TiO_2 NP photocatalysis may be used in water and wastewater treatment, as an advanced oxidation for chemical pollutants or a disinfection process for pathogens based on the generation of reactive species when TiO_2 NPs in suspension are irradiated by photons of wavelength below 390 nm [14]. The potential for TiO_2 photocatalytic degradation of a number of contaminants has already been highlighted [281, 282], though further

investigations are required to improve its cost-efficiency and to develop its application at the full scale [283].

The same photochemical properties that make TiO_2 appealing from an engineering standpoint also have implications for NP release into the environment. TiO_2 NPs are impacted by the presence of many components of natural waters including inorganic anions, which are ubiquitous at significant concentrations [29, 284]. The impact on TiO_2 reactivity by inorganic anions can be direct: interference with the physicochemical processes leading to reactivity, or indirect: changes in the NP stability and aggregation state which in turn alter reactivity [14]. For the direct mechanism, several studies have been published indicating that inorganic anions impact the fundamental physicochemical processes taking place during TiO_2 photocatalysis, including photon absorption, surface adsorption and photocatalytic degradation [285-292]. Anions compete for the active sites on TiO_2 surfaces, which can prevent the reaction of pollutants that must be adsorbed before degradation. The specific adsorption of various anions, such as phosphate, leads to a reduction at the TiO_2 surface in the amount of hydroxide ions, which are the precursors of hydroxyl radicals [293-296]. Furthermore, photocatalytic degradation is inhibited when reactive species are directly quenched by anions. This phenomenon follows the specific reactivity of each compound with the generated reactive species [297]. Given the difficulty in differentiating the chemical reactions involved, reactivity assessments have generally been limited to

monitoring model contaminant degradation, such as dyes or organic solvents, whose reaction pathways are complex and mostly unknown.

Similarly, most studies assessing the influence of inorganic ions on the reactivity of TiO_2 suspensions have been carried out without a detailed characterization of TiO_2 aggregates that would help to inform the importance of the indirect mechanism. The influence of inorganic anions on NP aggregation has been extensively documented for nanoparticle diffusion and transport in aquatic systems [298-302]. This area of research is of particular interest due to the increasing concern for environmental implications of nanomaterials. In particular, the interactions among TiO_2 nanoparticles can often effectively be described by DLVO theory, which accounts for van der Waals attraction and electrical double layer repulsion in determining the potential for aggregation [180, 181, 301]. Generally, the repulsive energy of the electric double layer is dominant for TiO_2 NPs in water. This energy barrier decreases with increasing ionic strength, corresponding to double layer compression, which decreases electrostatic repulsion. As a result, the ionic strength of the solution can be related to the stability of a electrostatically-stabilized NP suspensions [299]. Though some work has looked at the impact of aggregate size and structure on reactivity, there remains a lack of understanding of how ionic species and concentration impacts the characteristics of TiO_2 suspensions and their reactivity.

In this work, the reactivity of TiO_2 suspensions in the presence of inorganic species was assessed at the laboratory scale by monitoring the reaction of reactive species with probe compounds. Using highly selective chemicals (previously described in several publications [73, 75, 76]) allows one to assess the specific influence of inorganic ions on the availability of various reactive species in the development of radical pathways. Specifically, the oxidation of iodide (dosed as potassium iodide, KI) to iodine (I_2) was used to monitor photogenerated holes (h^+), and hydroxylation of terephthalic acid (TA) to 2-hydroxyterephthalic acid (2-HTA) was used to detect hydroxyl radicals ($^{\bullet}OH$). The products of these reactions are easily measurable by spectrometric and fluorimetric techniques [199]. TiO_2 NP suspensions were prepared via probe sonication, and the inorganic species (carbonate, chloride, nitrate, phosphate and sulfate) were dosed as potassium salts at several concentrations. TiO_2 suspensions were photoactivated by UV-A irradiation, and the reactive species concentrations were evaluated over time along with TiO_2 aggregate characterization. This research has strong implications not only for TiO_2 photocatalysis engineering but also for the assessment of the risk related to the environmental release of engineered nanomaterial.

4.2.2 Materials and Methods

4.2.2.1 Reagent Solutions

KOH, KI, I_2, $KHCO_3$, KCl, KNO_3, KH_2PO_4, K_2HPO_4 and K_2SO_4 were purchased from VWR International (USA). Stock solutions of inorganic anions (0.1 M) were

prepared in deionized water for carbonate. The starch solution was prepared by adding 0.5 g of starch (VWR International) in 100 mL of boiling deionized water and mixing until complete dissolution. After 12 h settling, the supernatant was collected. TA (0.5 mM) and 2-HTA (0.125 mM) solutions were prepared by dosing 16.72 mg of TA (Sigma-Aldrich, USA) and 4.69 mg of 2-HTA (Sigma-Aldrich) in 200 mL of deionized water, adjusting pH to 7.9 with KOH, and mixing on a magnetic stir plate overnight.

4.2.2.2 TiO_2 Dispersion and Suspension Characterization

Experiments were performed with P25 Aeroxide TiO_2 nanoparticles (NPs) (Evonik, Germany). TiO_2 stock suspensions (40 mg L^{-1}) were prepared by adding 2 mg of P25 TiO_2 to 50 mL of deionized water and stock solutions of inorganic anions, depending on the test conditions. Following the protocol of Taurozzi et al., NPs were dispersed via probe sonication (Q700, QSonica, USA) for 6 minutes in pulse mode (12 s ON / 3 s OFF) with 1/2″ diameter tip in the presence of a small concentration of inorganic anions (1 mM) [178]. pH was adjusted to 7.9 with KOH (0.1 M) after sonication, and the remaining inorganic anions were added to the desired concentration afterwards when stocks were diluted in the reaction beaker.

Laser diffraction (Mastersizer 3000, Malvern Instruments, England) was used to determine TiO_2 aggregate size and fractal dimension. In-line light scattering measurements were performed using a peristaltic pump located downstream of the instrument by which samples were fed from a beaker continuously mixed on a magnetic

stirrer at 400 RPM. Time resolved size measurements, reported in terms of median diameter (D_{50}) both as number weighted and volume weighted intensity, were taken every 2 minutes for 30 minutes. Meanwhile, static light scattering (SLS), consisting of measurements of the scattering intensity, I(q), over a range of scattering vectors, q, corresponding to 0.8 - 42° for each sample were recorded simultaneously by an array of detectors. From Equation 28, the aggregate fractal dimension, D_f, can be determined as the negative slope of the linear power law region when plotting log(I(q)) vs log(q) [215]:

$$I(q) = q^{-D_f} \quad \text{(Eq 28.)}$$

The multiple detectors of the Mastersizer correspond to scattering vectors from 0.18 – 9.47 μm^{-1}, with q related to the detector angle, theta, as follows

$$q = \frac{4\pi n}{\lambda} \sin\frac{\theta}{2} \quad \text{(Eq 29.)}$$

where n is the refractive index of the medium (1.33 for water) and λ is the wavelength of scattered light (633 nm) [194, 215]. Equation 28 holds when

$$qR_h > 1 \quad \text{(Eq 30.)}$$

i.e. for length scales, (q^{-1}) less than the radius of the aggregate, R_h.

TiO_2 nanoparticle pH titrations were performed on 50 mL suspensions of 20 mg L^{-1} P25 TiO_2 at various anion concentrations. Suspensions were continually stirred while pH was monitored and adjusted with either 0.01 M or 0.1 M KOH or HCl. At each pH step, electrophoretic mobility of the nanoparticles was measured (Zetasizer Nano ZS, Malvern Instruments, England). Zeta potential was then calculated via the Henry

equation. The isoelectric point (IEP) was identified as the pH for which the EPM of a suspension was zero.

4.2.2.3 TiO_2 Nanoparticle Reactivity Measurement

NP exposure to UV-A was performed in a box equipped with two 15 W fluorescent UV lamps (TL-D 15W BLB SLV, Philips, Netherlands) held at 22±1 °C through the use of a chiller. Samples were placed in 10 mL reaction beakers and continuously mixed on a magnetic stirrer at 400 RPM. The radiation intensity at the liquid upper surface was 1.9 mW cm^{-2}, centered at 365 nm (see Appendix B) and monitored by means of a ILT1400 radiometer equipped with a SEL033 UV-A filter (International Light Technologies, USA). The geometry of the reaction beaker (H=3.5 cm, Ø=5 cm) produced a 0.5 cm thickness liquid layer, including the stir bar (3 x 10 mm).

4.2.2.4 Photogenerated Holes

To evaluate the production of photogenerated holes in the presence of the inorganic anions, reaction beakers containing 20 mg L^{-1} P25 TiO_2, 50 mM KI and various concentrations of anion (0, 0.5, 1, 2.5, 5, 12.5 mM) were exposed to UV light. Solutions were irradiated for a total of 30 minutes, and all tests were repeated four times. Every 5 minutes a 0.5 mL aliquot was added to a solution of starch in a 1:1 volume ratio. The resulting absorbance at 585 nm was then measured in a plastic cuvette (10 mm optical path) vs. deionized water by spectrophotometer (Cary 100, Agilent, USA). Absorbance values were related to iodine concentration by a standard curve, which was evaluated

by spectrometric measures on non-irradiated samples over the range of 0.0125 to 0.125 mM iodine after subtracting the TiO_2 suspension contribution. The concentration of photogenerated holes was stoichiometrically estimated as twice the produced iodine concentration, according to the following reaction:

$$2I^- + 2h^+ \rightarrow I_2 \qquad \text{(Eq 31.)}$$

4.2.2.5 Hydroxyl Radicals

Hydroxyl radical production tests were performed on samples consisting of 20 mg L^{-1} P25 TiO_2, 0.125 mM TA, and various concentrations of inorganic anions (0, 0.5, 2.5, 5, 12.5, 25 mM of carbonate, chloride, nitrate, phosphate and sulfate) and irradiated for 30 minutes. All tests were repeated four times. Every 5 minutes a 0.5 mL aliquot was added to 0.75 mL deionized water in a 2 mL centrifuge tube. Samples were then centrifuged for 5 minutes at 12,000 RPM to separate the TiO_2 from the solution. 1 mL of the resulting supernatant was transferred to a plastic cuvette (10 mm optical path) and fluorescence was measured (Varian Eclipse fluorometer, Agilent, USA) at an excitation wavelength set to 315 nm and emission maximum at 425 nm. Fluorescence was related to the concentration of 2-HTA by a standard curve by diluting a 0.125 mM 2-HTA stock solution to obtain a range from 0.0025 - 0.1 M, adopting the same procedure as for the samples. Hydroxyl radical concentrations were estimated by the following reaction, assuming 80% trapping efficiency for $OH^{\bullet}$ by TA [87] and considering sample dilution in deionised water:

$$TA + {}^{\bullet}OH \rightarrow 2-HTA \qquad \text{(Eq 32.)}$$

4.2.3 Results and Discussion

The strong influence of inorganic anions on TiO_2 nanoparticle photocatalysis, resulting from the combination of chemical-physical phenomena is presented here first in terms of impacts on NP aggregation (Section 4.3.1). The anion influence on TiO_2 reactivity is then discussed in terms of photogenerated holes (Section 4.3.2) and hydroxyl radicals (Section 4.3.3).

4.2.3.1 TiO_2 Aggregate Characterization

Sonicating TiO_2 nanoparticles in deionized water created aggregates with a stable number weighted D_{50} of 0.095±0.004 μm and volume weighted D_{50} increasing from 0.591±0.296 μm to 6.84±7.63 μm over 30 minutes (Data in Appendix B). The difference in values arising from the weighting methods is due to the polydispersity of TiO_2 suspensions, indicating that the vast majority of aggregates exist at the smaller size class with relatively few large aggregates influencing the volume weighted D_{50}. This smaller fraction is expected to be the most photoactive, as non-ROS producing pathways (e.g. quenching, recombination) increase in frequency with aggregation [219]. Suspensions in DI were repeated five times; the large standard deviation associated with the volume weighted D_{50} arises from the instability of the TiO_2 aggregates in the mixed solution.

4.2.3.2 Aggregation in Inorganic Salts

Monitoring TiO_2 D_{50} in the presence of inorganic salts yielded two contrasting trends (i) anions that did not limit NP destabilization, and (ii) anions that stabilized NP suspensions through specific surface interactions. Figure 25 shows TiO_2 aggregation over time for each anion at 0.5 mM and 25 mM. Aggregates in chloride and nitrate aggregated significantly over 30 minutes at all concentrations, increasing from an initial TiO_2 number weighted D_{50} similar to that of aggregates suspended in DI to a final size of a micron or more (Data in Appendix B). On the other hand, phosphate, carbonate, and sulfate all had a stabilizing effect. The greatest effect was seen for phosphate for which no increase in aggregate size was observed, even at concentrations as high as 25 mM. Some aggregation proceeded for suspensions containing carbonate at 12.5 and 25 mM. The addition of sulfate in solution did result in a decrease in aggregation, though this was much less pronounced than for either phosphate or carbonate, and did not exhibit concentration dependence over the range examined.

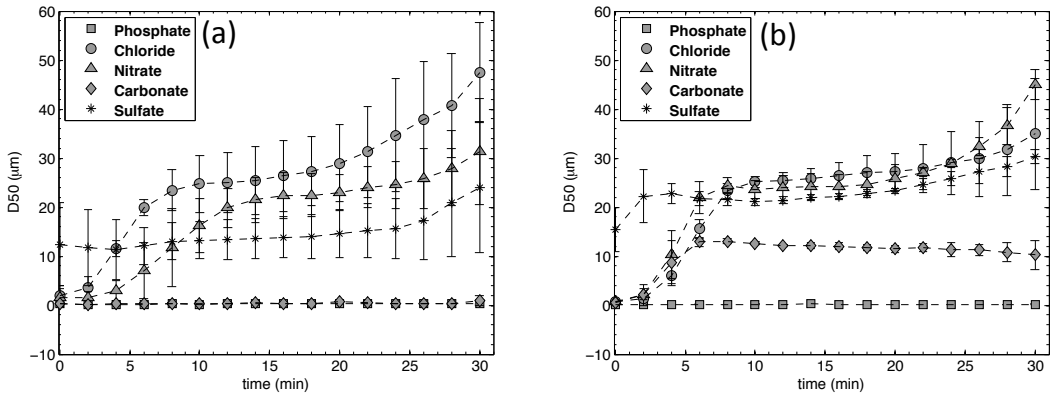

Figure 22: TiO_2 aggregation over time for each anion at (a) 0.5 mM and (b) 25 mM. Data shown is volume weighted D_{50} (mean±std)

Looking at the initial rate of aggregation for chloride (Figure 23) and nitrate (data in Appendix B), no clear influence of ionic strength can be discerned, although the attachment efficiency, α, is generally expected increase with salt concentration until it reaches unity when the critical coagulation concentration is reached. Calculations using the Gouy Chapman model indicate that attractive forces dominate (i.e. $\alpha = 1$) for 12.5 and 25 mM potassium chloride (data in Appendix B). For the lower three concentrations (0.5, 2.5, and 5 mM) however, the electrical double layer remains large enough that electrostatic repulsion should hinder aggregation. These results agree well with Solovitch et al. who determined the CCC for 50 mg L^{-1} anatase at pH 8 in unmixed experiments to be between 10 and 40 mM NaCl [303]. That no difference was observed in initial aggregation rates here, despite the differences in particle stability, highlights the strong influence of mixing on aggregation rate for these conditions. The initial aggregation reached a plateau after approximately 14 minutes; presumably this is the

point at which breakup and reordering due to shear becomes significant. Similar behavior was observed by Gardner et al. in studying the aggregation kinetics of hematite particles in a Couette device [213]. For suspensions to which carbonate was added, the initial rate of aggregation was greater for samples at 25 mM than for 12.5 mM of concentration, as would be expected under DLVO theory, though the aggregate size for both quickly stabilizes after which no further aggregation is observed.

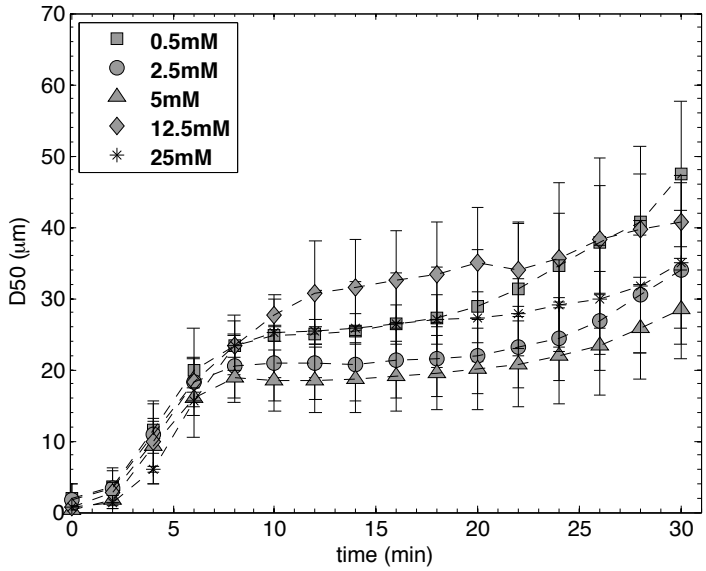

Figure 23: TiO_2 aggregation (volume weighted D_{50} mean±std) vs. time as a function of chloride concentration.

4.2.3.3 Fractal Dimension

SLS measurements were collected for each aggregation experiment. At early time points, the size of aggregates is small compared to the length scales probed, and plots of log(I) vs log(q) were not linear over a large enough range of the scattering vectors considered (0.110 μm to 5.62 μm) (Data in Appendix B). Thus, the constraint of Equation

30 is not met and related light scattering data were not sufficient to calculate D_f. Furthermore, as no aggregation was observed for any phosphate concentration and for low carbonate concentrations (<12.5 mM), fractal dimensions were not obtainable. For suspensions in which aggregation was observed, the average D_f values over the final three measurements (26-30 minutes) are shown in Figure 24. Broadly, D_f values were lower for suspensions that were observed to quickly aggregate (nitrate, 2.33±0.001; chloride, 2.32±0.002; and sulfate, 2.31±0.002 at 25 mM), indicative of more open

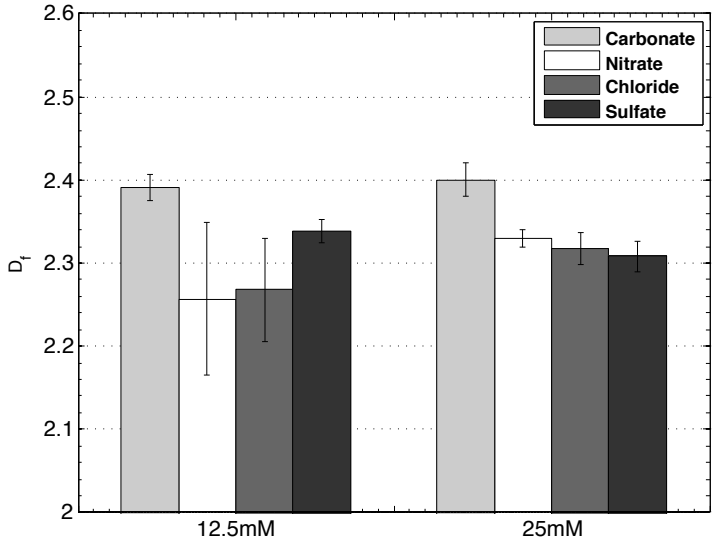

Figure 24: Fractal dimension of TiO_2 aggregates for all anions at 12.5 and 25 mM. D_f values are the average of the final 3 measurements (mean±std).

aggregates. Conversely, the higher fractal value for carbonate (2.40±0.02 at 25 mM) agrees well with the slower observed aggregation that would result in smaller, denser aggregates. The concentration of anion in solution did not significantly impact aggregate

structure. For nitrate, chloride, and sulfate, values of D_f are observed to center around 2.3 for all concentrations and fall within the range of what is considered reaction-limited aggregation, indicative of stable particles. This likely arises from shear due to mixing, resulting in aggregate breakup and reordering, leading to denser clusters. This lack of concentration dependence also agrees well with initial rates of aggregation discussed previously.

4.2.3.4 Aggregate Stability

To identify if the various anions impacted the surface chemistry of TiO_2 aggregates, NP suspensions were titrated and the IEP for each suspension was identified (Data in Appendix B). EPM vs pH was measured in the range of pH 3-9. As can be seen in Figure 28, the addition of chloride and nitrate, generally considered indifferent electrolytes, did not significantly impact the IEP (6.6±0.1 versus 6±1 [304]), while carbonate and phosphate interacted strongly with the surface, resulting in large shifts in the IEP, the extent of which varied with anion concentration. Sulfate depressed the IEP from that of chloride and nitrate to 5.6±0.2 but did not vary greatly with concentration. The impact of carbonate, however, was drastic. At 0.005 and 0.05 mM, the IEP mirrored that of sulfate, though increasing the concentration decreased the IEP to a low of 2.8 at 5 mM. The IEP then rebounded with a further increase in carbonate concentration. Phosphate proved to even more strongly influence the IEP as the concentration increased from 0.005 mM to 0.5 mM, at which point NPs were negatively charged for the

entire range of pH measured. Further increasing phosphate concentration resulted in the slight increase in IEP, though this was not as pronounced a recovery as was observed with carbonate. Titrations above 12.5 mM were not performed as the ionic strength interfered with EPM data quality.

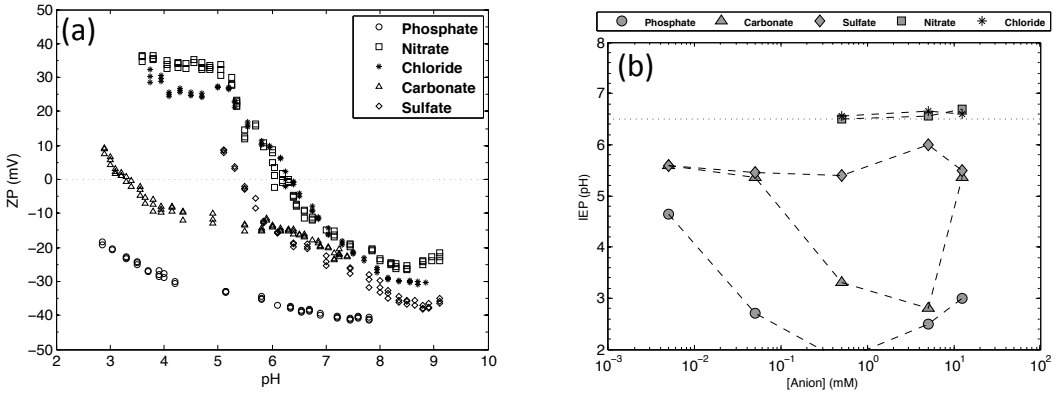

Figure 25: (a) Zeta potential vs. pH for all anions at 0.5 mM. (b) IEP vs. concentration for all anions. IEP for 0.5 mM phosphate was not determined as the ζ potential was negative over the range of pH tested.

That carbonate, phosphate, and sulfate were able to influence the IEP speaks to their ability to participate in inner sphere ligand exchange with the surface oxides and hydroxides present on TiO_2 [305-307]. The magnitude of anion influence increases with surface coverage and depends on the dissociation and binding constants of the species present [159, 227, 285]. The increase in IEP observed for phosphate and carbonate at concentrations of 5mM and higher may be due to changes in ligand complexation. Inner sphere complexes can form mono- bi- or tridentate complexes depending on ligand type, pH, lattice structure and surface defects [308-311]. These complexes are associated with different binding energies and associated protonation pKa values [40, 227, 312]. As

concentration increases and the more energetically favorable binding sites become filled, adsorption will transition to less favorable sites. Phosphate has been shown to favor bidentate complex formation with the surface of TiO_2, which becomes protonated at low pH. Monodentate adsorption results in a protonated complex that becomes doubly protonated at low pH [227]. The addition of sulfate quickly reaches a maximum impact beyond which the further introduction in solution has little to no effect, suggesting that the interactions of sulfate with the surface are less significant than phosphate and carbonate. These data fit well with observations of aggregate size (Section 3.1.2), in which TiO_2 suspended in phosphate and low concentrations of carbonate do not induce aggregation over the course of 30 minutes, in contrast to nitrate and chloride. Thus, the picture that arises in one in which the anions participating in specific surface interactions with TiO_2 strongly impact the stability of the NPs and the size of the aggregates formed in solution.

4.2.3.5 Influence of ROS Detection Method

KI was used as the probe compound for photogenerated hole oxidation. The addition of KI resulted in NP aggregation from an initial size similar to NPs in DI (0.099±0.004 μm, number weighted D_{50}) to 1.23±0.56 μm over 30 minutes (0.547±0.105 μm increasing to 31.13±8.23 μm, volume weighted D_{50}) (Data in Appendix B). The initial rate of this aggregation was indistinguishable from that observed for nitrate and chloride, discussed previously (Data in Appendix B).

Size data, both as number weighted and volume weighted D_{50}, over time for TiO_2 suspensions at various iodide concentrations (0, 50 mM) and relative size distributions are reported in Appendix B. While the probe itself induces aggregation, it does not do so in a manner that is appreciably different from the addition of the indifferent electrolytes. No significant aggregation was observed in the presence of terephthalic acid, thus aggregate size data were identical to that for DI.

4.2.3.6 TiO_2 Photoreactivity – Photogenerated Holes

The influence of inorganic anions on the production of photogenerated holes was assessed by via the oxidation of iodide. The initial KI concentration was determined by measuring the response at various concentrations using suspensions of TiO_2 in DI water (data in Appendix B) [199, 313]. A saturation trend in oxidation was observed, and 50 mM was selected as the optimal concentration. The high concentration of iodide required to reach saturation likely arises from the negative surface charge of TiO_2 at pH 7.9, both electrostatically limiting iodide transport to the aggregate surface and resulting in an increased concentration of hydroxide ions present in solution and at the NP surface.

Upon addition of the various anions, a change in the rate of iodide oxidation was only observed in the presence of carbonate and phosphate. Chloride, nitrate and sulfate at concentrations between 0.5 and 12.5 mM did not cause any significant change in iodide oxidation from samples containing only KI. Experimental results after 30 minutes

of irradiation at various carbonate and phosphate concentrations are shown in Figure 26. Experimental data for chloride, nitrate, and sulfate were not significantly different from results obtained for TiO_2 suspensions without inorganic ions and are not shown. Oxidized iodide concentrations for these three anions overlap the results when only KI is present in solution (data in Appendix B). The lack of statistically significant differences between series with or without anions for chloride, nitrate and sulfate was verified by means of Student's t-test (p-value < 0.005).

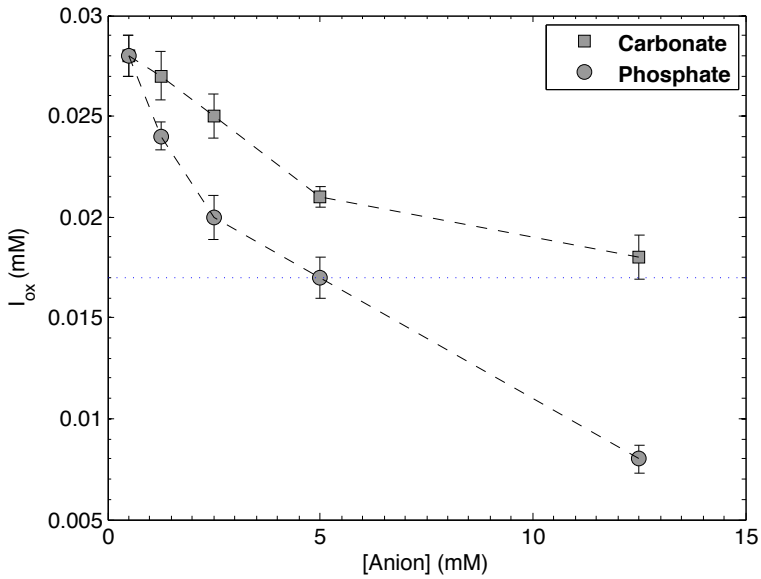

Figure 26: Oxidized iodide concentration (mean±std) versus anion concentration after 30 minute irradiation (50 mM KI) as a function of species in solution (carbonate, phosphate). The blue dotted line is the iodide concentration of TiO_2 suspensions containing only 50 mM KI.

The addition of carbonate and phosphate increased the rate of photogenerated hole oxidation for phosphate at concentrations up to 5 mM and for all carbonate concentrations tested as compared to solutions containing only the probe. The largest

increase was observed at 0.5 mM and was the same as that for carbonate and phosphate anions, after which increasing the concentration reduced hole oxidation to a level observed in DI suspensions. These findings agree with the trend of aggregate stabilization reported in Section 4.2.3.2, which would result in increased reactivity, and suggests that at low concentrations, little negative effect on reactivity due to specific surface interactions would be expected. The reduction in reactivity observed with increasing anion concentration is attributed to the presence of phosphate or carbonate occupying surface sites and preventing iodide from interacting with the photogenerated holes. The effect of phosphate addition was greater than carbonate, despite observed aggregation of carbonate at 12.5 mM, indicating that the decrease in photogenerated holes is primarily due to the greater surface interactions of phosphate and TiO_2.

The interactions between anions and TiO_2 nanoparticles has been described by Chen et al., as a Langmuir type adsorption model [286]. The oxidation of iodide can thus be modeled as a Langmuir-Hinshelwood (LH) mechanism, even when considering the presence of other anions in solution, per Equation 33 [313].

$$r = \frac{d[I^-]}{dt} = -K_r\theta_{I^-} = -K_R \frac{K_{A,I}[I^-]}{1 + K_{A,I}[I^-] + \sum_{Anion} K_{A,Anion}[Anion]} \qquad \text{(Eq 33.)}$$

Here r is the reaction rate, θ_{I^-} is the surface coverage by iodide, $[I^-]$ is the concentration of iodide, $K_{A,I}$ is the equilibrium constant of adsorption for iodide, $K_{A,Anion}$ is the equilibrium constant of adsorption for a given anion and K_R is the LH reaction

constant for iodide oxidation. Estimates of $K_{A,I}$ and K_R were calculated from the experimental data reported in Appendix B in the absence of other anionic species following the procedure employed by Herrmann and Pichat (see Appendix B), the results of which are shown in

Table 3 [313]. The high R^2 values indicate that the LH mechanism is appropriate for describing iodide oxidation. These values are comparable with those obtained previously for iodide oxidation in non-sonicated suspensions of TiO_2 at 40 mg L^{-1} [199].

Table 3: Estimated values of the equilibrium adsorption coefficient, K_A, for iodide, carbonate and phosphate and estimated values of LH reaction constants for iodide oxidation, K_R. R^2 values are the coefficients of determination.

Ionic species	K_A (M^{-1})	K_R (M s^{-1})	R^2
Iodide	13.2	2.24E-08	0.988
Carbonate	142.7	4.16E-08	1.000
Phosphate	251.8	4.02E-08	0.954

Similarly, the LH mechanism was used to model the effect of inorganic anions on the formation of photogenerated holes. Here it is essential to take into account the competition for the active sites in LH mechanism among inorganic anions. A procedure for $K_{A,Anion}$ and K_R estimation in the presence of anionic competition for surface adsorption is described in Appendix B, in which the equilibrium constant of adsorption for iodide was taken from the previous calculation in the absence of other inorganic anions. The LH mechanism fits the experimental data well (R^2>0.950). Larger values of

$K_{A,Anion}$ indicate greater active site occupation by a given anion compared to others at the same concentration. Hence, iodide, having the smallest $K_{A,Anion}$ value, is the least favored at the TiO_2 surface under the present operating conditions. $K_{A,Anion}$ for phosphate was much higher than for carbonate and indicates a greater affinity for the TiO_2 surface which serves to more strongly block iodine from the surface and reduce hole reactivity. $K_{A,Anion}$ for nitrate, chloride, and sulfate were not calculated, as no adsorption in the presence of iodide was observed. The influence of the associated cation, i.e. potassium, on reactivity was considered negligible, in agreement with previous works [314].

4.2.3.7 TiO_2 Photoreactivity - Hydroxyl Radicals

The generation of hydroxyl radicals was evaluated by monitoring the fluorescence of 2-HTA as a function of inorganic anion concentration. TA is a selective hydroxyl radical probe, whose reaction occurs via a single step hydroxylation process in the absence of surface adsorption [76]. At pH 7.9, the carboxylic acid groups on TA are deprotonated and the molecule is electrostatically repulsed from the negatively charged TiO_2 surface.

Table 4: Rate constants of hydroxyl radicals and inorganic anions.

Anionic species	Value ($M^{-1} s^{-1}$)	Reference
HCO_3^-	8.5×10^6	[70]
Cl^-	4.3×10^9	[70]
NO_3^-	1.4×10^8	[315]
HPO_4^{2-}	6×10^5	[316]
SO_4^{2-}	1.0×10^{10}	[317]

Concentrations of 2-HTA for various anionic species after 30 minutes of irradiation are shown in Figure 27 (a), while relative time series are reported in Figure 27 (b). For all anions, increasing the concentration in solution decreased the amount of ROS detected, as would be expected for potential hydroxyl radical quenchers. However, rate constants for the reaction of hydroxyl radicals with each inorganic anion, available from literature and reported in Table 4, do not provide a comprehensive explanation for this, as the expected impact on •OH detection differs from experimental results. For example, the given reactivity of sulfate with hydroxyl radicals ($1x10^{10}$ M^{-1} s^{-1}) is four orders of magnitude greater than carbonate ($8.5x10^{6}$ M^{-1} s^{-1}), although in this study carbonate produced the greatest decrease in •OH detection and sulfate produced the least.

While phosphate and carbonate have the smallest reaction rates, their introduction decreased total hydroxyl radical production to the greatest extent. This is best explained by considering the conditions that lead to hydroxyl radical generation, i.e. hole production and aggregate size. The specific interactions between the TiO_2 surface and carbonate and phosphate were shown to initially increase photogenerated holes, and for carbonate this is still seen in hydroxyl radical generation, however this effect is quickly counteracted by scavenging when increasing the carbonate concentration. Phosphate produces a strong initial decrease in •OH generation at 0.5mM despite the observed aggregate stabilization and increase in hole production, after which the impact of additional anion is relatively small. Indeed, by 12.5 mM the quenching

•OH detection for carbonate is equal that of phosphate. By 25 mM, the addition of carbonate decreased •OH production by c.a. 70%. This greater effect of carbonate than phosphate, contrary to what is observed for hole oxidation is likely due to the order of magnitude increase in k_{*OH} for carbonate. Furthermore, the strong impact of both anions, given their relative inactivity with •OH compared to sulfate, chloride, and nitrate (greater than two orders of magnitude smaller reaction rate), is attributable to their being drawn to and interacting with the TiO_2 surface. This not only limits the number of surface hydroxides capable of reacting with the photogenerated hole to produce •OH, but it also increases the local concentration of quenching agents (carbonate and phosphate) near the NP surface relative to tests using the same concentrations of the other anions, thus decreasing both the lifetime of generated hydroxyl radicals.

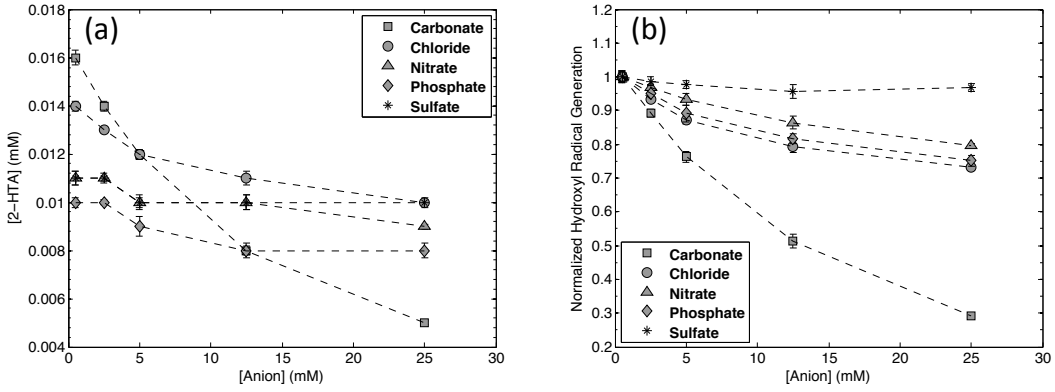

Figure 27: (a) 2-Hydroxyterephthalic acid concentration (mean±std) vs. anion concentration after 30 minute irradiation as a function of species in solution. (b) Hydroxyl radical generation normalized to 0.5 mM anion concentration (mean±std).

The trend for nitrate, chloride, and sulfate is more difficult to discern. A large initial decrease in •OH at 0.5 mM compared to DI is observed for sulfate and nitrate,

whereas chloride initially has little discernable impact. Surprisingly, the addition of up to 25 mM sulfate only decreased •OH detection by c.a. 3%. Since the interaction between TiO_2 surface and TA is negligible [76] and TiO_2 aggregate characteristics are similar, the negative influence of nitrate and chloride on terephthalic acid oxidation can be considered the result of the interplay of two primary phenomena: (i) a reduction in hydroxyl radical generation due to the occupation of active sites by anionic species instead of hydroxyl ions, (ii) the direct quenching of hydroxyl radicals by inorganic anions. The absorption of incoming photons by inorganic anions resulting in reduced NP photoactivation, is considered negligible [16]. The poor description given by the LH mechanism ($R^2 < 0.7$) supports this assertion that the impact on •OH is due to a combination of phenomena, where mass transfer and electrostatic interactions possibly play a relevant role.

4.2.4 Conclusions

In this work, TiO_2 reactivity has been explored both at the NP surface (photogenerated hole oxidation) and in the bulk solution (•OH detection). Only carbonate and phosphate inhibited the oxidation of iodide through specific surface interactions. Chloride, nitrate and sulfate either do not interact with TiO_2 or create relatively weak bonds (with respect to carbonate, phosphate) on the TiO_2 surface that do not hinder iodide. For sulfate, it would appear that while the anion does specifically interact with the surface, these interactions are not sufficient to limit iodide from

reaching and reacting with the surface. The lack of aggregate stabilization and the measured IEPs corresponding to bare TiO_2 suggest that for nitrate and chloride, no specific interactions take place. The response of •OH reactivity to the addition of anions is more complicated and arises from the multiple existing pathways by which the NPs can be impacted. The overall influence on bulk •OH concentration was observed to follow the trend carbonate > phosphate > nitrate > chloride ≈ sulfate.

Previous studies looking at the impact of anions on TiO_2 photocatalysis have monitored the overall degradation of pollutants using the LH mechanism, without differentiating direct hole oxidation from hydroxyl radicals [285, 291]. Others, such Chen et al. investigating the degradation of dichloroethylene, assumed adsorption as a necessary precursor to degradation, but ruled out the likelihood of direct hole oxidation [286]. The intensity of inorganic anion influence on TiO_2 reactivity differs in this study from what has been reported, among which, however, there is no general consensus. Differences between studies seem to be strongly related to experimental conditions, namely solution pH, degradation target chemistry, and TiO_2 characteristics (e.g. aggregate size, dispersed versus fixed catalyst), affecting the balance among the involved chemical-physical processes. As a result, generalization between studies is difficult. Often, little attempt has been made to discern surface reactivity from bulk oxidation, however as is evidenced here, the anion impact on hole generation can be different than the impact on ROS generation. Thus, the mechanism by which a

compound or organism is impacted will play a large role in determining the effect of changes in reactivity.

This work highlights the fact that the reactivity of NPs will be strongly influenced by the waters they are released into, due to the interplay of several phsyicochemical phenomena. Inorganic anion adsorption on the TiO_2 surface happens via a Langmuirian model and creates a competition for active sites with other compounds in solution, both contaminants and hydroxyl ions. The effect of this adsorption can consist of: (i) stabilizing NPs, (ii) hindering the interaction of pollutants, (iii) suppressing hydroxyl radical generation by substituting hydroxyl ions. Some waters containing chloride and nitrate may have little impact on reactivity but will reduce NP transport via aggregation, while waters containing even low levels of phosphate and carbonate may decrease "acute" reactivity but stabilize NPs such that their lifetime in the water column is increased. The ultimate impact of NP photoreactivity in environmental waters (risk) will be the combination of reactivity (hazard) and stability or transport (exposure).

4.3 Chlorpyrifos Degradation via Photoreactive TiO_2 Nanoparticles: Assessing the Impact of a Multi-Component Degradation Scenario

ABSTRACT

High concentrations of pesticides enter surface waters following agricultural application, raising environmental and human health concerns. Bioremediation, while an attractive strategy for mitigating the risk associated with contaminated waters, can require can require extensive periods of time. Furthermore, high concentrations of pollutants may be toxic to or limit the efficacy of bacteria. Alternatively, the use of photoreactive nanoparticles has shown promise for contaminant degradation and surface water remediation. However, it remains uncertain how the complexity of natural waters will impact the photodegradation process. Here, we investigate the photoreactivity of titanium dioxide nanoparticles, the capability to degrade the pesticide chlorpyrifos (CPF), and the effect of and impact on bacteria during the photodegradation process. Loss of chlorpyrifos in solution resulted solely from photocatalytic oxidation. Degradation of chlorpyrifos to chlorpyrifos oxon (CPF Oxon) and 3,5,6-trichloro-2-pyridinol (TCP) was observed and effectively modeled for the given reactor conditions. The relative affinity of bacteria and chlorpyrifos for the nanoparticle surface decreased the amount of ROS present in the bulk, measured using a hydrophilic probe, indicating that measurements in simplified systems are likely to overestimate reactivity in complex environments.

4.3.1 Introduction

Chlorpyrifos (CPF) is an organophosphate pesticide used for agricultural applications such as cotton, corn, and fruit trees, as well as at high concentrations in wood for anti-termite applications [318-321]. As a result, CPF has been frequently observed in agricultural runoff and urban streams [322-325]. Both CPF and its primary oxidation products, chlorpyrifos oxon (CPF Oxon) and 3,5,6-trichloropyridinol (TCP), are of considerable environmental concern due to high fish and aquatic invertebrate toxicity, as well as known human health concerns [322, 326-334].

CPF was designed to be susceptible to base catalysis, with a half-life in water on the order of days, though studies of adsorbed CPF indicate that the half-life can range from hundreds of days to years [321, 326, 335-337]. Gebremariam et al., in reviewing the literature, observed a significant spread in the extent of CPF adsorption to various soil types, though a strong linear relationship was seen with soil organic content, implicating the hydrophobic binding sites present on organic matter [321]. Rose et al. observed that the loss of CPF from a water column in the presence of natural colloidal matter occurred more rapidly than other common pesticides studied [338]. However, rainfall has been shown to be sufficient for CPF-particle resuspension, which may lead to increased bioavailability and transport [321, 326, 327].

Photocatalytic degradation holds promise for dealing with aquatic contamination [14, 15, 339-343]. Nanoscale TiO_2 is widely studied for remediation applications due to

its photochemical properties and ability to provide a steady, continual source of reactive oxygen species (ROS) [344, 345]. CPF degradation experiments employing TiO_2 as the radical generator often employ high concentrations of the catalyst (0.1 – 12 g L^{-1}) in an effort to maximize radical production and minimize treatment time, with CPF loss often occurring within hours [344, 346, 347]. What remains unclear, however, is to what extent the observed loss of CPF from the solution is due to sorption versus degradation. CPF's affinity for soils may not translate to TiO_2, as sorption of CPF increases with organic content [321]. Furthermore, little absorption has been seen for similar pesticides when employing metal oxide nanoparticles (NPs) [337, 348-350]. This question is of particular importance in light of the high surface area of NPs and their potential to act as pollutant transport vectors should incomplete degradation occur [351-353].

Additionally, many types of bacteria have been observed to degrade CPF, including *Bacillus* and *Acinetobacter* strains isolated from groundwater sources, either using the pesticide as the sole carbon source or cometabolically [319, 336, 354-358]. Biodegradation may be an appealing approach to CPF remediation, though longer residence times are necessary compared to chemical or external remediation techniques [359].

High levels of pollutants may also be toxic to bacteria and hinder bioremediation efforts. Toxicity studies of CPF and its degradation products have shown that there is an impact on both individual species and entire bacterial communities [360-362]. When

concentrations of CPF are high, pretreatment of contaminated water may improve remediation efforts. TCP was calculated to be 2.5 times less toxic than CPF for a model bacterium, indicating that pretreatment achieving even partial degradation of a pollutant may facilitate bioremediation efforts [322].

A mixed or sequential approach combining nanoremediation with a biological component may be a more efficient and cost effective treatment method. Within this context, our understanding of the microbial response in a UV/TiO_2 remediation system is currently lacking, with the concern existing that any nanoremediation strategy will harm the natural bacterial community. ROS production by the UV/TiO_2 system will possibly be of more consequence than the pollutant [146, 222, 360, 363-365].

In this paper we investigate the process of CPF loss in water utilizing UV/TiO_2, hypothesizing that CPF loss in the system is primarily due to photocatalytic degradation, rather than sorption. Additionally, we test the hypothesis that the UV/TiO_2 process will inactivate bacteria to a greater extent than will CPF or its degradation products, reducing the likelihood of bioremediation.

4.3.2 Materials and Methods

4.3.2.1 TiO_2 Suspension and Characterization

Experiments were performed with P25 Aeroxide TiO_2 (Evonik Industries, Essen, Germany), a nanoparticulate TiO_2 consisting of fused rutile and anatase crystalline phases at roughly a 20/80% ratio, respectively. TiO_2 NPs were suspended in a Minimal

Davis media (MD) designed to stabilize the particles, buffer the pH at 7.5, and maintain bacterial viability, as described by Lyon et al. [366] Suspensions were produced via probe sonication (Q700, QSonica, Newton, CT, USA) run in pulse mode (12s on, 3s off) for 6 minutes total, following the protocol from Taurozzi et al., and subsequently characterized in terms of aggregate size, surface charge, and ROS production [178]. Dynamic light scattering (ALV-CGS3, ALV-GMBH, Langen, Germany) and transmission electron microscopy (TEM) (Tecnai G^2 Twin, FEI, Hillsboro, OR, USA) were performed to determine aggregate size, while electrophoretic mobility measurements (EPM) were taken with the Zetasizer Nano ZS (Malvern, Bedford, MA, USA).

4.3.2.2 UV Irradiation and Photoreactivity

CPF was exposed to TiO_2 both in the presence and absence of UV light to investigate the relative effects of sorption and degradation. UV-A irradiation was performed with two 15 W fluorescent bulbs (Philips TLD 15W BLB, Koninklijke Philips, Eindhoven, The Netherlands) having a peak emission at 365 ± 15nm. Samples were placed in batch reactors and continually stirred using glass stir bars via magnetic stir plates with UV irradiation from above. For UV experiments involving CPF, reactors were covered with glass petri dishes to minimize loss due to volatilization. The temperature inside the reaction chamber was kept at 23°C. The net irradiance at the suspension surface was 2.3 mW cm^{-2} for bacterial inactivation experiments and 2.0 mW cm^{-2} for CPF degradation tests, measured by a UVX radiometer with UV-A filter (UVP,

inc., Upland, CA, USA). TiO_2 reactivity was also characterized with and without CPF to explore how CPF affinity for the TiO_2 surface relative to other species in water impacts degradation efficacy.

ROS production was measured via probe compounds and quenching agents. For hydroxyl radical (•OH) measurements, terephthalic acid (TA) (98% Sigma-Aldrich, St. Louis, MO, USA) and N-acetyl-L-cysteine (N-AC) (Sigma-Aldrich) were used as probe and quencher, respectively, where •OH generation was measured as the increase in fluorescent units (FSU) resulting from the oxidation of 125 μM TA to 2-hydroxyterephthalic acid (2-HTA) (ex. 315 nm / em. 425 nm). Superoxide (O2•-) was detected as the increase in FSU at 586 nm (excitation at 510 nm) resulting from the transformation of 50 μM dihydroethidium (DHE) in solution to 2-hydroxyethidium (2-HE) (Invitrogen, Thermo Fisher Scientific, Waltham, MA, USA). Superoxide dismutase (SOD) (Sigma-Aldrich) was used as the O2•- quenching agent.

Dark controls were run to test CPF adsorption to the NP surface, CPF was spiked into MD media containing TiO_2 nanoparticles at 0ppm (control), 20 mg L^{-1}, and 40 mg L^{-1} and allowed to mix in the dark. Reaction vials were covered tightly in aluminum foil and were periodically sampled over 24 h. All concentrations were run in triplicate.

4.3.2.3 Bacterial Cultures

Gram Positive *Bacillus subtilis* strain 168 ATCC 23857 and Gram Negative *Acinetobacter baumannii* ATCC 49466 (ATCC, Manassas, VA, USA) were chosen as model

bacteria based upon their environmental relevance, documented ability to biodegrade CPF, and cell membrane structure. Pure cultures of *A.baumannii* and *B.subtilis* were grown overnight at 37°C in tryptic soy broth. Cells were pelleted at 8,000 rpm for 10 minutes and washed thrice with MD. Cells were then resuspended in MD to a final concentration of 10^9 cells mL^{-1}. 2 mL aliquots of the bacteria suspension were added to each batch reactor.

To determine if CPF degradation products impact bacteria, we have exposed cultures of *B.subtilis* and *A.baumannii* to CPF, CPF oxon, and TCP, individually. Toxicity of the products arising from photocatalytic degradation was investigated by exposing CPF for 60 minutes to UV/TiO_2. Suspensions of *B. subtilis* and *A. baumannii* were then dosed with the resulting combination of CPF, TiO_2 nanoparticles, and CPF degradation products present in the system. Additionally, bacteria were exposed to the UV/TiO_2 to evaluate the biological impact of remediation attempts.

Samples taken from the reactors for inactivation measurements were serially diluted to obtain a final concentration of 10^3 CFU mL^{-1}. 100 µL of the final dilution was then spread onto tryptic soy agar plates in triplicate and allowed to grow overnight at 37°C. The resulting colonies were then counted, and ROS and CPF toxicity was calculated as log inactivation relative to time zero.

TEM images of Bacteria and TiO_2 NPs were obtained by depositing samples on lacey carbon grids. These were fixed with 2.5% glutaraldehyde, and sequentially dehydrated and washed with graded ethanol and 1x PBS, respectively.

4.3.2.4 Chlorpyrifos

Chlorpyrifos (99.5%, Chem Service, West Chester, PA, USA) stocks were made in methanol at 1.5 g L^{-1}, which were diluted in MD to working stocks at 1.5 mg L^{-1}. For all experiments, CPF was spiked into samples at 375 µg L^{-1}. Stocks of CPF degradation products CPF Oxon (analytical standard, AccuStandard, New Haven, CT, USA) and 3,5,6-trichloro-2-pyridinol (TCP) (analytical standard, Sigma-Aldrich) suspensions were similarly prepared.

4.3.2.5 Sample Preparation and Analysis

At each sampling point, a 0.2 mL aliquot was transferred to a 1 mL tapered base glass reaction vial (Kimble Chase, Vineland, NJ) along with 10 µL formic acid to aggregate TiO_2 nanoparticles. Samples were centrifuged for 2 min at 9,000 rpm and the supernatant transferred to an LC/MS vial and spiked with 100 µL each of 1 µg mL^{-1} deuterated chlorpyrifos and $^{13}C_6$-3,5,6-trichloro-2-pyridinol (Cambridge Isotopes, Cambridge, MA) and diluted to a final volume of 0.5 mL in 20% acetonitrile (ACN, Honeywell Burdick & Jackson, Muskegon, MI) to match initial LC mobile phase conditions (described below). Residue in the reaction vial was extracted three times with 300 µL ACN and 10 µL formic acid via sonication for 5 min followed by centrifugation

(described above). Extracts were combined, concentrated to 100 µL under N_2, spiked and diluted as described above. Glass pipettes were used at all times (e.g. when sampling individual time points and transferring aliquots during extractions).

Table 5: Multiple reaction monitoring transitions used in the quantification of CPF and its degradation products.

Compound[1]	Description	Transition[2]	Collision Energy (V)	S-Lens (V)	Polarity
D_{10}-CPF	Internal standard	359.9 > 98.9 (Q)	33	70	+
CPF	Target analyte	349.9 > 96.9 (Q)	33	70	+
		349.9 > 197.8 (c)	20	70	+
CPF Oxon	Target analyte	334 > 277.8 (Q)	16	70	+
		334 > 197.8 (c)	29	70	+
$^{13}C_6$-TCP	Internal standard	2.9200 > 162.9 (Q)	19	60	-
TCP	Target analyte	195.9 > 160.9 (Q)	18	60	-
		195.9 > 35.1 (c)	35	60	-

[1] Target analytes listed below an internal standard were quantified using that internal standard.

[2] Transitions used for quantitation are designated "Q" in parentheses; transitions used for confirmation are designated "c" in parentheses.

CPF and its degradation products were analyzed by LC/MS-MS using electrospray ionization in positive (CPF and CPF Oxon) and negative (TCP) modes with a Thermo Accela UPLC system and Thermo TSQ Vantage mass spectrometer (Thermo Scientific). Separation was achieved on a Synergi Polar RP column (50 mm x 2.0 mm, 2.5 µm particle size, Phenomenex, San Jose, CA) and a 400 µL min^{-1} gradient of 5 mM formic

acid (A) and 5 mM formic acid (B) in ACN with the following conditions: 0-0.2 m 70:30 A:B to 1:99 A:B at 3-4 min with return to initial conditions at 5 min and re-equilibration for 4 m. Source conditions included spray voltages +3.5 kV/-2.5 kV, vaporizer temperature 350ºC, capillary temperature 375ºC, sheath gas 45 psi and auxiliary gas 10 psi. Target analytes and internal standards were monitored using the transitions described in Table 5.

4.3.2.6 CAKE software package

The computer-assisted kinetic evaluation (CAKE) v3.1 software package, developed by Tessella (Abingdon, UK) was used to determine degradation rates and pathways. Single first order (SFO) fitting was employed for CPF degradation as well as CPF Oxon and TCP formation. CPF degradation was assumed to proceed to CPF Oxon, TCP, or an undetermined sink. CPF Oxon degradation was assumed to proceed to TCP or an undetermined sink. TCP degradation was assumed to proceed to an undetermined sink. Using this kinetic schema, the software then fits the data to the proposed pathways, returning rate constants and relative weights of each pathway.

4.3.3 Results

4.3.3.1 TiO_2 Characterization and Reactivity

Sonicating P25 in MD produced a narrow distribution of aggregates with an average radius of 94.7 nm and a polydispersity index (PDI) of 0.06 as determined by DLS, and confirmed with TEM. The resulting suspensions were stable, with no

aggregation observed over 6 h via time resolved DLS (Figure 57). TiO_2 aggregates were negatively charged at pH 7.5, with an electrophoretic mobility of -3.79 ± 0.11 $x10^{-8}$ m^2 V^{-1} s^{-1} (ζ potential of -48.4 ± 1.4 mV), and the presence of the media decreased the isoelectric point from the point of zero charge of bare P25 (pH ~6.5) to a pH of approximately 1.5 (Data in Appendix C). Both •OH and O_2•- generation was observed, with production rapidly reaching steady state. The use of N-AC and SOD effectively quenched •OH and O_2•- production, respectively (Figure 58).

4.3.3.2 CPF Interactions with the TiO_2 Surface

No significant loss of CPF from solution is observed under dark conditions for either of the NP concentrations or the controls (Figure 28). Concentrations of CPF observed in extracts were minimal, though no trend was observed either with increased time or TiO_2 concentration. Additionally, this occurs in the control samples as well as in the presence of TiO_2 and likely represents sorption of CPF to the glass walls of the sampler vials after the aliquot has been taken. When combining the supernatant and extract concentrations, CPF recovery compared to t = 0 for both dark and control samples ranged from 89.5 to 101.5%.

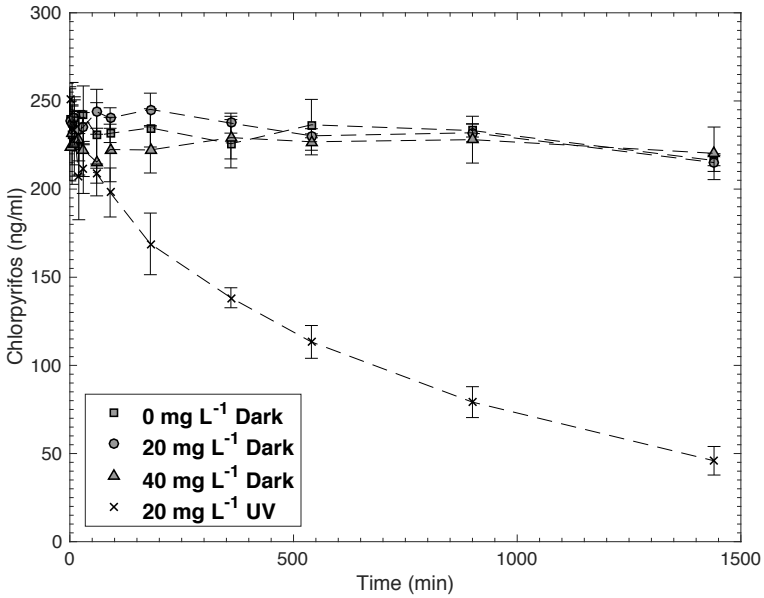

Figure 28: Supernatant CPF concentration vs. time as a function of TiO_2 concentration (0 - 40 mg L^{-1} dark and 20 mg L^{-1} UV).

4.3.3.3 CPF UV/TiO_2 Degradation

Suspensions of CPF and TiO_2 were exposed to UV light to initiate photodegradation. Approximately 50% of the CPF was removed after 9 h given the conditions of the photoreactor setup and TiO_2 concentration (20 mg L^{-1}). CPF can be susceptible to base catalyzed hydrolysis, however no degradation products were observed for any of the dark series (Data in Appendix C). Additionally, the working stock solutions showed no decrease in concentration with time (Data in Appendix C).

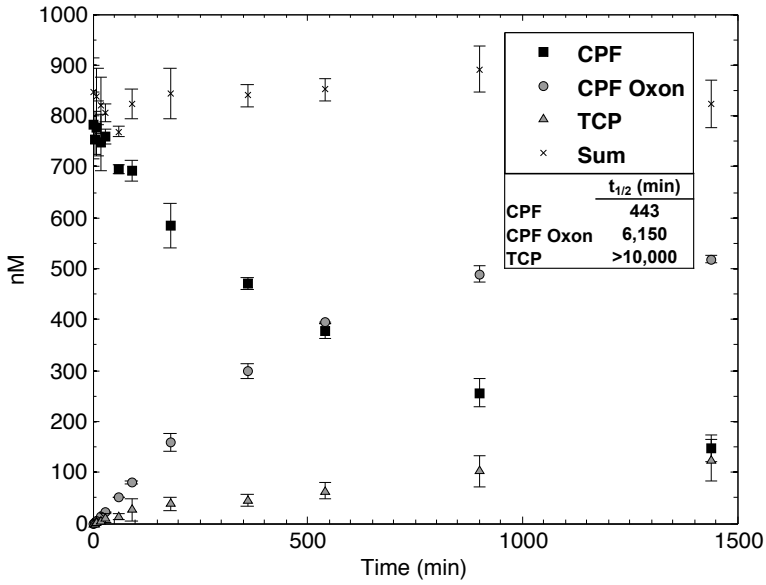

Figure 29: CPF and degradation product concentration vs. time in suspensions of 20 mg L^{-1} TiO_2 exposed to UV.

Degradation of CPF and CPF Oxon and TCP production are shown in Figure 29. Summing the three analytes returns an acceptable mole balance (90.8-105.3% recovery), indicating that the formation of additional primary degradation products is unlikely. After 24 h of continual UV exposure, 81% of CPF was degraded, and the rate of CPF Oxon formation slowed, though a decrease in CPF Oxon concentration was not observed over the sampling period.

Data were fit using the CAKE software package and followed first order reaction kinetics (Data in Apendix C). The half-life of CPF was calculated to be 443 minutes under the given conditions, while half-lives for CPF Oxon and TCP were calculated to be on the order of hundreds of hours (Figure 29, inset). CPF Oxon is the predominant

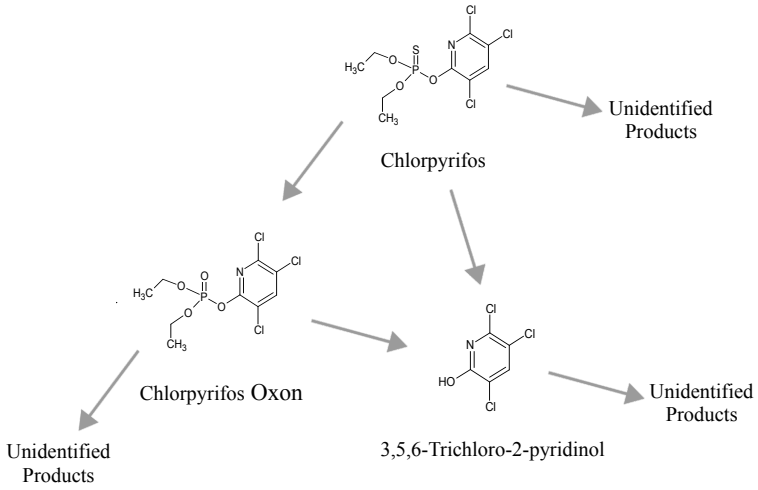

Figure 30: Potential degradation pathways considered by CAKE software.

degradation product produced via oxidation of the sulfur in the phosphorothioate group, and this pathway represents 84% of the calculated CPF Degradation. TCP formation, formed through ester cleavage, makes up the balance at 16%. In agreement with the mole balance achieved, no significant loss of CPF to an unidentified sink was identified, though this pathway was included as an option as illustrated in Figure 30. The further oxidation of CPF Oxon to TCP was not quantifiable, most likely due to reactor conditions resulting in little CPF Oxon degradation over 24 h.

4.3.3.4 Impact of UV/TiO_2 on Bacteria

The hydroxyl radical is primarily responsible for bacterial inactivation as determined through the use of ROS quenchers (Data in Appendix C). The addition of SOD did not alter the inactivation rate of either *A. baumannii* or *B. subtilis,* indicating

superoxide was not generated at sufficient concentrations to contribute to bacteria toxicity. Conversely, no inactivation was observed when bacteria were irradiated in a TiO_2 suspension to which the •OH quencher N-AC was added, further implicating •OH as the primary active agent. Strong inactivation was observed for both *A. baumannii* and *B. subtilis* when exposed to UV irradiated TiO_2. For *A. baumannii*, fewer than 10% of CFU remained after 60 minutes of irradiation, while *B. subtilis* was completely inactivated over the same timeframe.

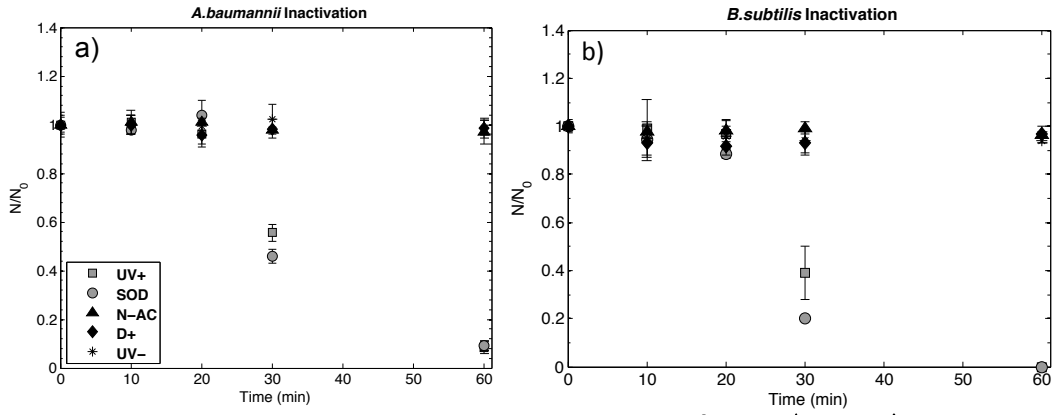

Figure 31: Inactivation of bacteria (*A. baumannii* and *B. subtilis*) under the following conditions: (UV+) 20 mg L^{-1} exposed to UV, (SOD) 20 mg L^{-1} TiO_2 exposed to UV in the presence of SOD, (N-AC) 20 mg L^{-1} TiO_2 exposed to UV in the presence of N-AC, (D+) 20 mg L^{-1} TiO_2 in the dark, and (UV-) 0 mg L^{-1} TiO_2 exposed to UV.

TEM of bacteria exposed to UV light both in the presence and absence of NPs for 60 minutes show small clusters of nanoparticles observed in close proximity to ruptured segments of cell membranes (Figure 32). These images further support the evidence

indicating that locally generated reactive oxygen species are most likely responsible for loss of membrane integrity and cell death.

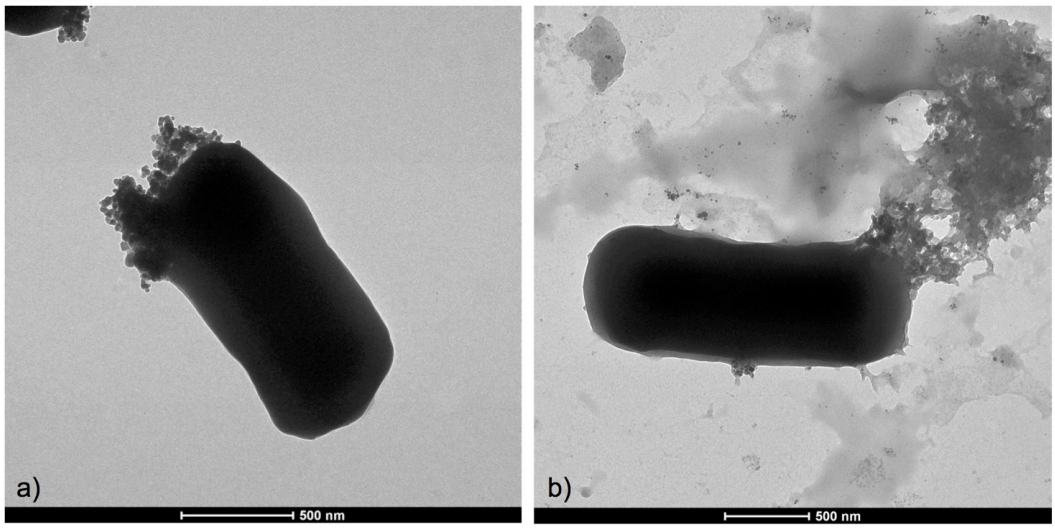

Figure 32: TEM images of *B. subtilis* with 20 mg L^{-1} TiO_2 (a) prior to UV exposure and (b) after 60 minutes UV exposure. Scale bars are 500nm.

To investigate if the sorption of an organic contaminant affects bacterial inactivation (either positively or negatively), bacteria were irradiated in the UV/TiO_2 system in the presence of CPF at 375 μg L^{-1}. Inactivation was measured after allowing CPF to sorb to the mineral surface for 60 minutes in the dark and compared to inactivation from TiO_2 not exposed to CPF. The presence of CPF did not produce a significant difference in inactivation from suspensions without CPF, as shown in Appendix C, Figure 61.

4.3.3.5 Impact of CPF and Degradation Products on Bacteria

The presence of CPF had no appreciable impact on bacterial inactivation rates (Data in Appendix C), either when irradiated immediately or following 60 minutes of mixing in the dark. Additionally, no inactivation was observed following incubation of bacteria for up to 1 h in the resulting combination of CPF, TiO_2 nanoparticles, and CPF degradation products created by 60 minutes of UV irradiation. Furthermore, CPF by itself did not inactivate *A. baumannii* or *B. subtilis* over 60 minutes of exposure. Finally, CPF oxon, and TCP, the primary degradation products, were dosed at the equivalent molar concentrations used for CPF to simulate complete transformation of the pesticide to a degradation product. Neither CPF Oxon nor TCP was found to be acutely toxic to either *A. baumannii* or *B. subtilis* (Data in Appendix C).

4.3.3.6 Impact of Bacteria and CPF on TiO_2 Reactivity

To determine the impact that the presence of additional constituents in suspension had on reactivity, •OH production was measured in both the presence and absence of CPF and *B. subtilis*. CPF was added to a TiO_2 suspension and mixed briefly in the dark prior to the addition of TA and exposure to UV-A for 5 minutes. The resulting suspensions contained 1.098 μM CPF and 125 μm TA. 2-HTA fluorescence represents the amount of hydroxyl radicals that are detected in the bulk. As can be seen in Figure 33(a), the presence of CPF decreased the amount of hydroxyl radicals detected by TA by 88±1.3%. No change in reactivity was observed compared to initial values when CPF and

TiO_2 were mixed up to 60 minutes before the addition of TA and illumination (Figure 33(b)). This is consistent with the lack of sorption observed in Section 5.3.2. Furthermore, time resolved DLS did not indicate TiO_2 aggregation in the presence of CPF (Data in Appendix C).

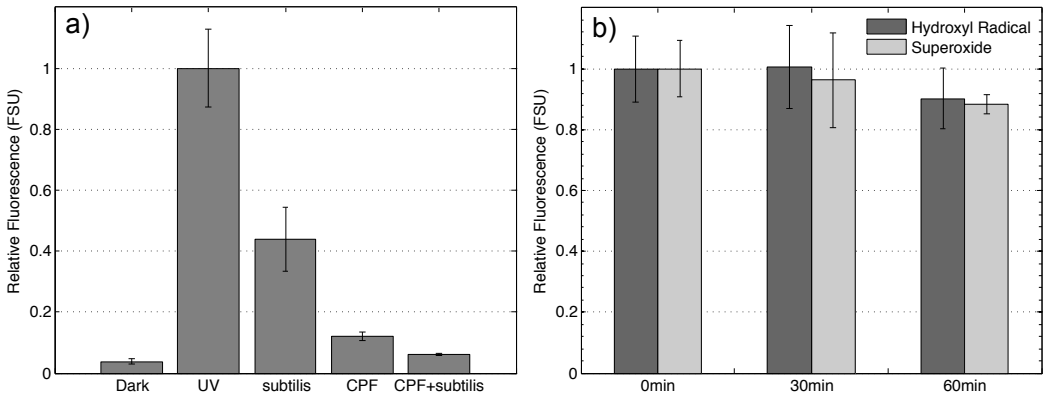

Figure 33: Reactivity measurements of 20 mg L^{-1} TiO_2 exposed to UV. (a) Detected •OH in the presence of various constituents. (b) Detected O2•- and •OH in the presence of CPF over 60 minutes.

Similarly, *B. subtilis* was added to a suspension of TiO_2 at a concentration of 10^8 cfu ml^{-1} and reactivity was subsequently measured via TA. The presence of bacteria decreased 2-HTA fluorescence by 56±10%. When both CPF and *B. subtilis* are present in suspension, fluorescence decreased by 94±0.4%. This value is greater than dark controls (96±0.8%), indicating that a small amount of hydroxyl radicals are still detected by the probe compound.

4.3.3.7 Impact of Bacteria on CPF Degradation

CPF degradation tests were performed in the presence of *B. subtilis* at 20 mg L^{-1}

TiO_2. Given the reactivity measurements observed in Section 5.3.6, it was expected that TiO_2 association with the bacteria would reduce the degradation rate of CPF. In fact, no difference was seen in CPF loss rates with bacteria compared to without (Figure 34). Dark controls indicated negligible CPF Oxon or TCP production, and 92-115% recovery over 24 h. (Data in Appendix C).

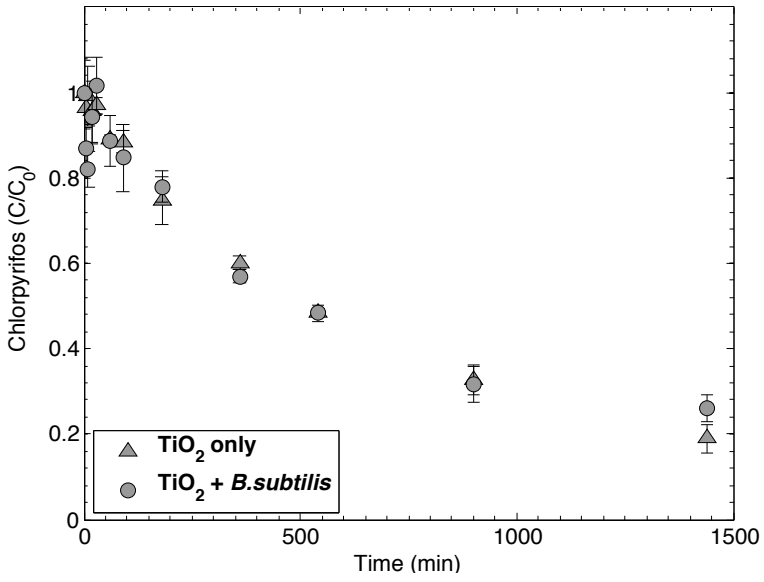

Figure 34: Degradation of CPF in the presence and absence of bacteria.

4.3.4 Discussion

4.3.4.1 TiO_2 Photocatalysis

Photodegradation rates depend upon many factors (e.g. UV flux, contaminant concentration, and photocatalyst loading) making direct comparisons of studies difficult. In this work, reactor conditions were selected to better observe the interactions between TiO_2, CPF, and bacteria. The CPF concentration used in this study (375 μg L^{-1})

was selected due to the low aqueous solubility of the pesticide. However there is great variability reported in the literature for CPF solubility, Solubility values as low as 300 μg L^{-1} have been reported, although Gebremariam et al. report an average of 600±330 μg L^{-1} in distilled water [321]. Frequently, degradation studies have far exceeded this solubility, with concentrations ranging from mg L^{-1} to hundreds of mg L^{-1}, often by using significant concentrations of co-solvents [346, 347, 367, 368]. By selecting a lower concentration of the pesticide, we minimize unexplained losses arising from the compound's hydrophobicity and the use of co-solvents that may quench produced ROS.

In addition to large CPF concentrations, degradation studies have often employed high catalyst loading with the goal of maximizing the photodegradation rate [344]. Generally, ROS production is seen to improve with increasing TiO_2 concentration up to the point when light penetration becomes the limiting factor in photoexcitation. The concentration at which this optimal production occurs varies widely depending on experimental setup [347, 369]. Even at the lower end, nanoparticle particle concentrations frequently employed are an order of magnitude greater than the 20 mg L^{-1} applied in the current study. Using a lower catalyst loading effectively prolongs the degradation process, allowing better insight into the potential pathways of CPF removal from solution.

4.3.4.2 CPF Adsorption

While high affinity of CPF for soil particulate matter has often been observed [322, 348, 370], generally, few attempts have been made to identify sorption versus degradation of CPF using TiO_2. Devi et al. report an 8% loss of CPF from suspension after mixing in the presence of 150 mg anatase for 10 minutes in the dark, which is ascribed to adsorption [332]. It is unclear, however what concentrations of CPF were used in this study, and an attempt to extract the pesticide off of the TiO_2 to validate the proposed does not appear to have been made.

Studies focusing on the interactions and surface catalyzed hydrolysis of chlorpyrifos methyl and other related pesticides using metal oxides have generally found little to no sorption. Nair et al., looking at adsorption of CPF onto Al_2O_3 found complete removal of the pesticide when the mineral surface was coated with Au and Ag NPs, but that no significant adsorption occurred with bare Al_2O_3 spheres [348]. Furthermore, Torrents et al. observed the slow loss of chlorpyrifos methyl from solution in a 10 g L^{-1} TiO_2 suspension, but concluded this decrease was likely due to hydrolysis rather than sorption [349]. The rate of hydrolysis by TiO_2 was greater than that for equivalent concentrations of Al_2O_3 or FeOOH. Clausen and Fabricius, utilizing α- and γ-FeOOH, showed that absorption, while significant for ionic pesticides, was negligible for nonionic pesticides [350].

These studies support our current observations for the nonionic chlorpyrifos, and suggest that the use of TiO_2 NPs alone will not contribute practically to CPF adsorptive removal from solution in a remediation scenario. As a result, loss of CPF is likely to occur almost entirely through photocatalysis. The timeline for TiO_2 surface catalyzed hydrolysis presented by Torrents et al. indicate that the order of days is necessary for tens of g L^{-1} of NPs to degrade CPF appreciably, while this study, using a thousand-fold less TiO_2, is capable of achieving a 50% reduction in CPF in 9 h [349]. Furthermore, the lack of specific interactions implies that other components of natural waters, such as bacteria or NOM, which may show a stronger affinity for TiO_2, are likely to further limit access to the TiO_2 surface.

4.3.4.3 CPF Degradation and Oxidation Products

Duirk et al. observed both CPF Oxon and TCP formation from oxidation of CPF using HOCl as the oxidant [371]. The relative amounts of the degradation products produced are in good agreement with the current study, in which the fraction of CPF transformed via oxidation of the sulfur, far exceeds cleavage of the ester bond to create TCP. Devi et al. present a similar pathway [332]. Thus, while ester cleavage may be the predominant pathway for surface catalyzed hydrolysis, oxidation produces an intermediary, which is then capable of forming TCP or further degrading via an alternative pathway.

4.3.4.4 Comparison of TiO_2 Reactivity in the Presence and Absence of CPF

The formation of ROS occurs at the surface of the TiO_2 nanoparticle, which then diffuses away from the surface into the bulk solution, nonspecifically reacting with targets it comes across [40]. As each compound in solution competes for a fraction of the finite amount of ROS generated, delivery depends not only on individual reaction rates but also proximity to the NP surface. Because •OH generated by heterogeneous photocatalysis is produced at a specific point (versus homogenous photocatalysis, e.g., hydrogen peroxide which is uniformly mixed in aqueous solutions) the closer a target is to the photocatalyst, the greater the subsequent radical dose. The use of a probe compound such as TA is capable of providing a benchmark of the •OH concentration in the bulk solution. In this study, CPF is observed to outcompete TA for hydroxyl radicals, as evidenced by the strong decrease in fluorescence observed in Figure 33 when CPF is introduced. This could result either from a greater reaction rate with •OH or from closer association with the TiO_2 surface.

The •OH reacts with TA and CPF at roughly equal rate of $3.3x10^9$ M^{-1} s^{-1} and $4.4x10^9$ M^{-1} s^{-1}, respectively [88, 372]. Given that the concentration of CPF present in solution (1.098 μM) was two orders of magnitude less than that of TA (125 μM), one would expect the presence of CPF to have a negligible impact in 2-HTA formation, and thus fluorescence. That this is not the case implies a hierarchy of affinity for the NP surface that brings CPF closer to the radical generator and increases the probably of CPF

oxidation over TA.

Though sorption of CPF onto the surface of TiO_2 is not observed (Section 5.3.2), relatively weaker hydrophobic interactions are likely to draw the nonionic CPF towards the NP surface. Additionally, the two partially positive ethyl functional groups attached to the more electronegative phosphorothioate in CPF will produce a small dipole moment that may encourage interaction with the negatively charged NP surface. These ion-dipole interactions are likely to be smaller in magnitude compared to ion-ion repulsive forces between TiO_2 and the negatively charged carboxylic groups on TA (pKa 3.5, 4.5) [88], but the effect will be the same in either case. These electrostatic interactions, coupled with the hydrophobic interactions of CPF, will draw CPF molecules closer to the surface of the negatively charged TiO_2 and relegate TA to a position further out in the bulk solution resulting in a greater exposure to hydroxyl radicals for the pesticide and effectively shielding the water-soluble probe compound.

4.3.4.5 Reactivity in the Presence of CPF and Bacteria

The nature of these interactions drawing CPF to the NP surface, however, is not so strong that it displaces bacteria or alters the rate of inactivation, as observed in Appendix C, Figure 61. These data, coupled with TEM images in which NPs are observed at the surface of bacteria both prior to and following UV exposure, indicate that NPs attach to the cell providing a direct pathway for •OH delivery. These results imply that the CPF remediation process itself (i.e. photoactivated TiO_2) will likely have a

greater impact on microbial viability than either the pesticide or its degradation products at concentrations below the solubility limit given the lack of acute toxicity observed.

Conversely, nor does the presence of bacteria impact CPF degradation over 24 h. This implies that, despite TiO_2 affinity for the bacterial surface, there remains sufficient •OH production for CPF degradation to continue unaffected. These data are in contrast to the decrease in detected •OH by TA in Section 4.3.3.6, and further indicate that differences in relative affinity for the NP act as significant deciders of delivered ROS dose.

4.3.5 Conclusions

The picture that emerges from the given system is one in which components of the water environment are impacted relative to their affinity for the TiO_2 NPs. Thus, association of TiO_2 with bacteria and with the hydrophobic CPF results in a greater •OH dose delivery than for the probe molecule TA for which there is less affinity. Arising from this are the implications that while investigating reactivity in simplified systems can provide a benchmark of NP reactivity, it may also overestimate photocatalytic efficiency in realistic environments, especially for hydrophilic contaminants, and that more research in complex systems should be undertaken to better understand the role that non-targeted entities may play in remediation scenarios.

5. Conclusions

The experiments described in this dissertation were designed to improve our understanding of how changes in NP surface chemistry impact the photoreactivity of a nanoparticle. This has been carried out through investigations focusing on surface functionalization, specific and non-specific interactions with anions in solution, and association with biological surfaces and organic molecules. NPs were characterized in terms of aggregate morphology (size and structure) and particle stability in addition to photoreactivity endpoints (radical probes, microbiological impact, and contaminant degradation). The results of this work have highlighted the important role that the NP surface will play in determining reactivity in a natural aquatic environment and have supported the hypotheses outlined in Chapter 1, namely 1) that functionalization of FNPs will reduce aggregation and impact ROS generation, 2) that water chemistry and interactions with organic or ionic compounds at the NP surface will determine the reactivity of the system, and 3) that multiple, coexisting constituents will compete for ROS delivery.

5.1 Bacteriophage Inactivation by UV-A Illuminated Fullerenes: Role of Nanoparticle-Virus Association and Biological Targets

Engineered functionalization of FNPs was shown to impact ROS production, reduce aggregation, and alter viral proximity, resulting in the following hierarchy of MS2 virus inactivation: aqu-nC60 < C60(OH)6 ≈ C60(OH)24 < C60(NH2)6, which

followed Chick-Watson inactivation kinetics. Changes to FNP surface functionalization were observed to significantly impact photoreactivity, with the addition of 24 hydroxyl groups to the C_{60} cage influencing the surface charge and increasing singlet oxygen production. As a result these fullerol aggregates were smaller and more stable than nC_{60}, and are expected to have a longer lifetime in the water column, which, combined with the increase in observed singlet oxygen production, would result in greater potential exposure and hazard, respectively.

The addition of amine functional groups both decreased the size of aggregates and the magnitude of surface charge while increasing the amount of ROS produced, suggesting that antiviral properties of fullerenes can be increased by adjusting the type of surface functionalization and extent of cage derivatization, thereby increasing the ROS generation rate and facilitating closer association with biological targets.

When comparing the extent, rather than type, of derivatization, few differences in aggregate characteristics were observed between $C_{60}(OH)_6$ and fullerol, that latter of which has often been used in research due to its relative ease of suspension. While the average fullerol aggregate was smaller than $C_{60}(OH)_6$, measurements of electrophoretic mobility are indistinguishable at the circumneutral pH of PBS. Furthermore, singlet oxygen generation of $C_{60}(OH)_6$ was only slightly less than that of fullerol. Thus, the hydroxylation of fullerenes expected to occur to in natural waters following UV

exposure will rapidly result in products that behave similarly to their more functionalized counterparts, capable of generating significant amounts of ROS.

What remains unclear is how engineered functional groups will impact the phototransformations that are expected to occur. As FNPs are tailored to specific products or uses, highly functionalized FNPs will become increasingly more prevalent, with pristine fullerenes becoming increasingly less likely to be released into the environment. This work implies, however, that these advanced FNPs will retain a significant degree of photoreactivity despite any transformations (e.g. degradation, oxidation, cleavage) that occur to large functional groups existing on the surface. How the aggregation state and affinity of a specially functionalized FNP for a biological surface changes with these transformations may be the largest factors in determining the delivered dose in natural waters.

5.2 Influence of Inorganic Anions on the Reactivity of TiO_2 Nanoparticles

Unlike the functionalization of fullerenes, changes to the crystalline lattice of TiO_2 nanoparticles following environmental release are unlikely, though this may indeed occur with some metal oxide nanoparticles, such as nano ceria, due to redox chemistry. While intrinsic properties of TiO_2 are expected to remain constant, surface interactions with organic matter, colloids, or, as shown in this work, inorganic anions present in water will significantly impact the reactivity of the system.

The influence of anions on surface reactivity and bulk ROS production has been demonstrated though the response is not always straightforward, as the greater impact of phosphate on direct hole oxidation compared to hydroxyl radical generation demonstrates. Thus, determining the potential hazard of a NP depends at least partially on the mode of action. For hydrophobic entities sorbed to the NP surface, a decrease in bulk ROS levels due to radical quenching by an anion may have no impact in perceived reactivity.

Furthermore, specific interactions with anions such as phosphate and carbonate undergoing in inner sphere ligand exchange have been shown to stabilize NPs due to increased negative surface charge. EPM was measured versus pH to demonstrate the specific interactions of phosphate and carbonate for which the pH of the IEP was concentration dependent. No change in IEP was observed in the presence of nitrate or chloride illustrating the lack of specific interactions. As a result, small concentrations of these anions may increase the overall risk of a nanoparticle, evidenced by the increase in both ROS generation and particle stability in waters containing 0.5 mM phosphate and carbonate compared to nitrate or chloride. Ultimately, this work demonstrates that to understand the reactivity of TiO_2 nanoparticles, the aquatic environment must be considered. Furthermore, this research suggests that reactivity is not static; that the transition of NPs from water of a given ionic composition to another of similar ionic strength may result in either an increase or decrease in reactivity.

5.3 Chlorpyrifos Degradation via Photoreactive TiO_2 Nanoparticles: Assessing the Impact of a Multi-Component Degradation Scenario

Chapter 4.3 studied the influence of ancillary components on bacterial inactivation or contaminant degradation by TiO_2, and ROS delivery was shown to depend on the coexisting constituents of a suspension. The presence of either bacteria or CPF strongly decreased bulk measurements of hydroxyl radicals, with almost no •OH detection in solutions containing both, indicating that proximity to the NP surface is important in determining ROS dose. However, the presence of bacteria had no impact on CPF degradation rates, nor did the presence of CPF diminish the rate of bacterial inactivation. Thus, while TEM images show aggregates of TiO_2 sorbed to the surface of bacteria, sufficient hydroxyl radicals are generated and escape delivery to the bacteria, reacting instead with CPF.

Ultimately, the implication of this study is that components in suspension will be impacted by photoreactive nanoparticles relative to their affinity for the NP surface. This agrees well with findings described in Chapter 4.1 in which various FNPs were observed to have differing affinities for a viral surface. This point source nature of photoreactive NPs, in which ROS is not uniform in solution, is a significant complicating factor in assessing NP risk and emphasizes the importance of the physical characteristics of an aggregate. This work suggests that estimating risk based off of simplified systems may poorly estimate photocatalytic efficiency in realistic environments; for hydrophilic

targets, the presence of constituents with greater affinity for the NP surface is likely to diminish the delivered dose.

5.4 Summary of Conclusions

This dissertation has demonstrated that the reactivity of a system is largely determined by the surface chemistry of a NP. These surface interactions may be intentional, such as functionalized FNPs, or incidental and resulting from the aquatic environment into which a NP is introduced. Additionally, the photocatalytic impact of a NP will depend on the characteristics of potential targets as on the characteristics of the NP itself.

5.5 Continuations of This Work

The studies described herein have necessarily employed simplified systems in order to understand the trends that impact reactivity. By no means have all the components of natural waters that may influence reactivity been considered in this work; prime candidates for future investigation include NOM and colloids such as clays or silicates, as well as engineered waters with greater complexity.

5.5.1 Natural Organic Matter

NOM presents a particularly intriguing case, as it can act both as a sensitizer and quencher of radicals. Studies have shown NOM exposed to sunlight produces sufficient amounts of ROS to inactivate bacteria and degrade organic compounds. Additionally, NPs coated in NOM have shown increased stability and mobility in column studies.

Understanding the conditions in which NOM may increase or decrease the total ROS of a NP containing system will greatly contribute to predictions of risk related to NP release. Furthermore, comparing the relative contribution of NP and NOM on ROS production can provide a benchmark of environmental impact.

5.5.2 Natural Colloids

Colloids, ubiquitous in rivers lakes and streams, are anticipated to outnumber NPs in all but the most concentrated release scenarios, and it is reasonable to expect heteroäggregation to dominate in most cases. Currently, heteroäggregation studies have been limited to the impact on aggregate formation and morphology. The influence of aggregate size and morphology in homoäggregates on ROS production (e.g., shielding of UV light and radical quenching) has been demonstrated, but the formation of heteroaäggregates is likely to add further pathways of excitation (e.g., charge transfer, electron or hole trapping).

5.5.3 Photoreactivity in Natural Systems – Towards Functional Assays

While investigations of simplified systems are important tools in understanding photoreactivity, the results presented in Chapter 4.3 illustrate the complexity that arises in conditions containing even mild resemblance to natural waters. Developing a comprehensive understanding of reactivity will require testing FAs in agreed upon representative environmental conditions. Among the necessary tasks then, are to determine reasonably simple reactivity endpoints and characterize anticipated exposure

conditions and relevant forms of released NPs. Water chemistry will impact NP aggregation, dissolution, fate and transport, and these physicochemical changes to NPs should continued to be studied to better inform risk assessment. Organismal impacts may vary between levels of complexity (e.g., fish versus bacteria) or even at the same level (e.g., gram positive versus gram negative bacteria), highlighting the need to identify appropriate endpoints.

5.5.3.1 Functional Assay Endpoint Considerations

Given the complexity in assessing potential toxicity, an appropriate FA endpoint such as exogenous ROS production could help identify combinations of NPs and situations for which hazard may be high. The goal should not be to measure each specific impact of a NP, but to identify and investigate the most likely impacts or types of NPs associated with higher risk. Similarly, instead of testing each susceptible organism under a number of conditions, a stronger and more productive approach would be to look at photoreactivity in cases for which that's the likely mode of action.

An example would be the release into aqueous environments of photocatalytic metal oxides that have the potential to be toxic to a number of microorganisms. Risk assessments of these particles ought reasonably to take into account their fate and transport in the anticipated environment as well as endpoints related to photoreactivity. The potential impact of these particles is unlikely to be the same if one considers their introduction into a stream or lake versus a WWTP, in which the majority of NPs have

been found to partition into the biosolids and may be later land applied as part of soil amendments. For these scenarios, the appropriate FAs would differ.

TiO_2 and Fullerenes are attractive model NPs for establishing FAs, as they are generally stable and mostly non-toxic in the absence of light. However, as has been demonstrated, their photoreactivity results in toxicity, measurements of which could serve as a realistic FA. In this dissertation, investigations into ROS generation have given a better understanding of potential for toxicity and degradation, measurements that incorporate the significant influences of aggregate size and morphology. Measuring ROS production does not invalidate the need for NP characterization or system property measurements; but with the understanding that NP aggregation will impact the underlying phenomena, it may be sufficient to measure ROS production as a determinant of hazard for a given set of conditions. Using this as a quantifiable endpoint, we can easily and systematically investigate what affects reactivity of NPs in the environment.

5.5.3.2 Environmental Release Considerations

Challenges to predicting risk for photoreactive nanoparticles include uncertainties in both aquatic chemistry and light exposure. While the intensity of sunlight can be largely predicted on a coarse (daily) scale based on season, geographic location, etc., results presented in this dissertation highlight the fact that NP transformations such as aggregation resulting from the aquatic chemistry are likely to

take place on a much finer scale (minutes to hours). As a result, NPs released into exposed waters at noon on a sunny day will present a greater hazard than those released into shaded waters or late in the evening. It may be sufficient to study reactivity under the worst-case scenario (i.e., using the greatest reasonable light flux) and apply a "light factor" ranging from 0 to 1 to adapt experimental results to anticipated release conditions. However, while this approach appears to be straightforward for unchanging NPs or aggregates, the impact of transformations my not be easily separated from UV exposure. It would be useful to measure reactive endpoints at high, low, and average light exposure conditions to determine what can be reasonably estimated.

Waters containing stabilizing agents such as phosphate, carbonate or natural organic matter are likely to increase the duration of NPs in the water column, thereby increasing the net flux of light to which they are exposed. Furthermore, water chemistry may impact the type of ROS produced. For example, irradiated FNPs in the presence of an electron donor favor superoxide production over single oxygen. In high nitrate waters, peroxynitrate may be generated or the carbonate radical in high carbonate waters. These secondary radicals, which have less oxidizing capacity, are largely dependent on *a priori* •OH generation and are less likely to necessitate quantification, though in waters where they are the predominant form of ROS to which organisms are exposed, they could be appropriate endpoints.

The identification of realistically anticipated environmental conditions would greatly facilitate the design of photoreactivity FAs. Initially, multiple ROS endpoints should be tested to adequately describe the reactivity of a NP. Priority should be given to the primary expected ROS endpoints (singlet oxygen for FNPs, superoxide and hydroxyl radical for semiconductors) as well as measurements of surface reactivity (direct hole oxidation). Ultimately the precise ROS measurement for a photoreactivity FA will depend on the water chemistry of the release scenario.

5.5.3.3 Nanoinformatics, Data Visualization, and Comparison

This work has shown that changing the anion concentration significantly impacts ROS generation in simplified systems. As we consider more realistic conditions, however, it will become important to rank or compare reactivity between greatly differing water chemistries. For example, it will be more difficult to understand and predict the reactivity of waters in which ionic strength, suspended solid content, and organic matter all vary.

The further development and employment of nanoinformatics databases, such as those being developed within CEINT (NIKC, N4mics) or by the EPA (NaKnowBase) will provide platforms for data visualization and comparison that enable complex relationships to be discerned from multiple studies consisting of multiple parameters. Comparisons of NP response between these relevant environmental conditions will help to identify the primary variables in determining reactivity. This, coupled with the

establishment of reasonably simple, appropriate FAs will move the process of NP risk assessment away from a case-by-case handling of each NP and enable regulation to keep pace with the advancements of nanotechnology.

Appendix A – Supporting Information for Chapter 4.1: Bacteriophage Inactivation by UV-A Illuminated Fullerenes: Role of Nanoparticle-Virus Association and Biological Targets

Suspension Preparation

A colloidal suspension of fullerene (aqu-nC_{60}) in ultrapure water (UPW) was prepared by sonicating 200 mL of UPW (resistivity > 18 MΩ cm and TOC< 30 μg/L) containing 100 mg C_{60} powder using a high-energy probe (S-4000, Misonix, Qsonica, LLC, Newtown, CT) for 10 hours (pulse time: ON for 10 min; OFF for 20 min) in the dark. Following the dispersion, the suspension was filtered through a 100 nm nylon membrane filter (Magna, GE Osmonics, Minnetonka, MN). The filtrate was then concentrated via rotavaporator (Büchi, Flawil, Switzerland). DLS measurements of the suspension pre- and post-concentration indicated no change in average aggregate size. The number weighted and unweighted particles size distributions of FNPs in aqueous suspension are shown in Figure 35.

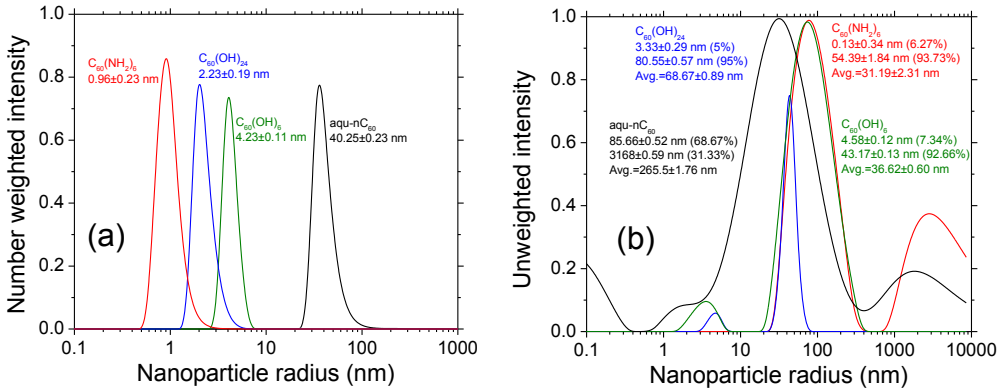

Figure 35: (a) Number weighted intensity and (b) unweighted intensity of fullerenes in suspension measured using dynamic light scattering at 90 degrees scattering angle.

Electrophortic Mobility Measurements

The Electrophoretic mobilities of the FNP suspensions as well as of MS2 virus are summarized in Table 6. As can be seen, all suspensions were negatively charged under our experimental conditions.

Table 6: Electrophoretic mobility and zeta potential of FNP suspensions and MS2 virus.

	EPM ($m^2/V.s$) $x10^{-8}$		ZP (mV)	
Suspension	avg	std (n=6)	avg	std (n=6)
$C_{60}(NH_2)_6$	-1.09	0.10	-13.9	1.2
$C_{60}(OH)_6$	-3.65	0.30	-46.6	3.9
aqu-nC_{60}	-1.76	0.29	-22.4	3.7
$C_{60}(OH)_{24}$	-3.57	0.30	-45.6	3.8
MS2	-1.09	0.09	-13.9	1.1

Standard Curve Preparation

Singlet oxygen production was determined by comparing the measured fluorescence of SOSG in fullerene suspensions versus a Rose Bengal (RB) standard curve. All SOSG measurements were performed in the absence of MS2 virus. RB standards produced a linear fluorescence response over a concentration range of 0.005 – 0.1 μM shown in Figure 36.

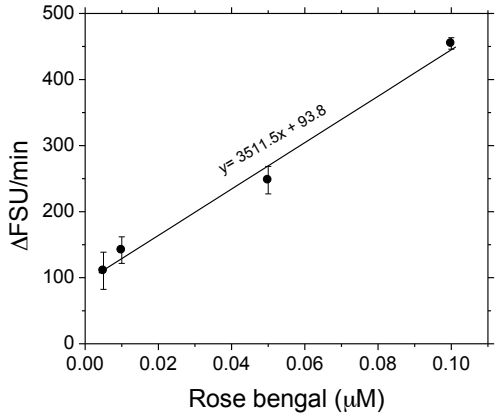

Figure 36: Change in fluorescence measured over one minute irradiance versus rose bengal standard concentration. Error bars indicate the standard deviation of triplicate measurements.

The rate of photons hitting the sample in photons per second was calculated as follows:

$$r_{photon} = \frac{irr \cdot a \cdot \lambda}{h \cdot c} \qquad \text{(Eq 34.)}$$

where irr is the irradiance in W/cm^2, a is the illuminated area of the reaction vial, c is the speed of light, λ is the wavelength, and h is plank's constant. Combining this with the RB standard solution absorption at 365nm, ABS_{365}, the quantum yield, Φ, and

Avagadro's number, N_A, gives the rate of singlet oxygen production, r_{1O2}, in molar concentration per time:

$$r_{^1O_2} = \frac{r_{photon}(1-10^{-ABS_{365}})\phi}{V \cdot N_A} \qquad \text{(Eq 35.)}$$

Figure 3 shows the fluorescence response of SOSG versus singlet oxygen production in the RB standards. Concentrations of irradiated fullerene suspensions were adjusted to maintain fluorescent responses within this linear standard range

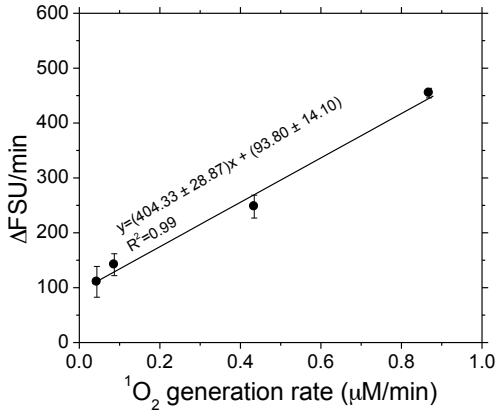

Figure 37: Rate of change in fluorescence measured over one-minute irradiance vs. calculated singlet oxygen production by the RB standards indicated in Figure 39 and calculated by Equations 34 and 35. Error bars indicate the standard deviation of triplicate measurements.

The UV-A Irradiance of the RB standards was 2.3 mW/cm^2 as measured by a UVX radiometer (UVP, Inc. Upland, CA). The output spectrum of the UV bulbs used in the study are shown in Figure 38.

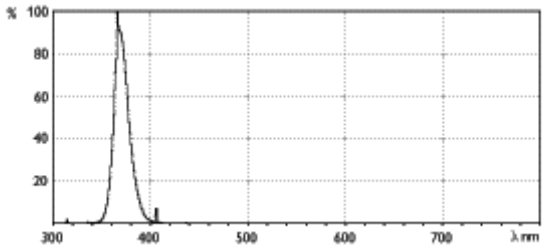

Figure 38: Output spectrum of the Philips 15W TL-D BLB bulbs used in the study. Output is centered at 365nm, and UV-A irradiance was measured at 2.3mW/cm².

Inactivation Kinetics and Singlet Oxygen Dose

To determine the steady state singlet oxygen concentration, $[^1O_2]_{ss}$, first the accumulation of singlet oxygen in suspension can be modeled as follows

$$\frac{d[^1O_2]}{dt} = r_{^1O_2} - k_d[^1O_2] \qquad \text{(Eq 36.)}$$

where k_d is the rate of quenching in water ($k_d = 2.4 \times 10^5$ sec^{-1})[373]. Making the steady state approximation, an equation for $[^1O_2]_{ss}$, in moles, can be calculated as

$$[^1O_2]_{ss} = \frac{r_{^1O_2}}{k_d} \qquad \text{(Eq 37.)}$$

Thus, from the Rose Bengal standard suspensions, the fluorescence response due to a given steady state singlet oxygen concentrations can be calculated as

$$\frac{dFSU}{dt} = k_{^1O_2}[1O2]_{ss}[SOSG] \qquad \text{(Eq 38.)}$$

where FSU is the detected fluorescence resulting from the cumulative reaction of SOSG with the produced $^1O_2$ over the irradiance time t, k_{1O2} is the second order rate constant, and $[^1O_2]_{ss}$ is the steady state $^1O_2$ concentration. By using a sufficiently large [SOSG] compared to produced $^1O_2$ and short irradiance times, the concentration of unreacted SOSG in solution can be assumed constant, giving the pseudo first order kinetics:

$$\frac{dFSU}{dt} = k'_{^1O_2}[1O2]_{ss} \qquad \text{(Eq 39.)}$$

Here, k'_{102} is the pseudo-first order rate constant whose units are FSU uM^{-1} min^{-1}. Typically, pseudo-first order and first order rate constants have units of concentration per concentration per time, which reduces to simply units of per time. In this study, we are modeling the increase in fluorescence, which does not have units of concentration, thus we arrive at our slightly modified rate constant. When plotting the observed increase in fluorescence versus calculated singlet oxygen concentration (Figure 39), the slope is $k'_{102} = 5.8x10^9$ FSU uM^{-1} min^{-1}. This value can then be used to convert the observed rate of fluorescence into the singlet oxygen concentration in solution and is the result of our experimental conditions, including the excitation and emission wavelengths of the Modulus fluorimeter used.

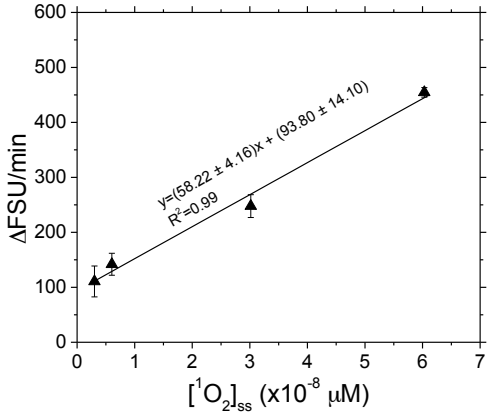

Figure 39: Change in fluorescence over given steady state singlet oxygen concentrations, determined from a Rose Bengal standard curve. Error bars indicate the standard deviation of triplicate measurements. The slope of this line is k' as indicated in Equation 39. Error bars indicate the standard deviation of triplicate measurements.

The method for calculating CT, the dose measurement for conventional disinfectants [275] and cationic fullerenes [33], is shown below

$$CT = \frac{FSU(t)}{k'_{^1O_2}} = [^1O_2]_0 t \qquad \text{(Eq 40.)}$$

where CT is the disinfectant concentration, C, multiplied by the contact time, t. The disinfectant concentration, C, in the FNP suspensions is taken to be the steady state $^1O_2$ concentration probed by SOSG on or very near the surface of the NP, calculated using the Rose Bengal experimental standard curve, above. Inactivation data for the FNP suspensions over 5 minutes is shown in Figure 15 and inactivation versus CT is shown in Figure 20 (These data are found in Chapter 4.1).

Table 7: MS2 inactivation rate constant during control experiments in UV-A. Average rate constant and standard deviation are shown here.

Chemicals added	Rate constant (min^{-1})
MS2+ UVA	0.034± 0.001
MS2+$C_{60}(NH_2)_6$ + β-carotene+UV-A	0.034 ± 0.003
MS2+$C_{60}(OH)_6$ + β-carotene+UV-A	0.033 ± 0.003
MS2+$C_{60}(OH)_{24}$ +β-carotene+UV-A	0.035 ± 0.002
MS2+aqu-nC_{60} + β-carotene+UV-A	0.035 ± 0.004

The results in Table 7 show that in the presence of β-carotene the inactivation rate is similar to UV-A alone indicating that the inactivation in the absence of β-carotene is mediated solely by UV-A sensitized $^1O_2$.

Table 8: MS2 viability during control experiments in the dark.

Chemicals added	**0 min**	**5 min**
MS2 dark	(1.75 ± 0.06) x 10^7	(1.75 ± 0.05) x 10^7
MS2+aqu-nC_{60} dark	(1.72 ± 0.09) x 10^7	(1.75 ± 0.06) x 10^7
MS2+$C_{60}(OH)_{24}$ dark	(1.70 ± 0.07) x 10^7	(1.69 ± 0.08) x 10^7
MS2+$C_{60}(OH)_6$ dark	(1.72 ± 0.05) x 10^7	(1.73 ± 0.07) x 10^7
MS2+$C_{60}(NH_2)_6$ dark	(1.73 ± 0.07) x 10^7	(1.76 ± 0.05) x 10^7

Results in Table 8 show that in the absence of UV-A, fullerenes had no effect on the viability of MS2.

Hyperspectral image analysis

Figure 40 illustrates the sequence of steps involved in processing a hyperspectral image of aqu-nC_{60} and MS2 virus sample. High resolution spectral and spatial information from hyperspectral images (Figure 40 (a) and (b)) were obtained by first applying the minimum noise fraction transform to estimate and segregate the noise to

generate coherent data (Figure 40 (c) and (d)). Next using two-cascaded principle component transformations, the noise in the image was converted to unit variance and the bands were resolved into corresponding standard principal components [374]. The Eigen values were analyzed using the minimum noise fraction bands (images) to aid in retrieving the most coherent images (images with Eigen values near 1 are mostly comprised of noise) (Figure 40 (e)). The coherent image was then analyzed in terms of pixel purity index (PPI) values computed by repeatedly projecting n-dimensional scatter plots onto a random unit vector (Figure 40 (f)). The extreme or spectrally "pure" pixels in each projection (those pixels that fell onto the ends of the unit vector) were recorded and the PPI image was created by noting the total number of times each pixel was marked as extreme. Next, the data cloud was rotated using the interactive n-Dimensional Visualizer (NDVI) algorithm to select, classify, and extract the endmembers (spectrally pure materials) of the nanoparticles and viruses (Figure 40 (g) and (h)). The selected endmembers were classified by mixture tuned matched filtering (MTMF) (Figure 40 (i) and (j)), which mapped the nanoparticles and viruses in the hyperspectral image. The final step in the analysis is supervised image classification (Figure 40 (k)-(n)). Similar steps were used for other nanoparticle-virus combinations to determine their relative association/proximity. Figure 40 (i) and (j) shows the infeasibility vs. MF score images, where MF-score =1 indicates perfect match. All materials with a score ≥ 0.7 and infeasibility <20 are chosen as a match to spectral signatures. Figures k-n shows the map

of MS2 and aqu-nC_{60} in noise-free image (Figure 40 (k) and (l)) and hyperspectral image (Figure 40 (m)-(n)), respectively.

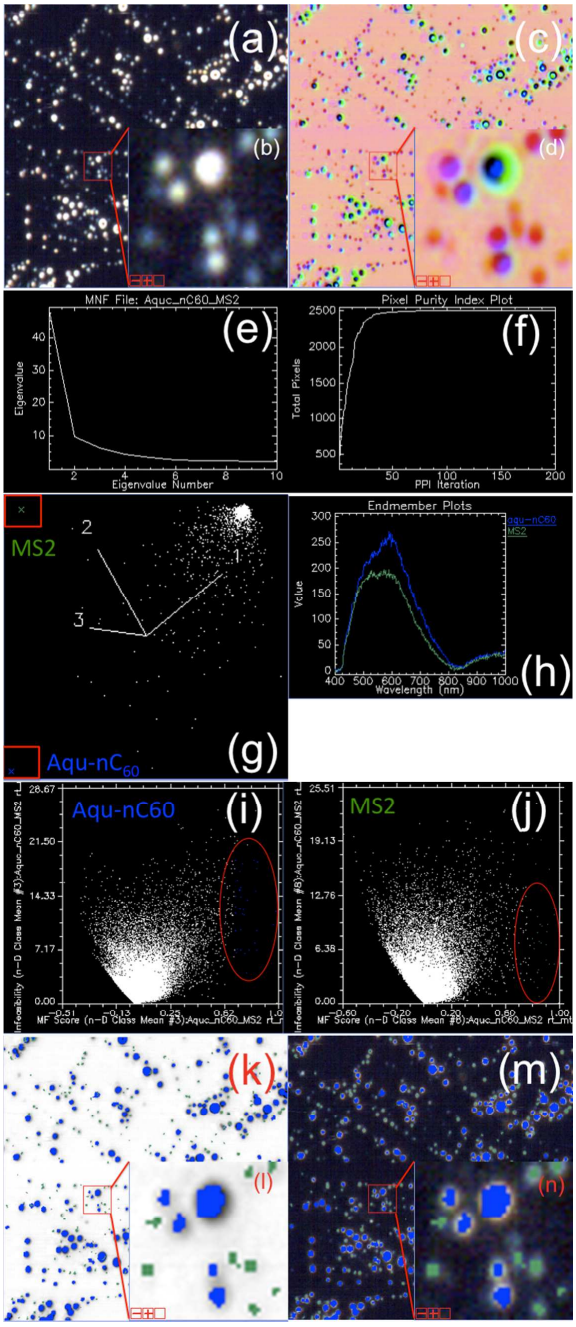

Figure 40: Hyperspectral image analysis of MS2+aqu-nC$_{60}$ in aqueous phase. Mixture tuned matched filtering was applied to map the distribution of MS2 and aqu-nC$_{60}$ in the image.

Table 9: Infrared frequencies (wavenumbers) and associated band assignments for MS2 bacteriophage.

Wavenumber (cm^{-1})	Assignment
1733	C=O, carbonyl groups
1710	Glu, ν(C=O)
1695-1670	Intermolecular β-structure
1690-1680	Intramolecular β-structure
1666-1659	'3-turn' helix
1657-1648	α-helix
1645-1640	Random coil
1640-1630	Intramolecular β-structure
1625-1610	Intermolecular β-structure
1606-1	Tyr-O^{-1}
1580	Gln,
1573	HisH, ν(C=C); Asp, $\nu_{as}(COO^-)$
1550-1510	N-H, secondary amide
1504	C=C, aromatic
1474	δas (CH_3)
1449	Pro, ν(C-N)
1405	Glu, $\nu_s(COO^-)$; Asp, $\nu_s(COO^-)$
1352-1361 1334-1342	Trp
1420-1181	Ser
1273-6	Trp; Trp-O^-
1244	RNA $\nu_{as}(PO_2^-)$
1218	RNA C-H, ring bend
1184	RNA $\nu_s(PO_2^-)$
1160	RNA ribose, ν(C-O)
1120	RNA ribose, ν(C-O)
1060	RNA ribose, ν(C-O)
1043	RNA ribose, ν(C-O)

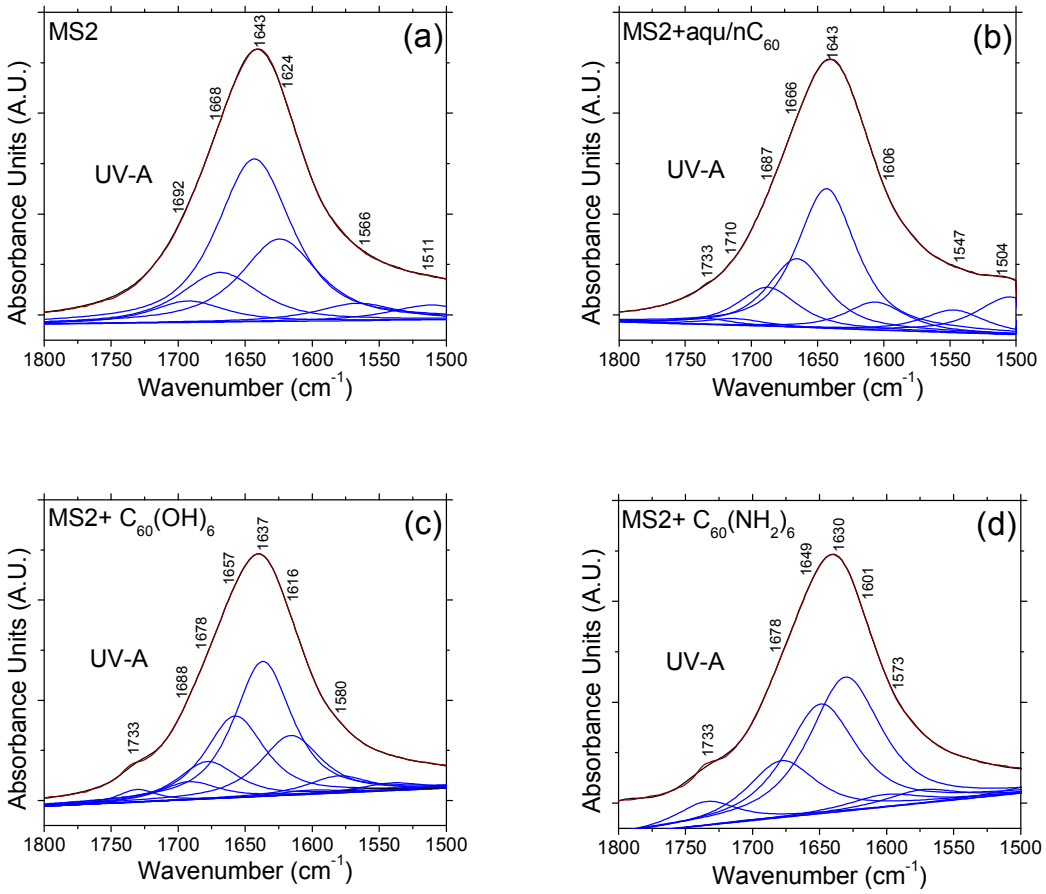

Figure 41: ATR-FTIR spectra of MS2 alone and MS2+fullerenes after UV-A exposure for 5 minutes showing evidence for carbonyl content and protein secondary structures.

Figure 41 shows the peak fits of amide I band of MS2 in the mid-infrared regions. This region specially represents all the vibrational frequencies associated with protein secondary structures.

Table 10: Location of amino acids (AA) on A- and coat-protein sequences that have the potential to react with $^1O_2$ at high second order reaction rates at physiological pH 7.1 [273, 373]

Protein sequence	No. of AA targets (A–protein+ coat protein) for $^1O_2$; approx. 2^{nd} order rate constants, $M^{-1}s^{-1}$; neutral pH
A-protein (1 copy/MS2) (GeneBank: ACV72076.1)	A-protein+ coat protein
1 mrafstldre netfvpsvrv yadgetedns fslkyrsnwt pgrfnstgak tkqwhypspy 61 srgalsvtsi dqgaykrsgs swgrpyeeka gfgfsldars cyslfpvsqn ltyievpqnv 121 anrastevlq kvtqgnfnlg valaearsta sqlatqtial vkaytaarrg nwrqalryla 181 lnedrkfrsk hvagrwlelq fgwlplmsgi qgayemltkv hlqeflpmra vrqvgtnikl 241 dgrlsypaan fqttcnisrr iviwfyinda rlawlsslgi lnplgivwek vpfsfvvdwl 301 lpvgnmlegl tapvgcsyms gtvtdvitge siisvdapyg wtverqgtak aqisamhrgv 361 qsvwpttgay vkspfsmvht ldalalirqr lsr	5+0: h (Histidine); k= $3.2x10^7$ 12+360: w (Tryptophan); k=2-$7x10^7$ (physical reaction) k=$3x10^7$ (chemical reaction) 16+720: y (Tyrosine); k=$0.8x10^7$ 8+360: m (Methionine); k=$1.6x10^7$ 3+360: c (Cysteine); k=$8.9x10^6$ All other amino acids: k <$0.7x10^7$
Coat protein (180 copies/MS2) (GeneBank: ACY07219.1)	
1 masnftqfvl vdnggtgdvt vapsnfangv aewissnsrs qaykvtcsvr qssaqnrkyt 61 ikvevpkvat qtvggvelpv aawrsylnle ltipifatns dcelivkamq gllkdgnpip 121 saiaansgiy	

Detailed Procedure of OxyBlot Protein Oxidation Assay.

The protocol provided by the manufacturer was adapted for quantification of protein oxidation products, specifically carbonyl groups formed by the reactions of $^1O_2$ with amino-acid side chains on MS2. Prior to quantifying the protein carbonyl, the MS2 samples from various treatments (at 5 min) were separately pooled together and concentrated to get a total protein concentration to between 3–4 μg μL^{-1}. The total amount of proteins was measured using the Modified Lowry Protein Assay Kit (Pierce Biotechnology, Rockford, IL) with bovine serum albumin (BSA) standards. The protein concentration was calculated by measuring the absorbances at 750 nm using UV-vis spectrophotometer. The procedure is as follows: 5 μl protein samples (3.5 μg μL^{-1}) were

first denatured using 5 μl 12% SDS and then mixed with 1x 2,4-dinitrophenylhydrazine (DNPH) incubated for 15 min during which 2,4-dinitrophenylhydrozone (DNP-hydrazone) derivative was formed upon reaction with carbonyls. After 15 min, the reaction was stopped by adding 7.5 μl of neutralization solution. A negative control was also prepared as described without protein. The derivatized proteins were separated into individual proteins by 12% sodium dodecyl sulfate polyacrylamide electrophoresis followed by Western blotting. The protein bands were transferred onto a PVDF membrane filter and then incubated first with the primary antibody (rabbit anti-DNP antibody) and then with secondary antibody (goat anti-rabbit IgG (horseradish peroxidase-conjugated). The filters were then treated with chemiluminescent reagents (luminol and enhancer). The luminol was converted to the light-emitting form at wavelength 428 nm by the antigen/primary antibody/secondary antibody/peroxidase complex (bound to the membrane) in a H_2O_2 catalyzed oxidation reaction. The light was detected by short exposure to blue light sensitive films. The oxidative status of each protein was then analyzed quantitatively by comparing the signal intensity of the same protein in different lanes on the same gel.

SDS-PAGE.

SDS-PAGE was performed using standard Laemmli gel method [375] to examine $^1O_2$ induced modifications in phage capsid proteins. Pre-cast SDS/12% (w/v) polyacrylamide gels (Tris-glycine gels) for the BioRad gel apparatus systems used

according to the manufacturer's instructions. The Tris-glycine running buffers and sample buffers were purchased from Invitrogen (Carlsbad, CA, USA). Phage samples were diluted by 50% (v/v) in 2x Tris-glycine sample buffer, incubated at 85 ^{o}C for 2 min, and then loaded directly into the wells on the gel. Each well contained 8 μg of protein. Electrophoresis was carried out for 2-3 h at 30 mA/gel and the gels were stained with 0.1% Coomassie brilliant blue R250 solution according to manufacturer's instructions and photographed.

Protein conformational changes are due to the oxidation by $^{1}O_2$

Figure 42 shows SDS–PAGE analysis of phage proteins obtained from various treatments: (1) MS2 in dark, (2) MS2+$C_{60}(NH_2)_6$ in dark, (3) MS2+UV-A, (4) MS2+$C_{60}(NH_2)_6$+UV-A, (5) MS2+$C_{60}(OH)_6$+UV-A, (6) MS2+aqu-nC_{60}+UV-A, and (7) MS2+$C_{60}(NH_2)_6$+β-carotene+UV-A. MS2 was mainly composed of A-protein (molecular mass: 44,000 Da) and coat protein (13,700 Da). Similar mobilities of A- and coat-protein in lanes B and C indicate that $C_{60}(NH_2)_6$ in dark had no effect on MS2, which is consistent with dark inactivation results under these conditions. The A- and coat-protein bands in lanes D and H are present at slightly higher location (indicates higher molecular mass) on the gel suggesting that UV-A alone could induce cross–linkages in proteins. Protein bands in Lanes E (or I), F and G appears to migrate slower when compared with the bands in Lanes B or C, which is due to oxidation by $^{1}O_2$. Note that A–protein in Lane E exhibits a higher molecular mass (> 44 KDa) than any other proteins in other lanes.

Similarly, A-proteins in Lanes F and G showed masses > 44 KDa but lower than the mass of A–protein in Lane E. Coat proteins in Lanes E (or I) F and G showed masses between 14.7–21.5 KDa, which is a consequence of oxidative damage by $^1O_2$.

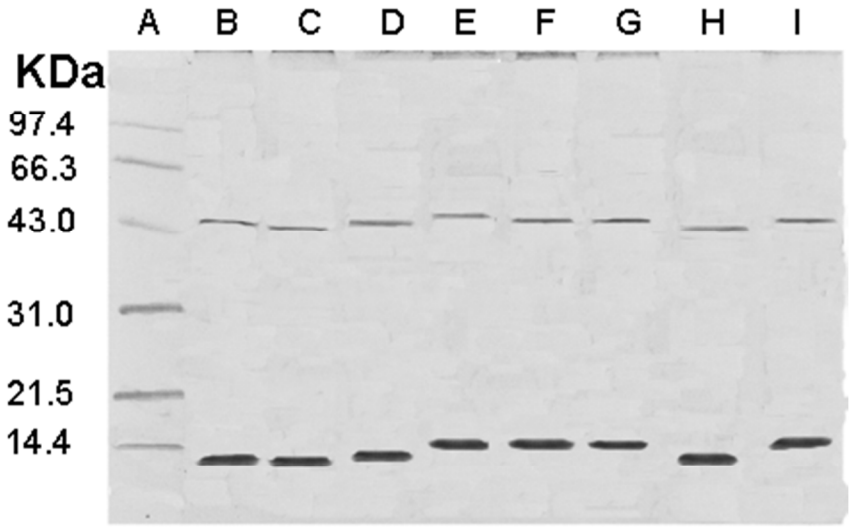

Figure 42: Analysis by SDS-PAGE showing the altered migrations of MS2 capsid proteins (A-protein and coat protein) following exposure to UV-A sensitized $^1O_2$. Lane A: molecular mass markers; Lane B: MS2 in Dark; Lane C: MS2+$C_{60}(NH_2)_6$ in dark; Lane D: MS2+UV-A; Lane E: MS2+ $C_{60}(NH_2)_6$+UV-A; Lane F: MS2+$C_{60}(OH)_6$+UV-A; Lane G: MS2+aqu-nC_{60}+UV-A; Lane H: MS2+ $C_{60}(NH_2)_6$+β-carotene+UV-A; Lane I: MS2+ $C_{60}(NH_2)_6$+UV-A

Appendix B – Supporting information for Chapter 4.2: Influence of Inorganic Anions on the Reactivity of TiO_2 Nanoparticles

Radiation intensity as a function of emission wavelength at the upper liquid surface

The emission spectrum of the UV lamps, as provided by the manufacturer, was used to determine the radiation intensity as a function of the emission wavelength at the liquid upper surface of the samples. Results are reported in Figure 43. A normal distribution with mean 365 nm and standard deviation 10 nm was assumed for Philips TL-D 15W BLB SLV spectrum. Radiometric readings were corrected by taking into account the spectral response of the sensor, as suggested in [376].

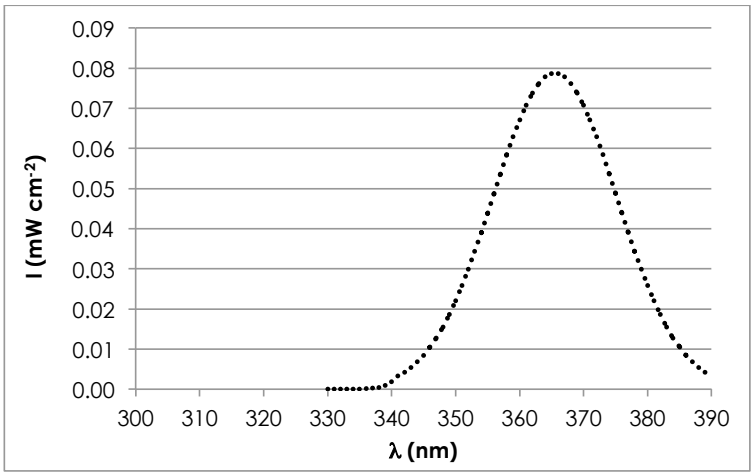

Figure 43: Radiation intensity vs. emission wavelength at the upper liquid surface of samples.

Characterization of size distribution of TiO_2 aggregates as a function of operating conditions

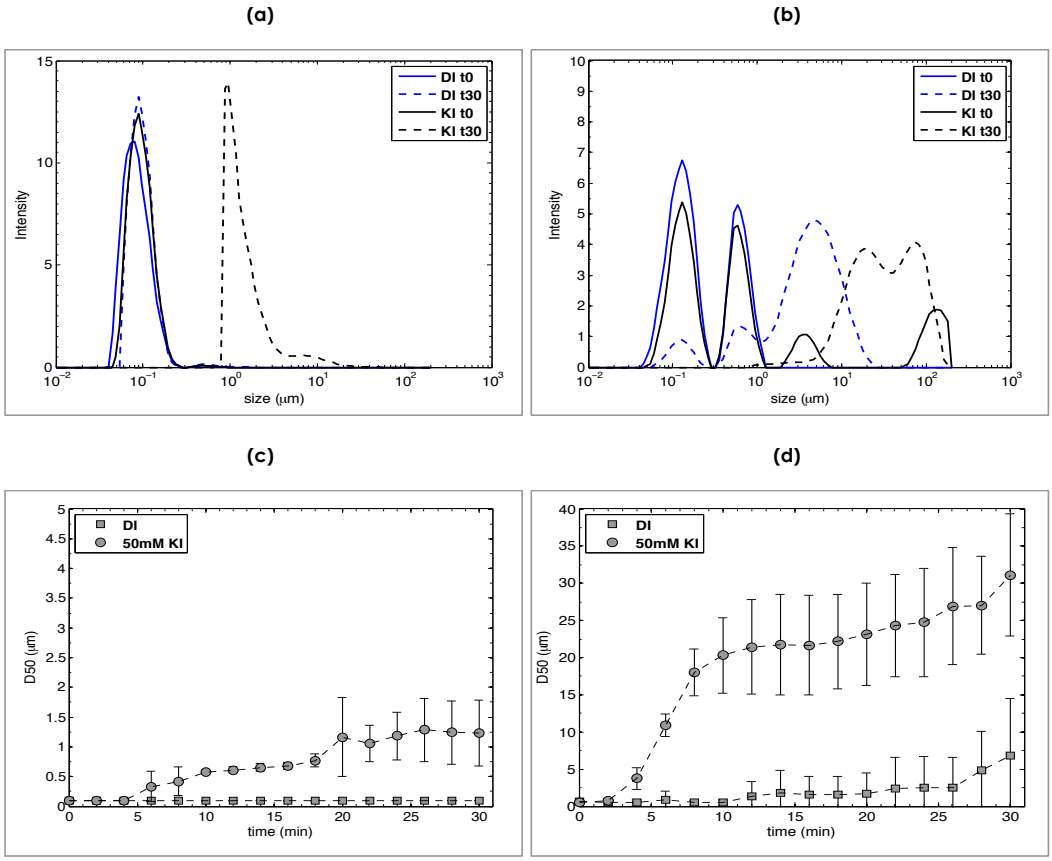

Figure 44: TiO_2 aggregate size as a function of KI concentration (0, 50 mM) at various times (0, 30 min) (a,b). TiO_2 aggregate D_{50} vs. time as a function of KI concentration (0, 50 mM) (c, d). Experimental results are expressed both as number weighted (a, c) and volume weighted (b, d).

Aggregation of TiO_2 NPs in inorganic anions

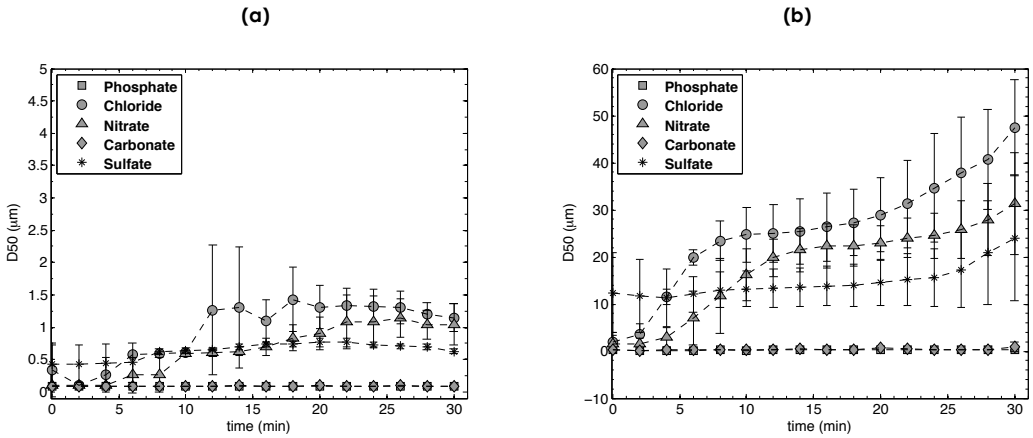

Figure 45: TiO_2 aggregate size over 30 minutes as a function of anion at 0.5mM, (a) number weighted D_{50}, and (b) volume weighted D_{50}.

(a) - Carbonate

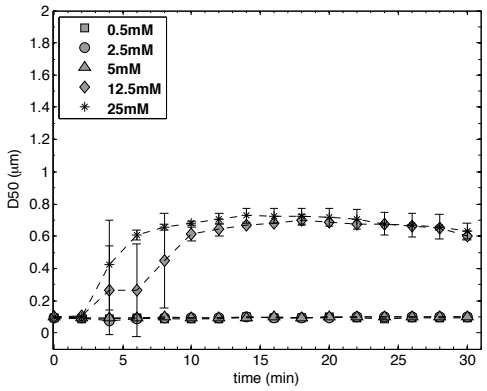

(b)

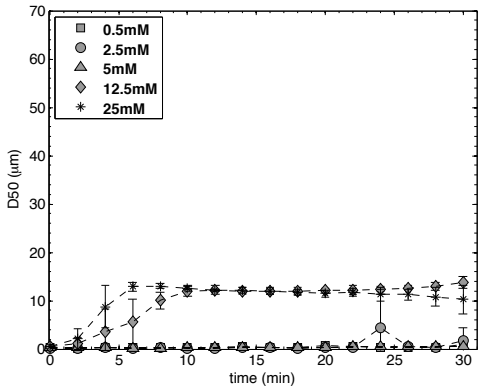

(c) - Phosphate

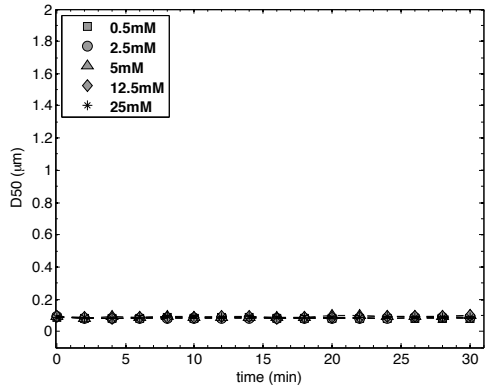

(d)

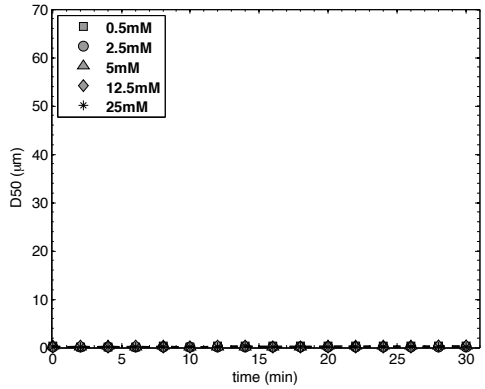

(e) - Nitrate

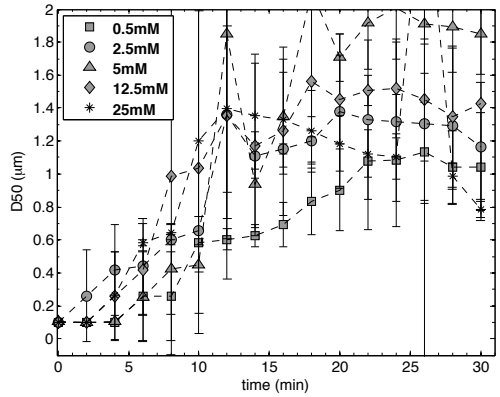

(f)

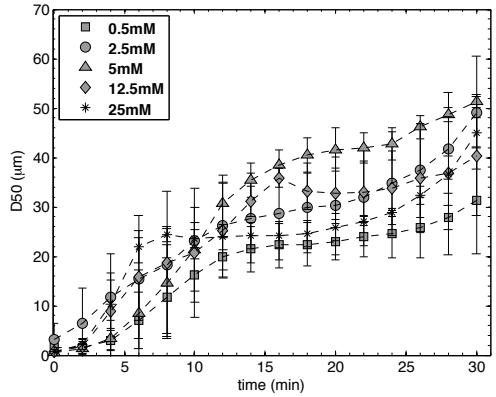

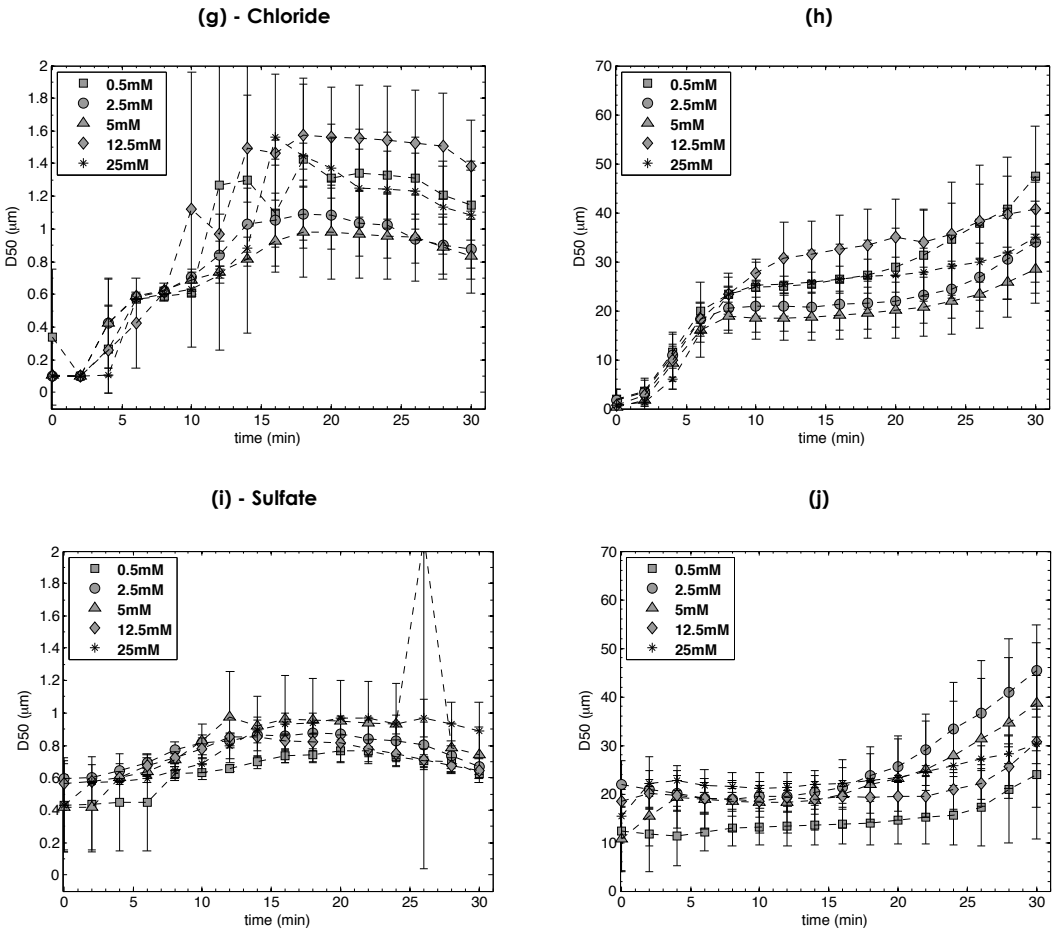

Figure 46: TiO_2 aggregate size over 30 minutes as a function of anion concentration, (a, c, e, g, i) number weighted D_{50} and (b, d, f, h, j) volume weighted D_{50}.

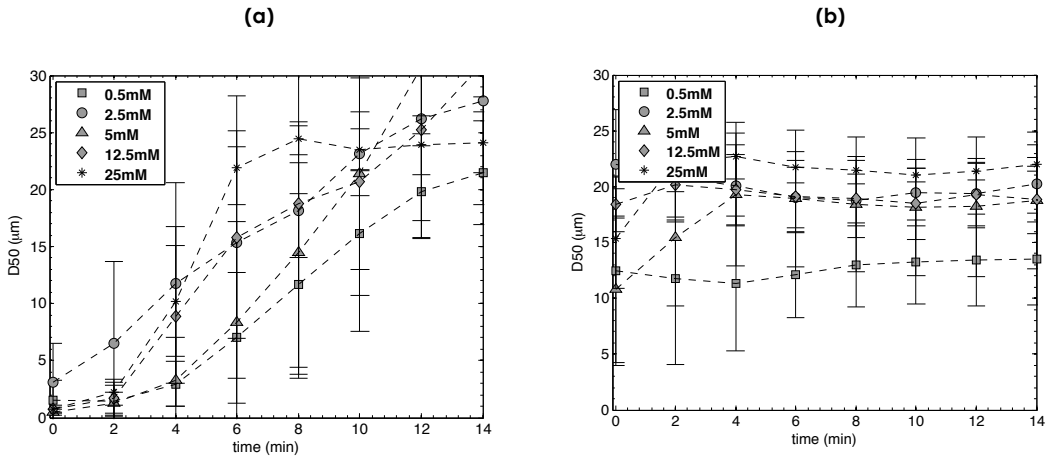

Figure 47: TiO_2 aggregate size over 14 minutes as a function of anion concentration, volume weighted D_{50} for (a) nitrate and (b) sulfate.

Gouy Chapman Calculations

DLVO potential energy curves were calculated using the Gouy Chapman approximation for two identical spheres, in which electrostatic repulsion, Φ_r, and Van der Waals attraction, Φ_a, can be calculated as follows:

$$\phi_r = \frac{32\pi\varepsilon k_B^2 T^2 \gamma_0^2 a}{e^2 z^2} e^{-\kappa x} \qquad \text{(Eq 41.)}$$

and

$$\phi_a = -\frac{A}{6}\left[\frac{2}{s^2-4} - \frac{2}{s^2} + \ln\left(\frac{s^2-4}{s^2}\right)\right] \qquad \text{(Eq 42.)}$$

Where

$$s = \frac{2a+x}{a} \qquad \text{(Eq 43.)}$$

and

$$\gamma_0 = \frac{\exp\left[\frac{2e\psi_0}{2k_BT}\right]-1}{\exp\left[\frac{2e\psi_0}{2k_BT}\right]+1} \qquad \text{(Eq 44.)}$$

Here, ε is the dialectric constant ($\varepsilon = \varepsilon_0 * \varepsilon_r$), k_B is the boltzman constant, T is temperature, a is the radius of the particle, x is the separation distance, A is the hammaker constant for TiO_2 ($A = 60 \times 10^{-21}$ J), e is the charge of an electron, I is the ionic strength, Ψ_0 is the surface potential (assumed to be equal to the measured zeta potential), and κ is the inverse debeye length, calculated as

$$\kappa^{-1} = \sqrt{\frac{\varepsilon k_B T}{2N_A e^2 I}} \approx \frac{0.304}{\sqrt{I}} \qquad \text{(Eq 45.)}$$

Calculations were performed for TiO_2 in the 1:1 electrolyte KCl from 0.5 to 25 mM. As the ionic strength increases, the zeta potential at pH 7.8 diminishes in magnitude (see Figure 50 (c), and compression of the double layer is observed, resulting in wholly negative potential energies for the highest two concentrations. Ionic strengths for which the zeta potential was not measured were estimated from available data.

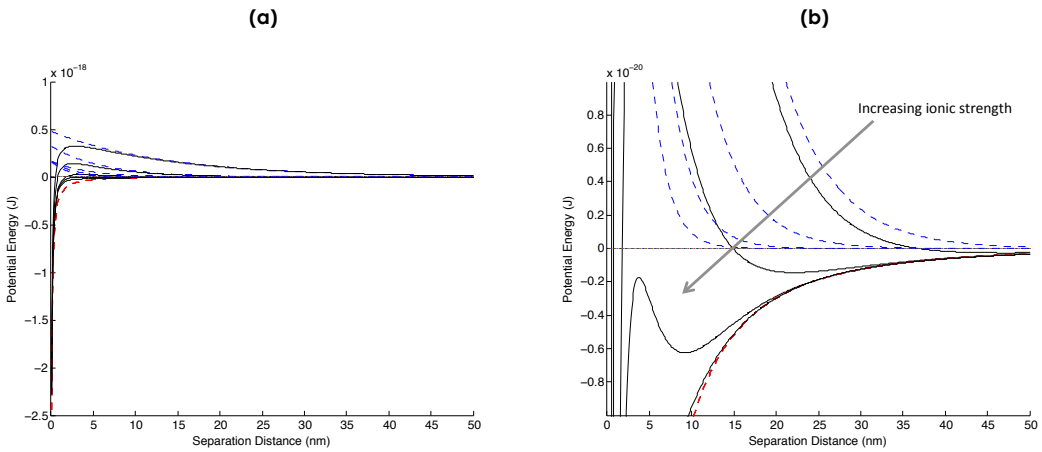

Figure 48: Potential energy curves of DLVO theory using the Gouy Chapman approximation for 20 mg L^{-1} TiO_2 as a function of KCl concentration (0.5 – 25 mM). (a) Full plot and (b) detail. Blue dashed lines are electrostatic repulsion, red dashed lines are Van der Waals attraction, and black solid lines are the summation of repulsive and attractive forces for a given ionic strength.

Fractal Dimension of TiO_2 NPs

(a) – 0.5mM Carbonate

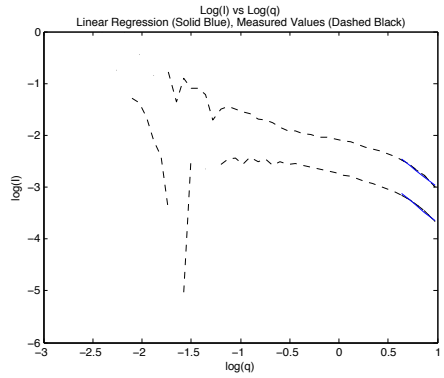

(b)

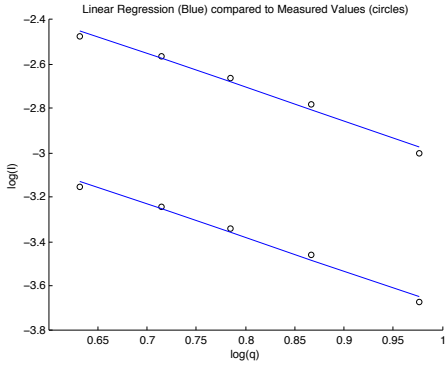

(c) – 25mM Carbonate

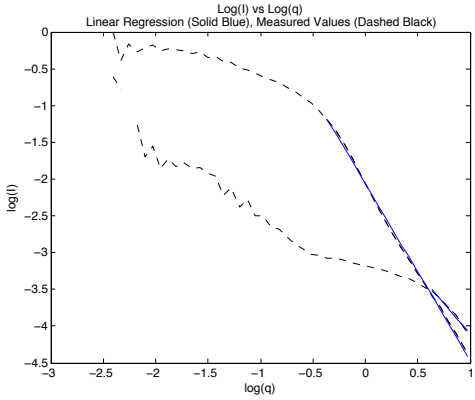

(d)

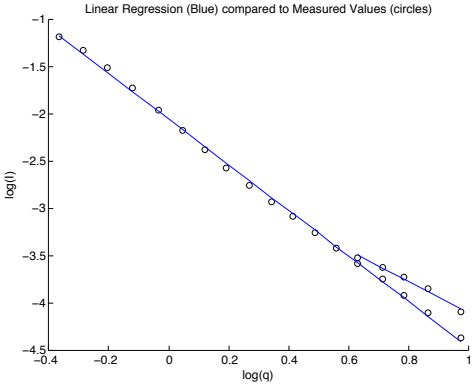

(e) – 0.5mM Phosphate

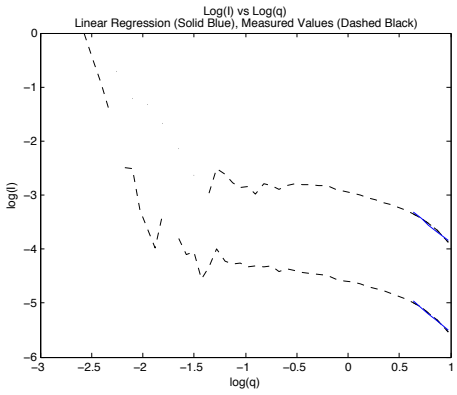

(f)

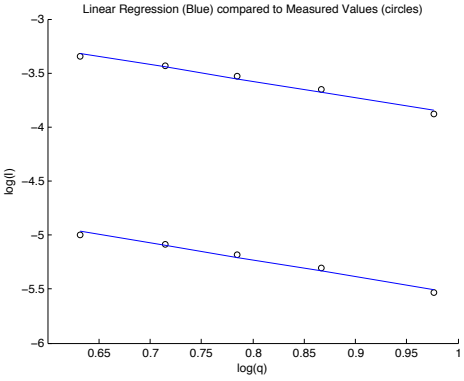

(g) – 25mM Phosphate

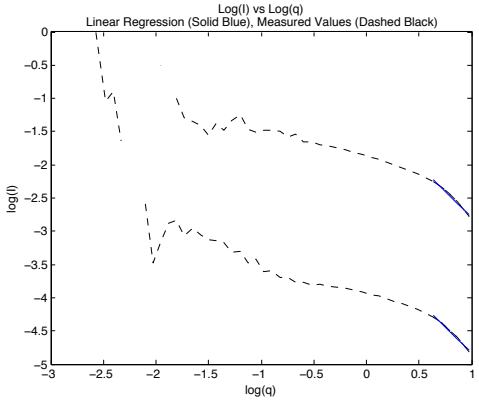

(h)

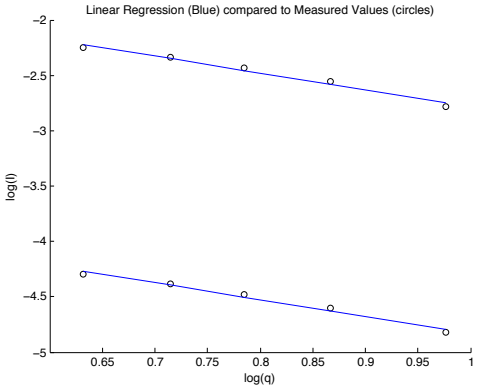

(i) – 0.5mM Chloride

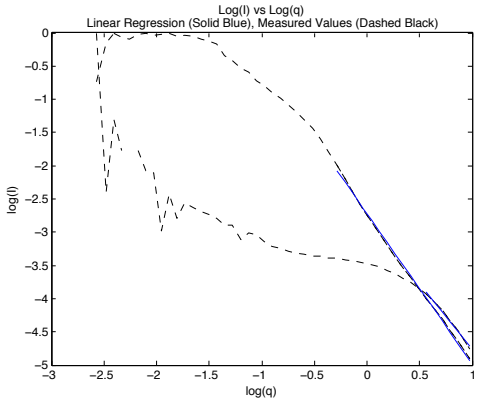

(j)

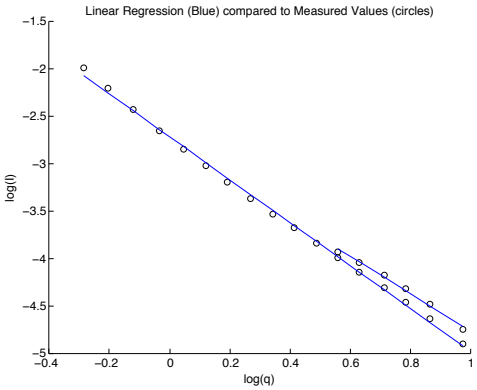

(k) – 25mM Chloride

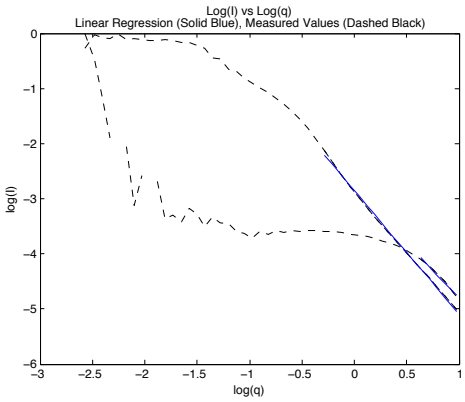

(l)

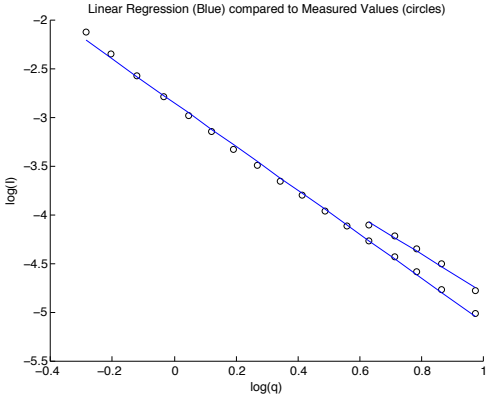

(i) – 0.5mM Nitrate

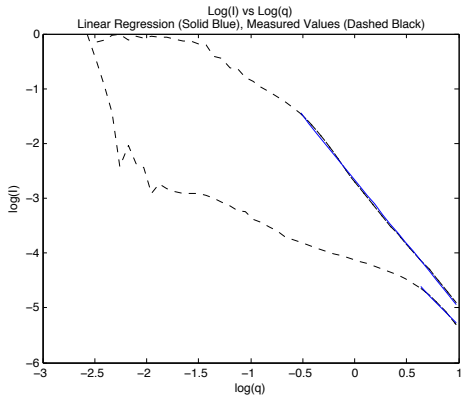

(j)

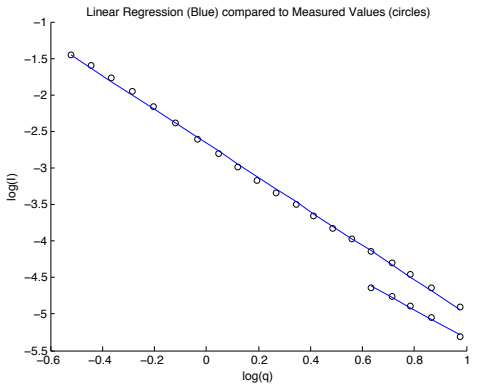

(i) – 25mM Nitrate

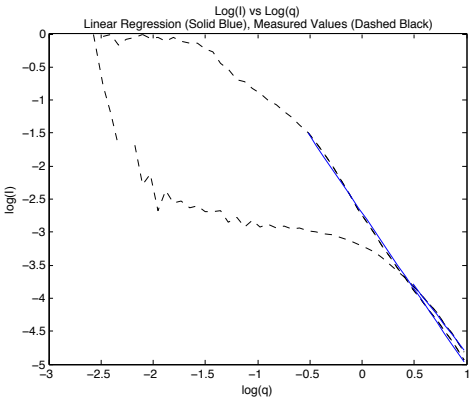

(j)

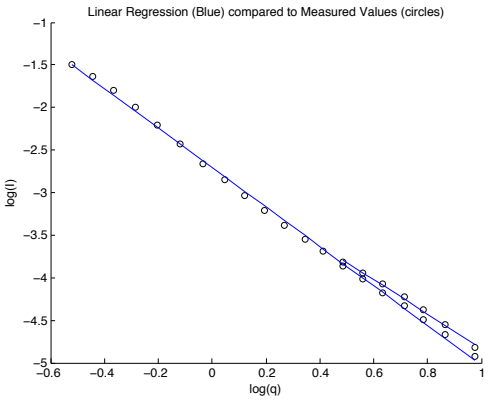

(i) – 0.5mM Sulfate

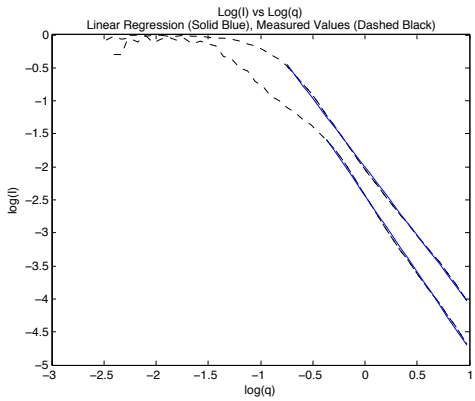

(j)

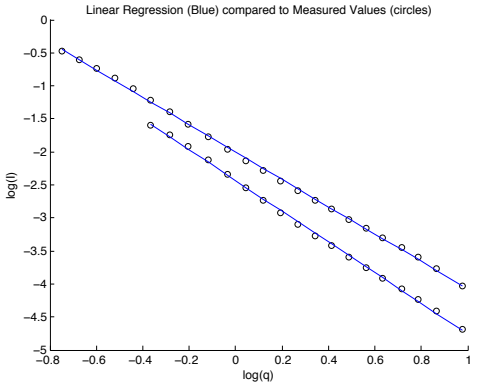

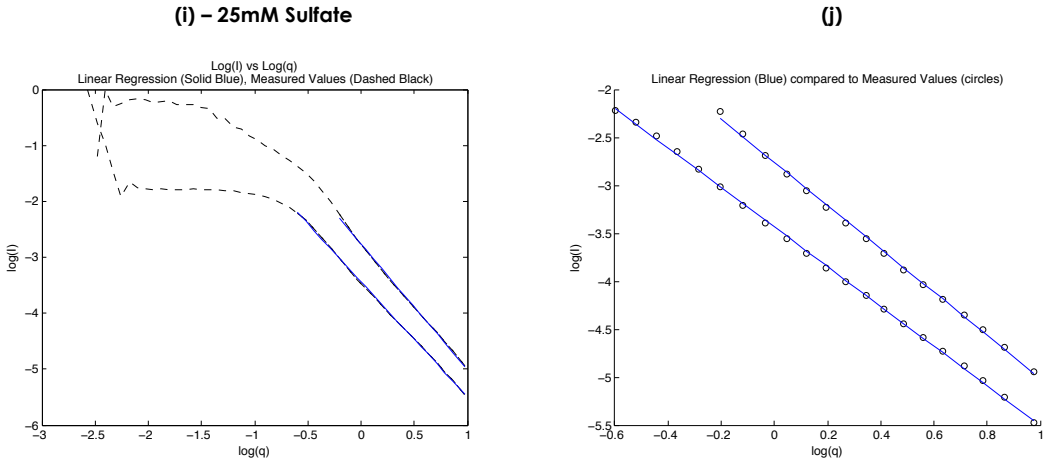

Figure 49: Representative SLS data and calculated fits at 0 and 30 minutes for each anion.

Zeta potential versus pH as a function of anion concentration

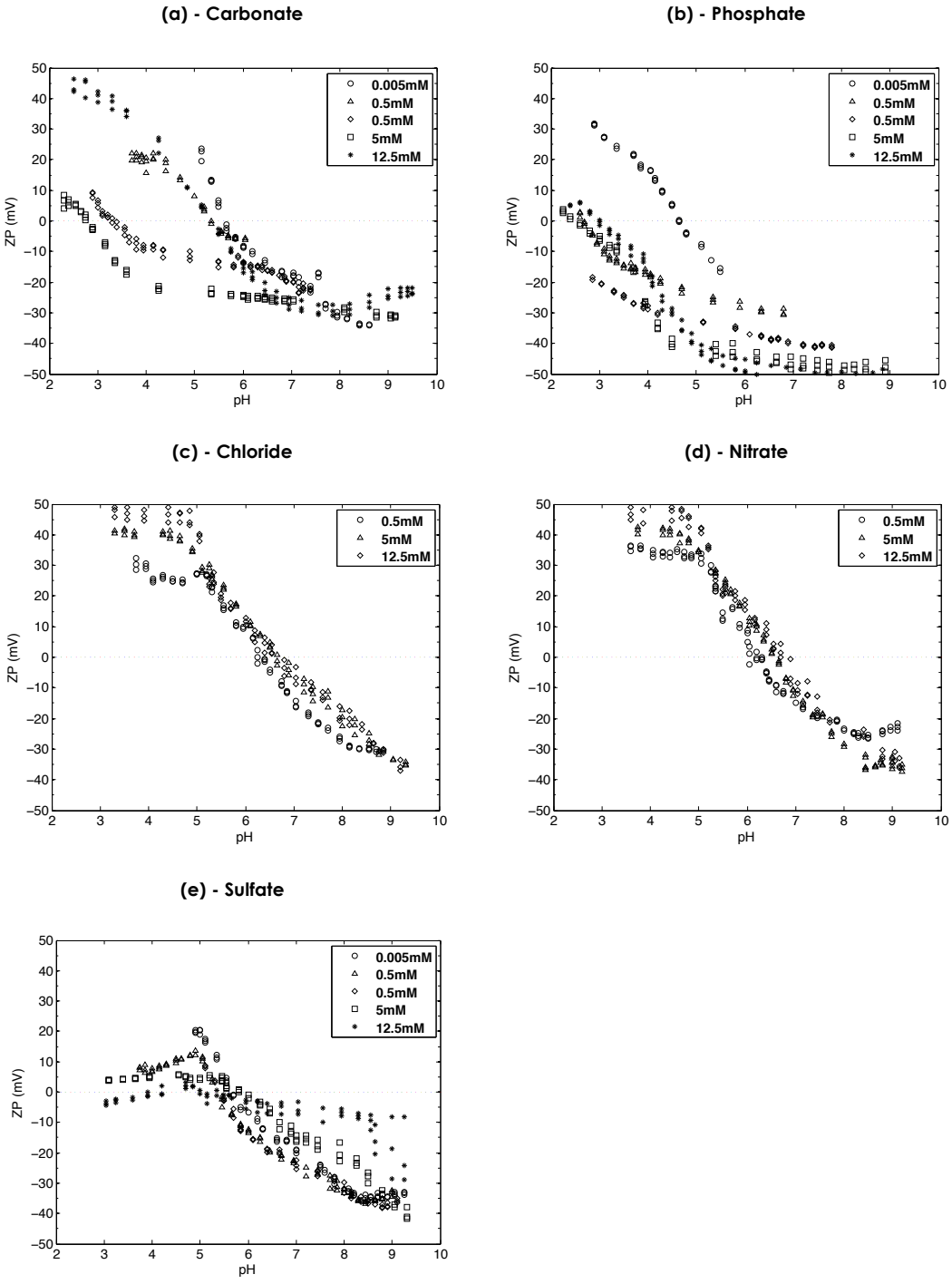

Figure 50: Zeta potential vs. pH as a function of anion concentration

Influence of initial iodide concentration on hole detection

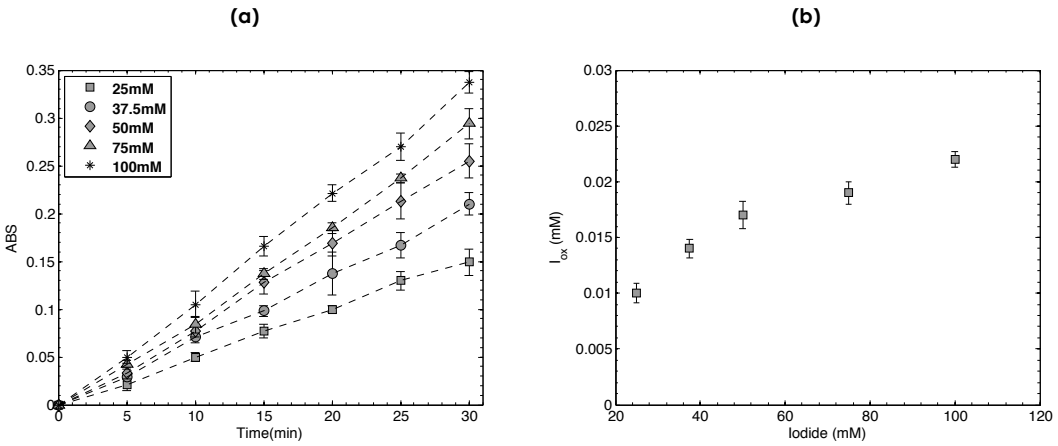

Figure 51: (a) Absorption from iodo-starch method vs. time as a function of initial iodide concentration and (b) photogenerated hole detection (measured as oxidized iodide concentration) after 30 minutes irradiation versus initial concentration.

Time series for iodide oxidation as a function of inorganic anion concentration

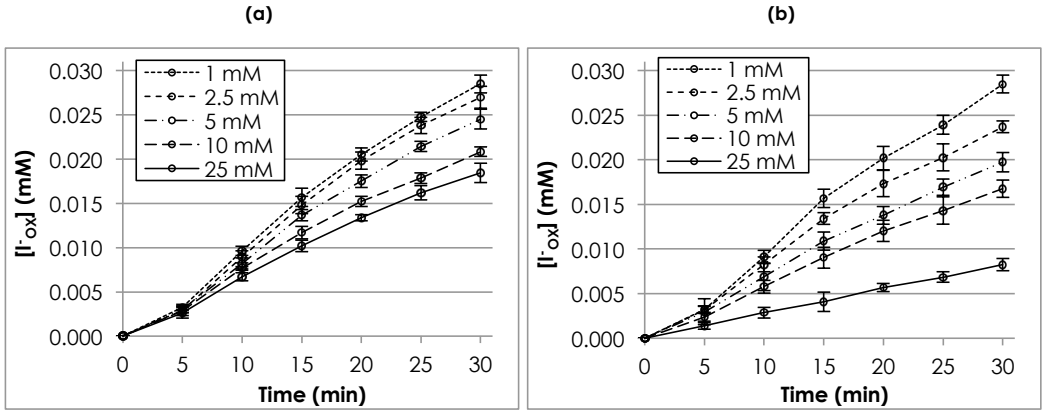

Figure 52: Oxidized iodide concentration (mean±std) vs. time as a function of inorganic anion concentration: (a) carbonate and (b) phosphate.

Langmuir-Hinshelwood linearization procedure for K_A and k_R constants estimation

By neglecting the presence of inorganic anions other than iodide, Equation 33 in Chapter 4.2 can be simplified and expressed showing the linear relationship between the

inverse of initial reaction rate and the inverse of initial iodide concentration, as follows [313]:

$$\frac{1}{r_0} = \frac{1}{K_{A,I^-} K_R} \frac{1}{[I^-]_0} + \frac{1}{K_R} = m \frac{1}{[I^-]_0} + q \qquad \text{(Eq 46.)}$$

With

$$K_R = \frac{1}{q} \qquad \text{(Eq 47.)}$$

and

$$K_A = \frac{q}{m} \qquad \text{(Eq 48.)}$$

The rate r_0 is obtained from experimental data by calculating the oxidized iodide concentration for each $[I^-]_0$ over time. K_A and K_R values were calculated by fitting experimental data shown with a linear regression, estimating m and q values by the least squares method, as in Figure 53.

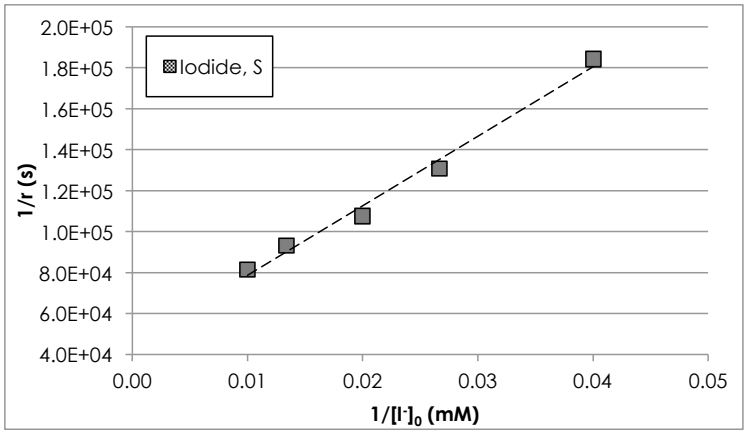

Figure 53: Experimental data linear regressions (1/r vs 1/[I-]$_0$) for iodide adsorption via Langmuir-Hinshelwood mechanism for sonicated TiO_2.

Equation 33 in Chapter 4.2 can be transformed so as to highlight the linear relationship between the inverse of the initial reaction rate and the initial inorganic anion concentration, as it follows [286]:

$$\frac{1}{r_0} = \frac{K_{A,Anion}}{K_{A,I^-} K_R [I^-]_0} [Anion]_0 + \frac{1 + K_{A,I^-}[I^-]_0}{K_{A,I^-} K_R [I^-]_0} = m[Anion]_0 + q \qquad \text{(Eq 49.)}$$

With

$$K_R = \frac{1 + K_{A,I^-}[I^-]_0}{qK_{A,I^-}[I^-]_0} \qquad \text{(Eq 50.)}$$

and

$$K_A = m \cdot K_R K_{A,I^-} [I^-]_0 \qquad \text{(Eq 51.)}$$

Experimental values at 0 and 12.5 mM were neglected in calculations because of the modifications on TiO_2 suspension characteristics. Results for linearization of experimental data by the proposed procedure are reported in Figure 54.

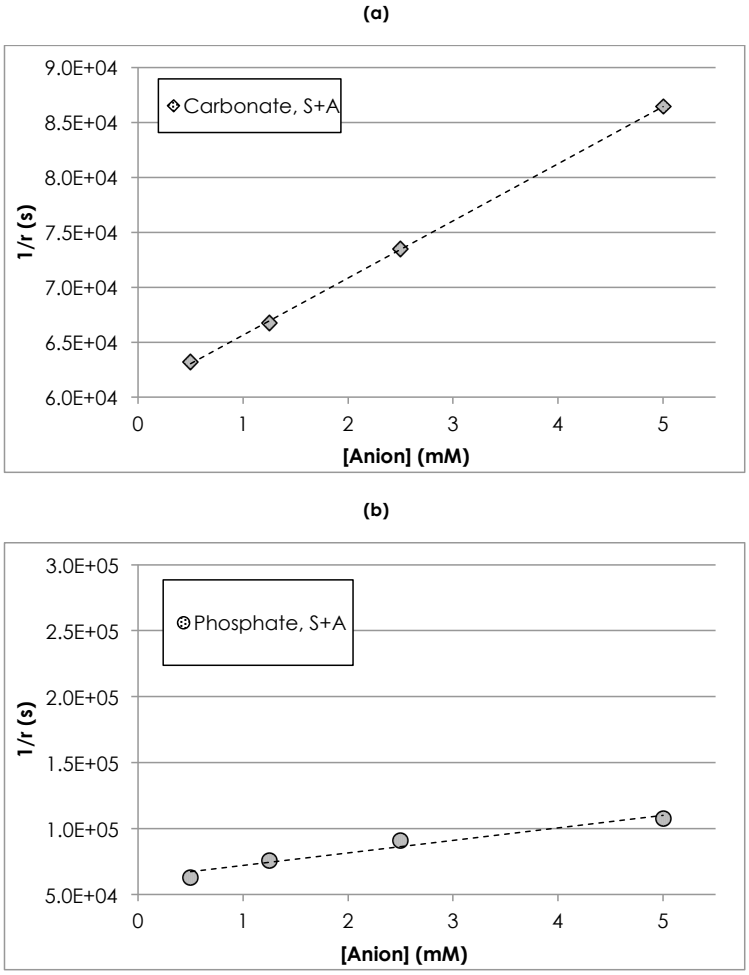

Figure 54: Experimental data linear regressions (1/r vs. [Anion]) for the competitive adsorption of inorganic anions with iodide via Langmuir Hinshelwood mechanism for (a) carbonate and (b) phosphate.

Time Series for terephthalic acid oxidation as a function of inorganic anion concentration

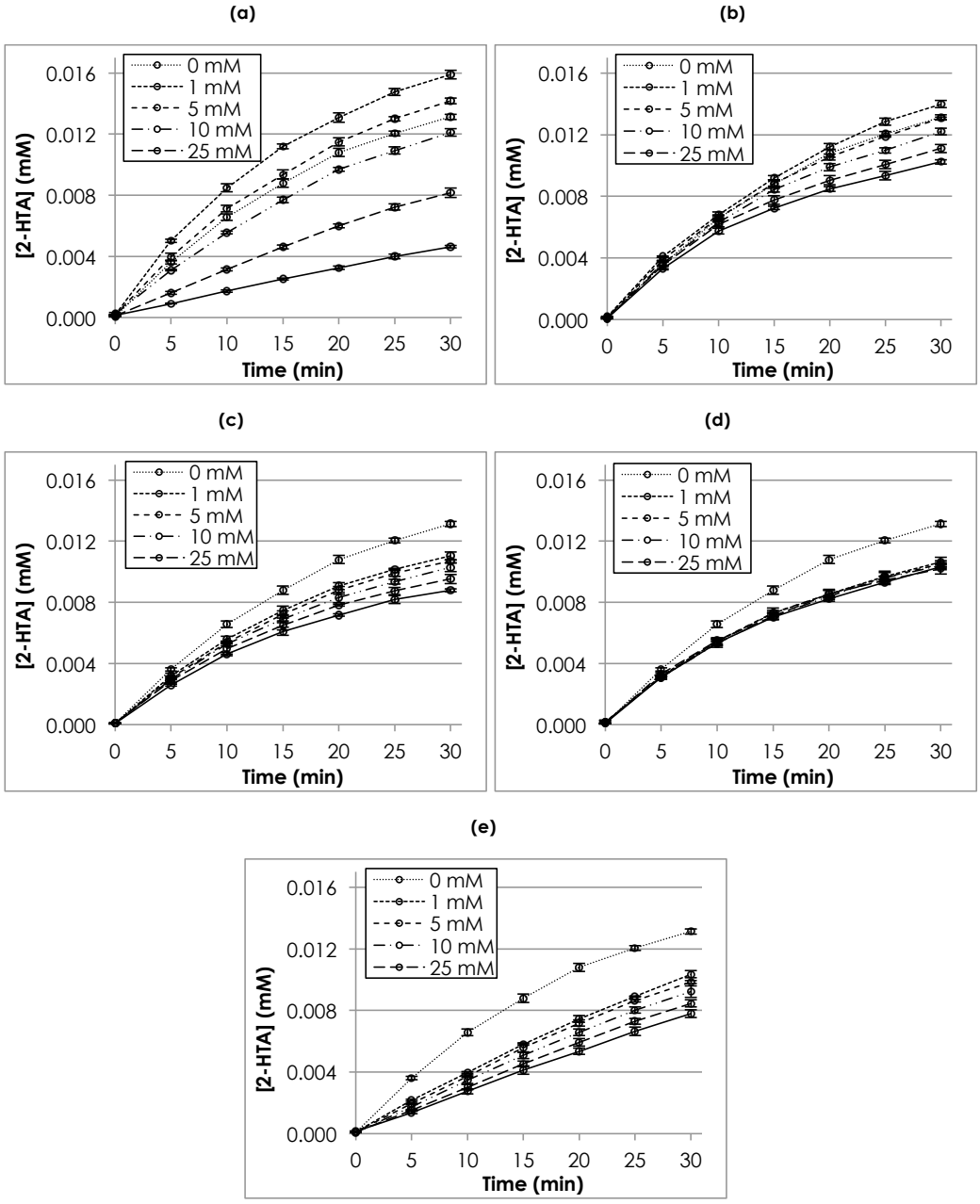

Figure 55: 2-Hydroxyterephthalic acid concentration (mean±std) vs. time as a function of inorganic anion concentration for various anionic species: (a) carbonate, (b) chloride, (c)nitrate, (d) sulfate, and (e) phosphate.

Normalized hydroxyl radical generation as a function of inorganic anion concentration.

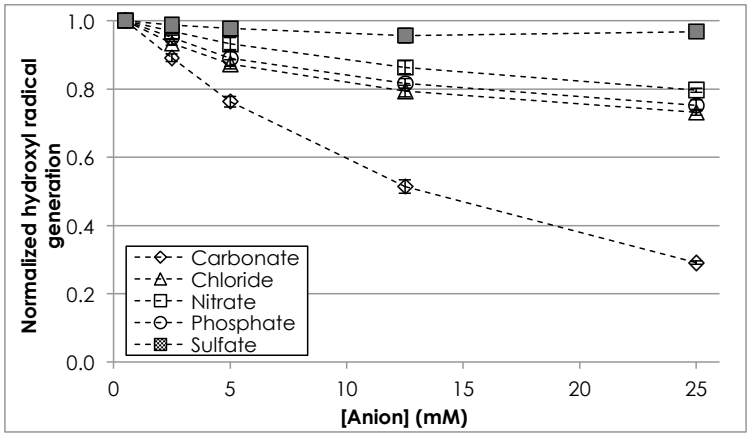

Figure 56: Normalized hydroxyl radical generation vs. inorganic anion concentration after 30 minute irradiation time as a function of anionic species in solution.

Appendix C – Supporting Information for Chapter 4.3: Chlorpyrifos Degradation via Photoreactive TiO_2 Nanoparticles: Assessing the Impact of a Multi-Component Degradation Scenario

TiO_2 Characterization and Reactivity

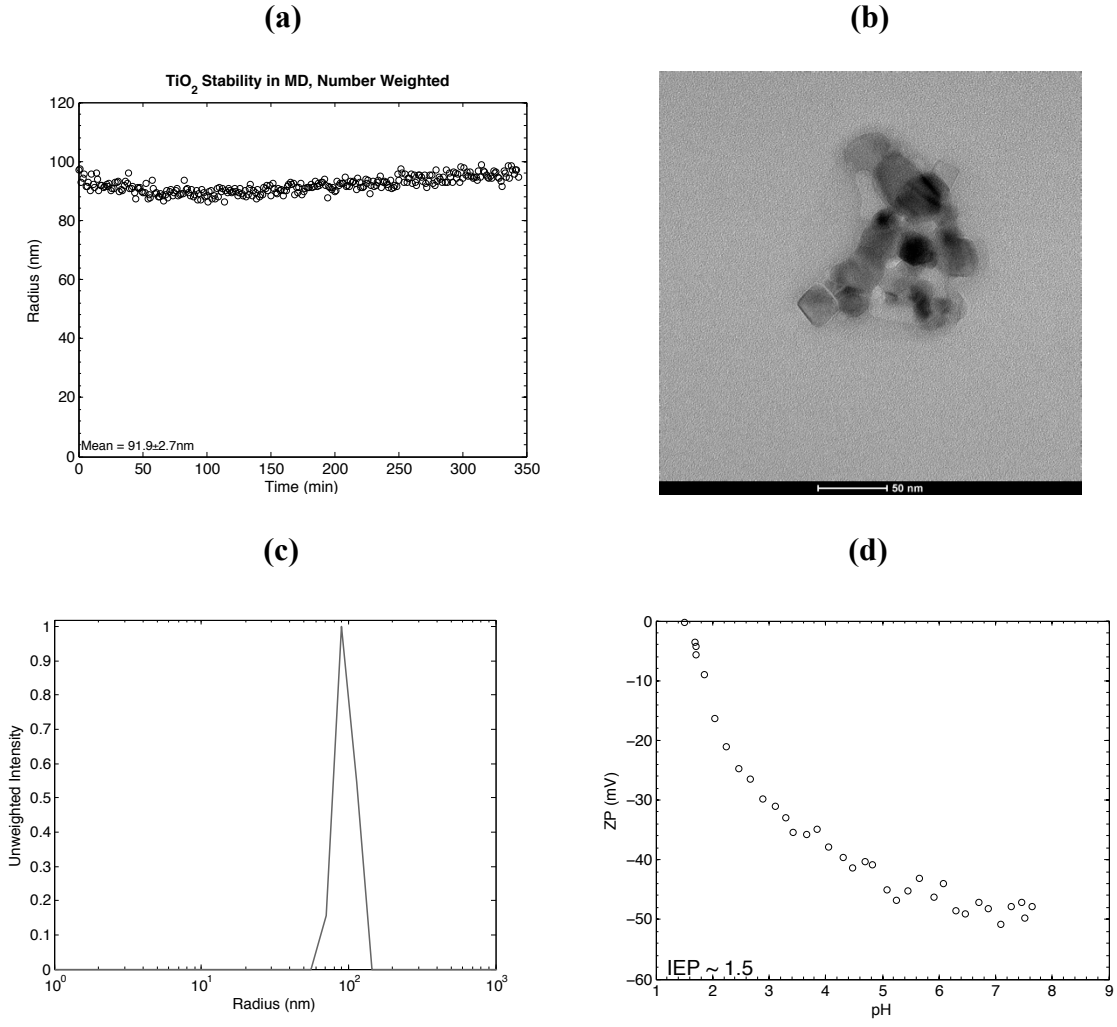

Figure 57: TiO_2 Characterization: (a) time resolved DLS, (b) TEM image of TiO_2 aggregate in MD media; scale bar is 50nm, (c) DLS of TiO_2 in MD media, unweighted, (d) ZP vs. pH of 20 ppm TiO_2 in MD, adjusted with HCl.

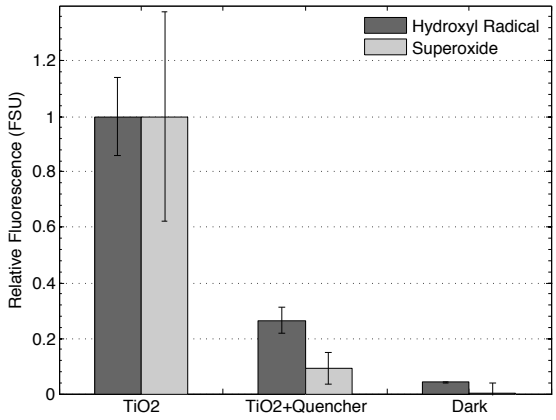

Figure 58: Reactivity measurements of hydroxyl radical and superoxide from 20 ppm TiO_2 in MD exposed to UV, exposed to UV in the presence of quenching agents, and in the dark.

Stability of TiO_2 in CPF

The presence of CPF was not observed to induce TiO_2 aggregation. Time resolved DLS was performed over 200 minutes during which time the aggregate size remained constant.

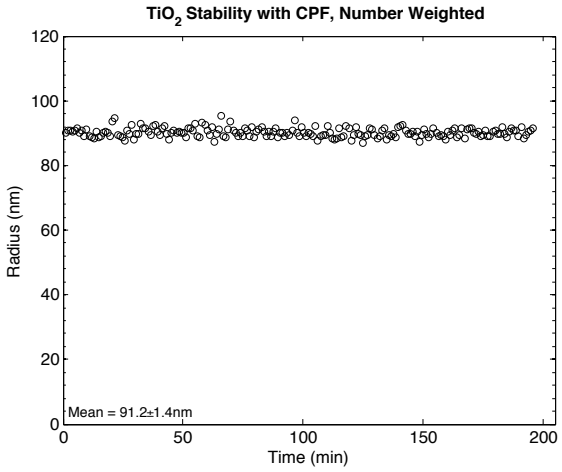

Figure 59: Number weighted TRDLS of 20 ppm TiO_2 in the presence of 385 ppb CPF.

CPF UV/TiO_2 Degradation

CPF can be susceptible to base catalyzed hydrolysis, however no degradation products were observed for any of the dark series. Additionally, the working stock solutions showed no decrease in concentration over time.

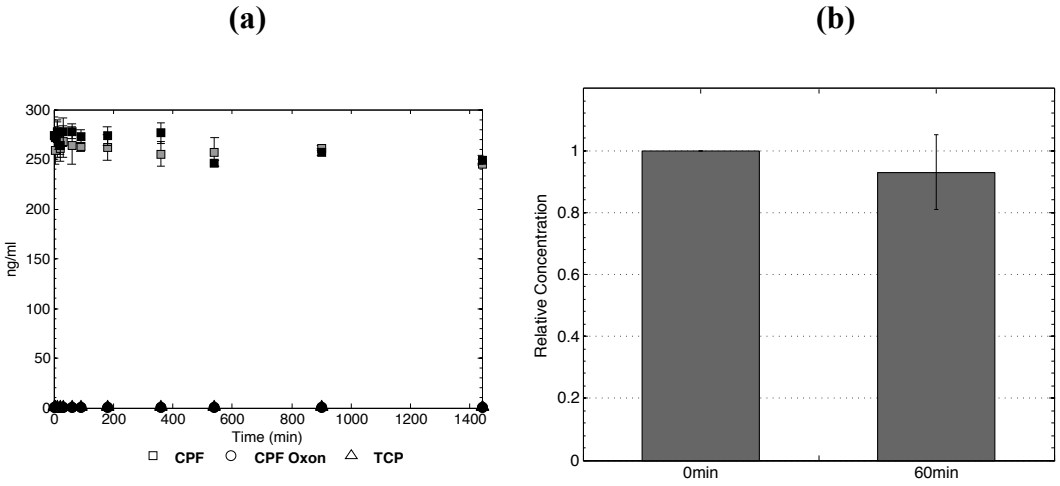

Figure 60: (a) CPF, CPF oxon, and TCP over time in the dark with 0 ppm TiO_2 (grey icons) and 20 ppm TiO_2 (black icons). (b) Relative working stock concentrations measured at 0, 60 minutes in the dark.

Bacterial Inactivation in the Presence of CPF

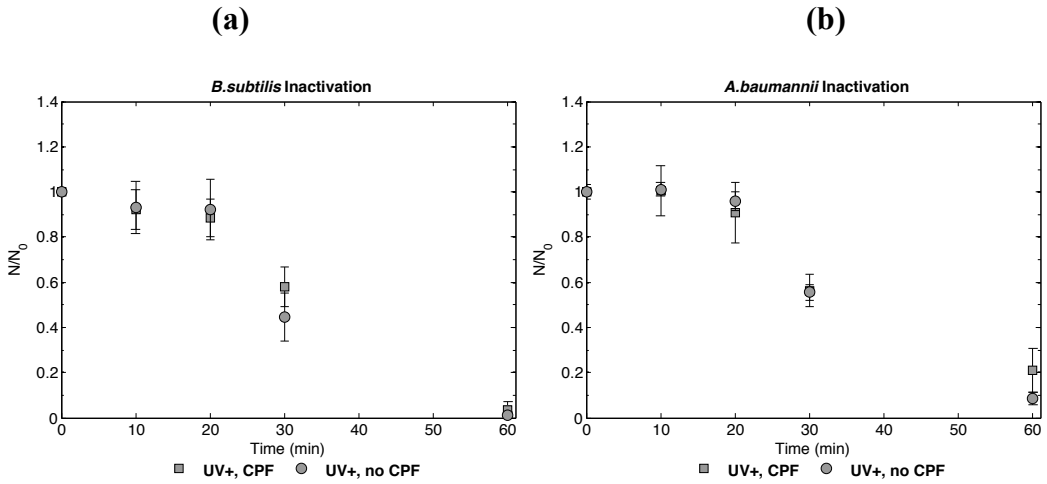

Figure 61: Bacterial inactivation due to 20 ppm TiO_2 exposed to UV in the presence and absence of CPF (a) *B. subtilis* and (b) *A. baumanii*.

CPF Degradation using CAKE Software

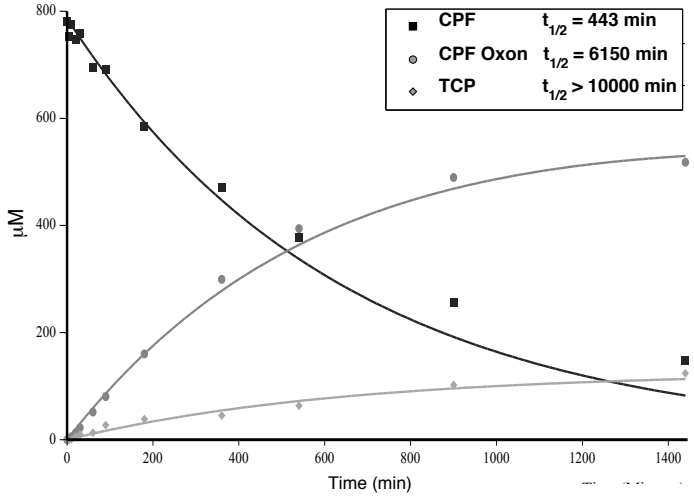

Figure 62: CAKE software fit of CPF, CPF Oxon, and TCP concentration versus time. Calculated half-lives are presented in the inset.

The following data are reported from the CAKE software package using single first order (SFO) kinetic fits of experimental CPF, CPF Oxon and TCP data.

Table 11: Initial values of CAKE sequence parameters

Parameter	Initial Value	Bounds	Fixed
Parent_0	781	0 to (unbounded)	No
k_Parent	0.1	0 to (unbounded)	No
f_Parent_to_A1	0.3333	0 to 1	No
f_Parent_to_B1	0.3333	0 to 1	No
k_A1	0.1	0 to (unbounded)	No
f_A1_to_B1	0.5	0 to 1	No
k_B1	0.1	0 to (unbounded)	No

Table 12: Estimated values from CAKE software.

Parameter	Value	s	Prob. > t	Lower (90%) CI	Upper (90%) CI
Parent_0	786.2	16.73	N/A	757.7	814.7
k_Parent	0.001566	6.30E-005	1.91E-020	0.001459	0.001673
f_Parent_to_A1	0.8393	0.02498	N/A	0.7967	0.8818
k_A1	1.13E-004	4.71E-005	0.01196	3.25E-005	1.93E-004
f_A1_to_B1	1.61E-015	16.33	N/A	-27.81	27.81
k_B1	0	0.008901	0.5	-0.01516	0.01516
f_Parent_to_B1	0.161	0.02491	N/A	0.1186	0.2034

Table 13: $\chi \leq$ the listed values from CAKE software.

Parameter	Error %	Degrees of Freedom
All data	6.87	27
Parent	4.38	10
A1	6.16	9
B1	14.7	8

Table 14: Decay time from CAKE software.

Compartment	DT50 (Minutes)	DT90 (Minutes)
Parent	443	1.47E+03
A1	6.15E+03	>10,000
B1	>10,000	>10,000

Table 15: Additional statistics from CAKE software.

Parameter	r≤ (Obs v Pred)	Efficiency
All data	0.9954	0.995
Parent	0.9972	0.9776
A1	0.9964	0.995
B1	0.9757	0.973

Inactivation due to Degradation Products

No inactivation was seen following up to 60 minutes incubation in 1 μM CPF Oxon or TCP. These concentrations were selected to test inactivation should complete transformation of CPF into either of the degradation products occur, and all samples were performed under dark conditions. The lack of inactivation indicates that neither of the degradation products are acutely toxic to bacteria.

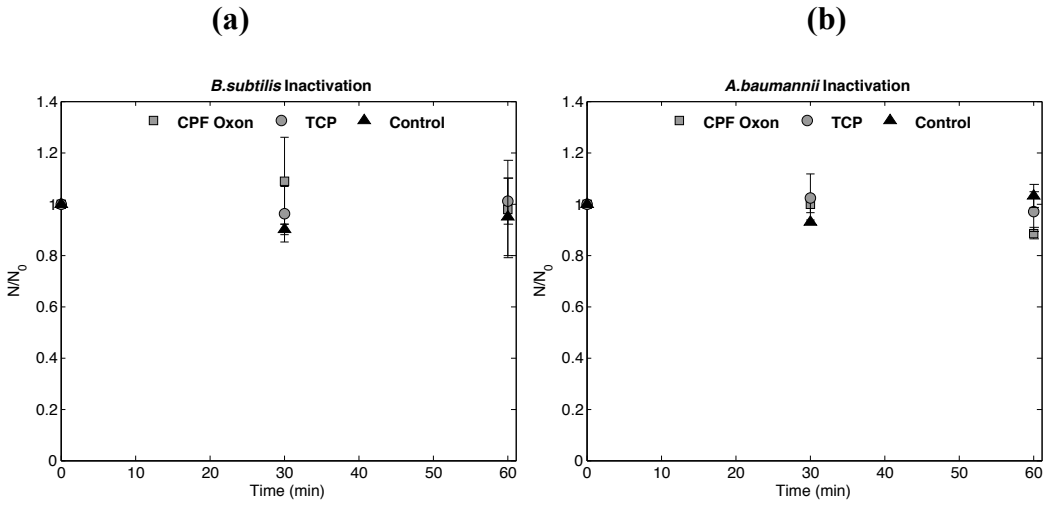

Figure 63: Bacterial inactivation tests under dark conditions in the presence of CPF Oxon and TCP (a) *B. subtilis* and (b) *A. baumanii.*

References

[1] M.F. Hochella, S.K. Lower, P.A. Maurice, R.L. Penn, N. Sahai, D.L. Sparks, B.S. Twining, Nanominerals, mineral nanoparticles, and earth systems, Science, 319 (2008) 1631-1635.

[2] Z. Su, W. Zhou, Y. Zhang, New insight into the soot nanoparticles in a candle flame, Chem Commun, 47 (2011) 4700-4702.

[3] J.L. Gardea-Torresdey, E. Gomez, J.R. Peralta-Videa, J.G. Parsons, H. Troiani, M. Jose-Yacaman, Alfalfa sprouts: a natural source for the synthesis of silver nanoparticles, Langmuir, 19 (2003) 1357-1361.

[4] N.F. Adegboyega, V.K. Sharma, K. Siskova, R. Zboril, M. Sohn, B.J. Schultz, S. Banerjee, Interactions of aqueous Ag+ with fulvic acids: mechanisms of silver nanoparticle formation and investigation of stability, Environ Sci Technol, 47 (2013) 757-764.

[5] A.R. Badireddy, J.F. Budarz, S.M. Marinakos, S. Chellam, M.R. Wiesner, Formation of Silver Nanoparticles in Visible Light-Illuminated Waters: Mechanism and Possible Impacts on the Persistence of AgNPs and Bacterial Lysis, Environ Eng Sci, 31 (2014) 338-349.

[6] F. Kang, P.J. Alvarez, D. Zhu, Microbial extracellular polymeric substances reduce Ag+ to silver nanoparticles and antagonize bactericidal activity, Environ Sci Technol, 48 (2014) 316-322.

[7] M.C. Roco, The long view of nanotechnology development: the National Nanotechnology Initiative at 10 years, J Nanopart Res, 13 (2011) 427-445.

[8] C.O. Hendren, X. Mesnard, J. Droge, M.R. Wiesner, Estimating production data for five engineered nanomaterials as a basis for exposure assessment, Environ Sci Technol, 45 (2011) 2562-2569.

[9] A.A. Keller, A. Lazareva, Predicted Releases of Engineered Nanomaterials: From Global to Regional to Local, Environmental Science & Technology Letters, 1 (2014) 65-70.

[10] J.-Y. Bottero, M. Auffan, D. Borschnek, P. Chaurand, J. Labille, C. Levard, A. Masion, M. Tella, J. Rose, M.R. Wiesner, Nanotechnology, global development in the frame of environmental risk forecasting. A necessity of interdisciplinary researches, Comptes Rendus Geoscience, 347 (2015) 35-42.

[11] A.A. Keller, S. McFerran, A. Lazareva, S. Suh, Global life cycle releases of engineered nanomaterials, J Nanopart Res, 15 (2013) 1-17.

[12] M.E. Vance, T. Kuiken, E.P. Vejerano, S.P. McGinnis, M.F. Hochella Jr, D. Rejeski, M.S. Hull, Nanotechnology in the real world: Redeveloping the nanomaterial consumer products inventory, Beilstein journal of nanotechnology, 6 (2015) 1769-1780.

[13] A. Fujishima, X. Zhang, D. Tryk, TiO2 photocatalysis and related surface phenomena, Surf Sci Rep, 63 (2008) 515-582.

[14] M.N. Chong, B. Jin, C.W. Chow, C. Saint, Recent developments in photocatalytic water treatment technology: a review, Water Res, 44 (2010) 2997-3027.

[15] M.R. Hoffmann, S.T. Martin, W.Y. Choi, D.W. Bahnemann, Environmental Applications of Semiconductor Photocatalysis, Chem Rev, 95 (1995) 69-96.

[16] M. Hoffmann, E.M. Hotze, M.R. Wiesner, Reactive oxygen species generation on nanoparticulate material, Environmental Nanotechnology. Applications and Impacts of Nanomaterials, (2007) 155-203.

[17] C.O. Robichaud, D. Tanzil, U. Weilenmann, M.R. Wiesner, Relative risk analysis of several manufactured nanomaterials: An insurance industry context, Environ Sci Technol, 39 (2005) 8985-8994.

[18] M.R. Wiesner, G.V. Lowry, P. Alvarez, D. Dionysiou, P. Biswas, Assessing the risks of manufactured nanomaterials, Environ Sci Technol, 40 (2006) 4336-4345.

[19] D. Hristozov, I. Malsch, Hazards and Risks of Engineered Nanoparticles for the Environment and Human Health, Sustainability, 1 (2009) 1161-1194.

[20] N.C. Mueller, B. Nowack, Exposure modeling of engineered nanoparticles in the environment, Environ Sci Technol, 42 (2008) 4447-4453.

[21] B. Nowack, T.D. Bucheli, Occurrence, behavior and effects of nanoparticles in the environment, Environmental pollution, 150 (2007) 5-22.

[22] J.A. Brant, J. Labille, C.O. Robichaud, M. Wiesner, Fullerol cluster formation in aqueous solutions: Implications for environmental release, J Colloid Interf Sci, 314 (2007) 281-288.

[23] W.-C. Hou, C.T. Jafvert, Photochemical transformation of aqueous C60 clusters in sunlight, Environ Sci Technol, 43 (2008) 362-367.

[24] J. Lee, M. Cho, J.D. Fortner, J.B. Hughes, J.H. Kim, Transformation of Aggregate C-60 in the Aqueous Phase by UV Irradiation, Environ Sci Technol, 43 (2009) 4878-4883.

[25] R.L. Johnson, J.T. Nurmi, G.S. O'Brien Johnson, D. Fan, R.L. O'Brien Johnson, Z. Shi, A.J. Salter-Blanc, P.G. Tratnyek, G.V. Lowry, Field-scale transport and transformation of carboxymethylcellulose-stabilized nano zero-valent iron, Environ Sci Technol, 47 (2013) 1573-1580.

[26] K.L. Chen, M. Elimelech, Aggregation and deposition kinetics of fullerene (C-60) nanoparticles, Langmuir, 22 (2006) 10994-11001.

[27] X.L. Qu, P.J.J. Alvarez, Q.L. Li, Impact of Sunlight and Humic Acid on the Deposition Kinetics of Aqueous Fullerene Nanoparticles (nC(60)), Environ Sci Technol, 46 (2012) 13455-13462.

[28] S.R. Chae, Y. Xiao, S. Lin, T. Noeiaghaei, J.O. Kim, M.R. Wiesner, Effects of humic acid and electrolytes on photocatalytic reactivity and transport of carbon nanoparticle aggregates in water, Water Res, 46 (2012) 4053-4062.

[29] E.M. Hotze, T. Phenrat, G.V. Lowry, Nanoparticle Aggregation: Challenges to Understanding Transport and Reactivity in the Environment, J Environ Qual, 39 (2010) 1909-1924.

[30] R. Asahi, T. Morikawa, T. Ohwaki, K. Aoki, Y. Taga, Visible-light photocatalysis in nitrogen-doped titanium oxides, Science, 293 (2001) 269-271.

[31] R. Daghrir, P. Drogui, D. Robert, Modified TiO2 for environmental photocatalytic applications: a review, Industrial & Engineering Chemistry Research, 52 (2013) 3581-3599.

[32] S.D. Snow, J. Lee, J.H. Kim, Photochemical and Photophysical Properties of Sequentially Functionalized Fullerenes in the Aqueous Phase, Environ Sci Technol, 46 (2012) 13227-13234.

[33] M. Cho, J. Lee, Y. Mackeyev, L.J. Wilson, P.J.J. Alvarez, J.B. Hughes, J.-H. Kim, Visible Light Sensitized Inactivation of MS-2 Bacteriophage by a Cationic Amine-Functionalized C60 Derivative, Environ. Sci. Technol., 44 (2010) 6685-6691.

[34] K.A. Brausch, T.A. Anderson, P.N. Smith, J.D. Maul, Effects of functionalized fullerenes on bifenthrin and tribufos toxicity to Daphnia magna: Survival, reproduction, and growth rate, Environ Toxicol Chem, 29 (2010) 2600-2606.

[35] M. Heinlaan, A. Ivask, I. Blinova, H.-C. Dubourguier, A. Kahru, Toxicity of nanosized and bulk ZnO, CuO and TiO 2 to bacteria Vibrio fischeri and crustaceans Daphnia magna and Thamnocephalus platyurus, Chemosphere, 71 (2008) 1308-1316.

[36] A. Fujishima, K. Honda, Electrochemical evidence for the mechanism of the primary stage of photosynthesis, Bulletin of the chemical society of Japan, 44 (1971) 1148-1150.

[37] K. Hashimoto, H. Irie, A. Fujishima, TiO2Photocatalysis: A Historical Overview and Future Prospects, Japanese Journal of Applied Physics, 44 (2005) 8269-8285.

[38] J.M. Coronado, A Historical Introduction to Photocatalysis, in: Design of Advanced Photocatalytic Materials for Energy and Environmental Applications, Springer, 2013, pp. 1-4.

[39] M.A. Henderson, A surface science perspective on photocatalysis, Surf Sci Rep, 66 (2011) 185-297.

[40] A.L. Linsebigler, G.Q. Lu, J.T. Yates, Photocatalysis on Tio2 Surfaces - Principles, Mechanisms, and Selected Results, Chem Rev, 95 (1995) 735-758.

[41] M. Pelaez, N.T. Nolan, S.C. Pillai, M.K. Seery, P. Falaras, A.G. Kontos, P.S. Dunlop, J.W. Hamilton, J.A. Byrne, K. O'shea, A review on the visible light active titanium dioxide photocatalysts for environmental applications, Applied Catalysis B: Environmental, 125 (2012) 331-349.

[42] J.-M. Herrmann, Heterogeneous photocatalysis: fundamentals and applications to the removal of various types of aqueous pollutants, Catalysis today, 53 (1999) 115-129.

[43] A.O. Ibhadon, P. Fitzpatrick, Heterogeneous photocatalysis: recent advances and applications, Catalysts, 3 (2013) 189-218.

[44] K. Nakata, A. Fujishima, TiO 2 photocatalysis: design and applications, Journal of Photochemistry and Photobiology C: Photochemistry Reviews, 13 (2012) 169-189.

[45] K. Nakata, T. Ochiai, T. Murakami, A. Fujishima, Photoenergy conversion with TiO 2 photocatalysis: new materials and recent applications, Electrochimica Acta, 84 (2012) 103-111.

[46] A. Kubacka, M. Fernandez-Garcia, G. Colon, Advanced nanoarchitectures for solar photocatalytic applications, Chem Rev, 112 (2011) 1555-1614.

[47] T.E. Agustina, H. Ang, V. Vareek, A review of synergistic effect of photocatalysis and ozonation on wastewater treatment, Journal of Photochemistry and Photobiology C: Photochemistry Reviews, 6 (2005) 264-273.

[48] Y. Lan, Y. Lu, Z. Ren, Mini review on photocatalysis of titanium dioxide nanoparticles and their solar applications, Nano Energy, 2 (2013) 1031-1045.

[49] R.P. Schwarzenbach, P.M. Gschwend, D.M. Imboden, Environmental organic chemistry, John Wiley & Sons, 2005.

[50] B. Singh, N. Sharma, Mechanistic implications of plastic degradation, Polymer Degradation and Stability, 93 (2008) 561-584.

[51] O.C. Zafiriou, J. Joussot-Dubien, R.G. Zepp, R.G. Zika, Photochemistry of natural waters, Environ Sci Technol, 18 (1984) 358A-371A.

[52] K.R. Wigginton, B.M. Pecson, T. Sigstam, F. Bosshard, T. Kohn, Virus inactivation mechanisms: impact of disinfectants on virus function and structural integrity, Environ Sci Technol, 46 (2012) 12069-12078.

[53] W. Hijnen, E. Beerendonk, G.J. Medema, Inactivation credit of UV radiation for viruses, bacteria and protozoan (oo) cysts in water: a review, Water Res, 40 (2006) 3-22.

[54] C. Wong, W. Chu, The direct photolysis and photocatalytic degradation of alachlor at different TiO 2 and UV sources, Chemosphere, 50 (2003) 981-987.

[55] V.J. Pereira, H.S. Weinberg, K.G. Linden, P.C. Singer, UV degradation kinetics and modeling of pharmaceutical compounds in laboratory grade and surface water via direct and indirect photolysis at 254 nm, Environ Sci Technol, 41 (2007) 1682-1688.

[56] G. Ruppert, R. Bauer, G. Heisler, The photo-Fenton reaction—an effective photochemical wastewater treatment process, Journal of Photochemistry and Photobiology A: Chemistry, 73 (1993) 75-78.

[57] R.G. Zepp, B.C. Faust, J. Hoigne, Hydroxyl Radical Formation in Aqueous Reactions (Ph 3-8) of Iron(Ii) with Hydrogen-Peroxide - the Photo-Fenton Reaction, Environ Sci Technol, 26 (1992) 313-319.

[58] N. Serpone, A. Salinaro, Terminology, relative photonic efficiencies and quantum yields in heterogeneous photocatalysis. Part I: Suggested protocol, Pure Appl Chem, 71 (1999) 303-320.

[59] F. Wilkinson, W.P. Helman, A.B. Ross, Quantum Yields for the Photosensitized Formation of the Lowest Electronically Excited Singlet-State of Molecular-Oxygen in Solution, J Phys Chem Ref Data, 22 (1993) 113-262.

[60] R.T. Di Giulio, P.C. Washburn, R.J. Wenning, G.W. Winston, C.S. Jewell, Biochemical responses in aquatic animals: a review of determinants of oxidative stress, Environ Toxicol Chem, 8 (1989) 1103-1123.

[61] E. Cabiscol, J. Tamarit, J. Ros, Oxidative stress in bacteria and protein damage by reactive oxygen species, International Microbiology, 3 (2010) 3-8.

[62] F.C. Fang, Antimicrobial reactive oxygen and nitrogen species: concepts and controversies, Nature reviews. Microbiology, 2 (2004) 820-832.

[63] C. Bogdan, M. Röllinghoff, A. Diefenbach, Reactive oxygen and reactive nitrogen intermediates in innate and specific immunity, Current opinion in immunology, 12 (2000) 64-76.

[64] G.W. Winston, R.T. Di Giulio, Prooxidant and antioxidant mechanisms in aquatic organisms, Aquatic toxicology, 19 (1991) 137-161.

[65] T. Kohn, M. Grandbois, K. McNeill, K.L. Nelson, Association with Natural Organic Matter Enhances the Sunlight-Mediated Inactivation of MS2 Coliphage by Singlet Oxygen, Environ Sci Technol, 41 (2007) 4626-4632.

[66] T. Kohn, K.L. Nelson, Sunlight-Mediated Inactivation of MS2 Coliphage via Exogenous Singlet Oxygen Produced by Sensitizers in Natural Waters, Environ Sci Technol, 41 (2007) 192-197.

[67] D.E. Latch, Microheterogenity of singlet oxygen distributions in irradiated humic acid solutions, Science, 311 (2006) 1743.

[68] S. Garg, A.L. Rose, T.D. Waite, Photochemical production of superoxide and hydrogen peroxide from natural organic matter, Geochim Cosmochim Ac, 75 (2011) 4310-4320.

[69] D.M. Leech, M.T. Snyder, R.G. Wetzel, Natural organic matter and sunlight accelerate the degradation of 17ß-estradiol in water, Sci Total Environ, 407 (2009) 2087-2092.

[70] G.V. Buxton, C.L. Greenstock, W.P. Helman, A.B. Ross, Critical-Review of Rate Constants for Reactions of Hydrated Electrons, Hydrogen-Atoms and Hydroxyl Radicals (.Oh/.O-) in Aqueous-Solution, J Phys Chem Ref Data, 17 (1988) 513-886.

[71] M. Cho, H. Chung, W. Choi, J. Yoon, Different inactivation behaviors of MS-2 phage and Escherichia coli in TiO2 photocatalytic disinfection, Applied and environmental microbiology, 71 (2005) 270-275.

[72] M.C. DeRosa, R.J. Crutchley, Photosensitized singlet oxygen and its applications, Coordin Chem Rev, 233 (2002) 351-371.

[73] G. Bartosz, Use of spectroscopic probes for detection of reactive oxygen species, Clinica chimica acta; international journal of clinical chemistry, 368 (2006) 53-76.

[74] T. Nagano, Bioimaging Probes for Reactive Oxygen Species and Reactive Nitrogen Species, J Clin Biochem Nutr, 45 (2009) 111-124.

[75] N. Soh, Recent advances in fluorescent probes for the detection of reactive oxygen species, Analytical and bioanalytical chemistry, 386 (2006) 532-543.

[76] K.-I. Ishibashi, A. Fujishima, T. Watanabe, K. Hashimoto, Detection of active oxidative species in TiO 2 photocatalysis using the fluorescence technique, Electrochemistry Communications, 2 (2000) 207-210.

[77] S.R. Chae, E.M. Hotze, M.R. Wiesner, Evaluation of the Oxidation of Organic Compounds by Aqueous Suspensions of Photosensitized Hydroxylated-C-60 Fullerene Aggregates, Environ Sci Technol, 43 (2009) 6208-6213.

[78] E.M. Hotze, A.R. Badireddy, S. Chellam, M.R. Wiesner, Mechanisms of Bacteriophage Inactivation via Singlet Oxygen Generation in UV Illuminated Fullerol Suspensions, Environ Sci Technol, 43 (2009) 6639-6645.

[79] Z. Wang, W. Ma, C. Chen, H. Ji, J. Zhao, Probing paramagnetic species in titania-based heterogeneous photocatalysis by electron spin resonance (ESR) spectroscopy—A mini review, Chemical Engineering Journal, 170 (2011) 353-362.

[80] D.M. Guldi, K.D. Asmus, Photophysical properties of mono- and multiply-functionalized fullerene derivatives, J Phys Chem A, 101 (1997) 1472-1481.

[81] L. Brunet, D. Lyon, E.M. Hotze, P.J.J. Alvarez, M.R. Wiesner, Comparative Photoactivity and Antibacterial Properties of C_{60} Fullerenes and Titanium Dioxide Nanoparticles, Environmental Science and Technology, 43 (2009) 4355-4360.

[82] S.R. Chae, M. Therezien, J.F. Budarz, L. Wessel, S.H. Lin, Y. Xiao, M.R. Wiesner, Comparison of the photosensitivity and bacterial toxicity of spherical and tubular fullerenes of variable aggregate size, J Nanopart Res, 13 (2011) 5121-5127.

[83] A. Gollmer, J. Arnbjerg, F.H. Blaikie, B.W. Pedersen, T. Breitenbach, K. Daasbjerg, M. Glasius, P.R. Ogilby, Singlet Oxygen Sensor Green(R): photochemical behavior in solution and in a mammalian cell, Photochemistry and photobiology, 87 (2011) 671-679.

[84] X. Ragas, A. Jimenez-Banzo, D. Sanchez-Garcia, X. Batllori, S. Nonell, Singlet oxygen photosensitisation by the fluorescent probe Singlet Oxygen Sensor Green, Chem Commun (Camb), (2009) 2920-2922.

[85] A. Okado-Matsumoto, I. Fridovich, Subcellular distribution of superoxide dismutases (SOD) in rat liver Cu, Zn-SOD in mitochondria, Journal of Biological Chemistry, 276 (2001) 38388-38393.

[86] H. Zhao, S. Kalivendi, H. Zhang, J. Joseph, K. Nithipatikom, J. Vásquez-Vivar, B. Kalyanaraman, Superoxide reacts with hydroethidine but forms a fluorescent product that is distinctly different from ethidium: potential implications in intracellular fluorescence detection of superoxide, Free Radical Biology and Medicine, 34 (2003) 1359-1368.

[87] K.-i. Ishibashi, A. Fujishima, T. Watanabe, K. Hashimoto, Quantum yields of active oxidative species formed on TiO 2 photocatalyst, Journal of Photochemistry and Photobiology A: Chemistry, 134 (2000) 139-142.

[88] S.E. Page, W.A. Arnold, K. McNeill, Terephthalate as a probe for photochemically generated hydroxyl radical, Journal of environmental monitoring : JEM, 12 (2010) 1658-1665.

[89] S. Eremia, D. Chevalierlucia, G. Radu, J. Marty, Optimization of hydroxyl radical formation using TiO2 as photocatalyst by response surface methodology, Talanta, 77 (2008) 858-862.

[90] C.S. Foote, R.W. Denny, Chemistry of Singlet Oxygen .7. Quenching by Beta-Carotene, J Am Chem Soc, 90 (1968) 6233-&.

[91] A.M. Wade, H.N. Tucker, Antioxidant characteristics of L-histidine, J Nutr Biochem, 9 (1998) 308-315.

[92] I.B.C. Matheson, J. Lee, Chemical-Reaction Rates of Amino-Acids with Singlet Oxygen, Photochemistry and photobiology, 29 (1979) 879-881.

[93] O.I. Aruoma, B. Halliwell, B.M. Hoey, J. Butler, The antioxidant action of N-acetylcysteine: its reaction with hydrogen peroxide, hydroxyl radical, superoxide, and hypochlorous acid, Free Radical Biology and Medicine, 6 (1989) 593-597.

[94] M. Gutiérrez, A. Henglein, F. Ibanez, Radical scavenging in the sonolysis of aqueous solutions of iodide, bromide, and azide, The Journal of Physical Chemistry, 95 (1991) 6044-6047.

[95] Y. Zhang, K. Aslan, M.J. Previte, C.D. Geddes, Plasmonic engineering of singlet oxygen generation, Proceedings of the National Academy of Sciences of the United States of America, 105 (2008) 1798-1802.

[96] D.C. Neckers, Rose-Bengal, J Photoch Photobio A, 47 (1989) 1-29.

[97] I.E. Kochevar, R.W. Redmond, Photosensitized production of singlet oxygen, Method Enzymol, 319 (2000) 20-28.

[98] H. Ukeda, S. Maeda, T. Ishii, M. Sawamura, Spectrophotometric assay for superoxide dismutase based on tetrazolium salt 3'-{1-[(phenylamino)-carbonyl]-3,4-tetrazolium}-bis(4-methoxy-6-nitro)benzenesulfonic acid hydrate reduction by xanthine-xanthine oxidase, Anal Biochem, 251 (1997) 206-209.

[99] W. Song, V. Ravindran, M. Pirbazari, Process optimization using a kinetic model for the ultraviolet radiation-hydrogen peroxide decomposition of natural and synthetic organic compounds in groundwater, Chemical Engineering Science, 63 (2008) 3249-3270.

[100] R. Zellner, M. Exner, H. Herrmann, Absolute Oh Quantum Yields in the Laser Photolysis of Nitrate, Nitrite and Dissolved H2o2 at 308 and 351 Nm in the Temperature-Range 278-353 K, J Atmos Chem, 10 (1990) 411-425.

[101] C. Flors, M.J. Fryer, J. Waring, B. Reeder, U. Bechtold, P.M. Mullineaux, S. Nonell, M.T. Wilson, N.R. Baker, Imaging the production of singlet oxygen in vivo using a new fluorescent sensor, Singlet Oxygen Sensor Green, Journal of experimental botany, 57 (2006) 1725-1734.

[102] F. Yan, Y. Zhang, K.S. Kim, H.K. Yuan, T. Vo-Dinh, Cellular Uptake and Photodynamic Activity of Protein Nanocages Containing Methylene Blue Photosensitizing Drug, Photochemistry and photobiology, 86 (2010) 662-666.

[103] P. Bilski, R. Dabestani, C.F. Chignell, Influence of Cationic Surfactant on the Photoprocesses of Eosin and Rose-Bengal in Aqueous-Solution, J Phys Chem-Us, 95 (1991) 5784-5791.

[104] C.L. Wu, K.G. Linden, Phototransformation of selected organophosphorus pesticides: Roles of hydroxyl and carbonate radicals, Water Res, 44 (2010) 3585-3594.

[105] C. Pierlot, V. Nardello, R. Schmidt, J.M. Aubry, Determination of physical (k(q)) and chemical (k(r)) rate constants for singlet oxygen quenching using the thermolysis of a naphthalenic endoperoxide in H2O and D2O, Arkivoc, (2007) 245-256.

[106] M. Benrahmoune, P. Thérond, Z. Abedinzadeh, The reaction of superoxide radical with N-acetylcysteine, Free Radical Biology and Medicine, 29 (2000) 775-782.

[107] M. Auffan, J. Rose, C. Chanéac, J.-P. Jolivet, A. Masion, M.R. Wiesner, J.-Y. Bottero, Surface reactivity of manufactured nanoparticles, in: Nanoethics and Nanotoxicology, Springer, 2011, pp. 269-290.

[108] D. Beydoun, R. Amal, G. Low, S. McEvoy, Role of nanoparticles in photocatalysis, J Nanopart Res, 1 (1999) 439-458.

[109] A. Sclafani, J.M. Herrmann, Influence of metallic silver and of platinum-silver bimetallic deposits on the photocatalytic activity of titania (anatase and rutile) in organic and aqueous media, J Photoch Photobio A, 113 (1998) 181-188.

[110] S. Banerjee, S.C. Pillai, P. Falaras, K.E. O'shea, J.A. Byrne, D.D. Dionysiou, New insights into the mechanism of visible light photocatalysis, The journal of physical chemistry letters, 5 (2014) 2543-2554.

[111] D.M. Guldi, M. Prato, Excited-state properties of C-60 fullerene derivatives, Accounts Chem Res, 33 (2000) 695-703.

[112] M.D. Diener, J.M. Alford, Isolation and properties of small-bandgap fullerenes, Nature, 393 (1998) 668-671.

[113] H.W. Kroto, A. Allaf, S. Balm, C60: Buckminsterfullerene, Chem Rev, 91 (1991) 1213-1235.

[114] D.J. Klein, T.G. Schmalz, G. Hite, W. Seitz, Resonance in C60 buckminsterfullerene, J Am Chem Soc, 108 (1986) 1301-1302.

[115] S. Leach, M. Vervloet, A. Després, E. Bréheret, J.P. Hare, T.J. Dennis, H.W. Kroto, R. Taylor, D.R. Walton, Electronic spectra and transitions of the fullerene C 60, Chemical Physics, 160 (1992) 451-466.

[116] J.A. Brant, J. Labille, J.Y. Bottero, M.R. Wiesner, Characterizing the impact of preparation method on fullerene cluster structure and chemistry, Langmuir, 22 (2006) 3878-3885.

[117] X.J. Chang, P.J. Vikesland, UV-vis Spectroscopic Properties of nC(60) Produced via Extended Mixing, Environ Sci Technol, 45 (2011) 9967-9974.

[118] D.Y. Lyon, L.K. Adams, J.C. Falkner, P.J. Alvarez, Antibacterial activity of fullerene water suspensions: effects of preparation method and particle size, Environ Sci Technol, 40 (2006) 4360-4366.

[119] D.Y. Lyon, L. Brunet, G.W. Hinkal, M.R. Wiesner, P.J. Alvarez, Antibacterial activity of fullerene water suspensions (nC60) is not due to ROS-mediated damage, Nano Lett, 8 (2008) 1539-1543.

[120] J. Brant, H. Lecoanet, M. Hotze, M. Wiesner, Comparison of electrokinetic properties of colloidal fullerenes (n-C60) formed using two procedures, Environ Sci Technol, 39 (2005) 6343-6351.

[121] S.R. Chae, A.R. Badireddy, J.F. Budarz, S.H. Lin, Y. Xiao, M. Therezien, M.R. Wiesner, Heterogeneities in Fullerene Nanoparticle Aggregates Affecting Reactivity, Bioactivity, and Transport, Acs Nano, 4 (2010) 5011-5018.

[122] J. Labille, A. Masion, F. Ziarelli, J. Rose, J. Brant, F. Villiéras, M. Pelletier, D. Borschneck, M.R. Wiesner, J.-Y. Bottero, Hydration and dispersion of C60 in aqueous systems: the nature of water− fullerene interactions, Langmuir, 25 (2009) 11232-11235.

[123] R. Taylor, D.R.M. Walton, The Chemistry of Fullerenes, Nature, 363 (1993) 685-693.

[124] V. Anantharaj, J. Bhonsle, T. Canteenwala, L.Y. Chiang, Highly electrophilic hexanitro[60]fullerenes, Elec Soc S, 98 (1998) 196-204.

[125] E. Nakamura, H. Isobe, Functionalized fullerenes in water. The first 10 years of their chemistry, biology, and nanoscience, Accounts Chem Res, 36 (2003) 807-815.

[126] T.H. Goswami, R. Singh, S. Alam, G.N. Mathur, Thermal analysis: a unique method to estimate the number of substituents in fullerene derivatives, Thermochim Acta, 419 (2004) 97-104.

[127] K.D. Pickering, M.R. Wiesner, Fullerol-sensitized production of reactive oxygen species in aqueous solution, Environ Sci Technol, 39 (2005) 1359-1365.

[128] A.R. Badireddy, E.M. Hotze, S. Chellam, P. Alvarez, M.R. Wiesner, Inactivation of Bacteriophages via photosensitization of fullerol nanoparticles, Environ Sci Technol, 41 (2007) 6627-6632.

[129] L.J. Kong, O. Tedrow, Y.F. Chan, R.G. Zepp, Light-Initiated Transformations of Fullerenol in Aqueous Media, Environ Sci Technol, 43 (2009) 9155-9160.

[130] J.W. Arbogast, A.P. Darmanyan, C.S. Foote, Y. Rubin, F.N. Diederich, M.M. Alvarez, S.J. Anz, R.L. Whetten, Photophysical Properties of C60, J Phys Chem-Us, 95 (1991) 11-12.

[131] C.S. Foote, Photophysical and Photochemical Properties of Fullerenes, Top Curr Chem, 169 (1994) 347-363.

[132] J. Lee, Y. Yamakoshi, J.B. Hughes, J.H. Kim, Mechanism of C-60 photoreactivity in water: Fate of triplet state and radical anion and production of reactive oxygen species, Environ Sci Technol, 42 (2008) 3459-3464.

[133] T. Hamano, K. Okuda, T. Mashino, M. Hirobe, K. Arakane, A. Ryu, S. Mashiko, T. Nagano, Singlet oxygen production from fullerene derivatives: Effect of sequential functionalization of the fullerene core, Chem Commun, (1997) 21-22.

[134] R. Bakry, R.M. Vallant, M. Najam-ul-Haq, M. Rainer, Z. Szabo, C.W. Huck, G.K. Bonn, Medicinal applications of fullerenes, International journal of nanomedicine, 2 (2007) 639.

[135] S. Bosi, T. Da Ros, G. Spalluto, M. Prato, Fullerene derivatives: an attractive tool for biological applications, European Journal of Medicinal Chemistry, 38 (2003) 913-923.

[136] S.Z. Wang, R.M. Gao, F.M. Zhou, M. Selke, Nanomaterials and singlet oxygen photosensitizers: potential applications in photodynamic therapy, J Mater Chem, 14 (2004) 487-493.

[137] J. Lee, Y. Mackeyev, M. Cho, D. Li, J.H. Kim, L.J. Wilson, P.J.J. Alvarez, Photochemical and Antimicrobial Properties of Novel C-60 Derivatives in Aqueous Systems, Environ Sci Technol, 43 (2009) 6604-6610.

[138] M. Cho, J. Lee, Y. Mackeyev, L.J. Wilson, P.J.J. Alvarez, J.B. Hughes, J.H. Kim, Visible Light Sensitized Inactivation of MS-2 Bacteriophage by a Cationic Amine-Functionalized C-60 Derivative, Environ Sci Technol, 44 (2010) 6685-6691.

[139] M. Kovochich, B. Espinasse, M. Auffan, E.M. Hotze, L. Wessel, T. Xia, A.E. Nel, M.R. Wiesner, Comparative Toxicity of C-60 Aggregates toward Mammalian Cells: Role of Tetrahydrofuran (THF) Decomposition, Environ Sci Technol, 43 (2009) 6378-6384.

[140] J. Lee, W.H. Song, S.S. Jang, J.D. Fortner, P.J.J. Alvarez, W.J. Cooper, J.H. Kim, Stability of Water-Stable C-60 Clusters to OH Radical Oxidation and Hydrated Electron Reduction, Environ Sci Technol, 44 (2010) 3786-3792.

[141] W.C. Hou, C.T. Jafvert, Photochemistry of Aqueous C-60 Clusters: Evidence of O-1(2) Formation and its Role in Mediating C-60 Phototransformation, Environ Sci Technol, 43 (2009) 5257-5262.

[142] Y.S. Hwang, Q.L. Li, Characterizing Photochemical Transformation of Aqueous nC(60) under Environmentally Relevant Conditions, Environ Sci Technol, 44 (2010) 3008-3013.

[143] U. Diebold, Structure and properties of TiO 2 surfaces: a brief review, Applied Physics A: Materials Science & Processing, 76 (2003) 681-687.

[144] C.J. Barbe, F. Arendse, P. Comte, M. Jirousek, F. Lenzmann, V. Shklover, M. Gratzel, Nanocrystalline titanium oxide electrodes for photovoltaic applications, J Am Ceram Soc, 80 (1997) 3157-3171.

[145] D.M. Blake, P.C. Maness, Z. Huang, E.J. Wolfrum, J. Huang, W.A. Jacoby, Application of the photocatalytic chemistry of titanium dioxide to disinfection and the killing of cancer cells, Separ Purif Method, 28 (1999) 1-50.

[146] M. Lazar, S. Varghese, S. Nair, Photocatalytic Water Treatment by Titanium Dioxide: Recent Updates, Catalysts, 2 (2012) 572-601.

[147] A. Fujishima, T.N. Rao, D.A. Tryk, Titanium dioxide photocatalysis, Journal of Photochemistry and Photobiology C: Photochemistry Reviews, 1 (2000) 1-21.

[148] T. Luttrell, S. Halpegamage, J. Tao, A. Kramer, E. Sutter, M. Batzill, Why is anatase a better photocatalyst than rutile?--Model studies on epitaxial TiO2 films, Scientific reports, 4 (2014) 4043.

[149] X. Kang, S. Chen, Photocatalytic reduction of methylene blue by TiO2 nanotube arrays: effects of TiO2 crystalline phase, Journal of Materials Science, 45 (2010) 2696-2702.

[150] H. Kominami, J.-i. Kato, S.-y. Murakami, Y. Ishii, M. Kohno, K.-i. Yabutani, T. Yamamoto, Y. Kera, M. Inoue, T. Inui, B. Ohtani, Solvothermal syntheses of semiconductor photocatalysts of ultra-high activities, Catalysis Today, 84 (2003) 181-189.

[151] B. Ohtani, J.-i. Handa, S.-i. Nishimoto, T. Kagiya, Highly active semiconductor photocatalyst: Extra-fine crystallite of brookite TiO 2 for redox reaction in aqueous propan-2-ol and/or silver sulfate solution, Chem Phys Lett, 120 (1985) 292-294.

[152] S. Bakardjieva, V. Stengl, L. Szatmary, J. Subrt, J. Lukac, N. Murafa, D. Niznansky, K. Cizek, J. Jirkovsky, N. Petrova, Transformation of brookite-type TiO2 nanocrystals to rutile: correlation between microstructure and photoactivity, J Mater Chem, 16 (2006) 1709.

[153] S. Bakardjieva, J. Šubrt, V. Štengl, M.J. Dianez, M.J. Sayagues, Photoactivity of anatase–rutile TiO2 nanocrystalline mixtures obtained by heat treatment of homogeneously precipitated anatase, Applied Catalysis B: Environmental, 58 (2005) 193-202.

[154] T. Hirakawa, Y. Nosaka, Properties of O(2)(center dot-) and OH(center dot) formed in TiO(2) aqueous suspensions by photocatalytic reaction and the influence of H(2)O(2) and some ions, Langmuir, 18 (2002) 3247-3254.

[155] D.C. Hurum, K.A. Gray, T. Rajh, M.C. Thurnauer, Recombination pathways in the Degussa P25 formulation of TiO2: Surface versus lattice mechanisms, J Phys Chem B, 109 (2005) 977-980.

[156] L.Z. Sun, J.R. Bolton, Determination of the quantum yield for the photochemical generation of hydroxyl radicals in TiO2 suspensions, J Phys Chem-Us, 100 (1996) 4127-4134.

[157] A. Turolla, M. Fumagalli, M. Bestetti, M. Antonelli, Electrophotocatalytic decolorization of an azo dye on TiO2 self-organized nanotubes in a laboratory scale reactor, Desalination, 285 (2012) 377-382.

[158] G. Mascolo, R. Ciannarella, L. Balest, A. Lopez, Effectiveness of UV-based advanced oxidation processes for the remediation of hydrocarbon pollution in the groundwater: a laboratory investigation, J Hazard Mater, 152 (2008) 1138-1145.

[159] C. Kormann, D.W. Bahnemann, M.R. Hoffmann, Photolysis of Chloroform and Other Organic-Molecules in Aqueous Tio2 Suspensions, Environ Sci Technol, 25 (1991) 494-500.

[160] S. Lakshmi, R. Renganathan, S. Fujita, Study on Tio2-Mediated Photocatalytic Degradation of Methylene-Blue, J Photoch Photobio A, 88 (1995) 163-167.

[161] V.K. Sharma, Aggregation and toxicity of titanium dioxide nanoparticles in aquatic environment—a review, Journal of Environmental Science and Health Part A, 44 (2009) 1485-1495.

[162] K. Sunada, Y. Kikuchi, K. Hashimoto, A. Fujishima, Bactericidal and detoxification effects of TiO2 thin film photocatalysts, Environ Sci Technol, 32 (1998) 726-728.

[163] Q. Li, S. Mahendra, D.Y. Lyon, L. Brunet, M.V. Liga, D. Li, P.J. Alvarez, Antimicrobial nanomaterials for water disinfection and microbial control: potential applications and implications, Water Res, 42 (2008) 4591-4602.

[164] D. Feng, N. Xie, C. Gong, Z. Leng, H. Xiao, H. Li, X. Shi, Portland cement paste modified by TiO2 nanoparticles: a microstructure perspective, Industrial & Engineering Chemistry Research, 52 (2013) 11575-11582.

[165] R. Khataee, V. Heydari, L. Moradkhannejhad, M. Safarpour, S. Joo, Self-cleaning and mechanical properties of modified white cement with nanostructured TiO2, J Nanosci Nanotechno, 13 (2013) 5109-5114.

[166] A. Maury-Ramirez, W. De Muynck, R. Stevens, K. Demeestere, N. De Belie, Titanium dioxide based strategies to prevent algal fouling on cementitious materials, Cement and Concrete Composites, 36 (2013) 93-100.

[167] A. Yousefi, A. Allahverdi, P. Hejazi, Effective dispersion of nano-TiO 2 powder for enhancement of photocatalytic properties in cement mixes, Construction and building materials, 41 (2013) 224-230.

[168] D. Sanchez-Quiles, A. Tovar-Sanchez, Sunscreens as a source of hydrogen peroxide production in coastal waters, Environ Sci Technol, 48 (2014) 9037-9042.

[169] A.P. Gondikas, F.v.d. Kammer, R.B. Reed, S. Wagner, J.F. Ranville, T. Hofmann, Release of TiO2 nanoparticles from sunscreens into surface waters: a one-year survey at the old Danube recreational Lake, Environ Sci Technol, 48 (2014) 5415-5422.

[170] A. Praetorius, J. Labille, M. Scheringer, A. Thill, K. Hungerbuhler, J.Y. Bottero, Heteroaggregation of Titanium Dioxide Nanoparticles with Model Natural Colloids under Environmentally Relevant Conditions, Environ Sci Technol, 48 (2014) 10690-10698.

[171] L. Windler, C. Lorenz, N. Von Goetz, K. Hungerbuhler, M. Amberg, M. Heuberger, B. Nowack, Release of titanium dioxide from textiles during washing, Environ Sci Technol, 46 (2012) 8181-8188.

[172] M. Fouqueray, P. Noury, L. Dherret, P. Chaurand, K. Abbaci, J. Labille, J. Rose, J. Garric, Exposure of juvenile Danio rerio to aged TiO2 nanomaterial from sunscreen, Environmental Science and Pollution Research, 20 (2013) 3340-3350.

[173] A. Al-Kattan, A. Wichser, S. Zuin, Y. Arroyo, L. Golanski, A. Ulrich, B. Nowack, Behavior of TiO2 released from nano-TiO2-containing paint and comparison to pristine nano-TiO2, Environ Sci Technol, 48 (2014) 6710-6718.

[174] C. Santaella, B. Allainmat, F. Simonet, C. Chanéac, J.r. Labille, M.l. Auffan, J.r. Rose, W. Achouak, Aged TiO2-based nanocomposite used in sunscreens produces singlet oxygen under long-wave UV and sensitizes Escherichia coli to cadmium, Environ Sci Technol, 48 (2014) 5245-5253.

[175] T. Ohno, K. Sarukawa, K. Tokieda, M. Matsumura, Morphology of a TiO2 Photocatalyst (Degussa, P-25) Consisting of Anatase and Rutile Crystalline Phases, J Catal, 203 (2001) 82-86.

[176] K.J.A. Raj, B. Viswanathan, Effect of surface area, pore volume and particle size of P25 titania on the phase transformation of anatase to rutile, Indian J Chem A, 48 (2009) 1378-1382.

[177] D. Jassby, J.F. Budarz, M. Wiesner, Impact of Aggregate Size and Structure on the Photocatalytic Properties of TiO2 and ZnO Nanoparticles, Environ Sci Technol, 46 (2012) 6934-6941.

[178] J. Taurozzi, V. Hackley, M. Wiesner, Preparation of a nanoscale TiO2 aqueous dispersion for toxicological or environmental testing, NIST Special Publication, 1200 (2012) 3.

[179] D. Thomas, S. Judd, N. Fawcett, Flocculation modelling: a review, Water Res, 33 (1999) 1579-1592.

[180] B. Derjaguin, L. Landau, The theory of stability of highly charged lyophobic sols and coalescence of highly charged particles in electrolyte solutions, Acta Physicochim. URSS, 14 (1941) 633-652.

[181] E. Verwey, J.T.G. Overbeek, Long distance forces acting between colloidal particles, Trans. Faraday Soc., 42 (1946) B117-B123.

[182] J.C. Crittenden, R.R. Trussell, D.W. Hand, K.J. Howe, G. Tchobanoglous, MWH's Water Treatment: Principles and Design: Principles and Design, John Wiley & Sons, 2012.

[183] K.L. Chen, S.E. Mylon, M. Elimelech, Aggregation kinetics of alginate-coated hematite nanoparticles in monovalent and divalent electrolytes, Environ Sci Technol, 40 (2006) 1516-1523.

[184] B. Espinasse, E.M. Hotze, M.R. Wiesner, Transport and retention of colloidal aggregates of C-60 in porous media: Effects of organic macromolecules, ionic composition, and preparation method, Environ Sci Technol, 41 (2007) 7396-7402.

[185] K.L. Chen, M. Elimelech, Interaction of Fullerene (C-60) Nanoparticles with Humic Acid and Alginate Coated Silica Surfaces: Measurements, Mechanisms, and Environmental Implications, Environ Sci Technol, 42 (2008) 7607-7614.

[186] Z.Q. Li, K. Greden, P.J.J. Alvarez, K.B. Gregory, G.V. Lowry, Adsorbed Polymer and NOM Limits Adhesion and Toxicity of Nano Scale Zerovalent Iron to E. coli, Environ Sci Technol, 44 (2010) 3462-3467.

[187] K.L. Chen, M. Elimelech, Influence of humic acid on the aggregation kinetics of fullerene (C-60) nanoparticles in monovalent and divalent electrolyte solutions, J Colloid Interf Sci, 309 (2007) 126-134.

[188] F. He, D.Y. Zhao, Preparation and characterization of a new class of starch-stabilized bimetallic nanoparticles for degradation of chlorinated hydrocarbons in water, Environ Sci Technol, 39 (2005) 3314-3320.

[189] S.H. Lin, Y.W. Cheng, J. Liu, M.R. Wiesner, Polymeric Coatings on Silver Nanoparticles Hinder Autoaggregation but Enhance Attachment to Uncoated Surfaces, Langmuir, 28 (2012) 4178-4186.

[190] K. Li, Y. Chen, Effect of natural organic matter on the aggregation kinetics of CeO 2 nanoparticles in KCl and CaCl 2 solutions: measurements and modeling, J Hazard Mater, 209 (2012) 264-270.

[191] C.V. Chrysikopoulos, V.I. Syngouna, Attachment of bacteriophages MS2 and ΦX174 onto kaolinite and montmorillonite: Extended-DLVO interactions, Colloids and Surfaces B: Biointerfaces, 92 (2012) 74-83.

[192] M.V. Smoluchowski, Smoluchowski, Versuch einer Mathematischen Theorie der Koagulationskinetic Kolloider Lösunger, Z. Phys. Chem, 92 (1917) 129-168.

[193] D.L. Swift, S.K. Friedlander, The coagulation of hydrosols by Brownian motion and laminar shear flow, Journal of colloid science, 19 (1964) 621-647.

[194] J.A. Raper, R. Amal, Measurement of Aggregate Fractal Dimensions Using Static Light-Scattering, Part Part Syst Char, 10 (1993) 239-245.

[195] M.Y. Lin, H.M. Lindsay, D.A. Weitz, R.C. Ball, R. Klein, P. Meakin, Universality in Colloid Aggregation, Nature, 339 (1989) 360-362.

[196] C.M. Sorensen, Light scattering by fractal aggregates: A review, Aerosol Sci Tech, 35 (2001) 648-687.

[197] S. Veerapaneni, M.R. Wiesner, Particle deposition on an infinitely permeable surface: Dependence of deposit morphology on particle size, J Colloid Interf Sci, 162 (1994) 110-122.

[198] J. Zhang, J. Buffle, Multi-method determination of the fractal dimension of hematite aggregates, Colloids and Surfaces A: Physicochemical and Engineering Aspects, 107 (1996) 175-187.

[199] A. Turolla, A. Piazzoli, J. Farner Budarz, M.R. Wiesner, M. Antonelli, Experimental measurement and modelling of reactive species generation in TiO2 nanoparticle photocatalysis, Chemical Engineering Journal, 271 (2015) 260-268.

[200] Z. Meng, S.M. Hashmi, M. Elimelech, Aggregation rate and fractal dimension of fullerene nanoparticles via simultaneous multiangle static and dynamic light scattering measurement, J Colloid Interf Sci, 392 (2013) 27-33.

[201] T. Rudalevige, A.H. Francis, R. Zand, Spectroscopic studies of fullerene aggregates, J Phys Chem A, 102 (1998) 9797-9802.

[202] D. Zhou, A.A. Keller, Role of morphology in the aggregation kinetics of ZnO nanoparticles, Water Res, 44 (2010) 2948-2956.

[203] A.Y. Kim, J.C. Berg, Fractal heteroaggregation of oppositely charged colloids, J Colloid Interf Sci, 229 (2000) 607-614.

[204] E. Barbot, P. Dussouillez, J.-Y. Bottero, P. Moulin, Coagulation of bentonite suspension by polyelectrolytes or ferric chloride: Floc breakage and reformation, Chemical Engineering Journal, 156 (2010) 83-91.

[205] V. Oles, Shear-induced aggregation and breakup of polystyrene latex particles, J Colloid Interf Sci, 154 (1992) 351-358.

[206] P. Adler, Streamlines in and around porous particles, J Colloid Interf Sci, 81 (1981) 531-535.

[207] D.H. Li, J. Ganczarczyk, Fractal geometry of particle aggregates generated in water and wastewater treatment processes, Environ Sci Technol, 23 (1989) 1385-1389.

[208] S. Chellam, M.R. Wiesner, Fluid mechanics and fractal aggregates, Water Res, 27 (1993) 1493-1496.

[209] S. Veerapaneni, M.R. Wiesner, Hydrodynamics of fractal aggregates with radially varying permeability, J Colloid Interf Sci, 177 (1996) 45-57.

[210] M. Han, D.F. Lawler, The (relative) insignificance of G in flocculation, Journal (American Water Works Association), (1992) 79-91.

[211] C.P. Johnson, X. Li, B.E. Logan, Settling velocities of fractal aggregates, Environ Sci Technol, 30 (1996) 1911-1918.

[212] X. Li, B.E. Logan, Collision frequencies of fractal aggregates with small particles by differential sedimentation, Environ Sci Technol, 31 (1997) 1229-1236.

[213] K.H. Gardner, T.L. Theis, T.C. Young, The significance of shear stress in the agglomeration kinetics of fractal aggregates, Water Res, 32 (1998) 2660-2668.

[214] A.K. Yeung, R. Pelton, Micromechanics: a new approach to studying the strength and breakup of flocs, J Colloid Interf Sci, 184 (1996) 579-585.

[215] G. Bushell, Y. Yan, D. Woodfield, J. Raper, R. Amal, On techniques for the measurement of the mass fractal dimension of aggregates, Adv Colloid Interfac, 95 (2002) 1-50.

[216] B. Gilbert, R.K. Ono, K.A. Ching, C.S. Kim, The effects of nanoparticle aggregation processes on aggregate structure and metal uptake, J Colloid Interf Sci, 339 (2009) 285-295.

[217] D. Jassby, M. Wiesner, Characterization of ZnS nanoparticle aggregation using photoluminescence, Langmuir, 27 (2011) 902-908.

[218] J. Lee, J.D. Fortner, J.B. Hughes, J.H. Kim, Photochemical production of reactive oxygen species by C-60 in the aqueous phase during UV irradiation, Environ Sci Technol, 41 (2007) 2529-2535.

[219] E.M. Hotze, J.Y. Bottero, M.R. Wiesner, Theoretical Framework for Nanoparticle Reactivity as a Function of Aggregation State, Langmuir, 26 (2010) 11170-11175.

[220] F. Prat, R. Stackow, R. Bernstein, W.Y. Qian, Y. Rubin, C.S. Foote, Triplet-state properties and singlet oxygen generation in a homologous series of functionalized fullerene derivatives, J Phys Chem A, 103 (1999) 7230-7235.

[221] E.M. Hotze, J. Labille, P. Alvarez, M.R. Wiesner, Mechanisms of photochemistry and reactive oxygen production by fullerene suspensions in water, Environ Sci Technol, 42 (2008) 4175-4180.

[222] L. Brunet, D.Y. Lyon, E.M. Hotze, P.J.J. Alvarez, M.R. Wiesner, Comparative Photoactivity and Antibacterial Properties of C-60 Fullerenes and Titanium Dioxide Nanoparticles, Environ Sci Technol, 43 (2009) 4355-4360.

[223] M.J. Paul, J.L. Meyer, Streams in the urban landscape, Annual review of Ecology and Systematics, (2001) 333-365.

[224] A. Nikanorov, L. Brazhnikova, Water chemical composition of rives, lakes and wetlands, Types and Properties of Water, 2 (2009) 42-80.

[225] D.B. Medinas, G. Cerchiaro, D.F. Trindade, O. Augusto, The carbonate radical and related oxidants derived from bicarbonate buffer, IUBMB life, 59 (2007) 255-262.

[226] N.S. Wigginton, K.L. Haus, M.F. Hochella, Jr., Aquatic environmental nanoparticles, Journal of environmental monitoring : JEM, 9 (2007) 1306-1316.

[227] P. Connor, A.J. McQuillan, Phosphate adsorption onto TiO2 from aqueous solutions: an in situ internal reflection infrared spectroscopic study, Langmuir, 15 (1999) 2916-2921.

[228] R.F. Domingos, C. Peyrot, K.J. Wilkinson, Aggregation of titanium dioxide nanoparticles: role of calcium and phosphate, Environmental Chemistry, 7 (2010) 61-66.

[229] J.A. Leenheer, J.P. Croue, Characterizing aquatic dissolved organic matter, Environ Sci Technol, 37 (2003) 18A-26A.

[230] G. VanLoon, S. Duffy, Organic matter in water, Environmental Chemistry: A Global Perspective, 2nd edn., Oxford University Press, New York, (2005).

[231] R.F. Domingos, N. Tufenkji, K.J. Wilkinson, Aggregation of titanium dioxide nanoparticles: role of a fulvic acid, Environ Sci Technol, 43 (2009) 1282-1286.

[232] J.T. Quik, I. Velzeboer, M. Wouterse, A.A. Koelmans, D. van de Meent, Heteroaggregation and sedimentation rates for nanomaterials in natural waters, Water Res, 48 (2014) 269-279.

[233] J.T.K. Quik, M.C. Stuart, M. Wouterse, W. Peijnenburg, A.J. Hendriks, D. van de Meent, Natural colloids are the dominant factor in the sedimentation of nanoparticles, Environ Toxicol Chem, 31 (2012) 1019-1022.

[234] J.M. Lopez-Lopez, A. Schmitt, A. Moncho-Jorda, R. Hidalgo-Alvarez, Stability of binary colloids: kinetic and structural aspects of heteroaggregation processes, Soft Matter, 2 (2006) 1025-1042.

[235] P.D. Yates, G.V. Franks, S. Biggs, G.J. Jameson, Heteroaggregation with nanoparticles: effect of particle size ratio on optimum particle dose, Colloid Surface A, 255 (2005) 85-90.

[236] H.R. Jafry, M.V. Liga, Q. Li, A.R. Barron, Simple route to enhanced photocatalytic activity of p25 titanium dioxide nanoparticles by silica addition, Environ Sci Technol, 45 (2011) 1563-1568.

[237] M.V. Liga, S.J. Maguire-Boyle, H.R. Jafry, A.R. Barron, Q.L. Li, Silica Decorated TiO2 for Virus Inactivation in Drinking Water - Simple Synthesis Method and Mechanisms of Enhanced Inactivation Kinetics, Environ Sci Technol, 47 (2013) 6463-6470.

[238] N. Siedl, S.O. Baumann, M.J. Elser, O. Diwald, Particle Networks from Powder Mixtures: Generation of TiO2-SnO2 Heterojunctions via Surface Charge-Induced Heteroaggregation, J Phys Chem C, 116 (2012) 22967-22973.

[239] C.B. Almquist, P. Biswas, Role of Synthesis Method and Particle Size of Nanostructured TiO2 on Its Photoactivity, J Catal, 212 (2002) 145-156.

[240] A. Nel, T. Xia, L. Madler, N. Li, Toxic potential of materials at the nanolevel, Science, 311 (2006) 622-627.

[241] C.O. Hendren, C.M. Powers, M.D. Hoover, S.L. Harper, The Nanomaterial Data Curation Initiative: A collaborative approach to assessing, evaluating, and advancing the state of the field, Beilstein journal of nanotechnology, 6 (2015) 1752-1762.

[242] P.A. Holden, J. Gardea-Torresdey, F. Klaessig, R.F. Turco, M. Mortimer, K. Hund-Rinke, E.A. Cohen Hubal, D. Avery, D. Barcelo, R. Behra, Considerations of Environmentally Relevant Test Conditions for Improved Evaluation of Ecological Hazards of Engineered Nanomaterials, Environ Sci Technol, (2016).

[243] M.R. Wiesner, G.V. Lowry, K.L. Jones, J. Hochella, Michael F, R.T. Di Giulio, E. Casman, E.S. Bernhardt, Decreasing Uncertainties in assessing environmental exposure, risk, and ecological implications of nanomaterials†‡, Environ Sci Technol, 43 (2009) 6458-6462.

[244] C.O. Hendren, G.V. Lowry, J.M. Unrine, M.R. Wiesner, A functional assay-based strategy for nanomaterial risk forecasting, Sci Total Environ, 536 (2015) 1029-1037.

[245] G.V. Lowry, B.P. Espinasse, A.R. Badireddy, C.J. Richardson, B.C. Reinsch, L.D. Bryant, A.J. Bone, A. Deonarine, S. Chae, M. Therezien, B.P. Colman, H. Hsu-Kim, E.S. Bernhardt, C.W. Matson, M.R. Wiesner, Long-Term Transformation and Fate of Manufactured Ag Nanoparticles in a Simulated Large Scale Freshwater Emergent Wetland, Environ Sci Technol, 46 (2012) 7027-7036.

[246] A.R. Badireddy, E.M. Hotze, S. Chellam, P.J.J. Alveraz, M.R. Wiesner, Inactivation of bacteriophages via photosensitization of fullerol nanoparticles, Environ. Sci. Technol., 41 (2007) 6627-6632.

[247] E.M. Hotze, A.R. Badireddy, S. Chellam, M.R. Wiesner, Mechanisms of Bacteriophage Inactivation via Singlet Oxygen Generation in UV Illuminated Fullerol Suspensions, Environ. Sci. Technol., 43 (2009) 6639-6645.

[248] L. Huang, M. Terakawa, T. Zhiyentayev, Y.-Y. Huang, Y. Sawayama, A. Jahnke, G.P. Tegos, T. Wharton, M.R. Hamblin, Innovative Cationic Fullerenes as Broad-Spectrum Light-Activated Antimicrobials, Nanomedicine: Nanotechnology, Biology, and Medicine, 6 (2010) 442-452.

[249] P. Morz, G.P. Tegos, H. Gali, T. Wharton, T. Sarna, M.R. Hamblin, Photodynamic therapy with fullerenes, Photochem. Photobiol. Sci., 6 (2007) 1139-1149.

[250] M.R. Hamblin, G. Jori, Photodynamic Inactivation of Microbial Pathogens: Medical and Environmental Applications, The Royal Society of Chemistry, Cambridge, UK, 2011.

[251] T. Kohn, M. Grandbois, K. McNeill, K.L. Nelson, Association with natural organic matter enhances the sunlight-mediated inactivation of MS2 coliphage by singlet oxygen, Environ. Sci. Technol., 41 (2007) 4626-4632.

[252] X.M. Yan, B.Y. Shi, D.S. Wang, H.X. Tang, The Eco-toxic aspects of aqueous nano-C-60 Fullerenes, Progr. Chem., 20 (2008) 422-428.

[253] J. Lee, M. Cho, J.D. Fortner, J.B. Hughes, J.H. Kim, Transformation of Aggregate C(60) in the Aqueous Phase by UV Irradiation, Environmental Science & Technology, 43 (2009) 4878-4883.

[254] E.M. Hotze, J. Labille, P.J.J. Alvarez, M. Wiesner, Mechanisms of photochemistry and reactive oxygen production by fullerene suspensions in water, Environ. Sci. Technol., 42 (2008) 4175-4180.

[255] P. Thevenot, J. Cho, D. Wavhal, R.B. Timmons, L.P. Tang, Surface chemistry influences cancer killing effect of TiO(2) nanoparticles, Nanomedicine-Nanotechnology Biology and Medicine, 4 (2008) 226-236.

[256] M.A. Rodgers, P.T. Snowden, Lifetime of O2(1Δg) in Liquid Water As Determined by Time-Resolved Infrared Luminescence Measurements, J. Amer. Chem. Soc., 104 (1982) 5541-5543.

[257] R.W. Redmond, I.E. Kochevar, Spatially Resolved Cellular Responses to Singlet Oxygen, Photochem. Photobiol., 82 (2006) 1178-1186.

[258] M. Cho, H. Chung, W. Choi, J. Yoon, Different inactivation behaviors of MS-2 phage and *Escherichia Coli* in TiO_2 photocatalytic disinfection, Appl. Environ. Microbiol., 71 (2005) 270-275.

[259] F. Rancan, S. Rosan, F. Boehm, A. Cantrell, M. Brellreich, H. Schoenberger, A. Hirsch, F. Moussa, Cytotoxicity and Photocytotoxicity of a Dendritic C_{60} mono-adduct and a Malonic Acid C_{60} Tris-adduct on Jurkat Cells, J. Photochem. Photobiol B: Biol., 67 (2002) 157-162.

[260] F. Käsermann, C. Kempf, Buckminsterfullerene and photodynamic inactivation of viruses, Rev. Med. Virol., 8 (1998) 143-151.

[261] J.Y. Kim, C. Lee, D.C. Love, D.L. Sedlak, J. Yoon, K.L. Nelson, Inactivation of MS2 Coliphage by Ferrous Ion and Zero-Valent Iron Nanoparticles, Environ. Sci. Technol., 45 (2011) 6978-6984.

[262] K.R. Wigginton, L. Menin, J.P. Montoya, T. Kohn, Oxidation of Virus Proteins during UV254 and Singlet Oxygen Mediated Inactivation, Environ. Sci. Technol., 44 (2010) 5437-5443.

[263] H. Grahn, P. Geladi, Techniques and Applications of Hyperspectral Image Analysis, John Wiley and Sons Ltd, Chichester, West Sussex, 2009.

[264] A. Barth, C. Zscherp, What vibrations tell us about proteins?, Q. Rev. Biophys., 35 (2002) 369-430.

[265] B.H. Stuart, Infrared Spectroscopy: Fundamentals and Applications, John Wiley & Sons Ltd, Chichester, West Sussex, 2004.

[266] A. Vainrub, O. Pustovyy, V. Vodyanoy, Resoltuion of 90 nm (x/5) in an Optical Transmission Microscope with an Annular Condenser, Optics Letters, 31 (2006) 2855-2857.

[267] D.C. Neckers, Rose bengal, J. Photochem. Photobiol. A: Chem., 47 (1989) 1-29.

[268] D. Jassby, J.F. Budarz, M.R. Wiesner, Impact of Aggregate Size and Structure on the Photocatalytic Properties of TiO_2 and ZnO Nanoparticles, Environ. Sci. Technol., (2012) DOI: 10.1021/es202009h.

[269] T. Ashikaga, A. Motoyama, H. Ichikawa, H. Itagaki, Y. Sato, Low-molecular Peptide Model of Protein Denaturation by UVA Irradiation and the Effect of Antioxidants, Alter. Anim. Tes. and Exper., 7 (2000) 30-36.

[270] J.P. McCormick, T. Thomason, Near-Ultraviolet Photooxidation of Tryptophan. Proof of Formation of Superoxide Ion, J. Am. Chem. Soc., 100 (1978) 312-313.

[271] E.W. Blanch, L. Hecht, C.D. Syme, V. Volpetti, G.P. Lomonossoff, K. Nielsen, L.D. Barron, Molecular Structure of Viruses from Raman Optical Activity, J. Gen. Virol., 83 (2002) 2593-2600.

[272] D.A. Kuzmanovic, I. Elashvili, C. Wick, C. O'Connell, S. Krueger, The MS2 Coat Protein Shell is Likely Assembled Under Tension: A Novel Role for the MS2 Bacteriophage A Protein as Revealed by Small-angle Neutron Scattering, J. Mol. Biol., 355 (2006) 1095-1111.

[273] M.J. Davies, Singlet oxygen-mediated damage to proteins and its consequences, Biochem. Biophys. Res. Commun., 305 (2003) 761-770.

[274] E. Shacter, Quantification and significance of protein oxidation in biological samples, Drug Metabol. Rev., 32 (2000) 307-326.

[275] J.C. Crittenden, R.R. Trussell, D.W. Hand, K.J. Howe, G. Tchobanoglous, Water Treatment: Principles and Design, 2 ed., John Wiley & Sons, Inc., Hoboken, NJ, 2005.

[276] J. Lee, Y. Mackeyev, M. Cho, D. Li, J.H. Kim, L.J. Wilson, P.J.J. Alvarez, Photochemical and Antimicrobial Properties of Novel C(60) Derivatives in Aqueous Systems, Environmental Science & Technology, 43 (2009) 6604-6610.

[277] T. Kohn, K.L. Nelson, Sunlight-mediated inactivation of MS2 coliphage via exogenous singlet oxygen produced by sensitizers in natural waters, Environ. Sci. Technol., 41 (2007) 192-197.

[278] D.M. Guldi, P.V. Kamat, Photophysical properties of pristine fullerenes, functionalized fullerenes, and fullerene-contianing donor-bridge acceptor systems, in: K.M. Kadish, R.S. Ruoff (Eds.) Fullerenes, Wiley-Interscience, New York, NY, 2000, pp. 225-281.

[279] A. Weir, P. Westerhoff, L. Fabricius, K. Hristovski, N. Von Goetz, Titanium dioxide nanoparticles in food and personal care products, Environ Sci Technol, 46 (2012) 2242-2250.

[280] O. Carp, C.L. Huisman, A. Reller, Photoinduced reactivity of titanium dioxide, Progress in solid state chemistry, 32 (2004) 33-177.

[281] S. Malato, P. Fernández-Ibáñez, M. Maldonado, J. Blanco, W. Gernjak, Decontamination and disinfection of water by solar photocatalysis: recent overview and trends, Catalysis Today, 147 (2009) 1-59.

[282] H. Choi, S.R. Al-Abed, D.D. Dionysiou, E. Stathatos, P. Lianos, TiO 2-based advanced oxidation nanotechnologies for water purification and reuse, Sustainability science and engineering, 2 (2010) 229-254.

[283] M. Lu, P. Pichat, Photocatalysis and water purification: from fundamentals to recent applications, John Wiley & Sons, 2013.

[284] F. Loosli, P. Le Coustumer, S. Stoll, TiO 2 nanoparticles aggregation and disaggregation in presence of alginate and Suwannee River humic acids. pH and concentration effects on nanoparticle stability, Water Res, 47 (2013) 6052-6063.

[285] M. Abdullah, G.K. Low, R.W. Matthews, Effects of common inorganic anions on rates of photocatalytic oxidation of organic carbon over illuminated titanium dioxide, J Phys Chem-Us, 94 (1990) 6820-6825.

[286] H. Chen, O. Zahraa, M. Bouchy, Inhibition of the adsorption and photocatalytic degradation of an organic contaminant in an aqueous suspension of TiO 2 by inorganic ions, Journal of Photochemistry and Photobiology A: Chemistry, 108 (1997) 37-44.

[287] R.A. Burns, J.C. Crittenden, D.W. Hand, V.H. Selzer, L.L. Sutter, S.R. Salman, Effect of inorganic ions in heterogeneous photocatalysis of TCE, Journal of Environmental Engineering, 125 (1999) 77-85.

[288] M. Mehrvar, W.A. Anderson, M. Moo-Young, Photocatalytic degradation of aqueous organic solvents in the presence of hydroxyl radical scavengers, International Journal of photoenergy, 3 (2001) 187-191.

[289] K. Wang, J. Zhang, L. Lou, S. Yang, Y. Chen, UV or visible light induced photodegradation of AO7 on TiO 2 particles: the influence of inorganic anions, Journal of Photochemistry and Photobiology A: Chemistry, 165 (2004) 201-207.

[290] M.H. Habibi, A. Hassanzadeh, S. Mahdavi, The effect of operational parameters on the photocatalytic degradation of three textile azo dyes in aqueous TiO 2 suspensions, Journal of Photochemistry and Photobiology A: Chemistry, 172 (2005) 89-96.

[291] C. Guillard, E. Puzenat, H. Lachheb, A. Houas, J.-M. Herrmann, Why inorganic salts decrease the TiO2 photocatalytic efficiency, International Journal of Photoenergy, 7 (2005) 1-9.

[292] A. Lair, C. Ferronato, J.-M. Chovelon, J.-M. Herrmann, Naphthalene degradation in water by heterogeneous photocatalysis: an investigation of the influence of inorganic anions, Journal of Photochemistry and Photobiology A: Chemistry, 193 (2008) 193-203.

[293] M. Kerzhentsev, C. Guillard, J.-M. Herrmann, P. Pichat, Photocatalytic pollutant removal in water at room temperature: case study of the total degradation of the insecticide fenitrothion (phosphorothioic acid O, O-dimethyl-O-(3-methyl-4-nitro-phenyl) ester), Catalysis Today, 27 (1996) 215-220.

[294] G.E. Brown, V.E. Henrich, W.H. Casey, D.L. Clark, C. Eggleston, A. Felmy, D.W. Goodman, M. Grätzel, G. Maciel, M.I. McCarthy, Metal oxide surfaces and their interactions with aqueous solutions and microbial organisms, Chem Rev, 99 (1999) 77-174.

[295] M.A. Anderson, D.T. Malotky, The adsorption of protolyzable anions on hydrous oxides at the isoelectric pH, J Colloid Interf Sci, 72 (1979) 413-427.

[296] S.B. Johnson, G.E. Brown, T.W. Healy, P.J. Scales, Adsorption of organic matter at mineral/water interfaces. 6. Effect of inner-sphere versus outer-sphere adsorption on colloidal stability, Langmuir, 21 (2005) 6356-6365.

[297] U. Diebold, The surface science of titanium dioxide, Surf Sci Rep, 48 (2003) 53-229.

[298] A. Fernandez-Nieves, F. De Las Nieves, The role of ζ potential in the colloidal stability of different TiO 2/electrolyte solution interfaces, Colloids and Surfaces A: Physicochemical and Engineering Aspects, 148 (1999) 231-243.

[299] R.A. French, A.R. Jacobson, B. Kim, S.L. Isley, R.L. Penn, P.C. Baveye, Influence of ionic strength, pH, and cation valence on aggregation kinetics of titanium dioxide nanoparticles, Environ Sci Technol, 43 (2009) 1354-1359.

[300] A.A. Keller, H. Wang, D. Zhou, H.S. Lenihan, G. Cherr, B.J. Cardinale, R. Miller, Z. Ji, Stability and aggregation of metal oxide nanoparticles in natural aqueous matrices, Environ Sci Technol, 44 (2010) 1962-1967.

[301] A.R. Petosa, D.P. Jaisi, I.R. Quevedo, M. Elimelech, N. Tufenkji, Aggregation and deposition of engineered nanomaterials in aquatic environments: role of physicochemical interactions, Environ Sci Technol, 44 (2010) 6532-6549.

[302] Y.H. Shih, W.S. Liu, Y.F. Su, Aggregation of stabilized TiO2 nanoparticle suspensions in the presence of inorganic ions, Environ Toxicol Chem, 31 (2012) 1693-1698.

[303] N. Solovitch, J.r.m. Labille, J.r.m. Rose, P. Chaurand, D. Borschneck, M.R. Wiesner, J.-Y. Bottero, Concurrent aggregation and deposition of TiO2 nanoparticles in a sandy porous media, Environ Sci Technol, 44 (2010) 4897-4902.

[304] M. Kosmulski, The significance of the difference in the point of zero charge between rutile and anatase, Adv Colloid Interfac, 99 (2002) 255-264.

[305] P. Velikovská, P. Mikulášek, The influence of Cl−, SO 4 2− and PO 4 3− ions on the ζ-potential and microfiltration of titanium dioxide dispersions, Separation and Purification Technology, 58 (2007) 295-298.

[306] B.P. Nelson, R. Candal, R.M. Corn, M.A. Anderson, Control of surface and ζ potentials on nanoporous TiO2 films by potential-determining and specifically adsorbed ions, Langmuir, 16 (2000) 6094-6101.

[307] V. Kazarinov, V. Andreev, A. Mayorov, Investigation of the adsorption properties of the TiO2 electrode by the radioactive tracer method, Journal of Electroanalytical Chemistry and Interfacial Electrochemistry, 130 (1981) 277-285.

[308] W. Stumm, The inner-sphere surface complex: A key to understanding surface reactivity, Advances in chemistry series, 244 (1995) 1-1.

[309] L.-F. Liao, C.-F. Lien, D.-L. Shieh, M.-T. Chen, J.-L. Lin, FTIR study of adsorption and photoassisted oxygen isotopic exchange of carbon monoxide, carbon dioxide, carbonate, and formate on TiO2, The Journal of Physical Chemistry B, 106 (2002) 11240-11245.

[310] R. Luschtinetz, J. Frenzel, T. Milek, G. Seifert, Adsorption of phosphonic acid at the TiO2 anatase (101) and rutile (110) surfaces, The Journal of Physical Chemistry C, 113 (2009) 5730-5740.

[311] K.D. Kwon, J.D. Kubicki, Molecular orbital theory study on surface complex structures of phosphates to iron hydroxides: Calculation of vibrational frequencies and adsorption energies, Langmuir, 20 (2004) 9249-9254.

[312] S.J. Hug, D. Bahnemann, Infrared spectra of oxalate, malonate and succinate adsorbed on the aqueous surface of rutile, anatase and lepidocrocite measured with in situ ATR-FTIR, Journal of electron spectroscopy and related phenomena, 150 (2006) 208-219.

[313] J.-M. Herrmann, P. Pichat, Heterogeneous photocatalysis. Oxidation of halide ions by oxygen in ultraviolet irradiated aqueous suspension of titanium dioxide, Journal of the Chemical Society, Faraday Transactions 1: Physical Chemistry in Condensed Phases, 76 (1980) 1138.

[314] A. Rincon, Effect of pH, inorganic ions, organic matter and H2O2 on E. coli K12 photocatalytic inactivation by TiO2Implications in solar water disinfection, Applied Catalysis B: Environmental, 51 (2004) 283-302.

[315] Y. Katsumura, P. Jiang, R. Nagaishi, T. Oishi, K. Ishigure, Y. Yoshida, Pulse radiolysis study of aqueous nitric acid solutions: formation mechanism, yield, and reactivity of NO3 radical, The Journal of Physical Chemistry, 95 (1991) 4435-4439.

[316] J. Kochany, E. Lipczynska-Kochany, Application of the EPR spin-trapping technique for the investigation of the reactions of carbonate, bicarbonate, and phosphate anions with hydroxyl radicals generated by the photolysis of H 2 O 2, Chemosphere, 25 (1992) 1769-1782.

[317] J. Holcman, T. Løgager, K. Sehested, Reactions of peroxodisulphate and SO 4-with selected radicals in aqueous solution, Laboratory Studies on Atmospheric Chemistry, (1992).

[318] L.E. Gomez, Use and benefits of chlorpyrifos in US agriculture, Dow AgroSciences LLC, (2009).

[319] Z. Chishti, S. Hussain, K.R. Arshad, A. Khalid, M. Arshad, Microbial degradation of chlorpyrifos in liquid media and soil, Journal of environmental management, 114 (2013) 372-380.

[320] S. Armenta, G. Quintás, S. Garrigues, M. de la Guardia, A validated and fast procedure for FTIR determination of Cypermethrin and Chlorpyrifos, Talanta, 67 (2005) 634-639.

[321] S.Y. Gebremariam, M.W. Beutel, D.R. Yonge, M. Flury, J.B. Harsh, Adsorption and Desorption of Chlorpyrifos to Soils and Sediments, Rev Environ Contam T, 215 (2012) 123-175.

[322] S. Baskaran, R.S. Kookana, R. Naidu, Contrasting behaviour of chlorpyrifos and its primary metabolite, TCP (3,5,6-trichloro-2-pyridinol), with depth in soil profiles, Aust J Soil Res, 41 (2003) 749-760.

[323] R.J. Gilliom, J.E. Barbash, C.G. Crawford, P.A. Hamilton, J.D. Martin, N. Nakagaki, L.H. Nowell, J.C. Scott, P.E. Stackelberg, G.P. Thelin, Pesticides in the nation's streams and ground water, 1992-2001, Geological Survey (US), 2006.

[324] E. Estevez, M. del Carmen Cabrera, J.R. Fernández-Vera, A. Molina-Díaz, J. Robles-Molina, M. del Pino Palacios-Díaz, Monitoring priority substances, other organic contaminants and heavy metals in a volcanic aquifer from different sources and hydrological processes, Sci Total Environ, 551 (2016) 186-196.

[325] M.P. Ensminger, R. Budd, K.C. Kelley, K.S. Goh, Pesticide occurrence and aquatic benchmark exceedances in urban surface waters and sediments in three urban areas of California, USA, 2008–2011, Environmental monitoring and assessment, 185 (2013) 3697-3710.

[326] K.D. Racke, D.D. Fontaine, R.N. Yoder, J.R. Miller, Chlorpyrifos degradation in soil at termiticidal application rates, Pestic Sci, 42 (1994) 43-51.

[327] K.R. Solomon, W.M. Williams, D. Mackay, J. Purdy, J.M. Giddings, J.P. Giesy, Properties and uses of chlorpyrifos in the United States, Reviews of environmental contamination and toxicology, 231 (2014) 13-34.

[328] A.W. Jarvinen, B.R. Nordling, M.E. Henry, Chronic toxicity of Dursban (chlorpyrifos) to the fathead minnow (Pimephales promelas) and the resultant acetylcholinesterase inhibition, Ecotoxicology and environmental safety, 7 (1983) 423-434.

[329] J.P. Giesy, K.R. Solomon, J.R. Coats, K.R. Dixon, J.M. Giddings, E.E. Kenaga, Chlorpyrifos: ecological risk assessment in North American aquatic environments, Springer, 1999.

[330] D.L. Eaton, R.B. Daroff, H. Autrup, J. Bridges, P. Buffler, L.G. Costa, J. Coyle, G. McKhann, W.C. Mobley, L. Nadel, D. Neubert, R. Schulte-Hermann, P.S. Spencer, Review of the toxicology of chlorpyrifos with an emphasis on human exposure and neurodevelopment, Critical reviews in toxicology, 38 Suppl 2 (2008) 1-125.

[331] M.E. DeLorenzo, G.I. Scott, P.E. Ross, Toxicity of pesticides to aquatic microorganisms: a review, Environ Toxicol Chem, 20 (2001) 84-98.

[332] L.G. Devi, B.N. Murthy, S.G. Kumar, Photocatalytic activity of V5+, Mo6+ and Th4+ doped polycrystalline TiO2 for the degradation of chlorpyrifos under UV/solar light, Journal of Molecular Catalysis A: Chemical, 308 (2009) 174-181.

[333] J. Risher, H.A. Navarro, Toxicological profile for chlorpyrifos, US Department of Health and Human Services, Altanta, (1997).

[334] D. Qiao, F.J. Seidler, T.A. Slotkin, Developmental neurotoxicity of chlorpyrifos modeled in vitro: Comparative effects of metabolites and other cholinesterase inhibitors on DNA synthesis in PC12 and C6 cells, Environ Health Persp, 109 (2001) 909-913.

[335] S. Baskaran, R.S. Kookana, R. Naidu, Degradation of bifenthrin, chlorpyrifos and imidacloprid in soil and bedding materials at termiticidal application rates, Pestic Sci, 55 (1999) 1222-1228.

[336] E.M. John, J.M. Shaike, Chlorpyrifos: pollution and remediation, Environmental Chemistry Letters, 13 (2015) 269-291.

[337] J.M. Smolen, A.T. Stone, Metal (hydr)oxide surface catalyzed hydrolysis of chlorpyrifos-methyl, chlorpyrifos-methyl oxon, and paraoxon, Soil Sci Soc Am J, 62 (1998) 636-643.

[338] M.T. Rose, A.N. Crossan, I.R. Kennedy, Dissipation of cotton pesticides from runoff water in glasshouse columns, Water, air, and soil pollution, 182 (2007) 207-218.

[339] D.S. Bhatkhande, V.G. Pangarkar, A.A.C.M. Beenackers, Photocatalytic degradation for environmental applications - a review, Journal of Chemical Technology & Biotechnology, 77 (2002) 102-116.

[340] U.I. Gaya, A.H. Abdullah, Heterogeneous photocatalytic degradation of organic contaminants over titanium dioxide: A review of fundamentals, progress and problems, Journal of Photochemistry and Photobiology C: Photochemistry Reviews, 9 (2008) 1-12.

[341] C. McCullagh, N. Skillen, M. Adams, P.K.J. Robertson, Photocatalytic reactors for environmental remediation: a review, Journal of Chemical Technology & Biotechnology, 86 (2011) 1002-1017.

[342] M.M. Khin, A.S. Nair, V.J. Babu, R. Murugan, S. Ramakrishna, A review on nanomaterials for environmental remediation, Energy & Environmental Science, 5 (2012) 8075.

[343] S. Kwon, M. Fan, A.T. Cooper, H. Yang, Photocatalytic Applications of Micro- and Nano-TiO2in Environmental Engineering, Critical Reviews in Environmental Science and Technology, 38 (2008) 197-226.

[344] A. Dârjan, C. Drăghici, D. Perniu, A. Duţă, Degradation of Pesticides by TiO2 Photocatalysis, (2013) 155-163.

[345] T. Ochiai, A. Fujishima, Photoelectrochemical properties of TiO2 photocatalyst and its applications for environmental purification, Journal of Photochemistry and Photobiology C: Photochemistry Reviews, 13 (2012) 247-262.

[346] A.C. Affam, M. Chaudhuri, Degradation of pesticides chlorpyrifos, cypermethrin and chlorothalonil in aqueous solution by TiO 2 photocatalysis, Journal of environmental management, 130 (2013) 160-165.

[347] A. Fadaei, M. Kargar, Photocatalytic degradation of chlorpyrifos in water using titanium dioxide and zinc oxide, Fresenius Environmental Bulletin, 22 (2013) 2442-2447.

[348] A.S. Nair, T. Pradeep, Extraction of chlorpyrifos and malathion from water by metal nanoparticles, J Nanosci Nanotechno, 7 (2007) 1871-1877.

[349] A. Torrents, A.T. Stone, Oxide surface-catalyzed hydrolysis of carboxylate esters and phosphorothioate esters, Soil Sci Soc Am J, 58 (1994) 738-745.

[350] L. Clausen, I. Fabricius, Atrazine, isoproturon, mecoprop, 2, 4-D, and bentazone adsorption onto iron oxides, J Environ Qual, 30 (2001) 858-869.

[351] T. Hofmann, F. von der Kammer, Estimating the relevance of engineered carbonaceous nanoparticle facilitated transport of hydrophobic organic contaminants in porous media, Environmental pollution, 157 (2009) 1117-1126.

[352] M.N. Moore, Do nanoparticles present ecotoxicological risks for the health of the aquatic environment?, Environ Int, 32 (2006) 967-976.

[353] L. Wang, Y. Huang, A.T. Kan, M.B. Tomson, W. Chen, Enhanced transport of 2,2',5,5'-polychlorinated biphenyl by natural organic matter (NOM) and surfactant-modified fullerene nanoparticles (nC60), Environ Sci Technol, 46 (2012) 5422-5429.

[354] N. Pino, G. Peñuela, Simultaneous degradation of the pesticides methyl parathion and chlorpyrifos by an isolated bacterial consortium from a contaminated site, International Biodeterioration & Biodegradation, 65 (2011) 827-831.

[355] B.K. Singh, A. Walker, J.A. Morgan, D.J. Wright, Biodegradation of chlorpyrifos by enterobacter strain B-14 and its use in bioremediation of contaminated soils, Applied and environmental microbiology, 70 (2004) 4855-4863.

[356] B.K. Singh, A. Walker, J.A.W. Morgan, D.J. Wright, Effects of Soil pH on the Biodegradation of Chlorpyrifos and Isolation of a Chlorpyrifos-Degrading Bacterium, Applied and environmental microbiology, 69 (2003) 5198-5206.

[357] J.M. Bifulco, J. Shirey, G. Bissonnette, Detection of Acinetobacter spp. in rural drinking water supplies, Applied and environmental microbiology, 55 (1989) 2214-2219.

[358] S. Anwar, F. Liaquat, Q.M. Khan, Z.M. Khalid, S. Iqbal, Biodegradation of chlorpyrifos and its hydrolysis product 3,5,6-trichloro-2-pyridinol by Bacillus pumilus strain C2A1, J Hazard Mater, 168 (2009) 400-405.

[359] F. Ahmad, S. Iqbal, S. Anwar, M. Afzal, E. Islam, T. Mustafa, Q.M. Khan, Enhanced remediation of chlorpyrifos from soil using ryegrass (Lollium multiflorum) and chlorpyrifos-degrading bacterium Bacillus pumilus C2A1, J Hazard Mater, 237 (2012) 110-115.

[360] Y. Ge, J.P. Schimel, P.A. Holden, Evidence for negative effects of TiO2 and ZnO nanoparticles on soil bacterial communities, Environ Sci Technol, 45 (2011) 1659-1664.

[361] G. Imfeld, S. Vuilleumier, Measuring the effects of pesticides on bacterial communities in soil: A critical review, European Journal of Soil Biology, 49 (2012) 22-30.

[362] P. Palma, V.L. Palma, R.M. Fernandes, A.M. Soares, I.R. Barbosa, Acute toxicity of atrazine, endosulfan sulphate and chlorpyrifos to Vibrio fischeri, Thamnocephalus platyurus and Daphnia magna, relative to their concentrations in surface waters from the Alentejo region of Portugal, Bull Environ Contam Toxicol, 81 (2008) 485-489.

[363] T.J. Battin, F.V. Kammer, A. Weilhartner, S. Ottofuelling, T. Hofmann, Nanostructured TiO2: transport behavior and effects on aquatic microbial communities under environmental conditions, Environ Sci Technol, 43 (2009) 8098-8104.

[364] L.K. Adams, D.Y. Lyon, P.J. Alvarez, Comparative eco-toxicity of nanoscale TiO 2, SiO 2, and ZnO water suspensions, Water Res, 40 (2006) 3527-3532.

[365] M. Biguzzi, G. Shama, Effect of titanium dioxide concentration on the survival of Pseudomonas stutzeri during irradiation with near ultraviolet light, Letters in Applied Microbiology, 19 (1994) 458-460.

[366] D.Y. Lyon, L.K. Adams, J.C. Falkner, P.J.J. Alvarez, Antibacterial activity of fullerene water suspensions: Effects of preparation method and particle size, Environ Sci Technol, 40 (2006) 4360-4366.

[367] V.G.G. Kanmoni, S. Daniel, G.A.G. Raj, Photocatalytic degradation of chlorpyrifos in aqueous suspensions using nanocrystals of ZnO and TiO2, Reaction Kinetics, Mechanisms and Catalysis, 106 (2012) 325-339.

[368] K. Sivagami, R.R. Krishna, T. Swaminathan, Photo Catalytic Degradation of Chlorpyriphos in an Annular Slurry Reactor, Journal of Water Sustainability, 3 (2013) 143-151.

[369] A. Verma, D. Dixit, Photocatalytic degradability of insecticide Chlorpyrifos over UV irradiated Titanium dioxide in aqueous phase, International Journal of Environmental Sciences, 3 (2012) 743-755.

[370] M.J. Redondo, M.J. Ruiz, G. Font, R. Boluda, Dissipation and distribution of atrazine, simazine, chlorpyrifos, and tetradifon residues in citrus orchard soil, Arch Environ Con Tox, 32 (1997) 346-352.

[371] S.E. Duirk, T.W. Collette, Degradation of chlorpyrifos in aqueous chlorine solutions: Pathways, kinetics, and modeling, Environ Sci Technol, 40 (2006) 546-551.

[372] K.L. Armbrust, Pesticide hydroxyl radical rate constants: measurements and estimates of their importance in aquatic environments, Environ Toxicol Chem, 19 (2000) 2175-2180.

[373] F. Wilkinson, W.P. Helman, A.B. Ross, Rate constants for the decay and reactions of the lowest electronically excited state of molecular oxygen in solution. An expanded and revised compliation, Journal of Physical and Chemical Reference Data, 34 (1995) 663-1021.

[374] A.A. Green, M. Berman, P. Switzer, M.D. Craig, A Transformation for ordering multispectral data in terms of image quality with implications for noise removal, IEEE Trans. Geosci. Rem. Sen., 26 (1988) 65-74.

[375] U.K. Laemmli, Cleavage of structural proteins during the assembly of the head of bacteriophage T4, Nature, 227 (1970) 680-685.

[376] I. Grčić, G. Li Puma, Photocatalytic degradation of water contaminants in multiple photoreactors and evaluation of reaction kinetic constants independent of photon absorption, irradiance, reactor geometry, and hydrodynamics, Environ Sci Technol, 47 (2013) 13702-13711.

Biography

Jeffrey Michael Farner Budarz was born on September 14, 1981 in Lafayette, Indiana. He received his BS in Chemistry from Purdue University in December of 2004 following interludes at Barrett, the Honors College at Arizona State University and Université Louis Pasteur in Strasbourg, France. After obtaining his undergraduate degree, he worked for Iowa's State Hygienic Lab, as an analytical chemist, performing water quality analyses for compliance with the EPA's SDWA and FIFRA. In August of 2008, he began his graduate work at Duke University in the Department of Civil and Environmental Engineering. He has authored or co-authored the following articles: Experimental Measurement and Modeling of Reactive Species Generation in TiO_2 Nanoparticle Photocatalysis. *Chem Eng J*, 2015; Formation and Persistence of Silver Nanoparticles in Visible Light Illuminated Aquatic Systems and their Effect on Bacterial Lysis. *EES*, 2014; Bacteriophage Inactivation by UV-A Illuminated Fullerenes: Role of Nanoparticle-Virus Association and Biological Targets. *ES&T,* 2012; Impact of Aggregate Size and Structure on the Photocatalytic Properties of TiO_2 and ZnO Nanoparticles. *ES&T*, 2012; Comparison of the Photosensitivity and Bacterial Toxicity of Spherical and Tubular Fullerenes of Variable Aggregate Size. *J Nano Res*, 2011; Heterogeneities in Fullerene Nanoparticle Aggregates Affecting Reactivity, Bioactivity, and Transport. *ACS Nano*, 2010. During his graduate work, Jeff received the Jeffrey B. Taub award from the Department of Civil and Environmental Engineering in 2011 and 2012.